Study and modelling of very high energy electrons (VHEE) radiation therapy

Maria Grazia Ronga

université PARIS-SACLAY

Study and modelling of very high energy electrons (VHEE) radiation therapy

Etude et modélisation de la radiothérapie par électrons de très haute énergie (VHEE)

Thèse de doctorat de l'université Paris-Saclay

École doctorale n°575 electrical, optical, bio : physics and engineering (EOBE)
Spécialité de doctorat: Physique et imagerie médicale
Graduate School : Sciences de l'ingénierie et des systèmes.
Référent : Faculté des Sciences d'Orsay

Thèse préparée dans l'unité de recherche **Laboratoire d'Imagerie Translationnelle en Oncologie (LITO), U1288 Inserm, Institut Curie, 91898, Orsay** sous la direction d'**Irène BUVAT**, Directrice de recherche, le co-encadrement de **Ludovic DE MARZI**, Physicien médical, et de **Pascal GIRAULT**, Responsable Developpement Science

Thèse soutenue à Paris, le 11 avril 2024, par

Maria Grazia RONGA

Composition du jury

Membres du jury avec voix délibérative

Elias KHAN Professeur, Université Paris-Saclay	Président
Magdalena BAZALOVA CARTER Professeure associée, University of Victoria	Rapporteure & Examinatrice
Vincenzo PATERA Professeur, Université La Sapienza	Rapporteur & Examinateur
Rachel DELORME Chercheuse, Université Grenoble Alpes	Examinatrice
Stéphane SUPIOT Médecin-chercheur, Nantes Université	Examinateur

THESE DE DOCTORAT

NNT : 2024UPAST036

université PARIS-SACLAY

ÉCOLE DOCTORALE
Physique et ingénierie : Electrons, Photons, Sciences du vivant (EOBE)

Titre: Etude et modélisation de la radiothérapie par électrons de très haute énergie (VHEE)
Mots clés: radiothérapie; électrons de très haute énergie; thérapie FLASH à très haut débit de dose; simulations de Monte Carlo; dose secondaire.

Résumé: Le développement de méthodes innovantes susceptibles de réduire la sensibilité des tissus sains aux radiations, tout en maintenant l'efficacité du traitement sur la tumeur, est un aspect central de l'amélioration de l'efficacité de la radiothérapie pour le traitement du cancer. Parmi les développements et innovations méthodologiques possibles, la combinaison d'une irradiation à ultra-haut débit de dose (FLASH) et d'électrons de très haute énergie (VHEE) pourrait permettre d'exploiter les avantages radiobiologiques de l'effet FLASH pour le traitement des tumeurs profondes. En particulier, les VHEEs dans la gamme d'énergie de 100 à 250 MeV seraient particulièrement intéressants d'un point de vue balistique et biologique pour l'application des irradiations FLASH en radiothérapie. Cette thèse étudie donc l'utilisation possible des VHEEs en radiothérapie et en particulier leur utilisation à ultra-haut débit de dose, évaluant ainsi la faisabilité de la radiothérapie FLASH-VHEE. Bien que prometteuse, plusieurs aspects de cette technique doivent être étudiés avant qu'elle puisse être employée dans un contexte clinique. Une première partie du travail étudie les paramètres de la machine nécessaires pour répondre aux contraintes des irradiations FLASH. À cette fin, un modèle analytique de calcul de la dose basé sur la théorie de la diffusion multiple de Fermi-Eyges a été développé et testé. Ce modèle analytique a également été utilisé pour concevoir et optimiser un système de double diffusion pour la thérapie VHEE et ainsi obtenir des tailles de champ supérieures à 15x15 cm^2, et pour évaluer la possible adaptation des méthodes de conformation conventionnelles du faisceau de particules pour la thérapie FLASH-VHEE. La deuxième partie de ce travail porte sur la planification du traitement par VHEE et l'évaluation des plans cliniques. Quatre cas cliniques représentatifs ont été étudiés, pour lesquels des plans de traitement par balayage de mini-faisceau (PBS) et par double diffusion (DS) ont été calculés. L'influence de l'énergie du faisceau sur la qualité du plan a été étudiée et les techniques PBS et DS ont été comparées. Une description temporelle de l'irradiation a également été réalisée ainsi que l'incorporation d'un facteur de modification FLASH lors de l'évaluation du plan et de son effet sur les tissus sains en mode FLASH. Enfin, l'estimation des doses liées aux particules secondaires et les questions de radioprotection ont été abordées. Un calcul de la dose secondaire due aux photons de Bremsstrahlung et aux neutrons provenant des deux systèmes de délivrance de la dose a été développé dans l'eau. La dose due aux particules secondaires reçues par divers organes a également été évaluée dans le cadre de traitements intracrâniens et afin de démontrer l'avantage des faisceaux VHEE par rapport aux faisceaux de protons en terme de dose neutrons hors champ. En résumé, les modèles analytiques accélérés et paramétrés dans cette étude permettent une estimation de la distribution de la dose produite par un système VHEE avec une bonne précision, ce qui fournit des informations importantes pour la conception éventuelle d'un système VHEE. Les résultats de ce travail pourraient soutenir le développement de la radiothérapie FLASH-VHEE.

université PARIS-SACLAY

ÉCOLE DOCTORALE
Physique et ingénierie : Electrons, Photons, Sciences du vivant (EOBE)

Title: Study and modelling of very high energy electrons (VHEE) radiation therapy
Keywords: radiotherapy; very high energy electrons; ultra-high dose rate FLASH therapy; Monte Carlo simulations; secondary dose.

Abstract: The development of innovative methods capable of reducing the sensitivity of healthy tissue to radiation, while maintaining the effectiveness of the treatment on the tumour, is a central aspect of improving the effectiveness of radiotherapy in the treatment of cancer. Among possible developments and methodological innovations, the combination of ultra-high dose rate irradiation (FLASH) and very high energy electrons (VHEE) could make it possible to exploit the radiobiological advantages of the FLASH effect for the treatment of deep tumours. In particular, VHEEs in the 100 to 250 MeV energy range would be particularly interesting from a ballistic and biological point of view for the application of FLASH irradiation in radiotherapy. This thesis therefore studies the possible use of VHEEs in radiotherapy, and in particular their use at ultra-high dose rates, thus assessing the feasibility of FLASH-VHEE radiotherapy. Although promising, several aspects of this technique need to be studied before it can be used in a clinical context. The first part of this work studies the machine parameters required to meet the constraints of FLASH irradiation. To this end, an analytical model for calculating the dose based on Fermi-Eyges multiple scattering theory was developed and tested. This analytical model has also been used to design and optimise a double-scattering system for VHEE therapy, in order to obtain field sizes greater than 15x15 cm^2, and to assess the possible adaptation of conventional particle beam conformation methods for FLASH-VHEE therapy. The second part of this work focuses on VHEE treatment planning and the evaluation of clinical plans. Four representative clinical cases were studied, for which pencil-beam scanning (PBS) and double scattering (DS) treatment plans were calculated. The influence of beam energy on plan quality was studied and the PBS and DS techniques were compared. A temporal description of the irradiation was also carried out, as well as the incorporation of a FLASH modification factor when evaluating the plan and its effect on healthy tissue in FLASH mode. Finally, the estimation of doses from secondary particles and radiation protection issues were addressed. A calculation of the secondary dose due to Bremsstrahlung photons and neutrons from the two dose delivery systems was developed in water. The secondary particle dose received by various organs was also assessed in the context of intracranial treatments and in order to demonstrate the advantage of VHEE beams over proton beams in terms of out-of-field neutron dose. In summary, the fast analytical models parameterised in this study allow the dose distribution produced by a VHEE system to be estimated with good accuracy, providing important information for the potential design of a VHEE system. The results of this work could support the development of FLASH-VHEE radiotherapy.

Contents

List of Acronyms

ADR Average Dose Rate

BED Biological Effective Dose

CCD Charge-Coupled Device

CONV Conventional dose rate

CPO Centre de Protonthérapie d'Orsay

CT Computed Tomography

CVD Chemical Vapour Deposition

DADR Dose-Averaged Dose Rate

DEAR Dynamic Electron Arc Radiotherapy

DKFZ Deutsches Krebsforschungszentrum Institute

DRVHs Dose Rate Volume Histograms

DS Double Scattering

DSBs Double-Strand Breaks

DTDR Dose Threshold Dose Rate

DVHs Dose Volume Histograms

EAT Electron Arc Therapy

EBRT External Beam Radiotherapy

EPR Electron Paramagnetic Resonance

FS Field Size

GTV Gross Tumour Volume

HI Homogeneity Index

ICRP International Commission on Radiological Protection

ICRU International Committee for Radiological Units

IMRT Intensity Modulated Radiotherapy

IOeRT Intraoperative electron Radiotherapy

IRSN Institut de Radioprotection et de Sûreté Nucléaire

LET Linear Energy Transfer

LOA Laboratoire d'Optique Appliquée

LPA Laser-Plasma Accelerators

LWFA Laser WakeField Acceleration

MC Monte Carlo

MERT Modulated Electron Radiation Therapy

MLC Multi-Leaf Collimators

NCI National Cancer Institute

NTCP Normal Tissue Complication Probability

NUPO Nonlinear Universal Proton Optimised algorithm

OAR Organs At Risk

PBS Pencil Beam Scanning

pPBS proton PBS

PDD Percentage Depth-Dose

PRF Pulse Repetition Frequency

PTV Planning Target Volume

PVT Polyvinyl Toluene

RBE Relative Biological Effectiveness

ROS Reactive Oxygen Species

RT Radiation Therapy

SAD Source Axis Distance

SDDRO Simultaneous Dose and Dose Rate Optimization

SFRT Spatially Fractionated Radiotherapy

SFUD Single Field Uniform Dose

SOBP Spread-Out Bragg Peak

SOEP Spread-Out Electron Peaks

SSBs Single-Strand Breaks

TCP Tumour Control Probability

TOPAS TOol for PArticle Simulation

TPSs Treatment Planning Systems

TR Therapeutic Range

TVLs Tenth-Value Layers

TVM Two-Voltage Method

UF University of Florida

UHDR Ultra-High Dose Rate

VHEE Very High Energy Electron

VMAT Volumetric Modulated Arc Therapy

WT Water Tank

Chapter 1

Introduction

Contents

1.1 General considerations and thesis outline

Cancer is one of the leading causes of disease/death worldwide, with around 14 million new cases and 8 million deaths each year. It is forecast that the incidence of newly diagnosed cancer cases worldwide will significantly increase from today's 18.1 million to 29.5 million by 2040 [1]. Radiotherapy has the potential to benefit approximately 50% of cancer patients during the course of their disease. However, major challenges remain as survival rates differ starkly between different cancer types – just 5% of those with lung or pancreas cancer survive 10 years after the diagnosis [2], with survival from pancreatic cancer barely improving at all, regardless of the radiotherapy technique used in these cases. The development of innovative approaches that would reduce the sensitivity of healthy tissues to irradiation while maintaining the efficacy of the treatment on the tumour is, therefore, of crucial importance for the progress of the efficacy of radiotherapy.

Very high energy electron radiotherapy could be a possible candidate to meet this need for a new type of irradiation technique. In particular, VHEE-RT would benefit from the potential radiobiological advantages of ultra-high dose rate pulsed irradiation. In this context, the aim of this thesis is to explore the possible use of very high energy electrons in radiotherapy and their potential application for ultra-high dose rate irradiation. The manuscript is structured as follows:

- Chapter 1 describes the use of ionising radiation in radiotherapy, the physics involved and the mechanisms underlying the biological response to radiation. It also introduces very high energy electrons, (history, ballistic properties, secondary particles) and their promising introduction in radiotherapy in combination with ultra-high dose rate irradiations. The ultra-high dose rate irradiations and their biological advantages are then presented. Finally, the MC simulation method is described, with a focus on the TOPAS toolkit used in the study.

- Chapter 2 discusses the Fermi-Eyges theory of multiple scattering and proposes a new parameterisation, for the VHEE energy range, for some of the quantities used in the theory. The model is then tested in water using MC simulations for broad beams and in the presence of inhomogeneities.

- In Chapter 3 the implemented model is used to study the application of two conformation techniques (pencil beam scanning and double scattering) for very high energy electrons. The experimental modelling of a laser plasma

electron beam (with an energy spectrum up to 300 MeV) and the modelling of a double scattering system for this laser accelerated beam are discussed.

- Chapter 4 focuses on treatment planning for very high energy electron beams. Four clinical cases are studied and a treatment plan for both conformation techniques is developed for each patient and then evaluated using MC simulations. The analytical model developed in Chapter 3 was also integrated into an open source treatment planning system software. The same treatment plans were also developed using this tool and evaluated by comparison with MC simulations.

- Chapter 5 examines the radiation protection issues associated with very high energy electrons. The production of secondary bremsstrahlung photons in water is investigated using MC simulation. In addition, the secondary dose from photons and neutrons for the treatment plans described in Chapter 4 is assessed for several organs and compared with the secondary dose from proton irradiations. The secondary dose contribution from a very high energy electron facility is also assessed.

This work (in the framework of a CIFRE contract) has been carried out as part of a collaboration between Institut Curie and Thales AVS-MIS to develop such VHEE-FLASH accelerator. The Institut Curie, a key player in the fight against cancer, indeed combines a world-renowned cancer research center with a state-of-the-art hospital complex that treats all cancers, including the rarest. Founded in 1909 by two-time Nobel Prize winner Marie Curie, the Institut Curie carry out the threefold mission of research, care, and the conservation and transmission of knowledge. The thesis took place in the Centre de Protonthérapie d'Orsay (CPO) (one of the three technical platforms of the Institut Curie's Radiotherapy Department), and at the U1288 Inserm/Institut Curie laboratory (Laboratoire d'Imagerie Translationnelle en Oncologie - LITO), which develops calculation models based on numerical simulations for oncology and methods for extracting parameters from images, known as radiomic characteristics, facilitating their objective and reproducible quantitative interpretation. Thales AVS MIS, a branch of the Thales group is a major player in power amplification and radiology. For more than 60 years, Thales AVS, through its "Thales Microwave and Imaging Sub-sytems" (MIS) entity, has been developing and producing radiofrequency tubes, X-ray detectors and power amplification solutions for sectors such as Space, Defence, Medical and Science.

1.2 Ionising Radiation Physics

Radiation can be divided into two categories: ionising and non-ionising radiation. Ionising radiation can ionise the atoms of the medium while it passes through matter when its energy is above the ionisation potential of the medium. In this process, the energy is transferred to the atomic electron of the medium being traversed, causing the electron to be ejected. Ionising radiation itself can be divided into two categories: directly and indirectly ionising radiation.

- *Directly ionising radiation* consists of charged particles, such as electrons, protons and heavy ions, which can interact directly with atomic electrons through the Coulomb force and ionise them. The interactions are continuous as the radiation passes through the medium, and at each interaction the beam particles lose a little bit of their energy and are continuously slowed down.
- *Indirectly ionising radiation* consists of neutral particles, such as photons (x or gamma rays) or neutrons. These radiations carry no electrical charge and can travel into the tissue before interacting, resulting in the emission of charged particles, which in turn deposit their energy through Coulomb interactions and further ionisation of atoms or molecules.

Both directly and indirectly ionising radiations are commonly used for the diagnosis and treatment of malignant diseases, so quantifying the energy released in radiation interactions is crucial for any clinical application [3].

1.2.1 Dosimetric Quantities

To describe radiation interactions, several quantities must be introduced. As mentioned above, the ionising radiation deposits its energy through interactions with the absorbing medium. The quantity that measures this loss of energy is the absorbed dose, often simply referred to as the dose. Absorbed dose is defined by the International Committee for Radiological Units (ICRU) in report 85 [4] as the ratio of the average energy delivered by the ionising radiation, $\mathrm{d}\bar{\epsilon}$, per unit mass, $\mathrm{d}m$:

$$D = \frac{\mathrm{d}\bar{\epsilon}}{\mathrm{d}m} \tag{1.1}$$

Its unit of measurement is Gray (Gy), equal to Jkg^{-1}. In 1990, the International Commission on Radiological Protection (ICRP) recommendation [5] introduced the radiation weighting factor, w_R, as an adimensional parameter to weight the absorbed dose by the type and energy of the radiation incident on human tissue. This weighted dose, called the equivalent dose, H_T, is thus defined as ICRP:

$$H_T = \sum_R w_R D_{T,R} \tag{1.2}$$

$D_{T,R}$ is the absorbed dose by the tissue T from radiation R. Although the equivalent dose, H_T, has the same dimensions as the absorbed dose, D, its unit of measurement is the Sievert, Sv. Each time ionising radiation interacts with the material, it loses a small part of its energy, depositing a certain dose. This energy loss at each step is quantified by the stopping power. The linear stopping power is defined as the mean energy loss in units of path length, $S = \mathrm{d}E/\,\mathrm{d}x$. ICRU 85 report [4] also defined the mass stopping power as the ratio between the energy lost dE over the path-length dx in the material of density ρ:

$$S = \frac{1}{\rho}\frac{\mathrm{d}E}{\mathrm{d}x} \tag{1.3}$$

The mass stopping power can be expressed in $MeVcm^2g^{-1}$ and described as the sum of individual terms corresponding to different interactions, as from equation 1.4: the *collisional stopping power*, resulting from interactions with atomic electrons causing ionisation or excitation, including energy losses due to the production of Cherenkov radiation; the *radiative stopping power*, includes energy losses which lead to Bremsstrahlung production; and the *nuclear stopping power*, which accounts for elastic Coulomb interactions.

$$S_{tot} = \frac{1}{\rho}\left(\frac{\mathrm{d}E}{\mathrm{d}x}\right)_{col} + \frac{1}{\rho}\left(\frac{\mathrm{d}E}{\mathrm{d}x}\right)_{rad} + \frac{1}{\rho}\left(\frac{\mathrm{d}E}{\mathrm{d}x}\right)_{nuc} \tag{1.4}$$

The total path length of a particle in the absorber is quantified by the range, defined as:

$$R = \int_0^{E_K} \frac{dE}{S_{tot}(E)}, \tag{1.5}$$

where E_K is the initial particle kinetic energy and S_{tot} is the total stopping power defined in equation 1.4.

1.2.2 Interactions of charged particles with matter

When a charged particle passes through a medium, several interactions occur. If the particle transfers some of its energy to the electrons surrounding the nucleus of the medium, a collisional interaction occurs. The particle is deflected at an angle from its original direction while the absorber atom is excited or ionised if the energy transferred is greater than the ionisation potential. Interactions with the nucleus can also occur. Heavy charged particles may undergo elastic collisions with atoms, while for electrons, most of these collisions are inelastic, resulting in the emission of a Bremsstrahlung photon [6].
As a result of all these interactions, the incident particles lose a small amount of energy and are continuously slowed down. However, the total number of particles in the beam does not change until the particles have no kinetic energy left.

The stopping power describes the energy loss in units of length, equation 1.4. For all charged particles, the collisional stopping power describes the relevant energy loss mechanism of the particle Coulomb interactions with the absorber electrons. The radiative stopping power is mainly relevant for electrons since bremsstrahlung production is the high-energy electrons' main energy loss process. Finally, the nuclear stopping power, which is only relevant for heavy charged particles, can be neglected in the energy range of radiotherapy, as it is only important at very low energies. In fact, for protons, the nuclear stopping power contributes more than 1% of the total stopping power in water at energies below 20 KeV [7]. As for the stopping power, also for the range (defined by equation 1.5), a distinction must be made between heavy and light charged particles. While heavy charged particles have a rectilinear path in the absorber, electrons can be scattered at large angles, and therefore, their path in the absorber is very tortuous. Therefore, the range that measures the total path length corresponds to the actual particle penetration depth for heavy charged particles, whereas for electrons it can be up to twice the penetration depth. We will, therefore, see that several range definitions can be used for practical applications of electrons.

Protons and heavy ions

It is mainly through Coulomb interactions with the electrons of the medium that protons and heavy ions lose their energy. The energy loss per unit of the path can be expressed by the Bethe-Block formula [8]:

$$S_{col} = 4\pi \frac{Z}{A} N_A \frac{z^2 c^2}{\beta^2} r_e^2 m_e \left[\ln \frac{2m_e c^2}{I} + ln\beta^2 - ln(1-\beta^2) - \beta^2 \right] \tag{1.6}$$

Z and A are, respectively, the atomic and mass number of the medium, N_A is the Avogadro's number, z is the charged particle charge, c is the speed light, $\beta = v/c$, where v is the proton velocity and I is the mean ionisation potential. The collisional stopping power, therefore, depends on some parameters of the absorber material, such as the Z/A ratio and the mean ionisation potential. Both of these parameters decrease as the Z of the material increases. The stopping power also depends on some parameters of the particle, such as the charge and velocity terms in z^2 and v^{-2}. As a function of particle energy, the collisional stopping power can be divided into three regions: at low energies, an initial rise to reach a maximum at about 1500 AI, where A is the atomic mass and I the mean ionisation excitation potential of the absorber; a subsequent fall-off proportional to $1/\beta^2$ to reach a minimum at about 3 $\beta\gamma$; a slow relativistic rise for relativistic energies. The heavy charged particles, therefore, have a characteristic depth dose profile in a medium, consisting of a low energy loss during penetration until a final peak at the end of the path, the so-called Bragg peak.

Electrons

The electron interactions in a medium differ from those of heavy charged particles because they interact with either the orbital electrons or the nuclei of the absorbing medium. The total stopping power of the electron is therefore the sum of the collisional and radiative stopping powers: $S_{tot} = S_{col} + S_{rad}$.
As for heavy charged particles, the interaction with the orbital electrons can lead to ionisation or excitation of the absorbed atom, resulting in a collisional energy loss described by the collisional stopping power. The collisional energy loss of electrons was again quantified by Bethe [9] as follows:

$$S_{col} = 2\pi r_e^2 \frac{Z}{A} \frac{m_e c^2}{\beta^2} \left[ln(E/I)^2 + ln(1+\tau/2) + F^-(\tau) - \delta \right] \tag{1.7}$$

with

$$F^-(\tau) = (1-\beta^2)[1 + \tau^2/8 - (2\tau+1)ln2] \tag{1.8}$$

and $\tau = E/mc^2$ is the electron kinetic energy in units of its rest mass.

At the same time, the electrons also interact with the nuclei of the absorbing medium through elastic or inelastic collisions. Elastic scattering results in no energy loss but in a change in particle direction. For the inelastic scattering process, however, the electron loses part of its energy through the emission of a Bremsstrahlung photon. This process is described by the radiative stopping power, which can be expressed as:

$$S_{rad} = \alpha r_e^2 Z^2 \frac{N_A}{A} B_{rad}(E + mc^2) \tag{1.9}$$

B_{rad} is a parameter that depends slightly on Z (of the absorbing material) and on the electron energy. Its value increases slowly with energy and, in the range of energy useful in Radiation Therapy (RT), it varies between 12 for an energy of 10 MeV and 15 for 100 MeV [6]. The dependence of equation 1.9 on the electron energy and on the Z of the absorbing material shows that the production of Bremsstrahlung photons is higher at high energy and for materials with a high atomic number. Indeed, at clinical electron energies the Bremsstrahlung contamination remains low, for example, less than 1% and 4% at 4 and 20 MeV respectively [3]. At higher energies, however, the production of Bremsstrahlung photons becomes significant, also considering that the photons produced have a maximum energy equal to that of the incident electron. The energy at which the collision loss rate equals the Bremsstrahlung one is called 'Critical Energy'. The ratio between the two energy losses can be approximated by [10]:

$$\frac{S_{rad}}{S_{col}} \approx \frac{EZ}{700} \tag{1.10}$$

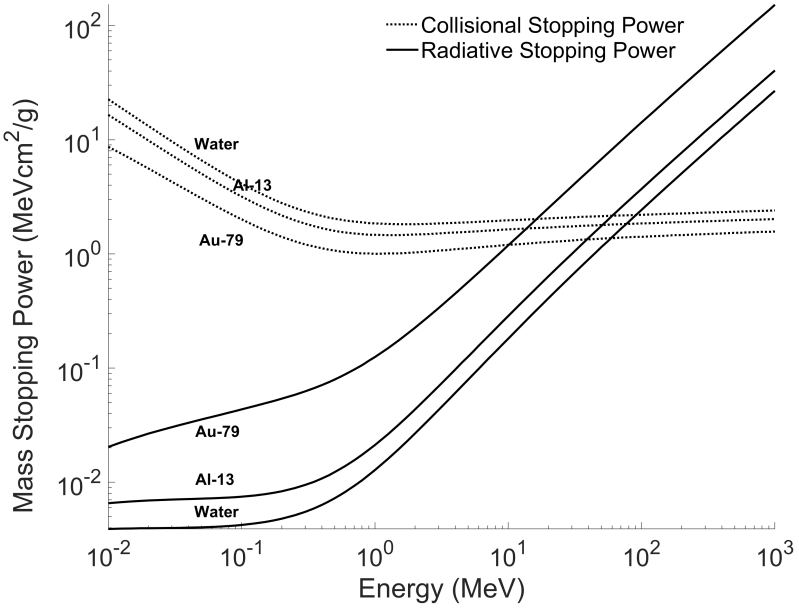

Figure 1.1: Electron stopping power in Al (Z=13), Au (Z=79) and Water as a function of the energy. The graph is obtained using the NIST tables [11].

where the energy, E, is expressed in MeV. At 100 MeV, for example, the relative contribution in aluminium (Z=13) will be ∼2, while in gold (Z=79) ∼10. In this range of energies, even though the value of the collisional stopping power remains constant, the radiative stopping power increases dramatically, as shown in figure1.1. As the photons created are therefore significant in very high energy electron beams, the processes by which photons interact with matter are briefly described.

1.2.3 Interactions of neutral charged particles with matter

Photons

Photon interactions with the absorber medium are very different from that of charged particles because, whereas charged particles are gradually slowed down, photons typically release all their energy in a single event, mainly transferring some or all of their energy to electrons. The intensity of a photon beam, therefore,

decreases exponentially and can be described as follows [3]:

$$I(x) = I(0)e^{-\mu(h\nu,Z)x} \tag{1.11}$$

where $I(0)$ is the initial intensity and $\mu(h\nu, Z)$ is the linear attenuation coefficient, which is a function of the photon energy and the atomic number Z of the absorber. The dependence on the material is given by the mass attenuation coefficient, μ_m, which is defined as the ratio of the linear attenuation coefficient, μ, and the density of the absorbing material, ρ, as $\mu_m = \mu/\rho$.

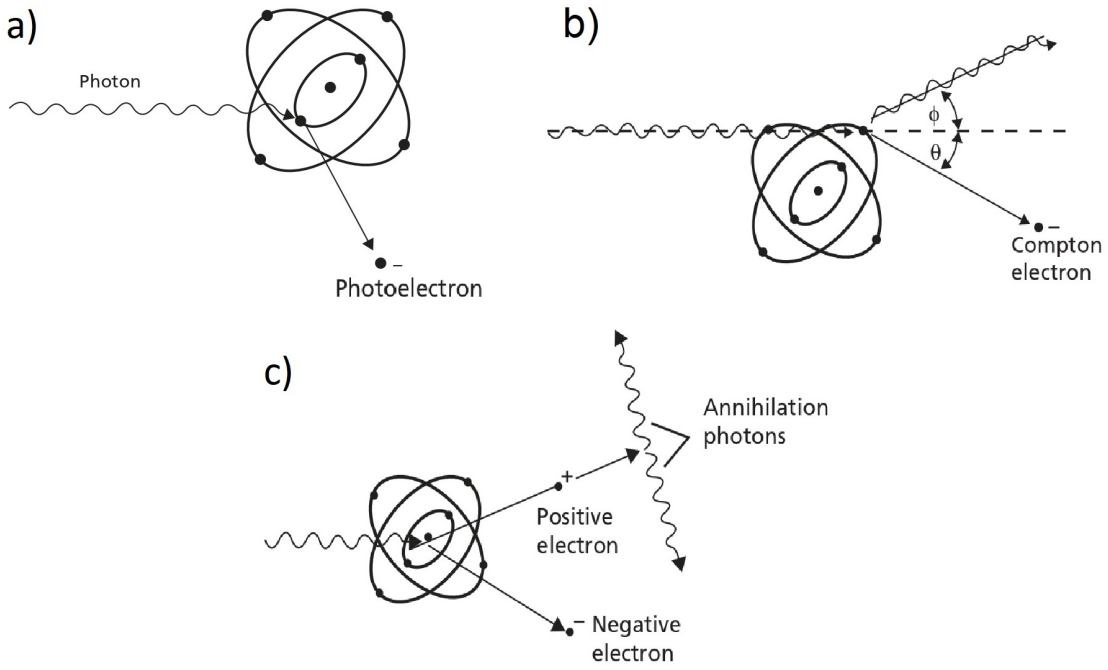

Figure 1.2: Main photon interaction processes (for the radiation therapy energy range): a) Photoelectric effect. b) Compton scattering. c) Pair production.

Photons can interact either with the nuclei or with the orbital electrons of the medium. Interactions with the orbital electrons are respectively the coherent scattering, the Compton scattering and the photoelectric effect, while the interactions with the absorber nuclei are the pair production and the photonuclear interactions. In the energy range investigated in this study (up to the order of a few hundred MeV), the three dominant photon interaction processes are photoelectric absorption, Compton scattering and pair production, also illustrated in figure 1.2. High energy photons (for example created by very high energy electrons) can also participate in photonuclear interactions, but their contribution to the total mass attenuation coefficient can be neglected (section 1.3.5). The mass attenuation

coefficient is, therefore, expressed as a sum of individual contributions:

$$\mu_m = \mu_{ph} + \mu_{co} + \mu_{pp} \tag{1.12}$$

At low energies (< 30 keV), the photoelectric effect is a likely interaction process for photons (see figure 1.2a and 1.3). In water, it is, for example, dominant up to about $10^{-2} MeV$, but in general, the attenuation coefficient varies as a function of Z^3 and thus increases with the Z of the absorbing material. The incident photon transfers all of its energy to an electron in the inner shell. A photoelectron is emitted whose energy is equal to the energy of the incident photon, $h\nu$, minus the binding energy E_b, $E = h\nu - E_b$. The vacancy left by the emitted electron is quickly filled by cascading electrons with the emission of another photon or an Auger electron, whose energy is around 0.5 keV and which is therefore reabsorbed at a short distance from its emission.
For photon energies between 30 keV and 30 MeV, Compton scattering (figure 1.3) becomes the dominant interaction modality [6]. This process occurs between an incident photon and an electron of the medium whose binding energy is much smaller than that of the photon. The photon is scattered at an angle from its original direction and transfers part of its energy to the electron, whose scattering angle is limited by the conservation of the momentum between $\pm\pi$. The probability for the Compton scattering to happen increases linearly with the Z of the absorbing material.
When the photon energy exceeds the 1.02 MeV threshold, pair production can occur (figure 1.3), which becomes the dominant interaction as the photon energy increases to several MeV. In this interaction, which takes place in the nuclear Coulomb field, the incident photon disappears and an electron-positron pair is produced. If the photon energy is greater than twice the electron mass rest energy ($m_e = 511$ KeV), the exceeding energy is shared between the two particles, which then lose energy in the absorbing medium. The positron will annihilate with an electron when it loses all its energy, releasing two annihilation photons of 0.511 MeV each.

Figure 1.3 shows the cross section of the described interactions in lead (Z=82). The figure also shows a resonance at about 10 MeV. In fact, for high energy photons, photonuclear interactions are also possible, where the photon is absorbed by the nucleus of the medium, resulting in the production of a secondary neutron or proton. Although the probability is much lower than the other interactions and the contribution to the total attenuation coefficient is only a few per cents, the photonuclear interaction must be carefully assessed in high energy radiation therapy because of the neutron production probability and the associated radiation protection issues [3]. In the following paragraph, the important points concerning neutron interactions are recalled.

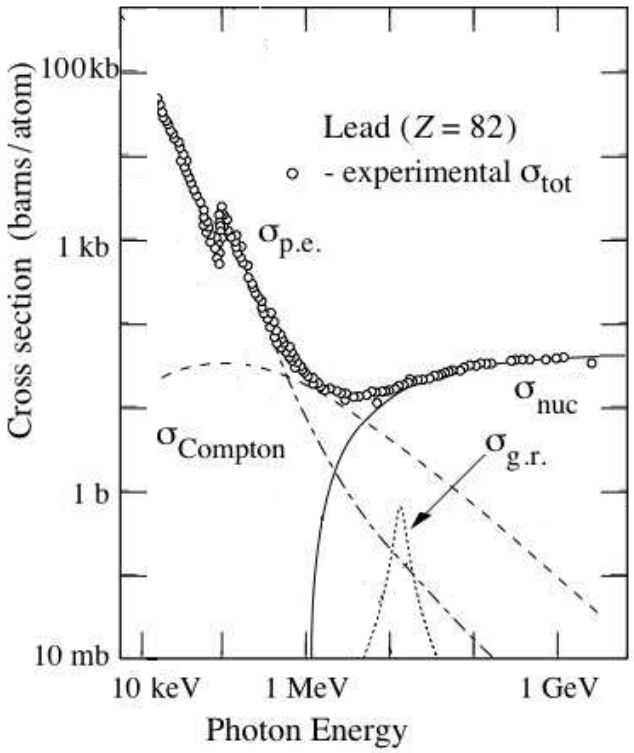

Figure 1.3: Photon cross section in lead: σ_{tot} is the total experimental cross section; $\sigma_{p.e}$ is the cross section for the photoelectric effect; $\sigma_{Compton}$ is the Compton scattering cross section; σ_{nuc} is the cross section for the pair production; and $\sigma_{g.r}$ is the giant resonance. Adapted from [12]

Neutrons

Neutrons, as photons, cannot interact via the Coulomb force because they carry no charge and can, therefore, travel many centimetres in a medium without interacting. They interact with the nuclei of the absorbing material, often resulting in the production of short-range secondary (heavy)-charged particles. At RT energies, they can be separated into fast and slow neutrons with a discrimination energy of 0.5 MeV. In elastic scattering, neutrons are deflected at an angle from their original direction, transferring some of their kinetic energy to the nucleus. The most efficient material for moderating fast neutrons is hydrogen. When interacting with hydrogen in elastic scattering, neutrons transfer, on average, half of their kinetic energy. However, since the neutron mass is similar to the mass of the proton, the energy transferred can be up to the total kinetic energy of the neutron. In inelastic scattering, the interacting nucleus results in an excited state and therefore the neutron loses a greater part of its energy than in the elastic collision. The nucleus will then de-excite, emitting a photon. When a slow neutron

interacts with a nucleus, resulting in the emission of a photon or a proton, neutron capture occurs. This interaction is used in low energy neutron detection because the process cross section is maximal for low energy neutrons. For fast neutrons, nuclear spallation process is also possible. In this case, the neutron hits the nucleus with sufficient energy to break it into several components. Heavier fragments, such as alpha particles and protons, carry most of the energy released and deposit it locally, while lighter fragments, such as neutrons and photons, carry their energy further away [8, 10].

1.2.4 Radiation therapy

RT uses both directly and indirectly ionising radiation to treat cancer. The most common technique is External Beam Radiotherapy (EBRT), which involves delivering an ionising beam from outside the patient's body to the site of the tumour. EBRT mainly uses photon radiation (X-rays and gamma rays) and electron beams, however proton and neutron beams are also used and have allowed for better dose distribution in deep-seated tumours. EBRT includes several radiotherapy techniques, each of them with specific advances and adaptations to the target tumour type [13], such as 3D conformal radiotherapy, Intensity Modulated Radiotherapy (IMRT), Volumetric Modulated Arc Therapy (VMAT), proton and heavy ion beam therapy, etc. These technologies have made it possible to always better target the dose to the 3D shape of the tumour while avoiding the normal tissue. For example, 3D conformal radiotherapy uses the patient's Computed Tomography (CT) scans, which provide 3D images and allow to adjust the treatment field position, thus improving the dose conformation to the target. On the other hand, IMRT uses inverse planning optimisation algorithms to adjust the intensity of each beam to better match the dose distribution to the shape of the target. This technique allows for multiple areas of high and low intensity by using multiple incident beams to deliver the dose, resulting in reduced toxicity (with respect to the target volume) to the surrounding healthy tissue for several tumour locations [14]. Another approach, used in the VMAT technique, consists of deliverying the dose in a single dynamic arc rotation (up to 360^o) using multileaf collimators to shape the treatment field. VMAT can improve the Organs At Risk (OAR) sparing compared to IMRT, can achieve similar conformity and better homogeneity, while reducing the treatment time, which is important for some uncomfortable immobilisations such as for head and neck treatments [15].

In radiotherapy, each of these techniques can now be used with different particles, which add specific features to the way the dose is distributed in tissues. One of the most important characteristics of a beam's interaction with a material is, therefore, the dose distribution. Figure 1.4 shows the Percentage Depth-Dose (PDD) distribution in water for indirectly ionising radiation such as a 18 MV photon

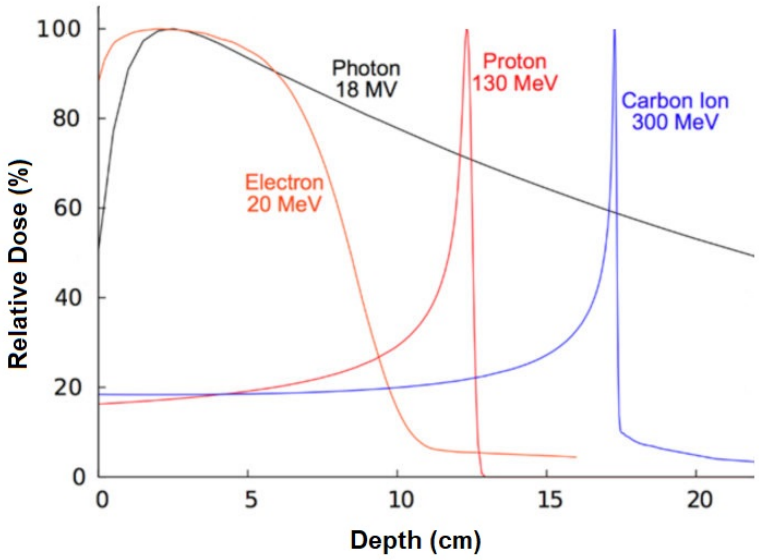

Figure 1.4: Percentage depth dose distributions in water for 20 MeV electron, 18 MV photon, 130 MeV protons and 300 MeV carbon ions beam. Adapted from [16].

beam and for directly ionising radiation, such as electrons, protons and carbon ion beams. The depth-dose profile depends on several parameters, such as the beam energy, but also the Field Size (FS) or Source Axis Distance (SAD) [8].

Electrons were among the main particles used in radiotherapy in the 1950s [3]. Their central axis percentage depth dose is shown in figure 1.5(a), which shows the central axis percentage depth dose for several electron energies (6,9,12 and 18 MeV). The electron dose distribution is characterised by a high surface dose followed by a build-up region, where the dose distribution reaches its maximum. After this maximum, the dose drops sharply to a stable low dose value, corresponding to the Bremsstrahlung tail. The rapid drop in dose after the maximum is the main advantage of using electrons over photon beams, as it allows the dose to the underlying normal tissue to be avoided. The initial build-up results in modest skin sparing, which also decreases with increasing energy. Electrons are currently used in radiotherapy to treat superficial tumours to a depth of 6 cm, such as skin or lip cancers. Clinical electrons have an energy range of 4-25 MeV and are usually produced using linear accelerators (linac) [17]. In addition to EBRT, electrons are also used in Intraoperative electron Radiotherapy (IOeRT), a technique that delivers a single dose of radiation to a tumour site during surgery [18].

The photon dose distribution is characterised by a lower entrance dose than that of electrons, followed by a build-up region to the dose maximum. This is followed by an exponential decrease to the exit dose where the radiation leaves the

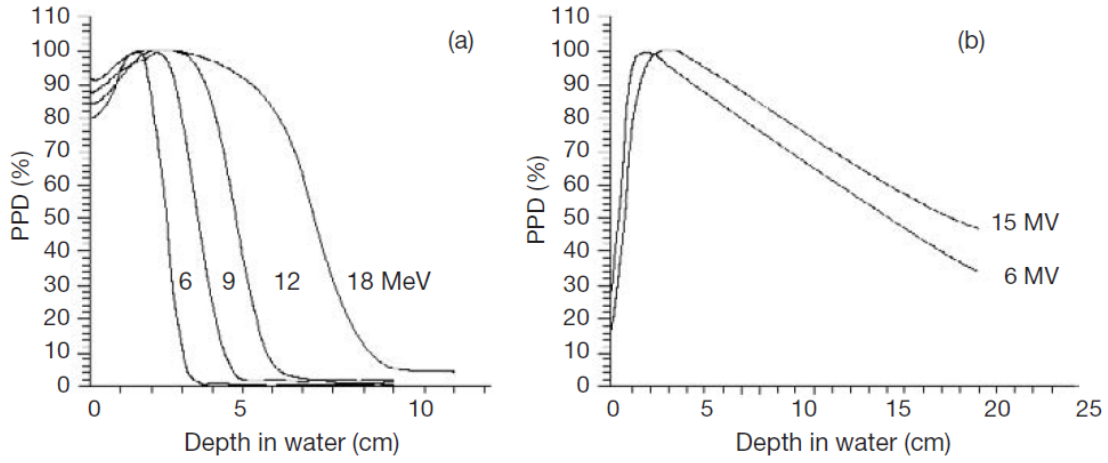

Figure 1.5: Central axis percentage depth dose distributions in water for (a) electron beams with energies of 6, 9, 12 and 18 MeV and (b) photon beams with energies of 6 and 15 MV [3].

patient body. The photon central axis percentage depth dose is shown in figure 1.5(b), which shows the central axis percentage depth dose for two energies of 6 and 15 MV. Because the entrance dose of photons is lower than that of electrons, the skin-sparing effect is greater, allowing deep tumour sites to be treated without affecting the skin. This skin-sparing effect is due to the fact that photons, being uncharged particles, deliver their dose through secondary electrons. The higher the photon energy, the higher the energy of the secondary electrons produced and, therefore, the secondary electron range. Thus, the skin-sparing effect and also the depth of the maximum photon dose increase with photon energy. Photons are the most commonly used particle for the treatment of deep-seated tumours. They are used in several external beam radiotherapy techniques, in both static (IMRT) and dynamic modes (VMAT) [6]. They are also used in stereotactic irradiations, where multiple non-coplanar photon beams are delivered with millimetric precision to a localised lesion [3].

Protons and heavy ions are the third treatment modality and are characterised by a sharp peak dose distribution (Bragg peak) at the end of their path. In fact, after this region, the proton dose is zero, while carbon ions still have a small dose contribution due to the nuclear fragmentation process. A mono-energetic (Bragg peak) beam is however too narrow to cover a thick tumour area, as can be seen in figure 1.4. Therefore, by combining several mono-energetic beams with different energies, it is possible to homogenise the dose at a certain depth and thickness, as in figure 1.6. This process is achieved using a Spread-Out Bragg Peak (SOBP) at the expense of an increase in the entrance dose. Protons and carbon ions in the 70-250 MeV energy range [19] and up to 400 MeV [20] can be used to treat

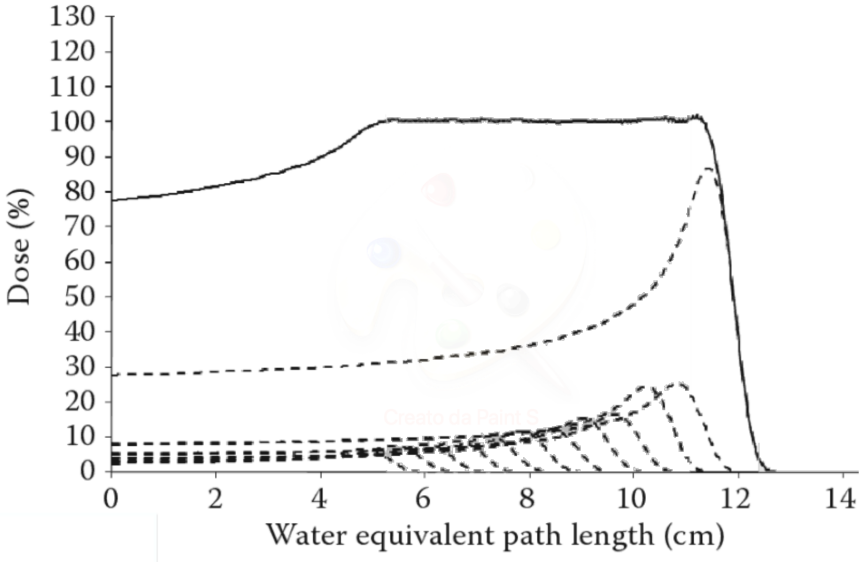

Figure 1.6: Generating the SOBP by adding multiple Bragg's picks (taken from [22]).

deep-seated tumours. Because of the dramatically lower integral dose to healthy tissue, they are particularly suitable for the treatment of paediatric diseases. However, less than 1% of radiotherapy patients are treated with these techniques as there are currently only about 100 proton therapy centres and about 15 carbon ion therapy centres [21].

1.3 Very High Energy Electrons

Very High Energy Electron (VHEE) radiotherapy, in the energy range of 100 to 250 MeV, first proposed in the 2000s [23, 24], would be particularly accurate and minimally affected by tissue heterogeneities (unlike low energy electrons or photons) [25], and could be applicable in a large number of deep anatomical localisations. It is also potentially less expensive than other particle therapy techniques (such as proton therapy) and would allow accelerated treatment, for example through electromagnetic scanning of charged particle beams, with high doses per fraction, thereby improving its effectiveness. It is also possible to take advantage of recent work on FLASH - in which a high dose is administered to the tissues in an extremely short time - allowing simultaneous reduction in the occurrence and severity of early and late complications affecting normal tissues, while maintaining control of the tumor (see section 1.5). In the following section, the current knowledge on VHEE radiotherapy and the potential for VHEE therapy to be translated into clinical contexts are presented.

1.3.1 Short history of electron radiotherapy

The history of electrons in radiotherapy dates back to the early 1950s if considering the first treatments on medical linear accelerators. It has undergone numerous developments, in parallel with the evolution of technologies and methods of cancer treatment, and then gradually limited itself to the treatments of the skin, eyes, salivary glands or part of the breasts. Indeed, due to their remarkable advantages over photon beams, i.e. high surface dose and rapid dose fall-off beyond maximum depth, electron beams between 5 and 20 MeV were commonly used for the treatment of superficial malignancies. Some groups have then worked on the adaptation of Multi-Leaf Collimators (MLC) by proposing to replace field shaping cut-outs, usually mounted on electron applicators close to the patient with a multi-leaf collimator for electron beam collimation [26]. A sophisticated approach that can be found in the literature is called Modulated Electron Radiation Therapy (MERT) which is based on energy and intensity modulation of the electron beam to conform the prescription dose to the distal edge of the tumor volume, while maintaining dose homogeneity within the target volume [27]. Various attempts to improve electron conformal therapy have been proposed, such as Electron Arc Therapy (EAT), MERT or Dynamic Electron Arc Radiotherapy (DEAR), which consists in delivering radiation while gantry rotation and dose-rate is modulated [28]. Thus, all the elements for the implementation of complex intensity modulated ERT in clinical routine seemed to be in place at the beginning of the 2010's (at least for superficial tumours), but the implementation did not finally take place due probably to the advent of modern IMRT techniques such as tomotherapy or VMAT. Possible improvements in deep-seated tumour treatments were also considered with the use of intensity- and energy-modulated

higher energy electron beams (15-50 MeV) in IMRT treatments, which proved to be of little significance in selected clinical cases [29].
For a long time, the accuracy of treatment-planning systems, initially based on the pencil-beam redefinition algorithm, was limited for certain clinical applications because they could not properly model electron therapy (e.g., skin collimation, internal collimation, variable-thickness bolus and arc therapy) [17]. In that regard, Monte Carlo dose algorithms have played a significant role in improving electron beam planning, as they have been shown to significantly improve dose calculation accuracy, for example with a more accurate handling of heterogeneities and irregular surface contours [30].

1.3.2 VHEEs and their potential application in radiation therapy

The use of VHEE between 50 and 250 MeV for radiotherapy was proposed and studied in detail in the early 2000s (see figure 1.7 for VHEEs depth dose distributions in water). A first series of papers demonstrated the interest of these beams from the point of view of their ballistic properties [23, 24, 31]. First, using Monte Carlo methods, it was shown that electrons in the range of energies between 150 and 250 MeV were sufficient to reach the deepest tumours in a patient. Depending on the beam arrangements (single, parallel opposed, or orthogonal), penetration of VHEE beams seemed, therefore, adequate to the most deep-seated tumours, even if the penetration is facilitated when the field size increases. Indeed, there is a strong dependence of d_{max} (depth of the maximum dose) on the geometrical size of the beam. The scattering of monoenergetic electron beams in air was simulated and shown to be rather moderate: the spread in air of a 0.86 mm FWHM electron beam (with 0.43 mrad angular spread) was for example increased from 2 to 7 mm for energies between 100 and 250 MeV after 1 m of air crossed. Indeed, the scattering power of charged particles is inversely proportional to the energy squared, which means that the lateral diffusion has a weak dependence on the energy. However, the lateral penumbra of VHEE beams deteriorates more quickly in-depth and is more pronounced for larger depths and lower beam energies compared to the penumbra of MV photon beams. Additionally, Lagzda et al. [25] studied the effects of tissue heterogeneities on VHEE beams and compared them with MV photon beams using simulations. It was found that uniform dose distributions were maintained at interfaces between organs and tissues of different densities (lung, air cavities, bone, muscle, fat) for VHEE. These results were later confirmed by experiments conducted at the VESPER test stand of the CLEAR facility (CERN, Switzerland), with a beam of 156 MeV and 1.2 mm standard deviation. The authors indeed showed that the longitudinal dose profiles in water of the VHEE beam were relatively unaffected (less than 5-8 % dose variation) when crossing different heterogeneities with densities 0.001 - 2.2 g/cm^3 [25]. Later, in the 2000s,

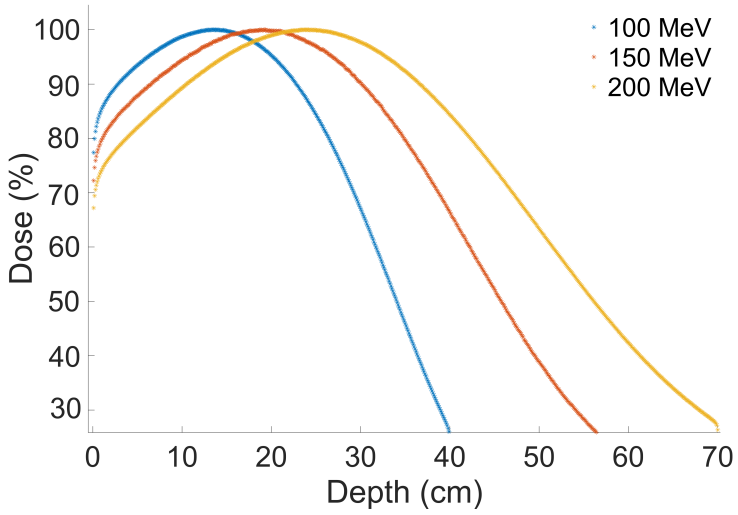

Figure 1.7: Depth dose distributions in water for 100, 150 and 200 MeV VHEE beams.

several laboratories achieved the ability to increase the energy of laser-accelerated electron beams to more than 100 MeV and to produce quasi-monoenergetic beams (170 $\pm$ 20 MeV) [32]. New studies based on realistic beam properties for this type of accelerator were then conducted (beam energy between 150 and 250 MeV, 15 MeV energy spread and 6 mrad FWHM initial angular distribution), showing that the dosimetric properties of the laser-accelerated VHEE beams would also be suitable for the treatment of deep-seated tumours, and that magnetic focusing of the electron beam would improve the lateral penumbra [33].

1.3.3 Accelerators for VHEE

Most medical accelerators are based on 3 GHz, S-band cavities with accelerating gradients far below 100 MV/m. The radiation beam from these accelerators then consists of short intense pulses of a few microseconds duration at repetition rates of about a hundred pulses per second. Today, thanks to the development of new technologies available at several test facilities worldwide, particularly in the framework of RF-devices for linear colliders [34], compact accelerating structure with more than 100 MV/m gradients could make VHEE a real option for cancer treatment. The progress made to achieve high accelerating gradient with X-band RF structures at 12 GHz could even be enhanced using plasma wakefield-based acceleration.

Betatrons or racetrack microtrons were first considered as potentially capable of delivering VHEE [31], but it was the linacs that became established in clinical

routine and then as capable of being upgraded to deliver very high energy. There are three main facilities that can be used today:

- Located at CERN (Switzerland), the probe beamline of the CLIC Test Facility was converted in 2017 into the CLEAR (CERN Linear Electron Accelerator for Research) [35]. This 25-meter-long linear accelerator produces bunched electron beams from a photoinjector coated with cesium telluride and after three S-band acceleration structures the beam achieves energy of about 220 MeV.
- The NLCTA (Next Linear Collider Test Accelerator) at SLAC (USA) produces high-brightness electron beams by an S-band RF photoinjector, achieving a final energy of 120 MeV after two high-gradient X-band RF linear accelerating structures (25 m long) [36].
- The SPARC (Sources for Plasma Accelerators and Radiation Compton with Lasers and Beams) linac at INFN-LNF (Italy) test bench consists of a photoinjector with a Cu photocathode and three S-band travelling wave accelerating sections, achieving an energy of approximately 170 MeV [37].

Many studies on the use of VHEE beams for clinical employment were already conducted at these installations, especially in the field of dosimetry in very high dose-rates conditions [38–42] and many other facilities are developing access to VHEE beams (such as the ultrabright electron beam test facility CLARA (compact linear accelerator for research and applications) at Daresbury (UK), the Photo Injector Test facility at DESY in Zeuthen (PITZ, Germany), the Argonne Wakefield Accelerator (AWA) test-stand at Argonne National Laboratory).

At present, the only accelerator solution that is being designed to produce a clinical compact system to perform image-guided FLASH-RT with photons or very high-energy electrons between 100–200 MeV is the PHASER system [43]. For this project, an innovative power-efficient linear accelerator structure and RF power sources have been engineered. The DRAGON (Distributed RF-coupling Architecture with Genetically Optimised cell design) structure can, in fact, provide high accelerating gradients (>100 MV/m).
Laser-Plasma Accelerators (LPA) can also produce VHEE through the interaction of a high power laser pulse (1018 W/cm^2) with a gaseous target. In this process, known as Laser WakeField Acceleration (LWFA), the laser pulse ionizes the gas at its leading edge and creates a plasma in which a strong travelling electrostatic gradient (100 GV/m) is formed. By properly trapping plasma electrons in the accelerating region of the travelling electric field, they can be accelerated up to the energy required for radiotherapy applications, i.e. above 50-100 MeV, in a very short accelerating region of a few millimetres. This feature has drawn attention

to LPAs as a possible candidate to generate VHEE for future applications, since the extremely short accelerating distance could result in lower costs compared to RF accelerators. Numerous LWFA mechanisms differing in the way electrons are trapped in the accelerating region of the travelling electric field have been developed in recent years [44, 45]. Among them, ionisation-injection [46, 47] is an efficient and widely-used method to produce energetic electrons. A comprehensive review of the main LWFA techniques can be found in [48].

1.3.4 Focusing VHEE beams

From the beginning of VHEE studies, the possibility of focusing charged particle beam in order to reduce the lateral spread of the dose deposition profile has been investigated. For example, an initial study carried out by the laser-plasma acceleration community [32] used MC simulations to demonstrate a possible improvement in the lateral penumbra of an electron beam when the particles were focused within a water phantom. A 170 MeV laser-plasma accelerated electron beam was hence refocused using a quadrupole triplet located 30 cm from the target. At a depth of 10 cm, the lateral penumbra of the focused beam was therefore reduced by $\sim$18% compared to the unfocused beam. In a subsequent study, the focusing of electron beams of 150-250 MeV was also investigated, demonstrating a significant improvement of the lateral penumbra and the possible benefits of using these focused beams on a clinical target [33].

The advantages of focusing a VHEE beam were more recently demonstrated at the CLEAR facility in various experimental campaigns. More than just a moderate reduction in the lateral penumbra, magnetic focusing is motivated by the objective of modifying central-axis depth dose distribution. Thus, it has been demonstrated experimentally and by MC simulations that the entrance dose and the depth of the maximum dose could be reduced or modified by using two quadrupole triplets [25, 39, 49]. During another experimental campaign, weighted sums of focused electron beams have been used to form Spread-Out Electron Peaks (SOEP) over a target region, by analogy with the SOBP found in proton therapy, and was performed experimentally by optimising the strength of a set of six quadrupoles, as shown by Whitmore et al. [50] with a 250 MeV electron beam (see figure 1.8 for an illustration of the concept). The SOEP obtained demonstrated a lower entrance dose than a similar SOBP with proton beams, but with a higher dose beyond the tumour. The study also showed a possible advantage of asymmetric focusing over symmetric focusing, resulting in a lower entrance dose for the asymmetric case.

VHEE beam focusing is, therefore, a promising technique for the translation of VHEE to clinical applications, although further investigation is needed. In particular, modelling the magnets and optimising their parameters using the treatment

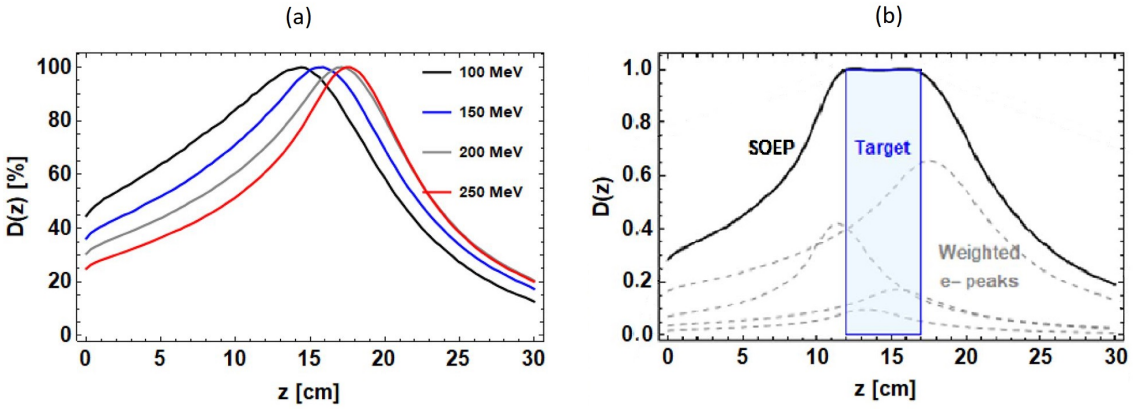

Figure 1.8: VHEE focused beams. a) Central-axis depth dose for focused VHEE (100, 150, 200 and 250 MeV beams). b) SOEP for a 250 MeV VHEE focused beam, composed of four weighted electron peaks (in grey). From Withmore at al. [50].

planning system could further enhance the benefits of focused beams.

1.3.5 Secondary Particle Production

Radiation fields of concern of very high-energy electron accelerators consist mainly of photons and neutrons. Indeed, prompt photon fields are produced by bremsstrahlung, which is the dominant electromagnetic process for high-energy electron beams interacting with matter and increases with the energy of the beam. This x-ray component is expected to be larger than 10% for energies above 50 MeV. High-energy electron bremsstrahlung theories have been documented in detail for a certain range of electron energies, showing good agreement with experimental data although small underestimations outside the 90-120 MeV range have been reported [51]. Therefore, the Bremsstrahlung component generated in the treatment head or in the tissues will be an important consideration from a radiation protection standpoint and for calculation of the energy deposition in different phantom materials, which will need to be validated in the energy range of VHEE.

Secondary neutrons will also be produced, although their contribution will be several orders of magnitude smaller than photons, as shown in figure 1.9 in terms of secondary particle equivalent dose rates in units of beam power. This quantity corresponds to the equivalent dose rate at 1 m from a target where a 1 kV electron beam is incident. This figure also shows that muon production is possible at high electron energies. Muons can be produced from bremsstrahlung radiation photons with higher energy than 211 MeV. However, this energy might be higher than the maximum energy at which VHEE could be used in RT. In the following paragraphs,

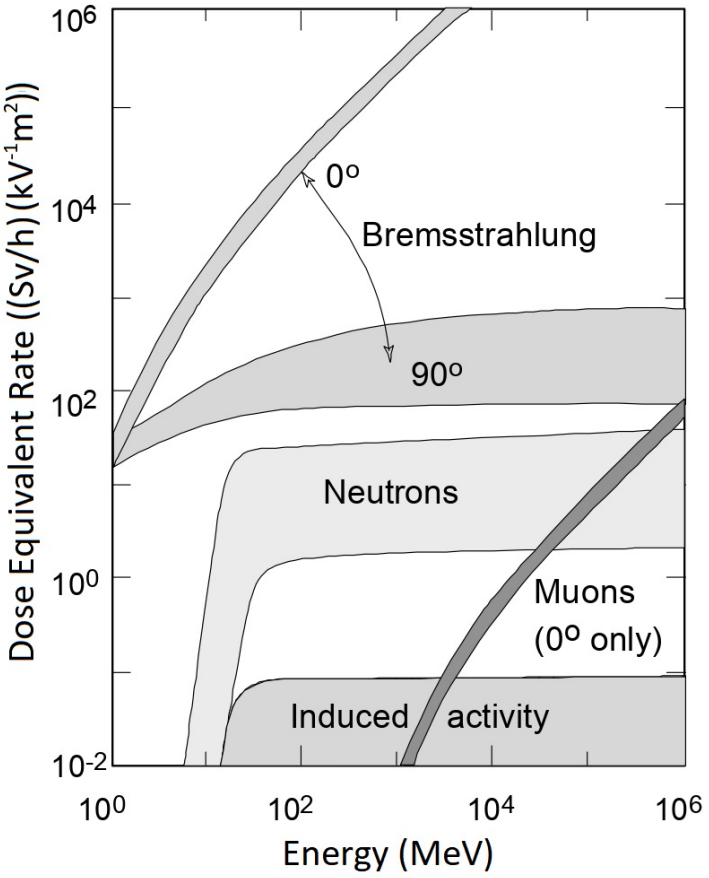

Figure 1.9: Electron secondary particles equivalent dose rates per unit beam power. The band widths indicate the expected variation that can be obtained depending on the target and its thickness. Image from [52].

the characteristics of these main secondary radiations are described in more detail.

Bremsstrahlung Photons

Very-high energy electrons lose a significant part of their energy in the form of Bremsstrahlung radiation [23], whose emitted power P is quantified by the Larmor formula:

$$P = \frac{dE}{dt} = \frac{1}{6\pi\epsilon_0}\frac{q^2a^2}{c^3} \tag{1.13}$$

q is the charge of the particle and a is its acceleration, which is inversely proportional to the mass of the particle. Therefore, the Bremsstrahlung radiation produced by an electron will be six orders of magnitude greater than that pro-

duced by a proton, as its radiative stopping power. According to Duane Hunt's law [53], the maximum energy that a photon produced by Bremsstrahlung can radiate is equal to the kinetic energy of the incident electron, $E_K = h\nu$. The angle at which this photon emission distribution is greatest is described by [3]:

$$\theta_{max} = arcos\left[\frac{1}{3\beta}(\sqrt{1+15\beta^2}-1)\right] \tag{1.14}$$

The Bremsstrahlung production in a thick target has two components: a forward peaked component, as described in equation 1.14, and a wide-angle component [52]. The forward component consists of the most energetic and penetrating photons; its spectrum is proportional to the energy of the incident electron beam and depends on the target's Z (as photons are also attenuated). The wide angle component, for electron beam energies above 50 MeV, has a shape that is independent of the incident electron beam energy and scales only with beam power. This component is formed by 99.9% of photons below 10 MeV, produced by small-angle bremsstrahlung emitted by secondary electrons traveling at large angles due to multiple scattering [52].

Neutrons

Neutrons are mainly produced by the nuclear interaction of high-energy photons since the nuclear cross section of photons is larger than that of electrons. Although neutrons are a relatively small fraction of the particles produced in the electromagnetic shower, they cannot be completely neglected. They are neutrally charged particles, so they do not interact via the Coulomb force and therefore represent the most penetrating component of the secondary particles generated in the cascade [52, 54]. Neutrons also have a higher damage capacity than other particles (for example photons or electrons). Indeed, their radiation weighting factor w_r, which is a function of energy, reaches a maximum of 20 at about 1 MeV, whereas w_r for electrons and photons has a constant value of 1 [5].

Three main photoneutron production processes by the high-energy bremsstrahlung photons are possible (note that the neutron production is also determined by electrodivision by electrons, figure 1.10): giant-resonance neutron production (10 MeV $<$ E $<$ 30 MeV), quasi-deuteron production and decay (50 MeV $<$ E $<$ 300 MeV) and intranuclear cascade and evaporation/photopion production (above the threshold of 140 MeV). A rapid rise in the amount of neutron production is therefore expected for electron energies in the range 10-20 MeV, followed by a slower rise above 30 MeV as the giant-resonance is the dominant process for VHEE beams. This two-steps process consists in a nucleus excitation after the absorption of a photon and a subsequent de-excitation by the emission of a neutron. The angular yield of neutrons is isotropic and has a cross section maximum for light

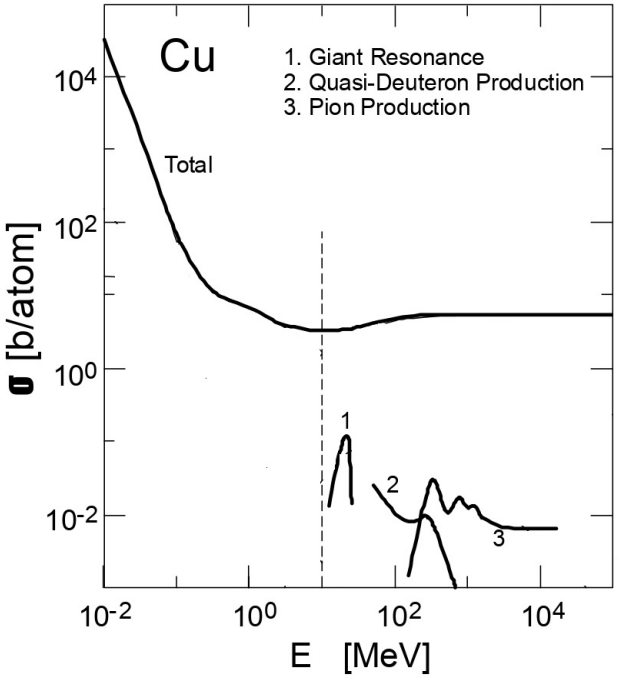

Figure 1.10: Cross-sections of major photon interactions in copper as a function of energy. Processes labelled 1 through 3 are photonuclear interactions leading to the production of neutrons. Adapted from [52]

nuclei around 20 MeV and for heavy nuclei around 15 MeV. At higher energies, between 30 and 300 MeV, neutrons can be produced by the photon interaction with a neutron-proton pair, hence the name quasi-deuterons production. Finally, for energies above a 140 MeV threshold, production of pions becomes possible. These pions then generate secondary neutrons as byproduct of their interactions with nuclei. However, this production has its first resonance peak around 300 MeV, beyond the probable maximum energy that will be used for VHEE radiation therapy [52,54]. The yield of neutrons for electron beams has then been quantified analytically in the early work on VHEE [23, 24] and estimated to be around 0.03 neutron per incident electron at 150 MeV. The increased neutron dose was estimated to be around 0.2 %, which corresponds to an equivalent neutron dose of 2 %, taking into account a neutron quality factor of 10 in order to be conservative from a radiation protection standpoint. The increase in dose from induced radioactivity was calculated to be approximately 0.01 % of the primary electron dose. The dose due to neutrons and induced radioactivity was then found to be lower than for energies up to 50 MeV, in particular since the predominant source of neutron dose occurs at the giant-resonance region (<30 MeV). Based on MC simulations, the total body neutron dose due to VHEE irradiation with pencil beam scanning was estimated to be around 1-2 orders of magnitude smaller than for scanned proton

beams and 15-18 MV photon IMRT [55]. These first estimations may however vary considerably depending on the type of beam delivery chosen in the future machines (type of collimation, scanned or scattered mode), as realistic conditions are lacking for shielding calculations.

1.4 Radiobiology basics

Radiotherapy uses ionising radiation to deliver a dose sufficient to sterilise cancer cells. This dose is a compromise between achieving tumour control and avoiding serious complications in healthy tissue. The relationship between the dose and the probability of a biological effect, i.e. the Tumour Control Probability (TCP) or the Normal Tissue Complication Probability (NTCP), is typically described by a sigmoid curve [56]. As shown in figure 1.11, these two probabilities tend to zero at low doses and to one at high doses, although for certain tumours the TCP never reaches the value of one with current treatments [3]. For a given dose, the therapeutic index is a quantitative measurement of the relative safety of an irradiation, and is a comparison between the TCP and NTCP. The aim of optimising radiotherapy treatments and developing new techniques is to increase this ratio in order to achieve better tumour control while limiting the treatment toxicity. Various factors, such as temporal or spatial fractionation of the dose in radiation therapy, combinations with surgery, chemotherapy and drug administration, can influence this ratio and make it more favourable.

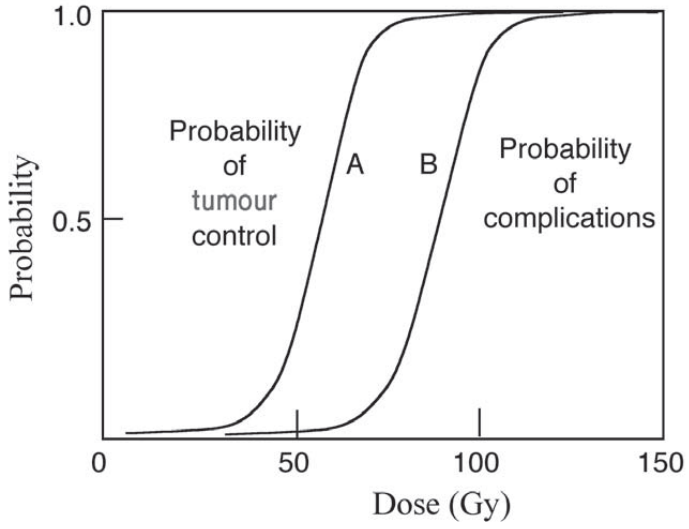

Figure 1.11: Representation of TCP in curve A and of NTCP in curve B. Taken from [3].

1.4.1 Radiation-induced DNA damage

DNA damage is the set of physical or chemical changes to the cells DNA that can affect the interpretation and transmission of genetic information [57]. Cells constantly deal with DNA damage and, depending on the specific damage, respond through specific pathways to detect and repair the lesions [58]. Various physical or chemical agents, including ionising radiation, can produce these lesions. Ionising radiation can cause direct or indirect damages to the DNA structure, or a combination of the two effects. Direct and indirect DNA damage also have different time scales, shown in figure 1.12. Direct damage occurs in the first phase of the radiation-induced process, the physical phase, which occurs between 10^{-18} and 10^{-6} s after irradiation. Indirect damage occurs in the next phase, the chemical phase, as a result of the complex chemical reactions that are completed around 0.1 s after irradiation. Finally, the following biological phase is related to DNA repair and late induced damage.

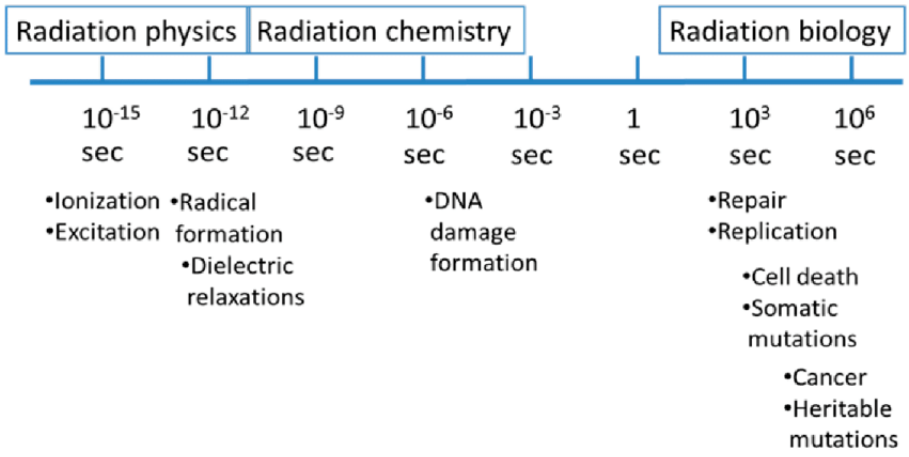

Figure 1.12: Time scale of DNA damage after irradiation (taken from [59])

Direct DNA damages are caused by the incident radiation's ionisation on the DNA molecule, and indirect one is caused by the radiolysis of the water surrounding the DNA, in particular to the Reactive Oxygen Species (ROS) production such as the highly reactive °OH radical [60]. The different reactions these radicals induce can lead to DNA strand breaks. Single-Strand Breaks (SSBs) occur when a single DNA strand is damaged or the two lesions on different strands are distant. Instead, Double-Strand Breaks (DSBs) happen when both DNA strands are damaged at a distance of a few base pairs [61], figure 1.13. DSBs are serious lesions, as a single unrepaired DBS can trigger cell death or lead to a mutation during

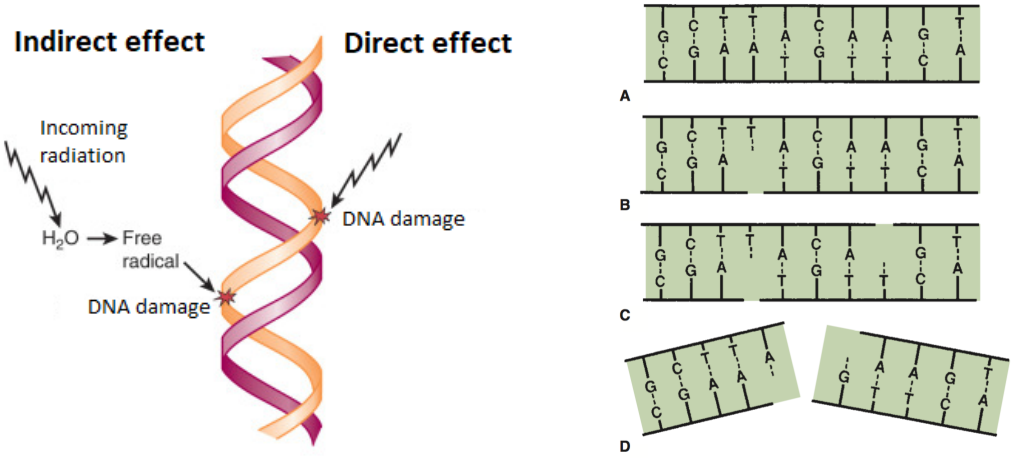

Figure 1.13: On the left: Representation of direct and indirect DNA damage. On the right: Diagrams of SSB and DSB (taken from [63]). Representation of the normal DNA helix (A); an SSB (B); a break in both strands well separated (C), repaired as independent breaks; and a DSB (D), break in both the strands separated by only a few base pairs.(taken from [61]).

DNA replication [57, 62]. Ionising radiation is, therefore, highly harmful for cells as multiple DNA lesions, resulting in cluster damages, can be caused by the track of each incident particle [60].

1.4.2 Linear Energy Transfer

A quantity which is analogous to the stopping power and frequently used to relate the radiation damage to the energy delivered as a particle beam passes through a medium is the Linear Energy Transfer (LET). For the same total energy deposited per unit mass, radiation with higher LET values, such as heavy charged particles, will indeed cause greater biological damage than radiation with lower LET values (typically photons and electrons). The LET differs from the stopping power (defined in equation 1.4), as it takes into account the energy transferred to the absorbing medium (dE_L, the mean energy lost by the charged particles via electronic interactions) instead of the energy lost by the particle in the medium. The LET is defined in the ICRU report 10a [64] as the ratio of the average energy locally transferred by a particle to the medium when travelling a distance dl:

$$L = \frac{dE_L}{dl} \tag{1.15}$$

The LET also differs from the stopping power in that it refers to the energy absorbed in a limited volume, whereas the stopping power has no spatial limitation in its definition. This spatial dependence is overcome by the ICRU Report 85 [4], which defines the restricted linear energy transfer as the ratio of dE_Δ and dl, where dE_Δ is the average energy lost by the charged particles due to electronic interactions when travelling a distance dl, producing secondary particles with a maximum energy of Δ, thus:

$$L = \frac{dE_\Delta}{dl} \tag{1.16}$$

Its unit of measurement is eV/m, often expressed as keV/μm. The definition in equation 1.16 no longer includes a distance cut-off but an energy cut-off and, for $\Delta = \infty$, the L_∞ quantity corresponds to the linear electronic stopping power, S_{col}.

1.4.3 Survival Curves

As described above, radiation damage is closely related to cell death. Cell survival curves show the relationship between the absorbed dose and the fraction of surviving cells, usually represented on a logarithmic scale. For proliferating cells, the survival fraction is the fraction of cells that retain their reproductive integrity after irradiation with a given dose, corresponding to the ability to generate a large colony starting from a single cell. For non-proliferating cells, the surviving fraction is the fraction of cells that retain their specific functions [61]. Highly ionising particles, corresponding to high LET particles such as neutrons or α particles, show an exponential decrease in the cell survival curve as a function of dose. Instead, low LET particles, such as X-rays, show a large initial shoulder, indicating a high capacity for damage repair followed by an exponential decrease at higher doses, as shown in figure 1.14. Several models have been proposed to describe the cell survival curves, including the linear quadratic model. This model consists of two exponential terms. The first term is proportional to the dose, D, and describes the initial shoulder of the curve. The second term is proportional to the square of the dose and characterises the second slope of the curves. The survival, S, is therefore described as:

$$S = e^{-\alpha D - \beta D^2} \tag{1.17}$$

where α and β are the two constants of the model. The ratio α/β describes the dose value at which the two contributions are equal and is often used to characterise the radiosensitivity of cells. Modifications to the model were then proposed, particularly for low doses for which a hypersensitivity phenomenon was observed and for high doses (the second-order term causes the function to tend too quickly towards 0, which is physically and experimentally inconsistent).

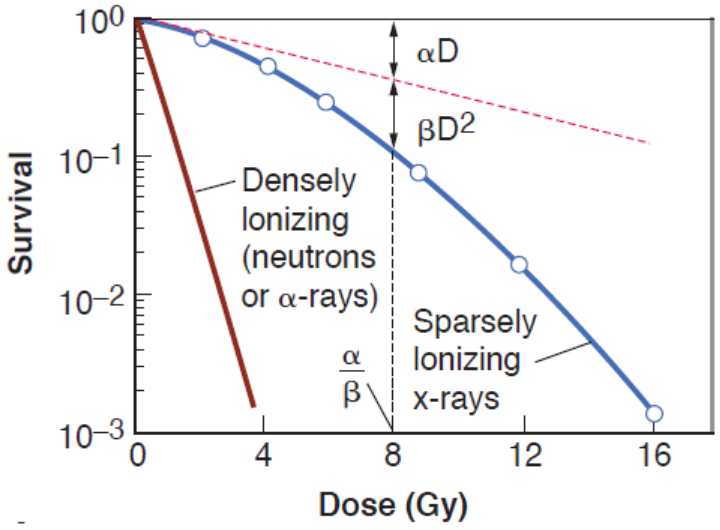

Figure 1.14: Survival curve for mammalian cells exposed to high and low LET radiation modelled using the linear-quadratic model (taken from [61]).

1.4.4 Relative Biological Effectiveness (RBE)

When assessing the biological effect of radiation, the type of radiation causing the effect must be taken into account, since the same dose under different irradiation conditions does not necessarily lead to the same biological effect [10]. A quantity that relates the induced damage to the radiation type is called the Relative Biological Effectiveness (RBE). It is defined as the ratio of the dose of a reference radiation, typically 250 kVp X-rays or ^{60}Co γ rays, to the dose of the considered radiation that produces the same biological effect [3]. The RBE can be estimated from clonogenic survival curves (if it is the endpoint in question) of a biological system obtained when comparing the radiation under consideration and the reference radiation. Thus, for a given survival fraction, the RBE is determined as the ratio between the reference dose and the isoeffective dose of the radiation being investigated.

The RBE, therefore, depends on the type of radiation and on the dose. It also varies with the type of cells examined, the LET, the dose rate, the oxygen concentration, and even the dose fractionation (if multiple fractions are used). Various models for the RBE have been developed, often depending on the LET (particularly for protons or ions). Indeed, it has been observed for many cell lines and particle types that RBE increases almost linearly with LET up to 10 keV/μm and reaches its maximum around 100 keV/μm, then decreases again, as shown in

figure 1.15. Dependence on dose rate is more complex: when irradiation conditions involve a time factor, for example, if the dose rate is low and repopulation or repairs may occur during treatment, the linear quadratic model has to be modified, for example introducing G, the Lea-Catcheside factor < 1 for long irradiation times [65]. On the other hand, differences in effectiveness can also be expected when dose rates are very high. Finally, there is also a dose fraction dependence, as lower doses per fraction of highly ionising particles have a higher RBE. The magnitude of this dependence depends on the initial survival curve shoulder (especially for X-rays), which can give a larger RBE at low doses compared to large doses and can be amplified with the number of fractions [61].

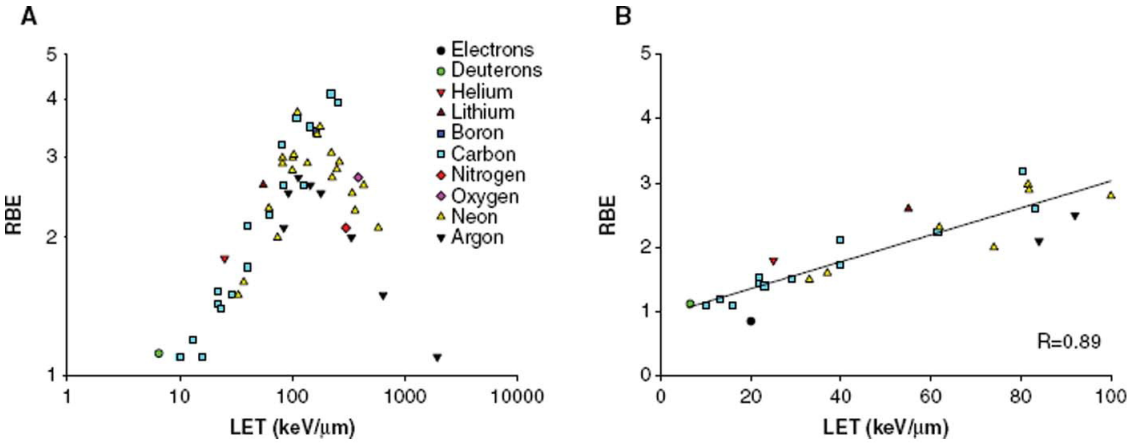

Figure 1.15: RBE-LET plot for T1 cells for multiple particles (A); RBE-LET curve for LET below 100 keV/μm (B). The solid line represents the curve line RBE=0.941 + (0.0209 LET) (taken from [66]).

1.4.5 Dose fractionation in radiotherapy

Time is one of the most important parameters affecting cell survival. However, most pre-clinical studies were carried out with a single dose of irradiation, which differs significantly from the clinical conditions under which patients are irradiated (a standard radiotherapy treatment is typically given over several weeks in about 5 sessions per week, with a dose of $\sim$2 Gy and a Conventional dose rate (CONV) of $\sim$1 Gy/min). For example, we know that the more hypofractionated the treatment, the greater the risk of complications for organs at risk. This can be quantified, for example, using the Biological Effective Dose (BED) or dose equivalent to x Gy

per fraction (EQD_x), which are expressed as follows:

$$BED = n \times d(1 + \frac{d}{\alpha/\beta}) \tag{1.18}$$

$$EQD_x = n \times d\frac{(1 + \frac{d}{\alpha/\beta})}{(1 + \frac{x}{\alpha/\beta})} \tag{1.19}$$

where n and d correspond respectively to the number of fractions and the dose per fraction of the plane under consideration. These relationships can be used to compare different treatments.

1.5 FLASH Radiation Therapy

In 2014, a pioneering study from Favaudon et al. [67] demonstrated, at Ultra-High Dose Rate (UHDR), the presence of a significant healthy tissue sparing effect while maintaining the same tumour control as CONV irradiations, named as the FLASH effect. The main characteristic advantage of the FLASH modality of irradiation is, therefore, to spare normal tissues from the late complications usually observed after radiation therapy at conventional dose rate while leaving the efficiency for tumours unchanged. Following this promising result, several subsequent studies investigated the FLASH effect to clarify whether it was observed in other animal models and understand its mechanism. The FLASH effect was then demonstrated in several organs of mice, such as the lung [67], intestine [68], skin [69–71], and brain, as well as cutaneous-muscular necrosis in rat tail [72], cat face, and pig skin [73]. The FLASH effect was also obtained using all the particles used in clinical practice, in addition to electrons, such as photons, protons, or carbon ions [74]. The molecular mechanisms underlying such differences are the main challenge for future studies of the FLASH effect. However, while the mechanisms underlying the biological effects have still to be elucidated, the FLASH effect has also been confirmed in the first human patient with promising results [75], supporting further studies and clinical trials.

1.5.1 Demonstration of a FLASH sparing effect

The breakthrough in vivo study by the Favaudon's team, which led to the definition of the FLASH effect, stems from the lung fibrogenesis comparison in mice

exposed to FLASH or CONV irradiation. For CONV irradiation, gamma rays or 4.5 MeV electrons were used at a mean dose rate of 0.03 Gy/s. FLASH irradiations were performed using the 4.5 MeV electron beam with an exposure duration of less than 500 ms, leading to a mean dose rate of 60 Gy/s. Mice received a dose of 17 Gy in FLASH or CONV mode through thoracic irradiation to compare the late fibrosis. No fibrosis was observed in mice exposed to a 17 Gy FLASH dose, while mice exposed to a 17 Gy in CONV mode developed pulmonary fibrosis 8 weeks after the thorax irradiation that progressively worsened (figure 1.16a). An escalating FLASH dose from 16 to 30 Gy was also administered to estimate the occurrence of fibrosis in FLASH mode, resulting in rare fibrotic patches only for the 30 Gy dose and 24 weeks after irradiation (figure 1.16b). The study also compared the growth of two xenografted human tumours (breast cancer and head and neck carcinoma) and a syngeneic orthotopic lung tumour in mice. FLASH irradiations were as effective as CONV in inhibiting or stopping the tumour growth (figure 1.16c), or even more effective than CONV at higher doses, with higher FLASH doses also exhibiting a skin-sparing effect. The 15 Gy FLASH dose was indeed less effective than 19.5 Gy CONV in slowing down the tumour growth. However, 19.5 Gy CONV and 20 Gy FLASH resulted in similar tumour control, while 25 Gy FLASH provided better tumour control.

1.5.2 First clinical applications of FLASH radiotherapy

In 2018, the first human patient was treated in FLASH therapy for a multiresistant cutaneous lymphoma at the Lausanne University Hospital [75]. Using a 5.6 MeV electron beam, a prescribed dose of 15 Gy was delivered in less than 90 ms. A complete tumour response was obtained with limited skin reactions. Although a comparison with the CONV modality was not possible as the patient was only treated with FLASH irradiation, a mild side effect was obtained compared to skin reactions with previous treatments. Complete tumour control was achieved (figure 1.17b), and a minimal skin reaction in the irradiated area was observed with a maximum at 3 weeks after irradiation (figure 1.17a). The same patient subsequently received a single electron dose of 15 Gy for two other tumours delivered at a dose rate of 0.08 Gy/s versus 166 Gy/s. In this case, a comparison was made between FLASH and CONV irradiation, showing no difference in acute reactions, late effects at 2 years and tumour control [76].

This first human application of the FLASH radiation therapy technique was followed in 2020 by a clinical trial performed with protons. This trial started at the Cincinnati Children's Proton Therapy Center [77], and first demonstrated the feasibility of proton FLASH therapy, for palliative treatment of extremity bone metastasis. The study showed that there was no fibrosis or vascular change in the treatment field, even when the skin received the total prescribed dose of 8 Gy. In addition, most patients experienced pain relief. The results obtained from

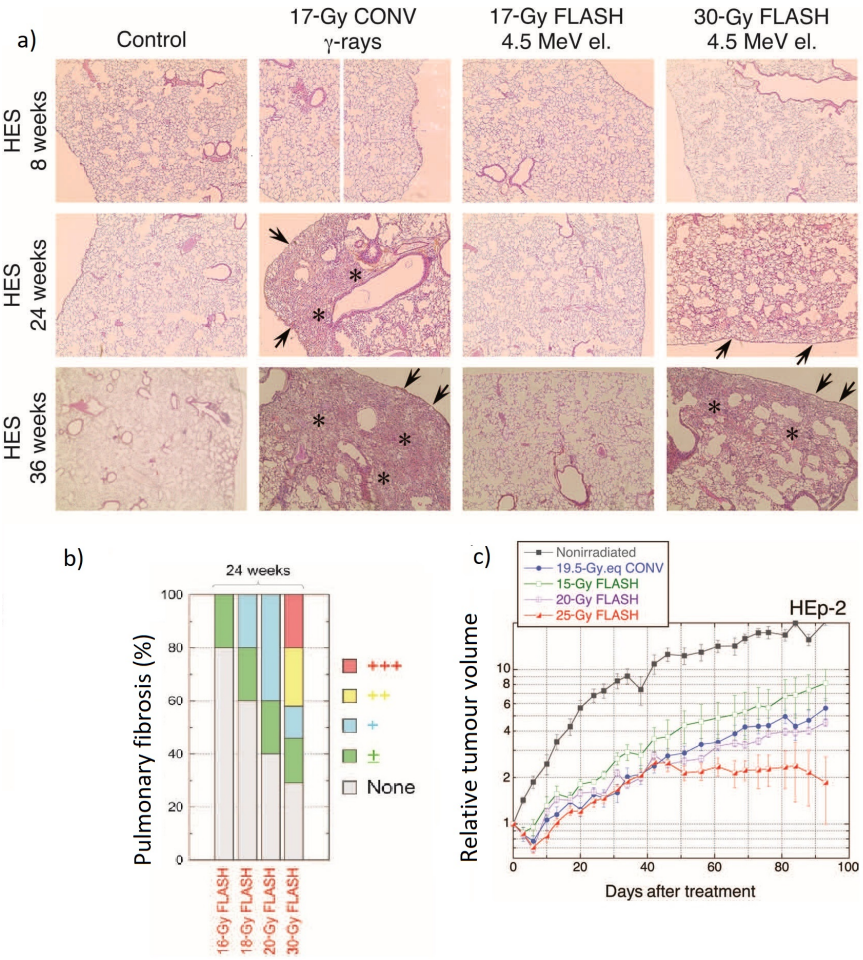

Figure 1.16: From Favaudon et al. [67] a) Comparison of lung fibrosis in mice exposed to a 17 and 30 Gy dose in FLASH and CONV mode through thoracic irradiation at 8, 24 and 36 weeks after irradiation. b) FLASH dose dependence of lung fibrosis incidence at 24 weeks after irradiation showing severe fibrosis only for a FLASH dose of 30 Gy. Scoring scale: None, ± minimal, + mild, ++ moderate, +++ severe. c) HEp-2 xenograft tumour growth for 19.5 Gy CONV dose and for 15,20,25 Gy FLASH dose. The 15 Gy FLASH dose was less effective than 19.5 Gy CONV in slowing down the tumour growth. 19.5 Gy CONV and 20 Gy FLASH resulted in similar tumour control, while 25 Gy FLASH resulted in better tumour control.

this first clinical trial are therefore promising and highlight the need for further, although cautious, investigation of the benefits of FLASH radiotherapy in other human tumour sites.
Clinical trials with pets (cats and dogs) have also been carried out, with mixed results. Excellent tumour control in radioresistant cases (melanoma, carcinoma, sarcoma), few short-term complications were initially observed, in any case in a

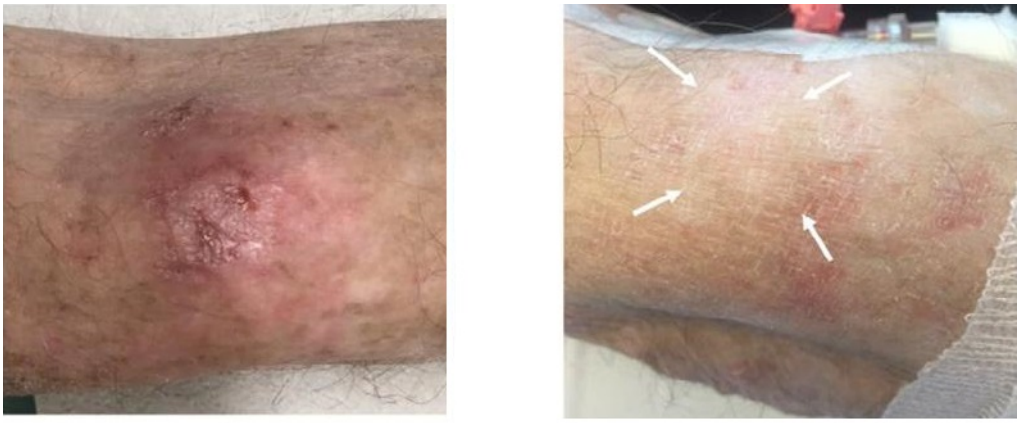

Figure 1.17: From Bouhris et al. [75] Evolution of the irradiated zone over time: a) 3 weeks after irradiation (peak of the skin reaction). b) 5 months after irradiation.

number compared with conventional irradiation but, more worryingly, a higher number of cases of osteonecrosis were obtained during treatments exceeding 30 Gy and 35 Gy in a single dose for cats and dogs respectively [78, 79].

1.5.3 Biological and physical mechanisms

The mechanisms that determine the FLASH effect have yet to be elucidated. However, several parameters, such as the mean dose rate, delivered dose, and total irradiation time, seem to trigger this differential response. In particular, a total irradiation time of a few hundred ms and a mean dose rate higher than 100 Gy/s seem required, even if the FLASH effect was reached and discovered at a lower dose rate of 40 Gy/s. The pulsed nature of the beam and its characteristics, such as pulse frequency and pulse duration or dose per pulse, may also influence the effect.

With regard to the study of the fundamental mechanisms behind the biological effect, a first hypothesis concerns immunovascular response and assumes that the very high dose rates of FLASH limit the activation of the transforming growth factor, a powerful immunosuppressive marker. Another hypothesis is to study the radiolytic yields of water as a function of the differences in dose rates between FLASH and CONV. Inter-trace interactions can occur when the chemical species created during the same pulse react with each other, modifying the resulting heterogeneous chemistry stage. This would favour oxygen consumption [80, 81] and several distinct hypotheses are linked to this oxygen concentration variation.

1.6 Radiation dosimetry

The clinical application of FLASH RT faces several challenges, of which accurate dosimetry and beam monitoring are crucial steps. Indeed, in RT, accurate dosimetry is essential to ensure the accuracy of safe treatment delivery and the radiation protection of clinical staff. However, the dose measurement and beam monitoring methods currently used in CONV RT are highly sensitive to variations in dose per pulse and dose rate. Many detectors, such as ionising chambers, require correction factors in the UHDR regime to compensate for saturation effects. This saturation effect is highly dependent on the time structure of the beam, which varies significantly depending on the beam acceleration technique. Clinical cyclotrons accelerate quasi-continuous proton beams, whereas the time structure of electron or photon beams accelerated by linacs is pulsed with a repetition rate of several hundred Hz and a pulse length of up to tens of μs, and even lower repetition rates are given by laser-driven techniques with pulses of less than 1 ns [82]. UHDR beam monitoring therefore requires high temporal resolution, but also other requirements that are satisfied by CONV beam monitoring systems, such as high spatial resolution and low beam perturbation. In addition, the ability to operate at both UHDR and CONV dose rates is a major feature.

Ionisation chambers

Ionisation chambers are the reference dosimeters for absolute and relative dose measurements in RT [83]. However, at UHDR their response is no longer linear due to recombination effects in the cavity of the detector, between opposite charges produced by ionisation. To estimate the absorbed dose, this phenomenon is usually accounted for by a recombination correction factor k_s, which can be evaluated using the Niatel model [84] which takes into account initial recombination and volume recombination ($k_{sat} = k_{s_{ini}} k_{s_{vol}}$) as follows:

$$k_s(V) = \frac{Q_{sat}}{Q(V)} = 1 + \frac{A}{V} + \frac{B}{V^2} Q_{sat} \tag{1.20}$$

where $\frac{A}{V}$ corresponds to the initial recombination and $\frac{B}{V^2}$ takes into account the effects of volume recombination. The charge saturation value, Q_{sat}, is then obtained by fitting the Jaffé curves (the inverse of the charge collected), $\frac{1}{Q}$, as a function of the inverse square of the chamber bias voltage, $\frac{1}{V^2}$ (for example for (pseudo)continuous beams). In addition, the simplified Two-Voltage Method (TVM) can be applied to estimate volume recombination when the initial recombination can be ignored, which, for quasi-continuous beams, satisfies the relation :

$$k_{sat} = \frac{(\frac{V_1}{{V_2}^2} - 1)}{(\frac{V_1}{{V_2}^2} - \frac{Q_1}{Q_2})} \tag{1.21}$$

where V_i is the bias voltage used to measure the charge Q_i (V_1= 300V and V_2= 100V in our case). This method is based on Boag's theory and is applicable when the inverse of the charge varies linearly with the inverse of the voltage for pulsed beams or with the inverse square of the voltage for continuous beams [85]. For some pulsed beams used in FLASH RT, these relationships are no longer valid and have had to be adapted.

Indeed, this correction factor is much lower for protons generated by a cyclotron than for electrons accelerated in linacs. For a quasi-continuous beam, the pulse duration and repetition time are indeed much smaller than the collection time of the ionisation chamber, and the delivered current can be averaged over the whole collection time [86]. For pulsed electron beams produced by linacs, with a few milliseconds repetition time, a very high charge density is produced by each single pulse and must be collected during the collection time of the detector also in the order of milliseconds. As a result, the collection efficiency of the ionisation chambers at UHDR can be greatly affected by the recombination factor which was found to be less than 50% for a PTW Advanced Marcus chamber [87], and less than 10% for the PTW Roos chamber for a 200 MeV VHEE beam [42]. To overcome this problem, several studies [87, 88] have described new methods for determining correction factors, while other studies have suggested modifying the geometry of detectors to improve their efficiency [89]. For example, one study [90] investigated the collection efficiency for different electrode distances at UHDR. Using a previously published numerical solution, it was shown that, for a suitably designed chamber with 0.5 mm electrode distance, it was possible to reduce the recombination correction to less than 5 % for a dose of 3 Gy per pulse. In a subsequent study, a new parallel plate chamber design with 0.25 mm electrode spacing was characterised. A high collection efficiency of more than 99% was achieved for a dose per pulse up to 10 Gy [91]. As ionisation chambers remain one of the most used detectors in radiation therapy dosimetry, improvements in their design and computational methods adapted to clinical routine are needed for the clinical translation of FLASH RT.

Radiochromic films

Radiochromic films are also widely used for reference radiotherapy dosimetry systems. The dose deposited within a thin sensitive layer of the film initiates polymerisation of the active component (expressed in terms of optical density change), the degree of which depends on the amount of energy deposited. High spatial resolution, relatively small energy dependent response, near tissue-equivalence and almost dose rate independent response make the radiochromic film suitable for UHDR dosimetry. However, they cannot be used for beam monitoring and online applications since they do not provide simultaneous dose measurement, and are often used for quality controls of the experimental setups, to estimate the deliv-

ered dose in 2D and also as a secondary reference against dose rate dependent dosimeters. Commonly used film types are the Gafchromic EBT3 or EBT-XD as well as the more recent OrthoChromic OC-1 films, which can be used up to 10, 40 and 100 Gy, respectively. The energy and dose rate independence of EBT3 films has been reported for electrons [92] in the energy range 4-12 MeV and for instantaneous dose rates up to $\sim 10^8$ Gy/s, and for 198 MeV protons up to 40 Gy/s [93]. A similar response between EBT3 and EBT-XD was obtained for 6 MeV electrons at mean dose rates up to 1050 Gy/s [94]. However, a recent study using protons generated by a cyclotron demonstrated a significant difference in the dose rate (at 0.25 Gy/s and 7500 Gy/s respectively) for EBT3 and EBT-XD films at doses above 10 Gy. This trend was not seen in OC-1 films for doses above 3 Gy [95]. Therefore, despite some limitations, the use of radiochromic films still remains widespread and useful for UHDR dosimetry.

Alanine dosimetry

Dosimetry using Electron Paramagnetic Resonance (EPR) generally uses solid materials such as alanine (an amino acid with a density close to that of water). Irradiation of this type of material leads to the generation of paramagnetic species (radicals that are stable over time), the number of which is proportional to the absorbed dose. The dose can be determined by estimating the absorption spectrum of unpaired electrons at a specific resonance frequency in a variable magnetic field. Alanine is a suitable detector for measuring the absorbed dose in photon and electron beams between 1 and 10^5 Gy, and for dose rates up to $5 * 10^5$ Gy/s for pulsed beams [96]. It is, therefore, a useful dosimeter for UHDR applications, as a good agreement (around 3%) can be obtained compared to other detectors, including radiochromic films or ionisation chambers [94]. In addition, studies have shown that alanine dosimetry provides the closest agreement between expected and measured doses [89]. Alanine is therefore a valuable tool for the translation of FLASH RT into clinical applications, as confirmed when it was used to determine the absolute dose in the first FLASH clinical trial [75].

Scintillation and Cherenkov radiation dosimetry

Plastic scintillators are fluorescent polymers that can emit light when subjected to ionising radiation. It is possible to modify both the intrinsic properties of the material (emission wavelength, scintillation decay constant) and the chemical composition by loading it with various elements from the periodic table. Fast' plastic scintillators already exist on the market, but have a number of disadvantages, such as relatively low scintillation efficiencies (the number of photons generated per quantity of energy deposited), or they are only supplied in bulk, i.e. they cannot be pixelated, or their emission wavelength is in the ultraviolet (typically 380 nm),

which means that they cannot be designed for large volumes (tens of cm^3) because they are highly self-absorbing. The accuracy of the measurement also depends on the way in which the parasitic signal corresponding to Cherenkov radiation, emitted (also in the ultraviolet-blue) when charged particles pass through a transparent material at a speed greater than that of light, is taken into account [89]. Various methods of scintillation-free signal subtraction, optical filtering and chromatic suppression can be used for this (reviewed in [97,98]). Scintillators are widely used in radiotherapy because of their unique ability to provide real-time dosimetry with high spatial resolution. For example, in a plastic scintillator made of Polyvinyl Toluene (PVT), polystyrene or acrylic naphthalene with one or more organic dyes, interaction with charged particles converts about 3% of the delivered dose into photons. The scintillator response does not depend on the dose rate and is also independent of the angle of incidence of the radiation.

Thanks to their real-time response, scintillators may be useful at UHDR to measure either the mean or the instantaneous dose rate. A possible approach to real-time dosimetry is also represented by gas scintillation detectors. A xenon-filled gas detector able to measure dose per pulse and 2D beam position was, for example, tested recently. This detector achieved a spatial resolution better than a few hundred microns and its response was shown to vary linearly within 1% of the delivered dose and up to a mean dose rate of 300 Gy/s [99]. A new plastic scintillator was also characterised in a 16 MeV pulsed electron beam [100] [101]. Linearity (better than 1%) and reproducibility of the scintillator compared to a pinpoint ionisation chamber placed at 10 cm water equivalent depth was demonstrated in the 4-20 Gy dose range and for pulse frequencies of 18-180 Hz. The scintillator dose response was also compared to EBT-XD film dose measurements and showed a satisfactory agreement between 4% and 6% for conventional and UHDR (100 Gy/s) conditions.
Other studies have characterised imaging scintillation and Cherenkov emission for surface dosimetry in UHDR conditions, as also done at conventional dose rates [89]. A study by Favaudon et al. investigated the feasibility and linearity of Cherenkov emission dosimetry using pulsed 5 MeV electron beams, obtaining good results in small fields at both conventional and UHDR, as no saturation effects were observed [102]. Another study compared a scintillator screen and Cherenkov emission from a water phantom with dose profiles from EBT-XD films. Both Cherenkov emission and scintillator signal were found to have a linear response with dose and to be dose rate independent in the range of 50 to 300 Gy/s [103]. These studies showed that, although further investigation is required, the application of scintillation and Cherenkov emission for FLASH RT dosimetry is very promising [82].

Diamond dosimetry

The use of natural diamond detectors to measure dose in photon and clinical electron beams was suggested as early as the 1980s, mainly because of diamond's semi-conducting properties at room temperature and atomic number (Z=6), which is close to that of biological tissue (Z=7.42 for soft tissue). However, only synthetic diamonds, produced fairly recently by Chemical Vapour Deposition (CVD), are of sufficient quality and size (notably independent of dose rate) for radiotherapy applications. Operating like a solid ionisation chamber, an electric field created inside the diamond enables the drift of charges created by ionisation during irradiation to be measured. This charge movement induces a transient current pulse, the amplitude and duration of which depend on the number, speed and mobility of the carriers set in motion (Shockley-Ramo theorem). Because transit times in thin diamonds are very short, it is possible not only to integrate intensity fluctuations but also to monitor them with excellent time resolution (charge collection time of the order of ns for 100 μm thickness). To limit or eliminate their external polarisation mode, they can also be operated with a Schottky contact to create an internal voltage difference within the detector. The use of diamond detectors in UHDR RT is therefore currently being investigated as they offer high radiosensitivity and excellent spatial resolution [89].
For example, the microDiamond 60019 detector (PTW, Germany) is a Schottky diode already used for photon and electron relative dosimetry [104]. To meet the specific requirements of UHDR, a new diamond-based Schottky diode has been developed, the flashDiamond 60025 fD, which showed a linear response up to 20 Gy/pulse [105]. The flashDiamond was used for the commissioning of an electron-Flash linac (SIT, Italy) at both conventional and UHDR modes [106]. Its response was proved to be linear for dose per pulse between 1.2 and 11.9 Gy. Furthermore, a good agreement was found for beam lateral or per cent depth dose profiles between the flashDiamond and reference dosimeters, such as an ionisation chamber, a conventional microDiamond detector, and EBT-XD films. Due to their extended linearity and dose measurement capabilities, diamond detectors are very promising candidates for conventional and UHDR dosimetry [89].

1.7 Monte Carlo simulations

1.7.1 General information

Monte Carlo (MC) numerical methods use random number generators to solve problems involving several independent variables. It is particularly useful for complex problems that cannot be solved analytically. MC codes describe a problem

using stochastic processes associated with a probability function. These random processes are repeated a large number of times in order to estimate the mean value of the quantity being evaluated with good accuracy. For example, in the case of a particle propagating in a medium, the scattering of that particle by other particles in the medium is associated with a probability and the following deviation to its initial trajectory is described by another probability function.
MC codes in particle therapy are particularly relevant for radiation transport purposes and well suited to radiotherapy modelling [107]. In fact, they allow the tracking of a large number of particles, called histories, characterised by a set of initial parameters such as their position, energy and energy spread or their spatial and angular distribution. Each history is tracked by updating the particle parameters until the particle is completely absorbed or its energy is below a threshold. This makes MC codes useful in many aspects of particle therapy, such as accurately assessing the outcome of an RT treatment using primary and secondary particle dose distributions. MC calculations are generally more accurate than analytical algorithms because they do not introduce simplifications on the multiple Coulomb scattering in complex geometries [108]. Several MC codes can be used in particle therapy, such as MCNPX [109], Geant4 [110], FLUKA [111] or GATE [112] and TOPAS [108], two toolkits developed to meet the specific needs of radiotherapy applications.

In particular, the Geant4 toolkit includes a wide range of features such as tracking, geometry, physics models and hits. In addition, thanks to the Geant4-DNA extension, it is also possible to model the interactions of ionising particles in water at the cellular length scale. Geant4 is widely used for several applications, going from high energy particle physics to medical physics [110]. It is implemented in C++ programming language and uses several class categories. The *track* class contains all the particle information in a particular simulation point, such as the energy, momentum, position and other quantities. The collection of all the tracks is defined as a *trajectory* . A *step* represents the changes in space or time between two endpoints of the propagation. The *process* class is responsible for implementing the physical interactions, while the *event* class is composed of the interaction of a primary particle with a target, followed by all the subsequent events. A series of events form a *run* [113]. Seven categories of physical processes cover the physics of photons, electrons, muons, hadrons and ions from 250 eV up to several PeV: *electromagnetic*, *hadronic*, *transportation*, *decay*, *optical*, *photolepton_hadron*, and *parameterization* [110].
Although Geant4 is accurate, it takes time for users to reach the level of competence required for its use in medical physics applications [108]. This has led to the development of a number of user friendly software tools that act as an interface to make GEANT4 more accessible without the need for object-oriented programming expertise [114], including GAMOS [115], GATE [112], PTSIM [116] and TOPAS [108].

1.7.2 Tool for Particle Simulations: the TOPAS toolkit

The TOol for PArticle Simulation (TOPAS) is a Monte Carlo platform based on Geant4, specifically designed for proton therapy applications. Launched in 2009, TOPAS is now freely available for research purposes, and is widely used for many particle therapy purposes [117]. TOPAS is implemented in C++ and does not require any external libraries other than the Geant4 libraries.
A TOPAS simulation requires a txt input file containing the initial parameter conditions. Parameters are defined by their type, name and value, where the type can be string (s), boolean (b), integer (i), or double (d). The parameter name depends on whether it is an element of Geometry (Ge), Beam Sources (So), Physics (Py), Scoring (Sc) or Graphics (Gr). The input file must contain all the physics lists required to describe the simulated process. Also, the input file must define the set of quantities to be scored, using a scorer. Several quantities can be scored using predefined scorers (e.g. the deposited dose, the beam fluence, etc.). If required, users can also implement their own elements, such as additional scorers, in C++ and use them as extensions. All the MC simulations performed in this thesis are performed using the TOPAS code. Simulation details are given in the following chapters.

Chapter 2

Analytical model for VHEE dose calculations

Contents

2.1 Introduction

Since its early developments in the mid-seventies, a significant work has been devoted to adapting analytical algorithms based on the Fermi-Eyges theory of multiple Coulomb scattering to dose calculations for electron beams [118]. Most of this work has been validated or developed for energies between 5 and 50 MeV (those used for clinical applications), but not for higher energies because of the

lack of accessible experimental and machine data. In addition, many accelerated computational methods have been proposed, mainly based on either pencil beam superposition algorithms, or Monte Carlo methods. The pencil beam model proposed by Hogstrom et al. [119], for example, is based on the idea of using the central-axis dose data obtained from the measurements to provide a term describing the dose variation with depth and using the Fermi-Eyges solution to model the lateral variations. Thus, this model and especially its variants (resampling or redefinition versions [120]) allow to take into account the influence of heterogeneities on scattering and electron path relatively accurately, but have subsequently been supplanted by MC-based electron-beam algorithms, which are fast enough to be considered for routine treatment planning and much more accurate for complicated cases. For the first studies and simulations of treatment plans with VHEE, the computation tools used were also mainly based on Monte Carlo simulation codes such as Geant4, GSnrc/DOSXYZnrc, PENELOPE, EGSnrc, VMC++ or FLUKA2, [33, 121–124]. Most of these codes are research tools which are not adapted to clinical situations and calculations in voxelised geometries (calculations are highly time-consuming), but are considered as references in terms of physical interactions and accuracy. Experimental dose values were also found to be consistent with MC simulations [25]. The adaptation of MC models in treatment planning systems specifically for the FLASH modality or for VHEEs also seems to have been initiated, a priori based on an extension of low-energy models [103, 123]. However, even though there is currently no theoretical model to describe the FLASH effect in mathematical models, it is likely that the time variable, as an additional degree of freedom in the (inverse) optimisation algorithms, will require considerable computational resources and slow down the calculations. To our knowledge, there are also no analytical calculation models that have been tested above 50 MeV for this type of application and the approximations proposed for multiple scattering with electron beams have not been evaluated at these high energies. This chapter, therefore, discusses in detail the derivation of an algorithm based on the Fermi-Eyges theory of multiple Coulomb scattering for VHEE dose calculation. Similarly to the Gaussian pencil beam model used for electron or proton beams, this pencil beam kernel will be separated into a central and an off-axis term, and the options we have chosen among the different possible models will be clarified. The objective is, first, to validate this simple and fast model, allowing the evaluation of dose distributions in water for electron energies up to 200 MeV, which can then be used, for example, for fast 3D dose and dose rate evaluations in the context of FLASH-VHEE applications. MC simulations will be used to compare the analytical calculations with simulations and to determine the parameterisations used in our model for the different electron energies considered.

2.2 Fermi-Eyges Theory of Multiple Coulomb Scattering

2.2.1 Basic equations

The Fermi-Eyges theory of multiple Coulomb scattering was formulated following the work of Fermi for the distribution function of a multiple-scattered particle [125] and Eyges' solution to Fermi's equation for the situation in which the penetrating particles' energy loss is significant [118]. This formulation, combined with other contributions (e.g. the diffusion theory of Bethe et al. [126]) and simplifications (there are other secondary processes to be included in a global algorithm such as bremsstrahlung production, large angle scattering and modification of energy by high-energy secondary electrons) was applied to produce practical pencil beam algorithm in electron dose calculation. These algorithms use the small-angle approximation, which neglects the rare scattering events that result in large angular deflections but assumes that multiple scattering is the result of many independent small angular deflections [9]. Under this approximation, the fluence of an initially narrow electron beam passing through a scattering foil can be approximated using a Gaussian function for both radial and angular distribution.

Considering a cylindrical coordinate system where $\theta^2 = \theta_x^2 + \theta_y^2$ (θ_x and θ_y are the projections of the polar angle θ of its direction onto the x-z and y-z planes) and $\rho^2 = x^2 + y^2$ (x and y the lateral coordinates), and the electron beam is traveling parallel to the z-axis, the differential planar fluence both in angular and lateral coordinates can be described as in equation 2.1 [9]:

$$\Phi(z,\vec{\rho},\vec{\theta}) = \Phi(0)\frac{1}{\pi\left[\overline{\theta^2}(z)\overline{r^2}(z) - (\overline{r\theta}(z))^2\right]^{1/2}}\exp\left(\frac{-(\overline{\theta^2}(z)\rho^2 - 2\overline{r\theta}(z)\rho\theta + \overline{r^2}(z)\theta^2}{\overline{\theta^2}(z)\overline{r^2}(z) - \left(\overline{r\theta}(z)\right)^2}\right) \tag{2.1}$$

where $\bar{r^2}$ is the mean square radius of the electrons at the z plane, which is given by the Fermi–Eyges solution (equation 2.2):

$$\overline{r^2}(z) = \bar{r_0^2} + 2r\bar{\theta}_0 z + \bar{\theta_0^2} z^2 + \int_0^z (z-u)^2 T(u)du \tag{2.2}$$

and

$$\bar{r\theta} = r\bar{\theta}_0 + \bar{\theta_0^2} z + \int_0^z (z-u)T(u)du \tag{2.3}$$

in which $\bar{r_0^2}$ is the initial mean square radial spread, $\bar{\theta_0^2}$ is the initial mean square angular spread, $r\bar{\theta}_0$ is the initial covariance and T is the linear scattering power. If the initial electron source is punctual, equation 2.2 simplifies into:

$$r^2(z) = \int_0^z (z-u)^2 T(u)du \tag{2.4}$$

Due to the azimuthal symmetry of the scattering process and if equation 2.1 is integrated over all angles θ_x and θ_y and normalised, the purely spatial distribution is obtained:

$$\Phi^{\rho}(z,\vec{\rho}) = \frac{1}{\pi\overline{r^2}(z)} exp(-\frac{\rho^2}{\overline{r^2}(z)}) \tag{2.5}$$

where $\overline{r^2}$ is described by equation 2.2. Similarly, regardless of the lateral position, the normalised angular distribution can be represented as from equation 2.6

$$\Phi(z,\vec{\theta}) = \frac{1}{\pi\bar{\theta^2}(z)} exp(-\frac{\theta^2}{\bar{\theta^2}(z)}) \tag{2.6}$$

with

$$\overline{\theta^2} = \overline{\theta_0^2} + \int_0^z T(u)du \tag{2.7}$$

According to Bruinvis et al. [127], the width of the radial dose distribution, defined in the study as $r_{1/e}$ because it corresponds to the radial width for the relative dose value of 1/e, can be calculated as $r_{1/e} = \sqrt{a_2}$, where a_i is defined as:

$$a_i(z) = \int_0^z (z-u)^i \, T(u)du \tag{2.8}$$

The two parameters a_0 and a_1 correspond respectively to the mean angular spread and the covariance obtained in the medium. Using this formalism, equation 2.2 can be solved in the case of a punctual beam scattered in a thick target using a trapezoidal integration method at each depth $z + \Delta z$ where:

$$\begin{aligned} a_0(z+\Delta z) &= a_0(z) + 1/2[T(z) + T(z+\Delta z)]\Delta z \\ a_1(z+\Delta z) &= a_1(z) + a_0(z)\Delta z + [2T(z) + T(z+\Delta z)]\Delta z^2/6 \\ a_2(z+\Delta z) &= a_2(z) + 2a_1(z)\Delta z + a_0(z)\Delta z^2 + [3T(z) + T(z+\Delta z)]\Delta z^3/12 \end{aligned} \tag{2.9}$$

If the source is not a point-source or if there are multiple scatterers along the considered beamline before the thick target, equation 2.8 is changed to include the contribution of the various elements:

$$\begin{aligned} a_0(z) &= \int_0^z T(u)du + \bar{\theta_0} \\ a_1(z) &= \int_0^z (z-u)T(u)du + \bar{\theta_0}z + r\bar{\theta_0} \\ a_2(z) &= \int_0^z (z-u)^2 T(u)du + \bar{\theta_0}z^2 + r\bar{\theta_0}z \end{aligned} \tag{2.10}$$

where $\bar{\theta_0}$ and $r\bar{\theta_0}$ must be determined at the entrance of the thick target using equations 2.3 and 2.7.

In section 1.2.1 the dose was introduced as a fundamental quantity for RT, which is strongly related to the beam fluence. Indeed, the 3D dose distribution given by a pencil beam incident on a phantom surface is proportional to its fluence, and can then be separated into two terms: a central axis term PDD(z) (for example extracted from a simulated depth-dose curve in a water phantom) and the off-axis term as formulated in equation 2.5. The dose contribution in water at depth z can be expressed by the product of the depth dose term PDD(z) and the fluence term $\Phi^p(z, \bar{\rho})$ as in equation 2.11:

$$D(z, \bar{\rho}) = PDD(z)\ \Phi^p(z, \bar{\rho}) \tag{2.11}$$

2.2.2 Linear scattering power calculation

Since the mean square scattering angle, θ^2, is the usual quantity to describe electron scattering in a medium, the mass angular scattering power T (by analogy with mass stopping power) is defined by ICRU 21 [128] as the variation in mean square scattering angle per unit of length (corresponding to the thickness of medium traversed by electrons), as follows:

$$\frac{T}{\rho} = \frac{1}{\rho}\frac{d\bar{\theta^2}}{dl}, \tag{2.12}$$

A differential formulation of T, proposed by Rossi et al. [129], is reported in ICRU 35 [130]:

$$\frac{T}{\rho} = \pi \left(\frac{2r_e Z}{(\tau+1)\beta^2}\right)^2 \frac{N_A}{A} \left\{ ln\left[1 + \left(\frac{\theta_m}{\theta_\mu}\right)^2\right] - 1 + \left[1 + \left(\frac{\theta_m}{\theta_\mu}\right)^2\right]^{-1} \right\} \tag{2.13}$$

where r_e is the electron radius, Z the atomic number, N_A the Avogadro's number, A the atomic weight, τ is the kinetic energy in unit of electron rest mass, θ_m is the cut off angle due the finite size of the nucleus and θ_μ is the screening angle:

$$\theta_\mu = 1.13\frac{\alpha Z^{1/3}}{\beta(\tau+1)} \tag{2.14}$$

and

$$\theta_m = \frac{2A^{-1/3}}{\alpha\beta(\tau+1)} \tag{2.15}$$

The formulation of T in equation 2.13 is obtained under several assumptions. First, the electric field of the nucleus is considered to be that of a point charge Ze. Also, the limited size of the nucleus and the shielding of its nuclear field by the outer electrons of the atom limit the validity of the formulation, which is therefore valid in a limited angular interval, between θ_m and θ_μ [129], defined in equations 2.14-2.15. The lower limit is given by θ_μ, which is the minimum angle at which the shielding of the electric field by the outer electrons of the nucleus does not affect the scattering probability given by the condition $\theta \gg \lambda\!\!\!^{-}/r_a$, where $\lambda\!\!\!^{-}$ is the reduced de Broglie wavelength and r_a is the atomic ray. The upper limit is given by considering the limited size of the nucleus, whose charge is assumed to be concentrated in a sphere of radius r_n rather than a point. The scattering probability is not affected by this assumption if $\theta \ll \lambda\!\!\!^{-}/r_n$ [129]. Furthermore, the derivation of T by equation 2.13 assumes small and independent deflections and does not depend on the scatterer's thickness. However, as reported by Green et al. [131], it overestimates the measured values of the scattering power, since it allows large angular contributions caused by single collisions beyond the cut-off angle θ_m. A restriction to small angles of the scattering power is therefore proposed by Andreo and Brahme [132], where large angular contributions are discarded, which is required for a proper application of the Fermi-Eyges multiple scattering theory. The limited scattering power, T_δ, which also in this formulation does not depend on the thickness of the scattering layer, is then given by:

$$\frac{T_\delta}{\rho} = \frac{d\bar{\Theta}_\delta^2}{dl} \tag{2.16}$$

with

$$\bar{\Theta}_\delta^2 = \pi \left(\frac{2r_e Z}{(\tau+1)\beta^2}\right)^2 \frac{N_A}{A} \; l \left\{ ln\left[1+\left(\frac{\delta}{\theta_\mu}\right)^2\right] - 1 + \left[1+\left(\frac{\delta}{\theta_\mu}\right)^2\right]^{-1} \right\} \tag{2.17}$$

θ_μ is defined as in equation 2.14, l is the path length and δ is the cut-off angle. The value of the cut-off angle that produces a good agreement with measured scattering power is $\delta = 0.5$ rad [132].

Another derivation of the scattering power T, which is described by one main parameter, the screening angle χ_c^2, and also depends on the scatterer thickness, was proposed by Molière in 1948 [133]:

$$T = \frac{\chi_c^2 B}{l} \tag{2.18}$$

where l is the thickness of the scatterer and B is a parameter related to the number of electron collisions, Ω_0, as they pass through the scatterer and is described by equation 2.19:

$$B - \ln B = \ln \Omega_0 \tag{2.19}$$

Following Molière's formalism, Ω_0, is related to the screening angle χ_a^2 by the 'unit probability angle' χ_c^2 as :

$$\Omega_0 = \chi_c^2/\chi_a^2 \tag{2.20}$$

with

$$\begin{aligned} \chi_a^2 &= 1.167\chi_0^2(1.13 + 3.76Z\alpha/\beta) \\ \chi_0^2 &= \lambda_0/(2\pi\alpha_{TF}) = c_1 Z^{1/3}/pc \qquad c_1 = 0.00424MeV \end{aligned} \tag{2.21}$$

and

$$\chi_c^2 = \frac{4\pi r_e^2 N_A Z^2}{A\gamma^2\beta^4}\rho l \tag{2.22}$$

where $\beta = v/c$, $\alpha = Z/(137\beta)$, r_e the electron radius, $\gamma = (1-\beta^2)^{1/2}$, α_{TF} is the Thomas-Fermi atom radius, ρ is the scatterer density, Z the atomic number and A the atomic weight [134]. Molière's theory depends only on χ_a^2, whose derivation, unlike that of Rossi [129] does not use the Born approximation cross section for an exponentially screened potential. Instead, it uses a Thomas-Fermi potential to determine the screening angle from a single scattering calculation. In its numerical formulation of the screening angle equation 2.21, the α^2 term represents the deviation from the Born approximation. Molière's theory also relates χ_a^2 to another parameter χ_c^2, whose physical meaning is that the total probability of a single scattering through an angle greater than χ_c is exactly one [126,133]. Taking equation 2.19 and replacing it with the equations 2.20-2.22 gives the B parameter for scattering power formulation as in Kainz et al. [135]:

$$B - \ln B = \ln \frac{6680\rho l(Z+1)Z^{1/3}}{\beta^2 A(1+3.34\alpha^2)} \tag{2.23}$$

An approximation to express B, accurate to within 1% for values of Ω_0 up to $\Omega_0 = 10^7$ and to 3% up to $\Omega_0 = 10^9$ was proposed by Scott [136]:

$$B = 1.153 + 2.583\ log_{10}\,\Omega_0 \tag{2.24}$$

In some studies, where small and large deflection angles are treated separately, a reduced Gaussian distribution is found to fit the width of the angular distribution better, as the Molière scattering power was found to overestimate this width [132]. The reduced Gaussian distribution is then defined from Molière's formulation as follows:

$$\theta_{RG}^2 = \theta_{Molire}^2\left(1 - \frac{1.33}{B}\right) \tag{2.25}$$

Electron mass angular scattering power in water ($MeV.cm^2.g^{-1}$)

Energy (MeV)	Rossi et al. (ICRU35 [130])	Andreo et al. [132]	Kainz et al. [135]
5	0.232	0.205	0.207
10	0.0695	0.0623	0.0509
20	0.02	0.0181	0.0127
50	0.0037	0.0034	0.002
70	0.0019	0.0018	0.001
100	9.48 *10^{-4}	9.35 *10^{-4}	5.06 *10^{-4}

Table 2.1: Electron mass angular scattering power in water comparison using equation 2.13 from ICRU 35, the Reduced Gaussian in equation 2.19 and Kainz formulation in equation 2.25

When evaluating the scattering power for a compound such as air or water, the Bragg-Kleeman rule [10] must be used as the scattering power determination assumes small and independent deviations for each atom. The scattering power of the compound can be determined by [134]:

$$T = \sum_i W_i T_i \tag{2.26}$$

where T_i and W_i are respectively the scattering power and the atom fraction of the ith element of the compound. If the traversed medium is air or water, the equation becomes equation 2.26:

$$\begin{aligned} T_{air} &= 0.78\, T_{nitrogen} \;+\; 0.21\, T_{oxygen} + \; 0.01\, T_{argon} \\ T_{water} &= 0.112\, T_{hydrogen} \;+\; 0.88\, T_{oxygen} \end{aligned} \tag{2.27}$$

The values of the electronic mass scattering power from Rossi's formulation are given in the ICRU 35 [130] up to 100 MeV. In table 2.1, these values of the mass scattering power in the energy range between 5 and 100 MeV are compared with other formulations given by equation 2.19 and equation 2.25. It is evident from the table 2.1 that the scattered power is strongly dependent on the energy of the electron beam. While for a thin target the energy dependence of the scattered power can be neglected as the energy loss is minimal, when the beam passes through a thick medium a proper evaluation of the beam energy is necessary to evaluate the scattered power correctly and then the mean angle scattering in the medium. In particular, the mean energy and not the most probable energy must be evaluated, as the most probable energy has been found to overestimate the scattering power [137].

2.2.3 Mean energy calculation

The mean energy of the electrons at depth z in a material is defined as follows:

$$\bar{E}(z) = \frac{\int_0^\infty E\Phi_E(z)dE}{\int_0^\infty \Phi_E(z)dE} \tag{2.28}$$

where $\Phi_E(z)$ is the electron differential fluence for the specific energy E at each depth z [138]. For small depths, the mean energy can be approximated with a linear approximation [130] (ICRU 35 equation 2.29):

$$\bar{E} = \bar{E}_0 - l\, S_{tot}(\bar{E}_0) \tag{2.29}$$

where l is the path length or material thickness and $S_{tot}(\bar{E}_0)$ is the total stopping power for the beam mean energy $\bar{E}_0$ before entering the slab of material [139]. At greater depths, a better approximation is given by an exponential decrease, at least for the first half of the electron path in the medium [130] (ICRU 35 equation 2.28):

$$\bar{E} = \bar{E}_0 - \frac{S_{tot}\, exp(-z\, \frac{S_{rad}}{\bar{E}_0}) - S_{col}}{S_{rad}} \tag{2.30}$$

where $S_{col}(\bar{E}_0)$ and $S_{rad}(\bar{E}_0)$ respectively the collisional and the radiative stopping power calculated for the initial energy $\bar{E}_0$. In the last part of the electron range in water, as the electron energy approaches zero before reaching the practical range R_p, the exponential approximation is no longer valid. Using Monte Carlo simulations, Bruinvis et al. [127] calculated the electron energy losses and variation of the mean energy as a function of depth in water for 5, 10 and 20 MeV electron beams, and derived a different equation to describe the energy drop:

$$\bar{E} = \bar{E}_0 - a[1 - exp(-b\, l)] \tag{2.31}$$

where a and b are parameters extrapolated from the simulations, only tabulated for specific energy values investigated in the study. Also, in that study, the variation of the total stopping power with decreasing energy with depth is described by a linear function $S_{tot}(E) = ba + b(E - E_0)$. For the MC derivation of the a and b parameters, only the mean energy variation for primary unscattered electrons is considered. This gives a noticeable difference in the mean energy when considering all the primary electrons, decreasing slightly less rapidly from the halfway electron range and reaching zero at about 1.2 times the range.

2.2.4 Range straggling calculation

The charged particles that make up a beam don't all stop at the same depth in the medium, even in the monoenergetic case. This variation in path length for particles of the same initial energy is called range straggling and is due to stochastic factors. For the same reason, the scattering of particles in a medium results in an energy spread [10]. This energy spread is accounted for when evaluating the mean scattering angle by using the mean energy of the beam to characterise the scattering power calculations. Scattering theory must also take into account range straggling, as the width of the Gaussian beam, calculated using equation 2.10, increases continuously with depth. To evaluate this effect at large depths and obtain the mean square radius of the beam distribution, a parameter has been proposed by Lax et al. [140, 141] :

$$\begin{aligned} \rho(z) &= exp\{-s^{b(c-s)}\} \\ s &= a(z_n/R_p) \end{aligned} \tag{2.32}$$

where R_p is the practical range and a, b and c adimensional parameters (whose proposed values are a=0.95, b=12 and c=1.5). This equation for range straggling has been used in the literature for 10-32 MeV electrons.

2.2.5 Realistic beam modelling

In the previous sections, the Fermi-Eyges theory of multiple scattering was described, mainly considering an initial point-like source, as from equations 2.4-2.5. However, this condition does not correspond to a realistic situation, as the particle beams used in RT are not point-like and rather characterised by a set of initial parameters, such as an initial radial spread and angular distribution. RT machines are also characterised by complex geometries with many elements, for example beam monitoring systems or scattering foils, which scatter the beam even more. Therefore, a realistic beam source and beamline geometry (described in figure 2.1) has to be considered in order to complete the beam model.
To take into account the initial source properties (angular spread and size), equations 2.1-2.3 have to be used to calculate the evolution of the beam radial spread along the beamline. Note that in this study, the theoretical beam model described is defined to produce constant beam sizes at phantom entrance of 5 mm regardless of beam energy, so little difference is expected in the source values depending on beam energy to get the same spot size (recall also that the relationship between the σ and the mean radial spread $r_{1/e}$ is $r_{1/e} = \sqrt{2}\sigma$). To calculate the total scattering in water, the beam mean radial spread, the divergence and the covariance have to be evaluated, corresponding to the parameters r_0, θ_0 and $r\theta_0$ in 2.2. This can be done by evaluating equation 2.2-2.3 and equation 2.7 at the interface of each element in the beamline and substituting them as initial values in the equation to

re-evaluate the same parameters at the next interface until reaching the entrance of the WT. The evolution of the mean radial scattering at each depth z+Δz can be evaluated using a trapezoidal integration for equation 2.10.

Double Gaussian model

The use of more complex geometry introduces a number of new variables into the model. These include the effects of single scattering events that involve the primary electrons and result in large deflection angles, which, although unlikely, can no longer be neglected, as for the photon Bremsstrahlung components. To account for the contribution of these large angles of scattering, which can cause the beam fluence to deviate from a Gaussian function, the total beam fluence can be expressed as the sum of two Gaussian functions fitted to the MC data, as:

$$\Phi(z,\vec{\rho}) = \frac{-w_2}{\pi\overline{r_1^2}(z)} exp\left(-\frac{\rho^2}{\overline{r_1^2}(z)}\right) + \frac{w_2}{\pi\overline{r_2^2}(z)} exp\left(-\frac{\rho^2}{\overline{r_2^2}(z)}\right) \tag{2.33}$$

where the parameter r_1, calculated using equation 2.2, corresponds to the width of the radial distribution of the primary electrons so that the first term in the equation represents the fluence of the primary electrons as from the single Gaussian model, equation 2.5. The terms r_2 and w_2 describe the lateral spread and the weight of the second Gaussian component. These parameters satisfy the following relationships: $r_1 < r_2$ and $w_2 < 1$.

2.3 Monte Carlo simulation geometry

In the work described below, simulations were performed with the TOPAS code (v3.8) based on the Geant4 Monte Carlo code (v10.07.p03), described in section 1.7.2. In the first part of the study, an ideal point-like electron source was placed at the entrance of a Water Tank (WT) to study the energy loss of electrons in water, for energies between 10 and 200 MeV with energy steps of 10 MeV. For the second part, a more realistic geometry was designed as described below.

Geometry settings The electron source was first chosen to be ideal in order to reduce the number of parameters and to study the mean electron beam energy decreasing in water and the different scattering power computation models (equations 2.13-2.18, for the mean square radius, r^2). The dimensions of the WT were varied from 10x10x10 to 10x10x70 cm^3 depending on the beam energy (the length of the WT was always larger than the given electron range in water). For the mean

energy calculation, only primary electrons were considered and the mean energy was scored with an energy binning scorer between 0 and 200 MeV with 1000 bins. The WT binning was performed along the z dimension with 1 mm resolution. The scorer was defined as follows:

s:Sc/Scorer/Quantity = "Fluence"
s:Sc/Scorer/Component = "WT"
s:Sc/Scorer/OutputType = "csv"
b:Sc/Scorer/OutputToConsole = "0"
s:Sc/Scorer/IfOutputFileAlreadyExists = "Increment"
i:Sc/Scorer/EBins = 1000
d:Sc/Scorer/EBinMin = 0 MeV
d:Sc/Scorer/EBinMax = 200 MeV
sv:Sc/Scorer/Report = 1 "Sum"
s:Sc/Scorer/OnlyIncludeParticlesOfGeneration = "Primary"

The scattering power models were studied using the same previous geometry however with a different binning for the WT: the electron doses were thus scored in a grid with a 1x1x1 mm^3 resolution, using the TOPAS "DoseToMedium" scorer. A second geometry derived from the CPO proton beamline was used, as shown in figure 2.1 in order to study the Fermi-Eyges theory of multiple scattering and range straggling phenomena for a more realistic VHEE beam model. An electron source was therefore placed 183.3 cm upstream from the WT. The beam then entered a 107.7 cm long vacuum box and then 75.6 cm of air before reaching the water phantom. Two scanning magnets were placed in the vacuum box to minimize the beam scattering along the beamline. The electron doses were scored in a grid with a 1x1x1 mm^3 resolution, using the TOPAS "DoseToMedium" scorer. The dose distribution was recorded in a 30x30x70 cm^3 water phantom with a binning of 1x1x1 mm^3, and was simulated for each energy using 10^7-10^8 particles. These settings allowed to achieve a relative statistical uncertainty of less than 3% (type A, calculated as the average statistical uncertainty of voxels with a dose higher than 50% of the maximum dose).

The MC data were compared to the analytical model for realistic treatment field dimensions (up to 15x15 cm^2) and at several centimetres in depth, as VHEE therapy is a promising technique for treating deep-seated tumours. MC dose distribution in water, as well as in the presence of inhomogeneities in the tissue equivalent material, were compared with numerical calculations as a test of the algorithm. The geometry of the simulation is shown in figure 2.1: figure 2.1(a) corresponds to configurations including only the WT, while the geometry in figure 2.1(b) is used to study the model in the presence of inhomogeneities. In this last case, a 5 cm thick slice of cortical bone or lung material was included at the entrance of the WT. Density values of 1.85 and 0.26 g/cm^3 were used to model

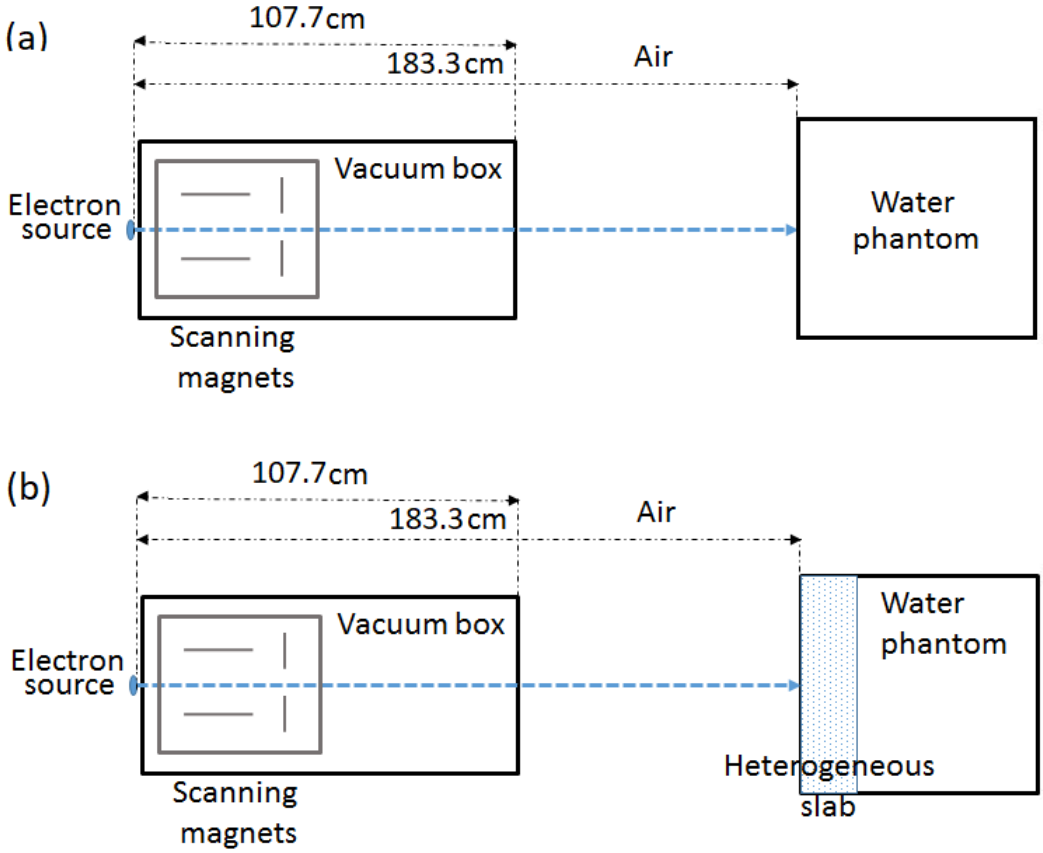

Figure 2.1: Geometry used for the Monte Carlo simulation of the pencil beam scanning beamline: (a) the electron source is placed at the entrance of a vacuum box. After passing through the vacuum box, the beam travels in air until it reaches the WT (b) the same beam line as in (a) with the addition of 5 cm slabs at the entrance of the WT to study the scattering model in the presence of inhomogeneities.

cortical bone and deflated lung, respectively, the relative composition of which was modelled according to the NIST database [11] and is given in table 2.2.

To evaluate the dose accuracy of the analytical model at the centre of large fields (comprising a large number of adjacent pencil beams), field size factors (FSF) were computed and simulated in water at the depth of the maximum dose and for square fields ranging from 1x1 to 15x15 cm^2. The fields consisted of 9 to 961 regularly spaced pencil beams (the spot size σ was always set to 5 mm and the distance between the spots was set to σ). The FSF was defined as the ratio of the dose at the centre of a given field to the dose at the centre of the 10x10 cm^2 field.

Relative composition			
Cortical bone		Inflated lung	
Hydrogen	0.05	Hydrogen	0.1
Carbon	0.14	Carbon	0.1
Nitrogen	0.04	Nitrogen	0.031
Oxygen	0.45	Oxygen	0.75
Magnesium	0.0022	Sodium	0.002
Phosphorus	0.1	Phosphorus	0.002
Sulfur	0.0032	Sulfur	0.003
Calcium	0.21	Chlorine	0.003
Zinc	0.0001	Potassium	0.002

Table 2.2: Relative composition for cortical bone and inflated lung from NIST tables [11].

Particle source settings and physics The TOPAS simulations were run with a physics list consisting of six modules: "g4em-standard-opt4", "g4h-phyQGSPBICHP", "g4decay", "g4ion-binarycascade", "g4h-elasticHP" and "g4stopping". Cut-offs for all particle productions were set to 0.01 mm. The minimum and maximum EM parameters were set to 100 eV and 200 MeV, and the number of bins per decade for stopping power and lambda bins were set to 100. All other parameters were set to their default values. It should be noted that the physics list "g4em-standard-opt4" uses the multiple scattering of the WentzelVI model for electrons with energy above 100 MeV and the Goudsmit–Saunderson model for electrons with energy below 100 MeV. Simulations were performed on the Joliot Curie-Rome computational cluster with 128-cores IntelSkylake@2.7GHz CPUs, providing approximately 4-5 CPU hours per million particles at 100 and 200 MeV, respectively. The electron source was defined as a mono-energetic bi-Gaussian source distribution and with Gaussian distributions for the position and momentum direction. The beam divergence and correlation were set to 1 mrad and 1, respectively, as typical for proton therapy installations with pencil beam scanning. However, a spot size σ dependent on the beam energy was used for the lateral distribution. Indeed, the size of the electron source was adapted to produce a spot with a 5 mm σ at the WT entrance for each energy, as described in table 2.3.

2.4 Results and validation tests

The validation of the Fermi-Eyges theory of multiple scattering for VHEE computations requires several steps. An energy parameterisation that accurately estimates the mean beam energy for large depths is first fitted. The various scattering power models used for the calculation of the mean square radius of the beam are then tested and selected. The large scattering angles, which are neglected in the

	Nominal energy (MeV)		
	100	150	200
Energy spread (MeV)	0.65	0.56	0.38
Spot size (mm)	1.3	2.1	2.4
Source divergence (rad)	0.001	0.001	0.001
Spot Correlation	1	1	1

Table 2.3: Source description used for MC simulations with the toolkit TOPAS/Geant4 (beam parameters at the vacuum box entrance in figure 2.1).

small-angle approximation, are also taken into account using a realistic beamline model. For this purpose, a two-Gaussian model is introduced and parameterised. Finally, the model is tested and compared to MC simulations for various field sizes and geometries. The results of these steps are described in the following sections.

2.4.1 Mean energy parameterisation

Figure 2.2 shows (on the top) the mean primary electron energy in water according to depth and practical range r_0 for irradiations with 10 and 20 MeV energy electrons. A comparison is proposed between the different equations used in the literature (equation 2.29-2.31) to calculate the mean energy and the values obtained from the MC simulations (calculated using equation 2.28). A fit using equation 2.31 was also included and used to calculate a and b parameter values that would be in better agreement with the mean energy values obtained from the MC simulation at large depths. As expected, all different parameterisations are in good agreement with the simulations for shallow water depths. For greater depths, however, the differences between models and simulations are greater as the electron energy increases. Differences of more than 50% are found for 100 and 200 MeV beams and from the mid-range, as can also be seen in figure 2.2 (lower part). The model proposed by Bruinvis et al. [127] was adapted for the 10-200 MeV energy range in order to calculate the scattering of electrons in water. Equation 2.31 was fitted to the MC data for the whole energy range from 10 to 200 MeV, showing a good agreement between the mean energy variation with depth and the simulations, as can be seen in figure 2.2 (lower part), especially at high energies. The mean absolute error is 9 MeV, 38 MeV, 0.5 MeV and 0.4 MeV for the ICRU 35 equations 2.29-2.30, Bruinvis et al. [127], and equation 2.31, respectively. The obtained parameters a and b for equation 2.31 are listed in table 2.4 with 95% confidence intervals and are shown in figure 2.3 together with their respective fits between 100 and 200 MeV.

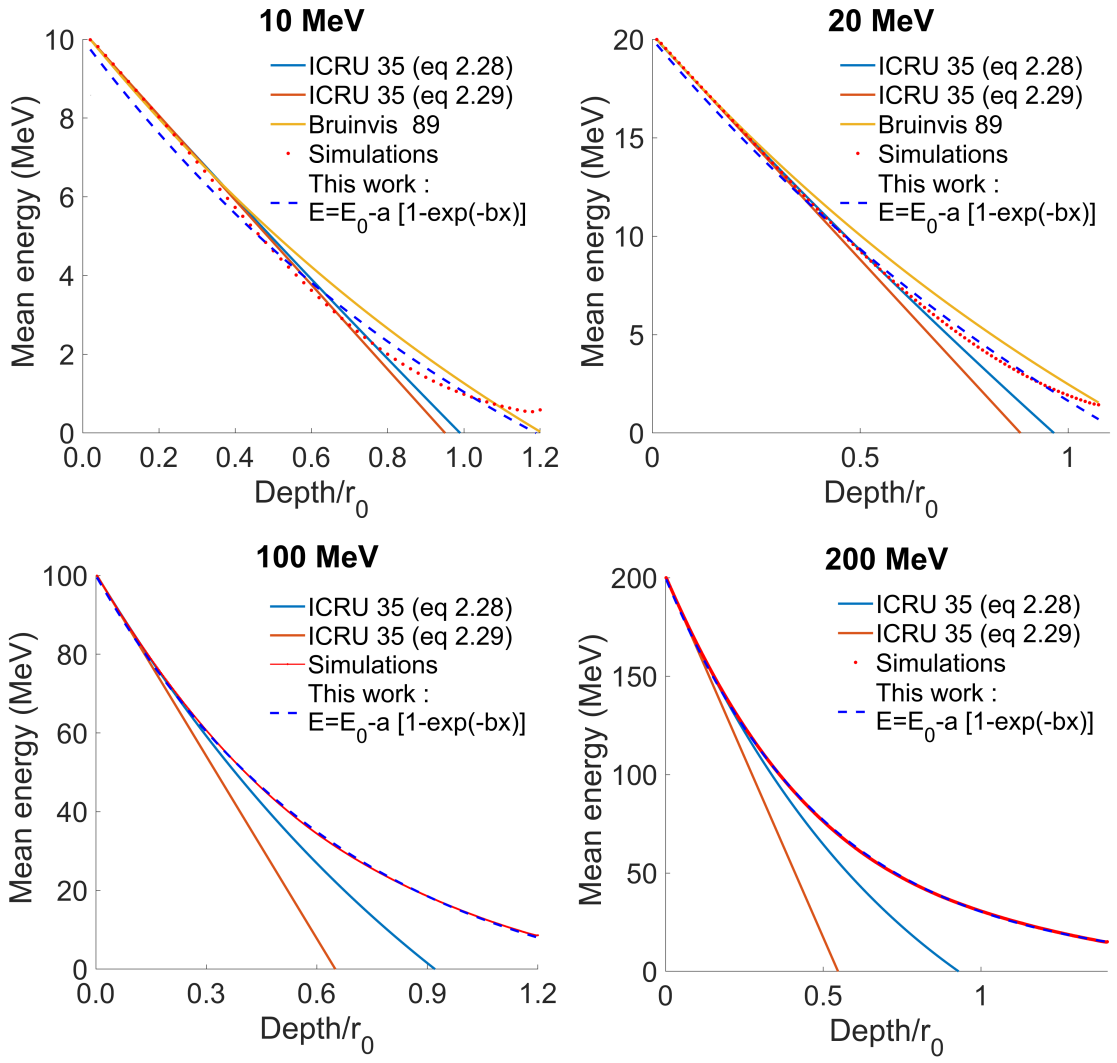

Figure 2.2: Electron mean energy variation according to depth (practical range r_0) in water for 10, 20, 100, and 200 MeV electron pencil beams, and as predicted by the different equations from ICRU35 (equation 2.29 and equation 2.30), from Bruinvis et al. [127] (only for 10 and 20 MeV) and from equation 2.31 (dashed line) with the parameters a and b obtained in this work fitting the equation to MC simulation data. The simulations (dotted lines) were performed with the TOPAS/Geant4 Monte Carlo toolkit and a theoretical electron source located at the entrance of the water phantom.

Energy (MeV)	a	b
10	16.6±1.7	0.155±2.3e-2
20	38.6±2.4	0.069±5e-3
100	110.90±0.30	0.04421±2.3e-4
150	154.34±0.20	0.04±1.19e-04
200	197.99±0.17	0.04±8.16e-05

Table 2.4: Parameter values (a and b) with 95% confidence interval of the mean energy model E(z) (described in equation 2.31) for four electron beam energies: 10, 20, 100 and 200 MeV.

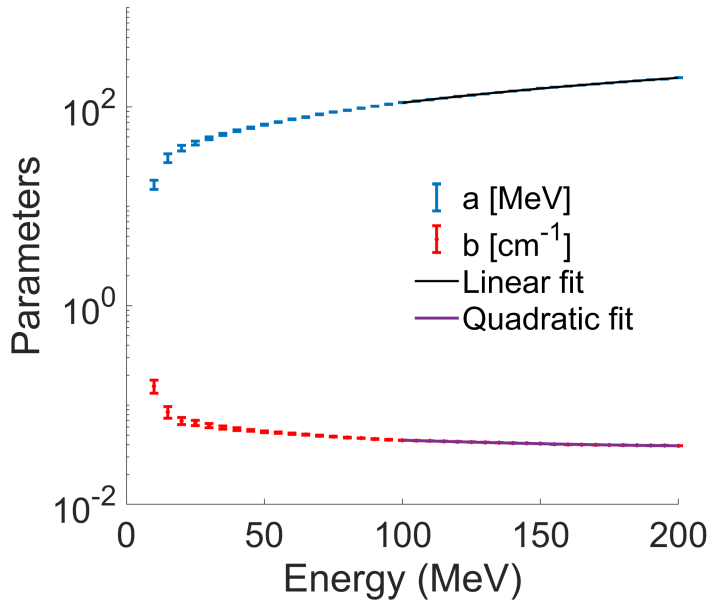

Figure 2.3: Variation of the parameters a and b (represented with the 95% confidence interval) from equation 2.31 according to the initial electron pencil beam energy (from TOPAS MC simulation data). The solid lines show an example of fits for a and b parameters limited to the 100-200 MeV energy range.

2.4.2 Scattering power and range straggling

Scattering power

Figure 2.4 compares the different scattering power models and their influence on the mean radial spread, $r_{1/e}$, for 10 and 100 MeV electron pencil beams. For all models, $r_{1/e}$ was calculated using equation 2.4, and mean energy from equation 2.31 with the parameters a and b obtained from fitting equation 2.31 to MC data. Thus, only the method for estimating scattering power varied between the models. The scattering power was calculated using equation 2.13 or its restricted version in equation 2.17 for comparison. The scattering power was also calculated as described by Kainz et al. [135], using equations 2.18-2.23, or with the reduced Gaussian formulation, using equation 2.25.
When the range straggling phenomenon is not considered, the lateral scattering of electrons in water is poorly evaluated by the various models in the final part of their path, as is shown in figures 2.4-2.5. In fact, the use of scattering power in Rossi's formulation leads to an overestimation of the radial width $r_{1/e}$, as already mentioned in several previous studies [130,131,134]. The restriction to small scattering angles is also not sufficient to reduce this overestimation, as shown by the Andreo model in the figure. In contrast, the Kainz et al. [135] formulation is the one that most accurately estimates the scattering of electrons for shallow depths when the range straggling model is included, as from figure 2.5. Therefore, in what follows, the Fermi-Eyges multiple scattering theory will be used with the Kainz et al. [135,140] formulation for the scattering power calculation.

Range Straggling

Figure 2.5 shows the modified $r_{1/e}$ calculation including the range straggling correction for 100, 150 and 200 MeV electrons (equation 2.32), whose parameters are reported in table 2.5 (for 100, 150 and 200 MeV). A close match of the Monte Carlo values could be obtained within 3 % and with a mean absolute error between simulated and calculated primary radial spread of 0.2 mm, 0.6 mm and 0.3 mm at 100, 150 and 200 MeV, respectively, with different parameter values for very high-energy electrons compared to their low-energy values. An example of how the parameterisation for equation 2.2 is obtained by evaluating the quantity r_{simu}/r_{calc} is shown in figure 2.5 for a 100 MeV pencil beam (corresponding to the ratio between the mean lateral scattering from the MC simulations and from the analytical model calculated with equation 2.4).

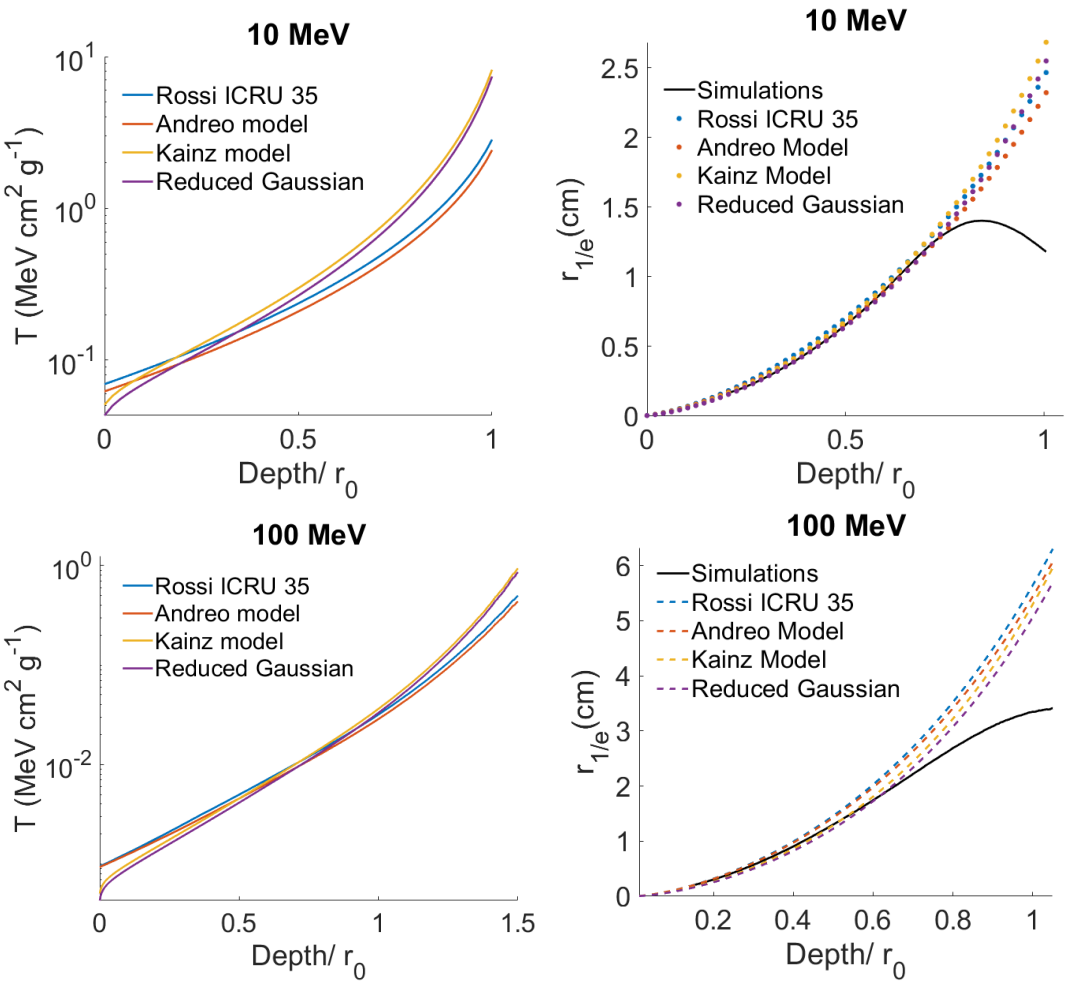

Figure 2.4: On the left, the evolution of the scattering power in depth for all models considered for 10 and 100 MeV initial pencil beam energy: Rossi model from equation 2.13; Andreo restricted model from equation 2.17; Kainz model as in equations 2.18-2.23 and the reduced Gaussian from equation 2.25. On the right: Effect of the different scattering models on the mean radius, $r_{1/e}$, for 10 and 100 MeV electron beams.

Energy (MeV)	**100**	**150**	**200**
a	0.038 ± 0.0002	0.884 ± 0.001	0.935 ± 0.001
b	21.31 ± 0.04	0.59 ± 0.01	0.56 ± 0.01
c	0.0457 0±0.001	4.4 0±0.003	4.69 ± 0.041

Table 2.5: Range straggling parameter values (a, b and c used in equation 2.32) for the VHEE energies of 100, 150 and 200 MeV with a 95% confidence interval.

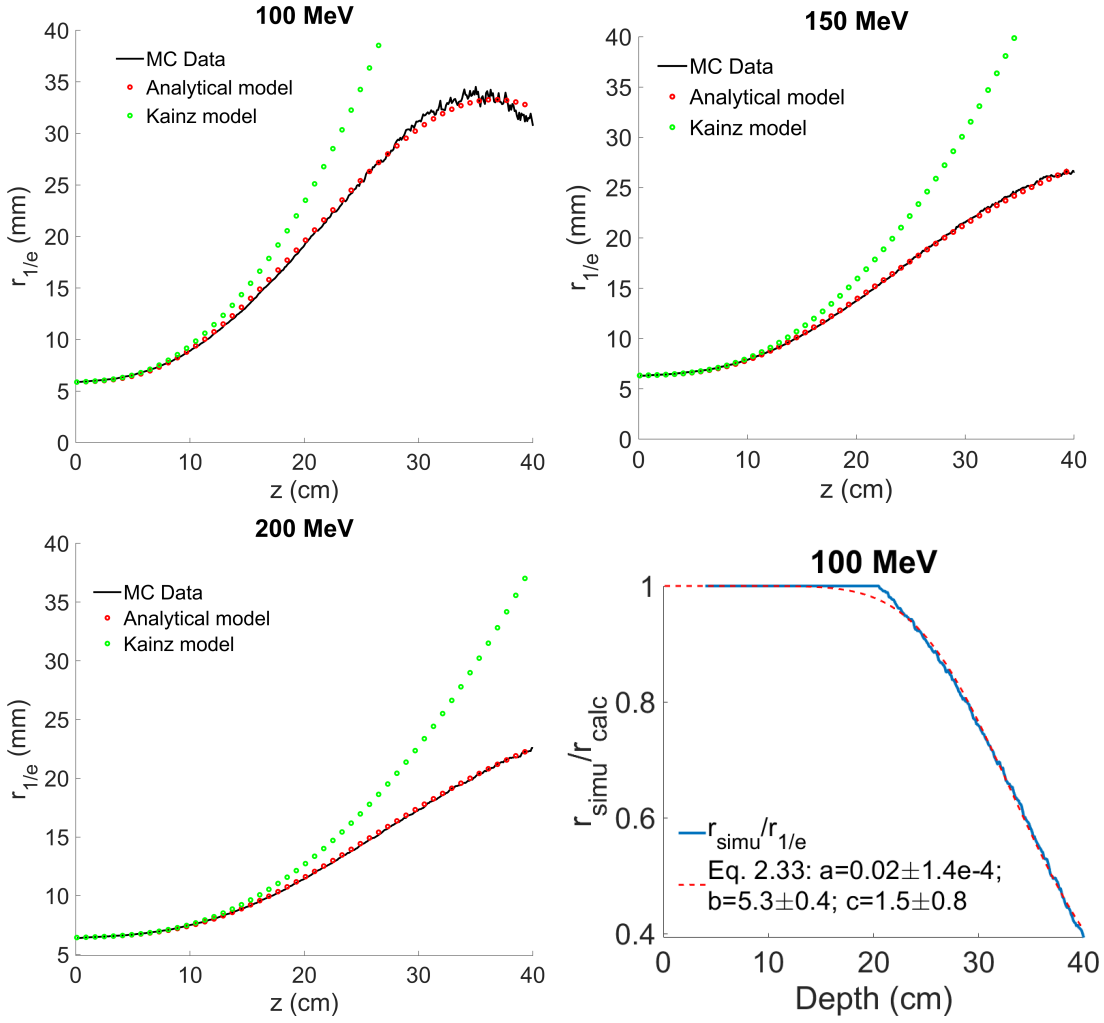

Figure 2.5: Comparison of the evolution of the radial distribution $r_{1/e}$ with depth between the MC simulation and the analytical model without (green dotted line) and including the range straggling model (red dotted line) described in equation 2.32. Realistic VHEE pencil beams of 100, 150 and 200 MeV energy are considered as sources. The beamline geometry included in both the analytical model and the simulations is shown in figure 2.1(a). The ratio between the two widths obtained from the MC simulations r_{simu} and the analytical model without the straggling correction $r_{1/e}$ for 100 MeV pencil beam is also shown (bottom on the right), with the parameters to describe the straggling obtained from fitting the $r_{simu}/r_{1/e}$ curve to equation 2.32.

2.4.3 Lateral profiles parametrisation

Double Gaussian model

Figure 2.6 shows the weight and the radial spread of the double Gaussian component in equation 2.33 for 100, 150 and 200 MeV VHEE pencil beams. The figure also shows the agreement (between the analytical model and MC simulation) up to the 0.1% of the dose for the lateral beam distribution of a 100 MeV pencil beam for the two depths of 10 (red curves) and 20 cm (blue curves). The figure also includes the single Gaussian model to show that, for low percentage dose values, the single Gaussian model gives a poorer agreement with the MC simulation curves than the double Gaussian. This difference has been found to affect the radial spread of the VHEE beams in the first half of their range in water when considering a realistic beam source. However, this was found to have a greater effect when evaluating larger fields than for single pencil beams, where only a small difference in the mean lateral spread, the $r_{1/e}$ evolution in water was obtained in the first half of the range, as from the lower part of figure 2.6 where the $r_{1/e}$ evolution with depth from single and double Gaussian models and MC simulation data for a 100 MeV pencil beam is also shown.

2.4.4 VHEE analytical model evaluation for broad beams

Isodose distributions

Figure 2.7 shows a comparison between the isodose distributions in water obtained by the analytical model and the MC simulation data for 100, 150 and 200 MeV and for three field sizes of 5x5, 10x10 and 15x15 cm^2. The analytical model is shown as dashed curves and the MC simulation data as solid curves, and the beamline geometry is described in figure 2.1(a). The dose distributions are normalised to the maximum of the dose matrix value and sampled every 0.1 between 0.1 and 1. Good agreement, between the MC and analytical curves, is obtained over the whole depth range, for all energies and field sizes. Distance-to-agreement (DTA) tests, which measure the distance between each MC dose point and the nearest point on the analytical dose distribution [142], give a maximum of 1 mm (DTA) over two orders of magnitude. 2D gamma analysis was also performed and, with a pass criterion of 2%/2mm, more than 91% of the evaluated points passed the gamma index test for 5x5 cm^2 field, more than 97% for 10x10 cm^2 field and more than 95% for 15x15 cm^2 field. The gamma index test is performed in a 2D space, where one axis corresponds to the dose difference and the other to the DTA distance. For each point (x,y), the Euclidean distance between the dose difference and the DTA is calculated. The minimum value of this distance corresponds to the $\gamma(x, y)$. A comparison between the on-axis PDDs of the analytical and MC

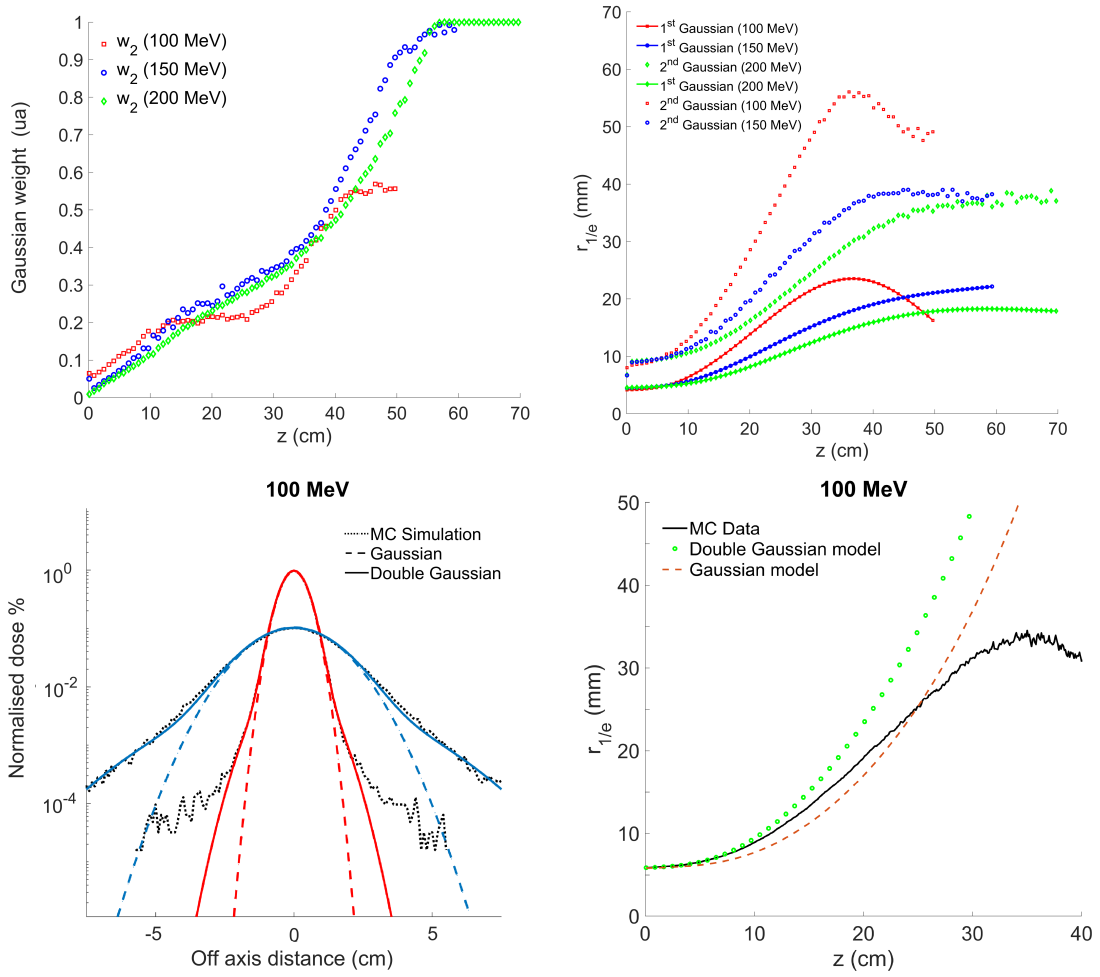

Figure 2.6: Top: w_2 and r_2 parameters of the double Gaussian model in equation 2.33 derived from MC simulation data for 100, 150 and 200 MeV VHEE pencil beams. Bottom left: Comparison between MC simulated lateral beam profiles (dotted curve) and the analytical single Gaussian (dashed curve) and double Gaussian models (solid curve) for a 100 MeV pencil beam at two depths of 10 (red curves) and 20 cm (blue curves) in water. Bottom right: Comparison between the mean lateral spread, $r_{1/e}$, evolution with depth from single and double Gaussian models and MC simulation data for 100 MeV pencil beam.

dose distributions for the different field strengths and energies is shown in figure 2.8. An agreement within 2% is obtained between MC and analytical PDDs with an average point difference of less than 1%, 0.6% and 0.7% at 100, 150 and 200 MeV respectively.

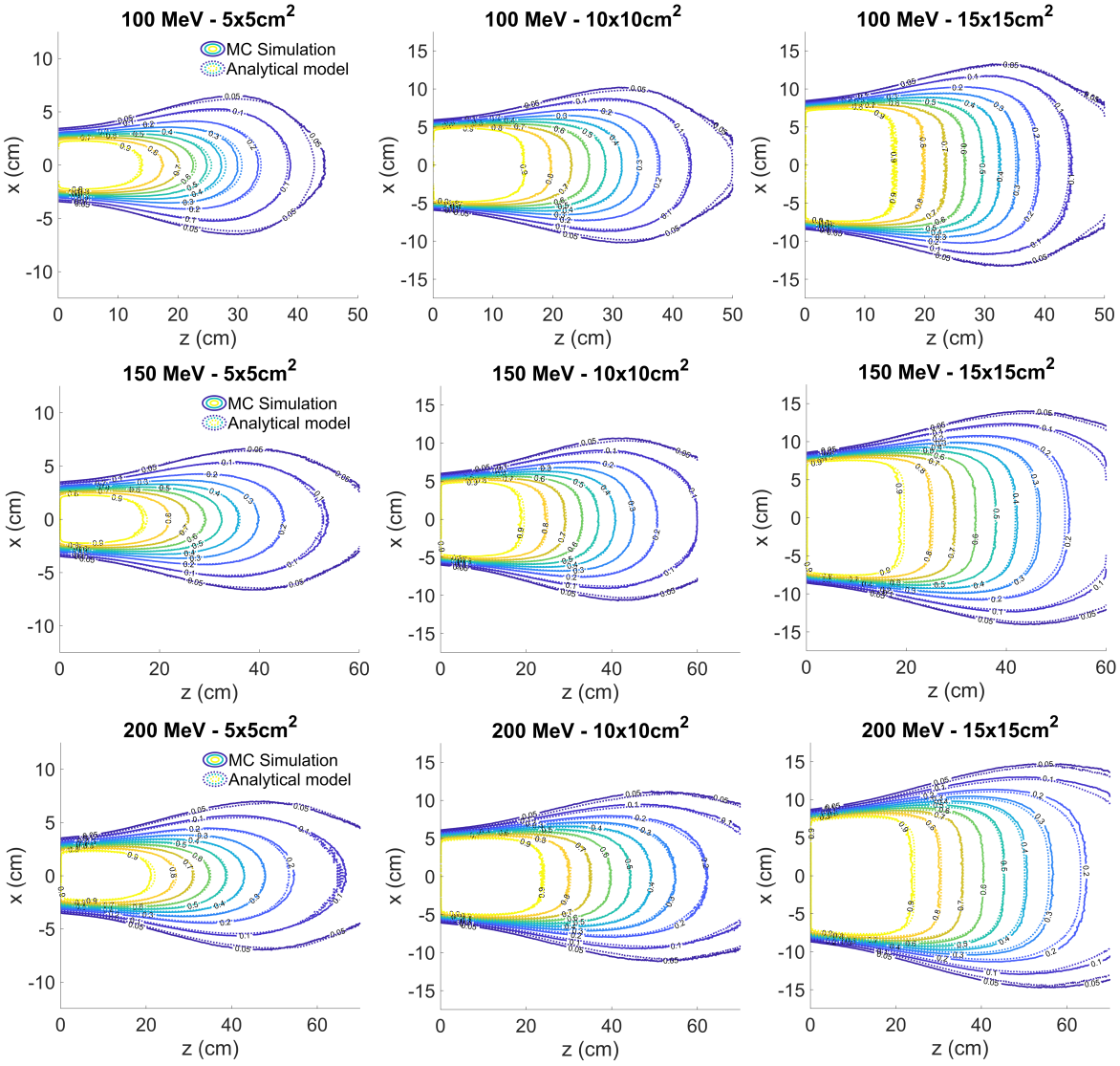

Figure 2.7: Isodose distributions for 100, 150 and 200 MeV broad beams in water for 5x5, 10x10 and 15x15 cm^2 fields. Comparison between the analytical VHEE model, dashed curves in the figure, and the MC simulation data, solid lines. The isodose distributions are normalised to the maximum dose value and shown between 0.1 and 1.

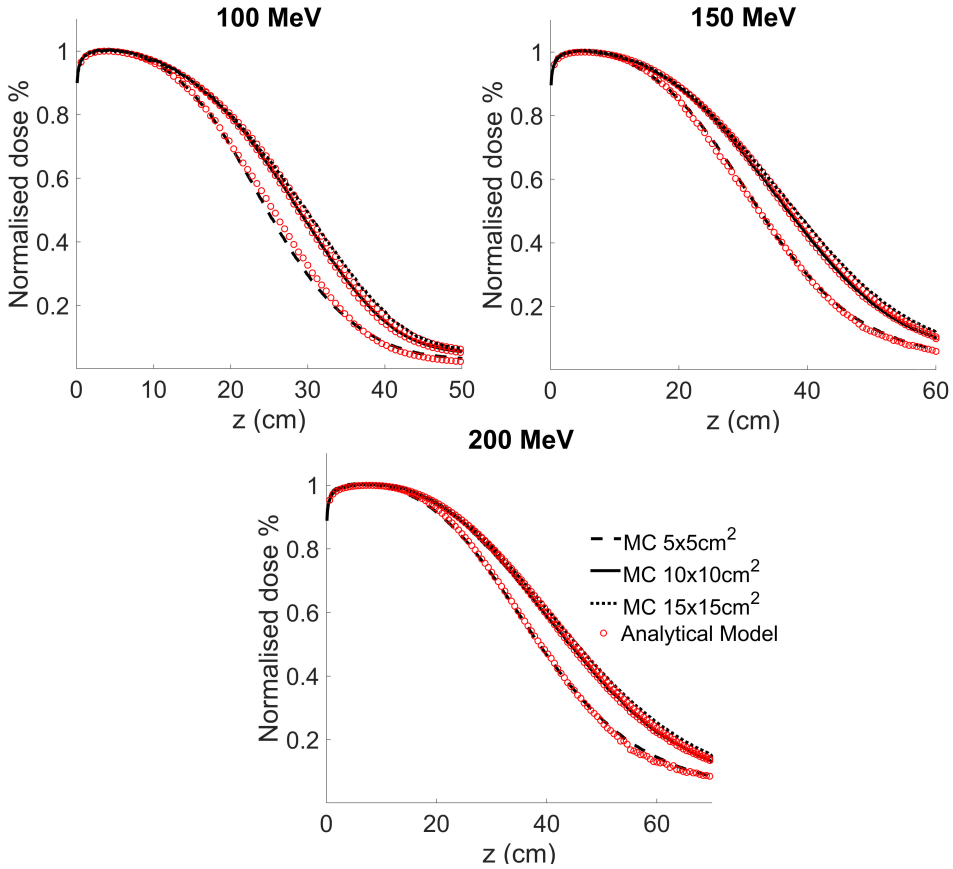

Figure 2.8: PDD comparison between MC (solid lines) and analytical (dashed lines) dose distributions for 100, 150 and 200 MeV broad beams sizes of 5x5, 10x10 and 15x15 cm^2.

Field size factors

Field size factors (FSFs), corresponding to the ratio of the dose at the centre of a field to that of a 10×10 cm^2 field, were evaluated for three energy levels of 100, 150 and 200 MeV and for several field sizes between 1x1 and 15x15 cm^2 (1x1, 2x2, 4x4, 8x8, 10x10 and 15x15 cm^2). The maximum doses correspond to depths of 50, 110 and 140 mm at 100, 150 and 200 MeV, respectively. The FSFs have been evaluated for both MC and analytical dose matrices and for single and double Gaussian descriptions of the electron fluence and are shown in figure 2.9. The figure shows that the analytical model reproduces the same trend as the MC simulations used as a reference. In fact, the FSFs increase with field size for both the case and all energy values. It can also be seen that the single Gaussian and double Gaus-

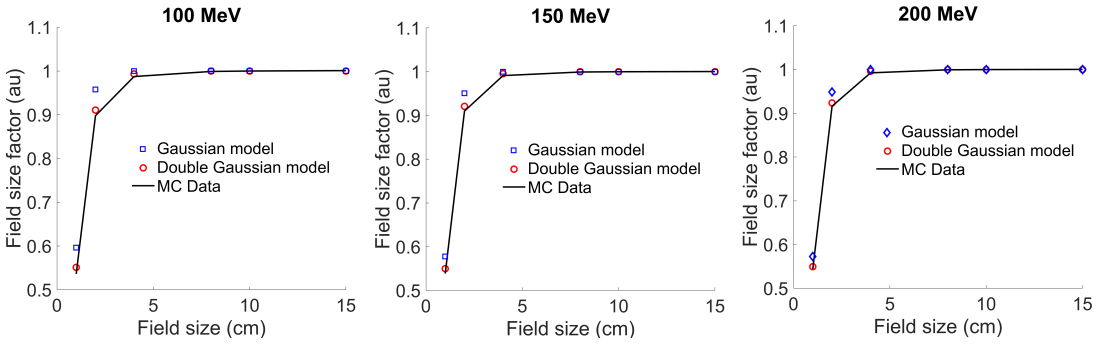

Figure 2.9: Field size factors (FSFs) for 100, 150 and 200 MeV broad beams from 1x1 to 15x15 cm^2. Comparison between MC and analytical data (from single and double Gaussian electron fluence modelling).

sian models reproduce the dependence of the FSFs on the field size to a different approximation, within 1.5% and 6%, respectively. The mean difference between the two models and the MC simulation data also confirms a better description of the beam fluence and hence the dose matrix obtained from the double Gaussian model compared to the single Gaussian description. Actually, for 100, 150 and 200 MeV broad beams, the mean difference for the single Gaussian model is 2.2%, 1.5% and 1.2% respectively, while for the double Gaussian model it is much lower at 0.5%, 0.5% and 0.3% respectively. However, the lowest agreement was found for the smaller field sizes of 1x1 and 2x2 cm^2 for both fluence models.

2.4.5 Evaluation of the model in inhomogeneous regions

Figure 2.10 shows the variation of the radial spread when a VHEE pencil beam of 100 (left) or 200 MeV (right) is incident in water or in a 5 cm slab of cortical bone or inflated lung in water. The beamline geometry is shown in figure 2.1(b). The analytical $r_{1/e}$ is compared with the MC simulation data, shown as solid line curves. The width $r_{1/e}$ was calculated using equation 2.4 and included the range straggling dependent model (equation 2.32). The scattering power, for the cortical bone and the inflated lung, was calculated using the Bragg-Kleeman rule described by equation 2.26, whose parameters are described in table 2.2. In this case, the mean energy variation with depth for the inhomogeneous zones was calculated using equation 2.30, as the mean energy was found to deviate from the model for much larger depth values than the one considered of 5 cm, as shown in figure 2.2. For water, however, equation 2.31 was used, considering in both cases a depth value equal to the equivalent path in water (for the inhomogeneous zone) plus the effective depth traversed in water. From the figure 2.10 it can be seen that the model is close to the range values obtained from the MC simulations and also predicts the saturation of the function in all geometric configurations, as shown

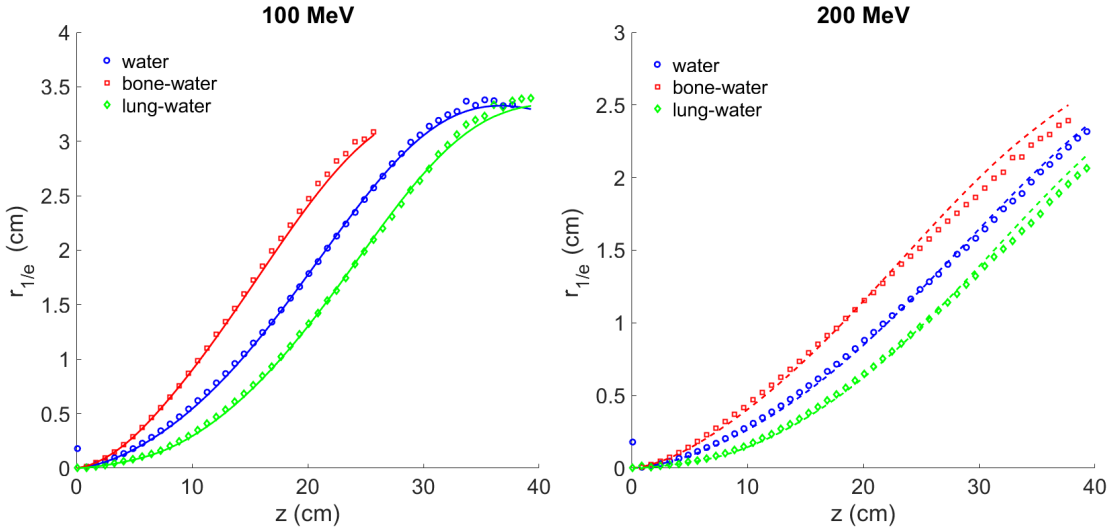

Figure 2.10: Variation of the width of the radial spread with depth for 100 (on the left) and 200 MeV (on the right) VHEE pencil beams incident on water or on a 5 cm thick slab of cortical bone or inflated lung in water. The analytical model is compared with the MC simulations indicated by the solid lines (geometry in figure 2.1(b)).

by the 100 MeV curves. A good agreement, within 3%, is obtained between the model and the simulations, with a mean absolute error between the calculated and the simulated radial spread of 0.3 mm at 100 MeV and 0.4 mm at 200 MeV, respectively.

2.5 Discussion

The adaptation of the Fermi-Eyges model of multiple scattering to VHEE required numerous modifications. For example, calculation results were strongly dependent on the mean energy approximation and the scattering model used. In addition, a double Gaussian kernel model for the description of the beam fluence (which included a parametrisation of the range straggling phenomena) was required to accurately describe a realistic VHEE pencil beam, as is often the case when modelling proton beams [143]. The resulting dose distributions (see figure 2.7) showed good agreement with MC simulations. In a subsequent part of this study, the developed analytical model will be used together with MC simulation to design a VHEE accelerator nozzle. The model helps to speed up the process by searching

the solution space for multiple parameters and finding an optimal configuration, which would have taken much longer using MC simulations alone.
The results in figure 2.7 also highlight field size dependent effects, probably due to secondary particle production in the WT, which could possibly be improved by modelling the primary electron and secondary photon components separately in the pencil beam model. Indeed, while secondary photon production is limited for low energy electrons [3], the photon contamination dose component, mainly arising from interactions in the phantom, is expected to increase significantly at very high electron energies. The inclusion of photon contribution modelling in the model could significantly improve the agreement with MC simulation data. While analytical expressions exist for estimating the bremsstrahlung contamination independently of electron dose in the energy range from 1 to 50 MeV [144], this has yet to be tested at higher energies. A precise quantification of photon dose for both scattered and scanned beams will be described in a later chapter to partially overcome this limitation.
The fact that VHEEs scatter less than low-energy electrons and are also less sensitive to tissue heterogeneity or density uncertainties is also mentioned in different studies. In Bohlen et al. [123], the lateral penumbra of VHEE beams was compared with that of high-energy photons (6–15 MV), showing that those of VHEE could be much larger than those of photons except in the first 5-10 cm. The results obtained in this work also confirmed these orders of magnitude since a factor of 2 is obtained when comparing the radial width evolution in depth between 10 MeV and 100 MeV electron beams (in figure 2.4).
However, one of the advantages of VHEEs is that they are light charged particles that can be focused at large depths, thereby improving their physical characteristics. The study by Whitmore et al. [50] showed that it is possible to focus VHEE beams using quadrupole magnets at the depths required for deep-seated tumors. Thus, the authors showed that they could maintain a beam size of approximately 1 cm at the focal point for VHEE energies between 150 and 250 MeV, while also allowing for the possibility of producing spread-out electron peaks similar to proton spread-out Bragg peaks with reduced entrance and exit doses.
Existing Treatment Planning Systems (TPSs) do not currently take into account the temporal aspects of dose delivery. However, after the recent development of FLASH proton therapy with scanned beams, several metrics have been proposed to compute 3D Dose-Averaged Dose Rate (DADR) distributions, while considering each spot relative dose contribution [145–148]. New algorithms were then proposed using these metrics, and by modifying the optimization method to a Simultaneous Dose and Dose Rate Optimization (SDDRO) method, to optimize tissue-receiving dose rate distribution as well as dose distribution (or even dose-averaged linear energy transfer) distribution [149]. For such algorithms, the dose and optimizer calculations are usually separated and can use the results of accurate MC calculations. There are, however, multiple proposed dose delivery parameters of possible importance for enabling the FLASH effect. These may include dose, dose deliv-

ery duration and mean dose rate, intra-pulse dose and dose rate, spot spacing, scanning times and beam pauses, among others [103]. In this context, simple and fast calculation models could be useful to quickly test a large number of configurations or parameters before the optimum solution is reached. Therefore, the next sections also discuss the implementation and testing of the VHEE pencil beam scanning double Gaussian model in an open source TPS (matRad) environment, which could enable further pre-clinical investigations, including treatment plan optimisation and evaluation.

2.6 Conclusions

A simple and efficient model to describe the small-angle scattering of electrons, taking into account the energy loss and range straggling of the electrons, has been developed and tested against MC simulations. Analytical radial dose profiles of pencil beams in water show satisfactory agreement with those produced by Monte Carlo simulations in the 100-200 MeV energy range. However, further improvement of the method would require the inclusion of a model for the large angle scattering of the electrons and for the contribution of bremsstrahlung photons (which will be further discussed in Chapter 5). The next chapter describes how such Fermi-Eyges theory of multiple scattering adapted to VHEEs can be used to design two beam conformation systems tailored to FLASH applications, in particular, a double scattering system.

Chapter 3

Conformation techniques for FLASH-VHEE therapy

Contents

3.1 Introduction

The growing interest in the use of VHEEs for RT is closely linked to their potential combination with UHDR irradiation. Indeed, the combination of these two techniques could lead to the treatment of deep-seated tumours while taking advantage of the biological benefits of the FLASH effect, thus better sparing the patient's healthy tissues. However, many unknowns remain regarding the exact specifications to be met in order to generate an optimal biological effect (such as the dose ranges, dose per pulse, total irradiation time, spatial and temporal fractionation schemes, etc.). In addition, most of the recent work on small animals has been conducted with electron beams between 5 and 7 MeV generated by linear accelerators [150, 151], or by proton accelerators with beams of over 220 MeV, with scattering delivery technique [93, 152, 153] which limits the field size (a few cm^2) or the target-to-source distance ($<$1.5m). The use of scanned beams is also a possible beam delivery technique in FLASH therapy and has the advantage of solving some of the difficulties associated with scattered beams, such as beam shaping, a significant increase in the secondary particle dose to the patient and transmission losses that increase with field size [154]. Moreover, the FLASH effect was also recently demonstrated for proton pencil beam scanning, which is key to the clinical development of FLASH therapy with charged particles [155–157].
Most clinical beams in radiotherapy can conceptually be described as narrow beams emerging from an accelerator, converted to a broad beam by either a Pencil Beam Scanning (PBS) or a double scattering Double Scattering (DS) system. A scattering system usually uses one or two foils, depending on the target size, to achieve a homogeneous dose distribution adapted to the maximum lateral tumour dimension. In contrast, the magnetic scanning of small pencil beams allows the treatment of tumours with improved 3D conformation.
Regardless of the conformation method employed (the basic principles of which will be outlined in the first section of this chapter), the maximum size of the treatment field is therefore limited to meet the constraints on the irradiation time. In PBS, the main limitation will be related to the time needed to irradiate while scanning the beam over the whole surface of the irradiation field, for example, because of the stabilisation time of the magnetic fields within the magnets or the time required by the electronics to read the signals or dose measurements. The Pulse Repetition Frequency (PRF) of the accelerator is another important factor since it will determine the number of pencil beam positions that can be delivered per second. For scattered beams, the peak current of the accelerator is one of the main parameters to consider. Indeed, the larger the uniform field size to be obtained, the thicker the scatterers will have to be, thereby limiting the intensity transmitted to the point of irradiation. Several methods for optimizing the design of such beamlines and treatment heads have already been proposed for FLASH therapy, either in proton therapy [147], or for low energy electrons of a few MeV [158].

These models have not been studied extensively for ultra-high dose rate VHEE. Therefore, one of the main objectives of this chapter is to assess the possibility of adapting conventional conformation methods to the FLASH-VHEE technique. The analytical formalism (presented in Chapter 2) based on Gaussian multiple Coulomb scattering theory is used to design a double scattering system for electron beams [131], and MC simulations were performed to validate the analytical calculations. The MC simulations also allowed an accurate quantification of the absolute number of electrons and the dose rate required for using the broadened electron beam in the range of application of FLASH therapy. As described in Kainz et al. [135], who improved Green's model [131], a Gaussian function is also used to design the contoured profile of the second scatterer. The model from Kainz et al. also paid special attention to the calculation of the angular scattering power at very high energies, which was evaluated using a thickness-dependent formula (equation 2.18). The optimisation of the system parameters was automated within an in-house Matlab (Mathworks, US, R2018a) script and tested for energies between 100 and 200 MeV. The second objective presented in this chapter is also to perform a comprehensive comparison between DS and PBS, especially by considering instantaneous spots and field dose rates, total dose, machine characteristics, field size and homogeneity to meet the FLASH dose rate requirements. These considerations will help identify the relationship between beam current and dose rate, which can be used to define the specifications of new machines.

3.2 Conformation techniques in radiation therapy

Two main conformation techniques are used in RT to convert the narrow beam emerging from an accelerator into a broadened beam. These conformation systems are either based on passive scattering or active scanning of the pencil beam and are placed between the patient and the accelerator system (usually in a vacuum environment ending with a thin exit window). While the scanning system is usually placed in vacuum, the scattering system is normally placed in air, and the compactness of the system is a design issue for this type of machine.
Scattering systems use high density foils to scatter and shape the beam fluence distribution in order to irradiate the target uniformly while maintaining the smallest possible lateral penumbra. In most systems, a first scattering foil made of metal with a high atomic number, Z, is used in order to maximize the ratio of the scattering to the stopping power (and therefore minimize energy loss in the system). In practice, Tantalum (Z=73), Gold (Z=79), Tungsten (Z=74), or Lead (Z=82) are most often used. After passing through the scattering foil, the beam can be characterised by its fluence distribution, as shown in figure 3.1, which can be used to simulate and optimise the transverse spreading of a theoretical system. Grusell et al. [159] previously addressed the optimal thickness of the first scatterer

and found empirically that its minimum thickness for a given radius of the uniform beam profile could be computed analytically. In practice, the total thickness of both scatterers must also be minimised. An optimum design is then obtained when, after scattering in a first foil, the standard deviation of the Gaussian beam profile at the isocenter is greater than 60% of the required field size, which is the rule of thumb that can be followed [160]. The second scatterer is used to flatten the beam profile and obtain a homogeneous dose distribution at the isocenter, as shown in figure 3.1. This second scatterer profile usually follows a Gaussian distribution (as the incident beam profile): it is thicker in its centre to scatter the beam's central part more than on the edges. Thus, by decreasing its thickness as a function of the radial distance, the second scatterer is able to produce a homogeneous beam fluence distribution at the isocenter. A collimator system is also usually used to minimise the lateral penumbra of the beam and limit secondary particles. Collimation systems are generally combined with patient-specific collimators (e.g. typically made of brass or tungsten), used to match the shape of the field to the transverse target profile.

Active scanning delivery systems use scanning magnets and consist of the electromagnetic scanning of small pencil beams. A two-dimensional pencil beam pattern can thus sequentially be delivered to irradiate the target volume uniformly. Two sets of dipole magnets, one for the x-direction and one for the y-direction, are used (the geometry of such a system is shown in figure 3.1(c)): the advantage of the latter technique is that the pencil beams do not interact with active components in the treatment head of the accelerator. The main advantage of PBS over the DS technique is a better dose conformality for complex target geometries, thanks to the possible 2D optimisation of the pencil beams intensity and position. PBS delivery is mainly used in proton therapy at the moment, but electron beam applications have also been used in the past [161].

In the next sections, the options and models developed to simulate the transverse spreading of a theoretical VHEE beam interacting with a scattering or a pencil beam scanning system will be presented. In particular, the analytical model based on the Fermi-Eyges theory and Green's work [131], applied to the design of a conformation system for VHEEs, will be described in detail.

3.3 Double Scattering Model

3.3.1 General considerations

The double scattering model proposed by Green et al. [131] can be used to optimise several scattering system parameters such as the scatterers thicknesses, material, distances and geometry of the beamline for electrons up to 50 MeV and

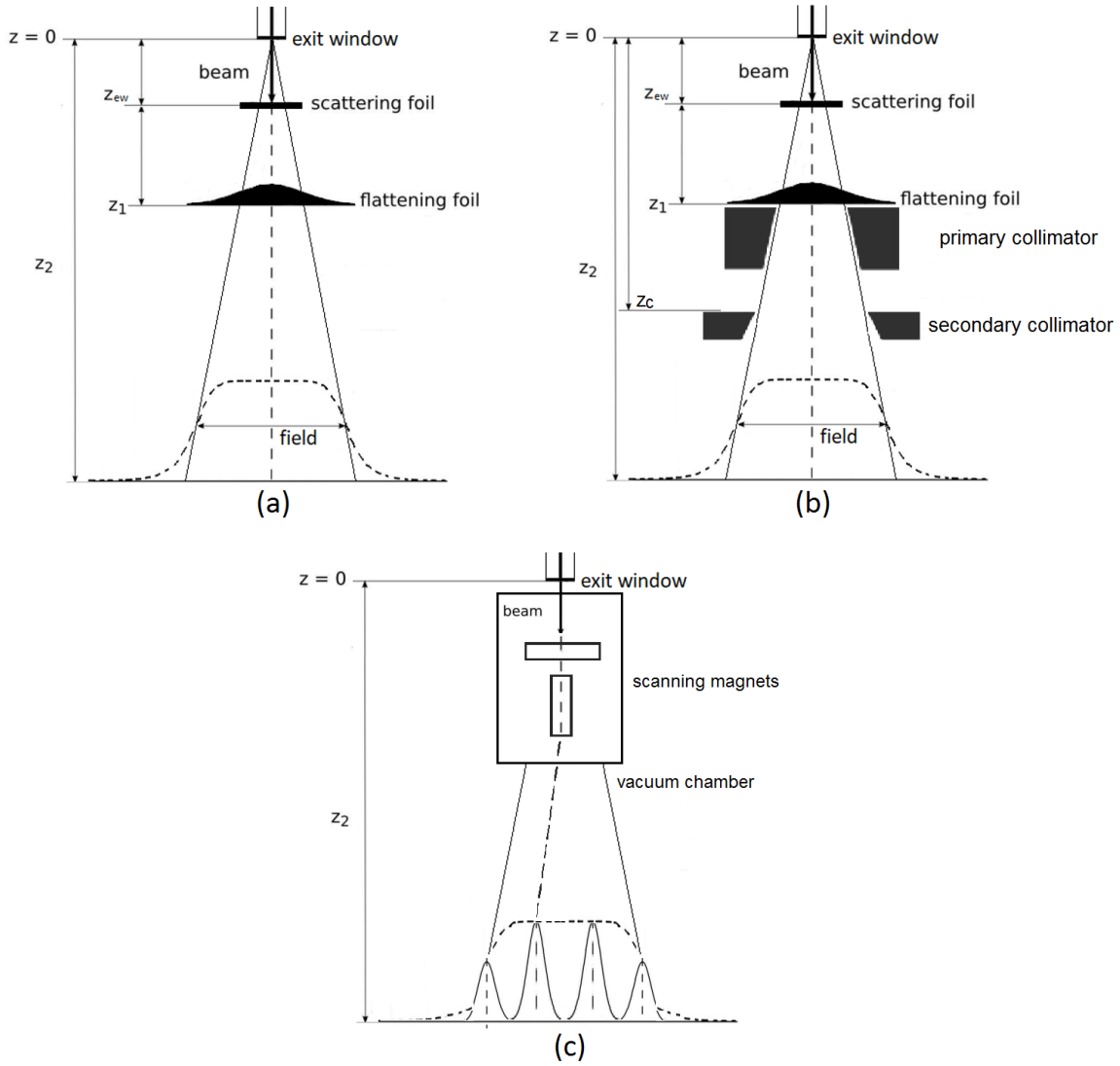

Figure 3.1: Diagram with geometrical parameters and their distances from the vacuum exit window for (a) the dual scattering foil system (b) the dual scattering foil system with collimators and (c) the pencil beam scanning system. z_{ew} is the distance between the accelerator exit window and the first scatterer, z_1 is the distance between the first and second scatterer, z_2 is the distance between the proximal surface of the water phantom and the electron source.

has been applied in several subsequent studies about dual scattering systems in the clinical range of electron energies [135,137]. However, this formalism has never been applied to higher energies, which is the purpose of this study. The geometry of the system considered for a possible application to VHEEs is shown in figure 3.2, and consists of an accelerator exit window, a first scatterer and a second scat-

terer of variable thickness whose profile is described by a Gaussian distribution function. The position of the exit window is defined as z_0 and corresponds to the starting point of the analytical modelling, where a point-like beam is placed. The first scattering is placed at a distance z_{ew} from the exit window, while the second scatterer position is z_1. Finally, the distance between the exit window and the target volume, corresponding to the phantom surface, is z_2. At the position of the second scatterer, z_1, the beam fluence is described by $\Phi_1^p(\vec{\rho}, z_1)$, where $\vec{\rho}$ is the radial coordinate for this plane. At the phantom surface, z_2, the beam planar fluence is instead described by $\Phi(\vec{r}, z_2)$, where r is the radial coordinate on the phantom plane. The scattering thicknesses are given by t_{prim} for the first scattering foil and by t_{sec} for the second, whose thickness varies with $|\vec{\rho}|$.

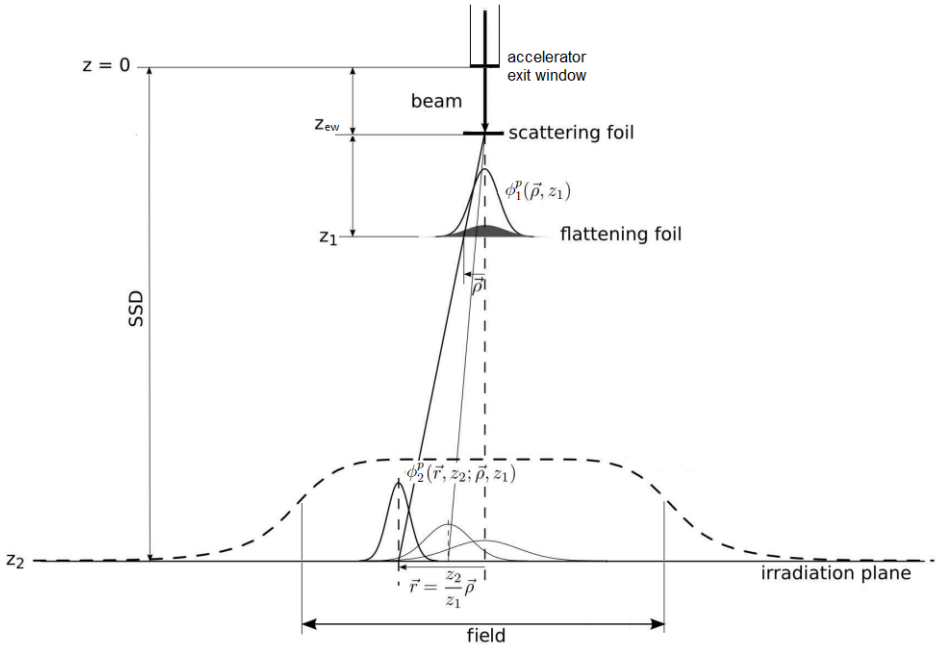

Figure 3.2: Geometry of the double scattering system and typical fluence profiles for scattered beams. On the z-axis, the accelerator exit window is at z=0; the first scatterer is at $z = z_{ew}$. At the second scatterer location, $z = z_1$, the beam fluence is described by a Gaussian distribution. However, the convolution of this Gaussian beam from the first scatterer with the contribution from the scattering in the second Gaussian element results in a beam homogeneous profile at the phantom surface, $z = z_2$.

3.3.2 First Scatterer Design

The first step in DS optimisation is to define the first scatterer parameters. Its position, thickness and material are therefore optimised. In most DS systems, a high Z material is chosen for the first scatterer, so several different materials (tantalum, tungsten, and gold) were tested. Using equation 2.5, the planar fluence at the plane z_1 of a point beam incident on a scattering foil can be described using a Gaussian function whose radial scattering is given by equation 2.4 (with z=z_1). As proposed in Kainz's work [135], and considering that $z_1 \gg t_{prim}$ and the linear scattering power of the material is constant, equation 2.4 can be used to describe the radial width, σ_0, at the plane z_1 by:

$$r^2 = 2\,\sigma_0^2 = T_{prim}\,t_{prim}\,z_1^2 + 1/3\,T_{air}\,z_1^3 \tag{3.1}$$

where T_{prim} and t_{prim} are the linear scattering power and the thickness of the first scatterer and T_{air} is the air scattering power calculated using the Bragg-Kleeman rule as described in equation 2.26. The scattering power is calculated using the Kainz's formulation according to equations 2.18,2.22,2.23. Unlike Kainz's work, our DS system is also made of an exit window; therefore, considering $z_1 \gg t_{ew}$, equation 3.1 becomes:

$$r^2 = 2\,\sigma_0^2 = T_{ew}\,t_{ew}(z_1 + z_{ew})^2 + T_{prim}\,t_{prim}\,z_1^2 + 1/3\,T_{air}\,z_1^3 \tag{3.2}$$

where T_{ew} and t_{ew} are the linear scattering power and the thickness of the exit window. After the exit window, the electron beam is diverging, so the general formulation for the radial spread presented in equation 2.19 should be used. As the exit window is very thin (0.0125 cm), its contribution to the angular spread is neglected, and the only contribution left from the exit window in equation 3.2 depends on $(z_1 + z_{ew})^2$. The distance between the exit window and the first scatterer should be minimised to maintain the system's main scattering source as far as possible from the irradiation point, which is the reason why $z_{ew} = 2$ is used in the following. The radial spread of the Gaussian beam after a single scatterer in the irradiation plane z_2 is finally given by equation 3.2. To calculate the different terms, the mean beam energy after the first scatterer is obtained using equation 2.29 (as the energy loss in the system is lower than half of the initial beam energy, the equation can indeed be applied).

3.3.3 Second Scatterer Design

Once the first scatterer geometry has been defined, the second scatterer can be modelled and optimised independently as follows. A homogeneous lateral fluence at the phantom's location is computed taking into account a Gaussian profile

shape for the second scatterer, which can be analytically expressed depending on the radial coordinate $h(\rho)$ as follows:

$$h(\rho) = H\ exp\left(\frac{-\rho^2}{2R^2}\right) \tag{3.3}$$

where h is the thickness of the second scatterer at a radial distance ρ from the central axis, H is the maximum thickness and R is the maximum width of the radial distribution. A flat beam profile at the plane z_2 can be produced using such a Gaussian-shaped scatterer, adapted to the Gaussian-shaped fluence profile of the beam (see figure 3.2). The electrons on the edges of the beam indeed scatter on a thinner thickness than at the scatterer centre, contributing to a Gaussian distribution at the z_2 plane location with a smaller radial spread and a higher maximum dose profile at $\vec{r} = \frac{z_2}{z_1}\vec{\rho}$. The final profile being the sum of the different Gaussian profiles at the different thicknesses and positions of the scatterer, each Gaussian contribution is described with $\Phi_2(r, z_1, \rho, z_2)$ as in equation 3.4:

$$\Phi_2(r, z_1, \rho, z_2) = \frac{1}{2\pi\sigma_2^2} exp\left(-\frac{(\bar{r} - \frac{z_2}{z_1}\bar{\rho})^2}{2\sigma_2^2}\right) \tag{3.4}$$

where $2\sigma_2^2$ corresponds to the square of the radial width calculated using equation 2.2, whose scattering power is evaluated for the specific thickness $h(\rho)$ and for the energy corresponding to the mean beam energy to half the thickness of the scattering in the foil, i.e. for a thickness of $h(\rho)/2$. If $z_2 \gg t_{sec}$, the radial spread can be calculated as :

$$2\sigma_1^2 = 2\sigma_0^2 + T_{sec,i}\ t_{sec,i}\ (z_2 - z_1)^2 + 1/3\ T_{air}\ (z_2 - z_1)^3 \tag{3.5}$$

where $2\sigma_0^2$ is described by equation 3.2. The final electron planar beam fluence Φ, resulting on a plane of interest at z = z_2, from the combined effects of scattering in both foils, can then be expressed as a convolution of the two distributions:

$$\Phi(r, z_2) = \int_0^{2\pi} \int_0^{R_{max}} \Phi_1(\rho, z_1)\Phi_2(r, z_1, \rho, z_2)\rho d\rho d\Phi \tag{3.6}$$

where $\Phi_1(\rho, z_1)$ is given by equation 2.5, and denotes electron planar fluence on the second foil in plane z_1 due to scattering in the first foil, while $\Phi_2(r, z_1, \rho, z_2)$ is given by equation 3.4 and corresponds to the planar fluence at point r in the plane of interest at z_2, calculated at distance ρ at the plane z_1. In practice, the numerical integration of equation 3.6 is performed for a limited number of points and can be rewritten as:

$$\Phi(r, z_2) = \sum_{i=1}^{N_p} \sum_{j=1}^{N_\phi} G_i\ G'_{i,j}\ \rho_i\ \Delta\rho\ \Delta\Phi \tag{3.7}$$

where $\Delta\rho$ and $\Delta\Phi$ are the lengths of the steps in the radial and angular cylindrical coordinates, respectively, while G_i and $G'_(i,j)$ are defined as follows:

$$G_i = \frac{1}{2\pi\sigma_0^2} exp\left(-\frac{\rho_i^2}{2\sigma_0^2}\right) \tag{3.8}$$

and

$$G'_{i,j}(r) = \frac{1}{2\pi\sigma_{1,i}^2} exp\left(-\frac{(\frac{z_2}{z_1}\rho_i^2)^2 + r^2 + 2r\rho_i\frac{z_2}{z_1}cos(\Phi_j)}{2\sigma_{1,i}^2}\right) \tag{3.9}$$

where $2\sigma_0^2$ and $2\sigma_{1,i}^2$ are the squares of the radial widths at the z_1 and z_2 planes, respectively, calculated with equation 2.2. The intervals of the numerical integration chosen in this work are $[0, \rho_{max}]$ with $\rho_{max} = 3\sigma_0$ cm and $[0, \Phi_{max}]$ with $\Phi_{max} = 2\pi$ rad.

3.3.4 Double scattering optimisation process

The free parameters (thickness, material, shape and position) of the layers comprising the scattering system must, therefore, be determined to obtain a homogeneous lateral dose profile of a given field size for various energies ranging from 100 to 200 MeV. As equation 3.5 strongly depends on the distance between the scatterers, $(z_2 - z_1)^3$, and even if the air scattering power, T_{air}, is small and of the order of 10^{-4} $MeVcm^2g^{-1}$, its contribution becomes relevant when the quantity $(z_2 - z_1)^3$ is large. Therefore, the distance between the scattering foils is set to 10 cm, as in the case of low energy DS systems [135, 137].
We, therefore, designed an optimisation objective function to determine the parameters of the system which minimise the difference between a theoretical profile F and the computed fluence distribution profile Φ:

$$\begin{aligned} F(X > 0) &= 1 + \frac{1}{2}\left(erf\left(\frac{X - \frac{X_{lim}}{2}}{\sigma}\right) + erf\left(\frac{X + \frac{X_{lim}}{2}}{\sigma}\right)\right) \\ F(X \leq 0) &= 1 - \frac{1}{2}\left(erf\left(\frac{X - \frac{X_{lim}}{2}}{\sigma}\right) + erf\left(\frac{X + \frac{X_{lim}}{2}}{\sigma}\right)\right) \end{aligned} \tag{3.10}$$

where X_{lim} is the desired field size and X is the axis coordinate. This function also minimises the flatness of the field (i.e., the flat region around the central axis where the fluence values are above 95% of the maximum fluence, defined in equation 3.5):

$$Flatness = 100\,\frac{D_{max} - D_{min}}{D_{max} + D_{min}} \tag{3.11}$$

The optimisation algorithm was developed in Matlab® to automatically estimate the optimal thicknesses of the two foils (thinnest thickness and minimum H value producing flat lateral dose profiles over the irradiation field while minimising the total energy loss in the system) and adjust the Gaussian shape of the flattening foil. Calculation times to evaluate the parameters are of the order of a few minutes.

3.4 Pencil beam scanning model and temporal parameters

To compare the previous double scattering system with an active PBS technique in the VHEE energy range, dose assessment was carried out using both MC simulations and the analytical calculation algorithm for PBS applications described in Chapter 2, with a similar configuration as described in section 2.3 and shown in figure 2.1(a). Analytical models and parameter optimisation were performed using the Matlab® computing environment. In addition, the scripts were enhanced to determine the number and locations (x,y) of the spots needed to cover a specific field size. The dose and dose rates were estimated as a summation of the pencil beam contributions that cover the lateral field size dimensions. In particular, for the dose calculation, equation 2.11 described in Chapter 2 was used. Also, as in PBS mode a two-dimensional pencil beam pattern is sequentially delivered to irradiate the target volume uniformly, it is possible to estimate the total irradiation duration using a formalism describing the different steps constituting the scanning, the irradiation and considering system hardware properties and possible dead times. The calculations used to estimate irradiation times and dose rates are therefore also presented in the following paragraphs.

3.4.1 Calculation of pencil beam scanning irradiation times

The total time to deliver the dose for each PBS plan was evaluated following the formalism described in Dowdell et al. [162]. As the beam in a linear electron accelerator is pulsed, the pulse repetition frequency (usually of the order of a few hundred Hz) was also included in the calculation to take into account the pauses between each pulse. The total irradiation time to deliver the dose can be defined as follows:

$$t_{total} = t_{dose} + t_{move} + t_{equipment} \tag{3.12}$$

where $t_{equipment}$ is the equipment time related to hardware properties, t_{move} is the

time to move the beam from one position to another, and t_{dose} is the time to deliver the dose for each beam. During delivery, the beam is stationary to ensure that the prescribed dose is delivered to the required position. The time required to deliver a given dose can be expressed as:

$$t_{dose} = \frac{Nq}{I} \tag{3.13}$$

where N is the absolute number of particles, I is the beam current, and q is the particle charge. $t_{equipment}$ corresponds to the time to turn on and off the source and the time for the dosimetry system to read out.

$$t_{equipment} = t_{on} + t_{off} + t_{readout} \tag{3.14}$$

The time to move between adjacent spots, t_{move}, can be defined as the time required for the scanning magnets to stabilise, $t_{settling}$, plus the time to move from one spot to the following position, t_{scan}, as:

$$t_{move} = t_{settling} + t_{scan} \tag{3.15}$$

with

$$t_{scan} = \frac{d}{\frac{dx}{dt}} = \frac{d}{U_{x,y}\ SAD_{x,y}\ \frac{Z_{eff}}{L\alpha\beta\rho}} \tag{3.16}$$

where $\frac{dx}{dt}$ is the scanning speed of the magnet, $SAD_{x,y}$, the source-to-axis distance, is the distance between the scanning magnets and the treatment isocenter, $U_{x,y}$ is the maximum voltage of the scanning magnet, Z_{eff} is the effective length of the magnetic field and L is the inductance of the scanning magnets; $\beta\rho$ is the magnetic rigidity and α is the field to current parameter [A/T], which depends on the intensity gradient dI to be applied to move a spot from one position to another. It is generally defined by a function fitted to measurements on the magnets and is typically of the order of a few ms. The values of the parameters used for the time computation are given in table 3.1, where the magnet parameters are the same as for the CPO proton beamline [163]. Calculations were adapted for $SAD_{x,y} \sim 1$m, which would be suitable in the case of a compact beamline.

3.4.2 Dose rate models in PBS mode

The dose rate is an essential parameter related to the characterisation of the FLASH effect, as described in section 1.5. However, while accurate estimation of 3D dose rates is relatively straightforward with scattered beams where the entire

Magnets and equipment parameters	X	Y
U_{xy} [V]	350	350
L_{xy} [H]	0.0477	0.00472
α [A/T]	1315.8	2519.6
$\beta\rho$ [T.m]	0.34-0.67	0.34-0.67
Z_{eff} [m]	0.3	0.3
SAD_{xy} [mm]	1344	951

Table 3.1: Parameter values used for the PBS delivery system.

treatment field is irradiated simultaneously, it is much less evident with scanned beams as the total dose received by a voxel is the sum of the contributions of several pencil beams, which are irradiated at different times. It, therefore, seems more appropriate to define the dose rate as a property associated with a single spot location rather than as a general property of the entire irradiated field. However, no experiment has yet answered the question of whether the benefits of FLASH could be equivalent for various delivery modes and dose rate definitions [147]. Multiple formalisms have been proposed to define the dose rate in PBS, which can be divided into three groups:

- the dose averaged dose rate (DADR) and its variants, which consider the instantaneous dose rate without taking into account the scanning time;
- the dose rate definitions that include a dose threshold (i.e., average dose rate ADR, Dose Threshold Dose Rate (DTDR));
- the dose rate definitions that take into account the FLASH contribution in each voxel (the dose in a voxel is delivered under various conditions of dose and dose rate, not all in FLASH mode).

A more detailed description of these definitions is given below.

Dose Averaged Dose Rate

A first definition of the DADR proposed by Van de Water et al. [146] consists of averaging the instantaneous dose rate over all the spots while weighting the dose contribution of each spot with respect to its (x, y) location:

$$DADR(x,y) = \sum_{j=1}^{n} \frac{(d_{(x,y),j} w_j)(d_{(x,y),j} Bl_j)}{\sum_{j=1}^{n} d_{(x,y),j} w_j} \tag{3.17}$$

where DADR(x,y) is in [Gy/s], (x,y) is the voxel coordinates, j is the spot number, n is the total number of spots, w is the spot weight [electrons], d is the dose-influence matrix [Gy/electrons], and Bl is the beam intensity [electrons/s]. Equation 3.17, by definition, does not consider the scanning time between the spots. However, this dead time is much larger than t_{dose}, the time needed to deliver the required dose to the spots, so it should be considered somehow in the dose rate definition in PBS mode. The DADR definition can, therefore, be considered as an upper bound in the dose rate estimation [164].

A study by Zhang et al. [147] proposed to introduce a correction to equation 3.17 to account for the scanning time. The DADR, for a plan where all the spots have the same weight, becomes (corresponding to setting $w_i = 1$ in equation 3.17):

$$DADR(x,y) = \frac{D_{tot}(x,y)\ Bl\ T_1}{T_1 + T_2} \tag{3.18}$$

where T_1 is the t_{dose} for the considered spot and T_2 is the scanning time to move the beam to the next spot. However, evaluating the irradiation time as the time to deliver the dose for the specific (x,y) location plus one displacement to the following spot probably continues to overestimate the dose rate. On the other hand, considering the total irradiation time (over all the spots) leads to an underestimation of the dose rate. In fact, most of the dose to a voxel (x, y) is due to the nearby spots, while the most distant spots contribute very little to its dose. Taking this into account, an alternative definition of the dose rate has been proposed, which consists of setting a dose threshold in the calculation of the irradiation time.

Dose threshold in the dose rate definition

A dose threshold for the dose rate calculation was first introduced in a study by Van Marlen et al. [145]. This threshold, d, was chosen as a constant value of d = 0.01 Gy, corresponding to 0.5 % of the prescribed dose. The consequence for the dose rate calculation is therefore the dependence on the total irradiation time T(x, y), defined as:

$$T(x,y) = \sum_{i:D_i(x,y)\geq d} t_i \tag{3.19}$$

with t_i is the irradiation time for spot i. Using this definition, only the irradiation time of the spots that contribute more than the dose threshold to a specific location is considered for computing the total irradiation time for that location. Thus, the total irradiation time for a voxel could be much smaller than the field total irradiation time. However, this definition (equation 3.19) still does not take into account the scanning time and beam pauses. A study by Folkerts et al. [148]

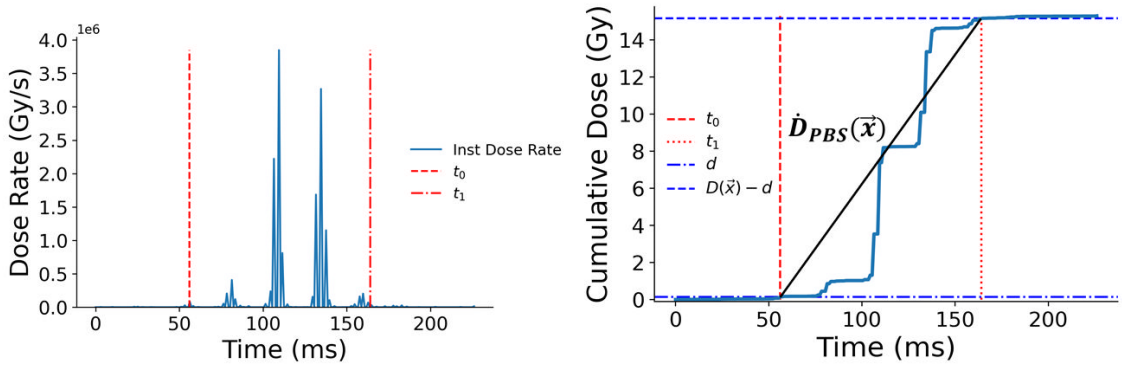

Figure 3.3: Example of dose rate and dose accumulation according to time, and graphical example of the time window (T(x,y) in equation 3.21) for a point located at the centre of a PTV according to the definition proposed by [148].

introduced the scanning time into the dose rate definition while maintaining the dose threshold condition. The Average Dose Rate (ADR) is therefore defined as:

$$ADR(x,y) = \frac{D_{tot}(x,y) - 2d}{T(x,y)} \tag{3.20}$$

where d is the dose threshold corresponding to two particular moments of the irradiation t_0 and t_1, respectively, the time the dose threshold d and the dose $D_{tot} - d$ are reached, as in figure 3.3. T(x,y) is the interval between these two times and includes the scanning time:

$$T(x,y) = t_1 - t_0, \tag{3.21}$$

Folkerts' study also considers the effect on the dose rate of varying the dose threshold and shows that as the threshold is increased, the dose rate tends to approach that of a single point (the instantaneous dose rate). For a prescribed dose of 10 Gy, a threshold set arbitrarily to 0.1 Gy is typically chosen, corresponding to 1% of the dose. When the scanning time is also taken into account, the ADR definition of dose rate gives the lowest dose rate compared to equations 3.17-3.18.

Finally, Kang et al. [165] proposed an intermediate definition between the previous ones, the DTDR. It is defined as the minimum instantaneous dose rate given by all the spots that deposit in the voxel a dose higher than the dose threshold d:

$$DTDR(x,y) = min(\dot{D}(x,y)) \quad if D(x,y) > d \tag{3.22}$$

FLASH windows

The previous equations (equations 3.19-3.22) assign a dose rate value to each voxel using different definitions of the parameters influencing it (e.g. the irradiation time, dose threshold, or scanning time). However, an additional consideration can be made. While in scattering mode, the dose is delivered or not under FLASH constraints, this might not be the case in PBS for every voxel, as the FLASH constraints can be met for part of the total dose delivered. Furthermore, these moments where the FLASH constraints are met may not be consecutive, resulting in multiple FLASH windows and alternate with dose contributions delivered under CONV conditions. The biological consequences of irradiating with a complex combination of FLASH and non-FLASH contributions and the subsequent influence on the final FLASH effect are still unknown, even if we assume that the total irradiation time variable must be significant. The work of Van Marlen et al. [145] proposed that a quantification of the dose rate distribution may be essential. Thus a FLASH contribution for a given voxel definition, F(x,y), was proposed:

$$F(x,y) \ = \sum_{i:dr_i(x,y)\geq 40} \frac{D_i(x,y)}{D_{tot}(x,y)}.100\% \tag{3.23}$$

where $dr_i(x,y)$ is the dose rate in Gy/s for the spot i at location (x,y); $D_i(x,y)$ is the dose delivered by the spot i and $D_{tot}(x,y)$ is the total dose to the voxel at position (x,y). Equation 3.23 considers 40 Gy/s as the dose rate threshold for the FLASH effect to occur, as initially reported in the study by Favaudon et al. [67]. A subsequent study by Krieger et al. [166] also investigated the FLASH window definition. In this study, the FLASH effect is assumed to occur during all the time windows where the following constraints on the threshold dose (D_t) and dose rate (DR_t) are met:

$$d(t_1) - d(t_0) \geq D_t \tag{3.24}$$

and

$$\frac{d(t_1) - d(t_0)}{t_1 - t_0} \geq DR_t \tag{3.25}$$

These conditions may be met in several time windows during the irradiation. The authors also propose a "persistence time" defined as the time interval after a window of about 200-500 ms after which the FLASH effect is expected to persist, regardless of the dose or dose rate during that interval. This window approach was also used in a subsequent study by Schwarz et al. [164], but without considering the persistence time. The window length was determined as the ratio of the threshold dose to the threshold dose rate (i.e., a dose rate threshold of 40 Gy/s and a dose threshold of 4 Gy results in a time window of 100 ms). Anyway, the sparing effect when re-irradiating the same voxels (after hundreds of ms or seconds) at a

FLASH dose rate remains to be investigated.

3.5 Monte Carlo simulation geometry

In order to evaluate the relationships between the absolute number of particles, dose rate and beam source currents and to compare analytical calculations with simulations, the various treatment head geometries were modelled using the TOPAS (Tool for Particle Simulation v3.8 with Geant4.10.07p03) MC simulation code. Dose distributions were simulated in water, with a number of histories adapted to achieve a relative statistical uncertainty of less than 3% (type A, calculated as the average statistical uncertainty of voxels with a dose higher than 50% of the maximum dose). For the DS beamline simulation, the exit window and first scatterer, made of Nickel and Gold, respectively, were modelled as simple foils of different thicknesses separated by air. The second scatterer, a Gaussian-shaped disk composed of Aluminium, was accurately simulated by combining stacks of cones with different radii. The incident electron beam was modelled with zero angular spread, no radial spread, and monoenergetic incident energy to match simulation and analytical calculations, as in Carver et al. [137]. As scattered beams are generally never used without an inner collimation system, a simple collimation system consisting of two tungsten elements was included in the simulations. The geometry of such a system is shown in figure 3.1b: a first circular collimator is placed at the exit of the second scatterer, as well as a second circular collimator further in the treatment head at a distance $z_c = 80$ cm from the electron source, both modelled by 8-cm thick solid tungsten rings. A realistic source was used for the PBS mode, as described in section 2.3.

3.6 Experimental validations

A laser-plasma accelerator installed at the Laboratoire d'Optique Appliquée (LOA), in Palaiseau of the Ecole Polytechnique (in the Salle Jaune) was used to generate VHEE electrons with a polyenergetic spectrum between 20 and 300 MeV. Tests were carried out on the design method for the second scatterer, in parallel with an experiment carried out by Alessandro Flacco of LOA who kindly allowed us to characterise the beam. The interaction of a focused laser pulse of 30 fs for 2.5 J with a gaseous target (5% N2/He) generates electrons (by the effect of an electric field on a cavity created by the laser pulse). The laser propagation in this medium generates a travelling electron field that accelerates the electrons. The resulting electron beam, which is about 1 cm wide at half-height is transported through the air (over a distance of about 40 cm) to various characterisations. An average

dose rate of between 10^{-3} - 0.5 Gy/s (frequency used 1 to 2 Hz) is obtained for an instantaneous dose rate of between 1x10^{11} and 5x10^{11} Gy/s. A schematic representation of the experimental setup is shown in figure 3.4, whose preliminary beam alignment was obtained with a scintillator screen coupled to a Charge-Coupled Device (CCD) camera.

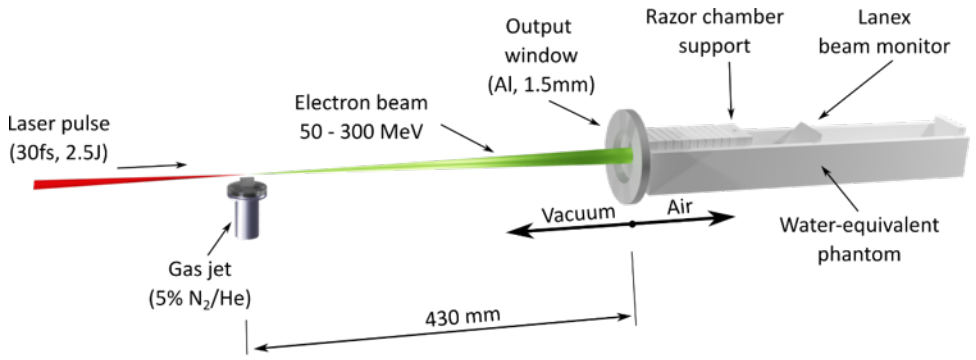

Figure 3.4: Schematic of the set-up used for measurements in Salle Jaune (LOA) with fs laser-plasma accelerated electrons.

This experimental work was carried out in two stages: the first enabled the necessary experimental characterisation of the beam to be obtained so that the MC simulation of the beamline could be developed and the geometry of a scatterer optimised. A second experiment was used to test this second scatterer on the beam produced.

3.6.1 Dosimetry

The VHEE beam is generated over a few tens of centimetres, after which several detectors were placed in the air at the exit of the system, in a volume of about 30 cm in length. Radiochromic films (EBT-XD) were used to measure the lateral beam profiles in air or in a water equivalent phantom (RW3 slabs), due to their dose rate independence and high spatial resolution. The films, previously calibrated with conventional proton beams using a 0.125 Semiflex cylindrical ionization chamber as described in [93], were mainly used to measure the lateral beam profile in air. As the relative stopping power of high-energy protons and electrons is relatively close (outside the Bragg peak region), we considered that any correction linked to differences in TEL or energy spectrum was not required. This point would merit a much more detailed study but was not possible given the limited beam time available for the experiment.

In order to characterise the beam (size and divergence), the films were placed in the air at different distances from the exit of the accelerator system, allowing the emittance of the beam source to be estimated. EBT-XD films were also placed horizontally between RW3 slabs clamped together to allow measurement of the depth dose profile and characterisation of the beam spectrum.

The dose response at ultra-high dose rates of different detectors was also compared with each other. A NanoRazor chamber (3 mm^3 active volume), a Medscint HyperScint RP 100 scintillator (1x1x1 mm^3 active volume described in more detail in section 1.6) and alanine pellets (5 mm diameter) were used. The scintillator calibration (removal of Cerenkov etc) was performed according to the manufacturer's instructions using a conventional radiotherapy linac, and cross-calibrated against a 226.9 MeV proton beam in terms of absorbed dose. This detector was previously tested and validated at Institut Curie for its use in FLASH conditions, up to 10^6 Gy/s, with a 7 MeV electron beam. The alanine pellets were calibrated and read at the Institute for Radiation Protection and Nuclear Safety (IRSN) in France. A cross-calibration factor was derived for the alanine pellets by taking the mean ratio between the absorbed dose in water measured with the Advanced Markus chamber and the alanine pellets calibrated with MV X-rays for different dose values. The delivered dose, proportional to the concentration of radicals generated, can be accurately assessed with alanine in ultra high dose rate beams as shown in some recent studies (described in section 1.6). In order to compare the response of the different detectors, they were irradiated simultaneously on the beamline. The Razor ionisation chamber was placed vertically between RW3 plates, followed by an EBT-XD film, an alanine pellet and finally the scintillator probe placed horizontally on the central beam axis, as shown in figure 3.5.

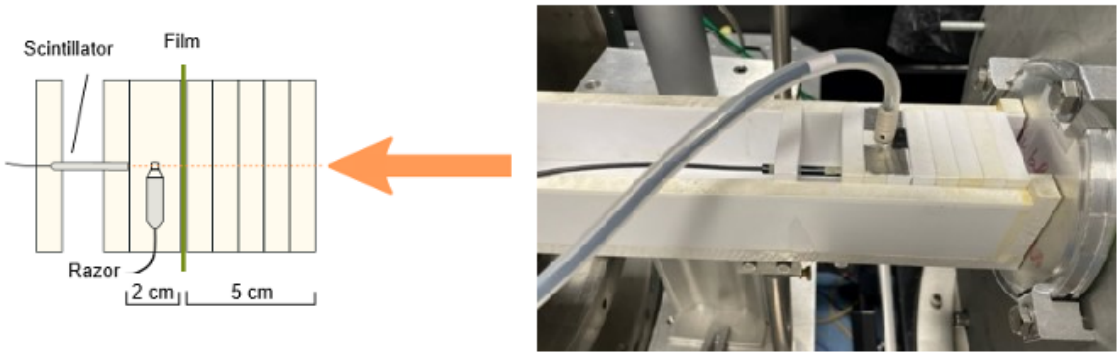

Figure 3.5: Experimental set-up: a Razor ionisation chamber is placed vertically between RW3 slabs, followed by a film, alanine and a scintillator probe placed horizontally on the central beam axis.

3.6.2 Simulations and beam commissioning

The Monte Carlo simulation code TOPAS was used to model the electron beam. The particle source was modelled considering its poly-energetic spectrum and several parameters (e.g. beam divergence, size and position) were optimised to fit the MC model to the experimental data. This was done using a non-linear least squares method to define the best fitting source description file. After the beam modelling stage, the analytical model described in the previous sections was used to construct an efficient double scattering system adapted to the beam emittance and energy. The double scattering foil was designed for a polyenergetic electron beam with a central energy approximation (∼150 MeV) and for an electron energy spectrum (50-298 MeV) as measured during the first experiment in November 2022, also shown in figure 3.6. Actually, for this optimisation, the exit window of the accelerator system (Al ∼1.5 mm) was considered as a first scattering foil, so that only the second scatterer was optimised to obtain a ∼2 cm homogeneous beam profile. The source is defined using a bi-Gaussian function, with Gaussian distributions for both the position and momentum. The multiple scattering theory allowed the geometry of the system to be designed, optimised and tested using MC simulation.

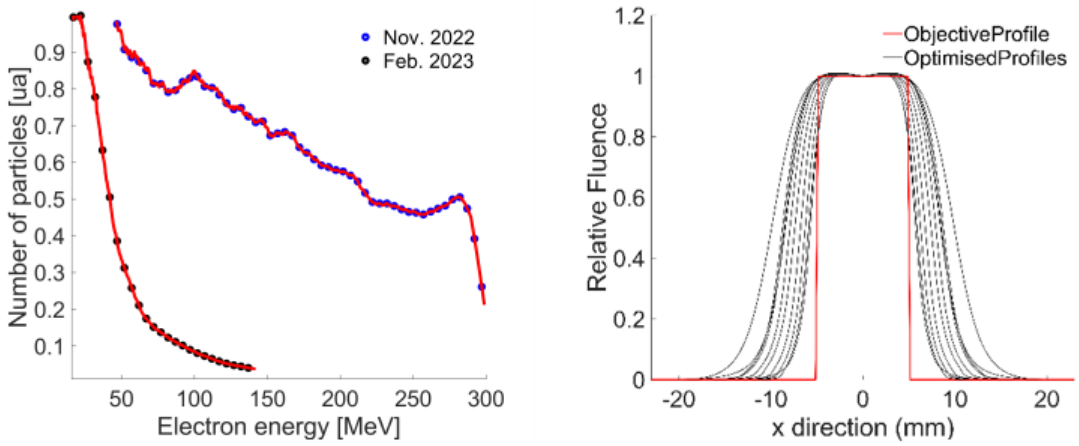

Figure 3.6: On the left: Energy spectrum of the VHEE beam during both experiments (Nov. 2022: 50-298 MeV, and Feb. 2023: 16-140 MeV). On the right: Double scattering optimisation process.

3.7 Results

The comparison of two theoretical conformation systems (double scattering and pencil beam scanning) is presented in this section, together with the results of the experimental tests carried out during our work.

3.7.1 Double scattering system for VHEEs

First scatterer optimisation

The first step in optimizing a double scattering system is to set the thickness of the first scatterer. The simulated variation in beam width at different distances from the source, from 1 to 2 metres, is shown in figure 3.7 for three different materials (tungsten, tantalum and gold) and for 100 and 200 MeV beam energies.

In particular, we can see that the smaller the SAD and the lower the beam energy, the smaller the scatterer thickness. The minimum scatterer thickness required to achieve a given field size at the isocenter can be estimated according to the selected beamline distance.

Second scatterer optimisation

The second optimisation step consists of determining the geometry of the second scatterer, knowing the beam fluence in its plane. Therefore, the analytical primary electron fluence profile is optimised and estimated using equation 3.6 and compared to Monte Carlo simulations. As can be noted in figure 3.8, the analytical model closely reproduces the results of the MC simulations. The average maximum difference calculated within the flat region of the distribution over both simulated energies is 1.9% for the 5x5 cm^2 and 1.8% for the 10x10 cm^2 treatment field size. The source parameters (current of primary electrons at the accelerator exit, necessary charge) are given in table 3.2, indicating the orders of magnitude required to deliver VHEE irradiations and those required to achieve FLASH dose rate (in the order of Gy/pulse).

For a predefined field size (e.g., 10x10 cm^2), a compromise has therefore been found between scatterer thickness and the SAD. In particular, the required thickness of the scatterers increases as the electron energy increases, resulting in a significant loss of total energy in the scattering system (from 10 to 40 MeV, depending on the initial beam energy). In order to limit the scatterer thickness and thus the energy loss for the 200 MeV electron beam, the SAD was increased from 1m, as in the 100 MeV case, to 1.5 m. Similarly, the intensity required to achieve ultra-high

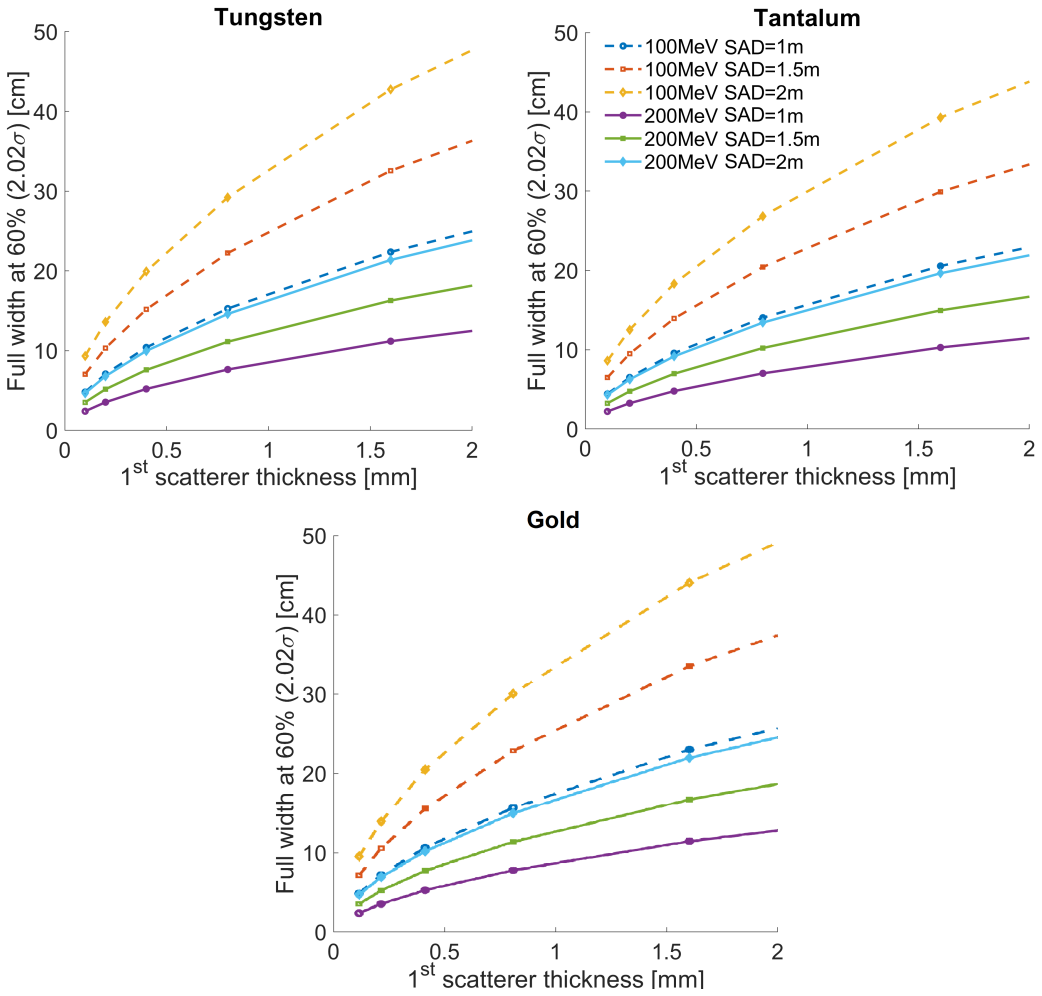

Figure 3.7: Computation (MC data) of the width (at 60%) of a Gaussian beam at isocenter as a function of the 1^{st} scatterer thickness and for two different energies (100 and 200 MeV) and three source-to-axis distance (1, 1.5 and 2 m)

dose rates increases sharply as beam energy increases, as the SAD is increased in order to achieve large field sizes while limiting the maximum scatterer thickness. This will probably limit the possibility of using passive scattering for beam sizes larger than a few tens of cm.

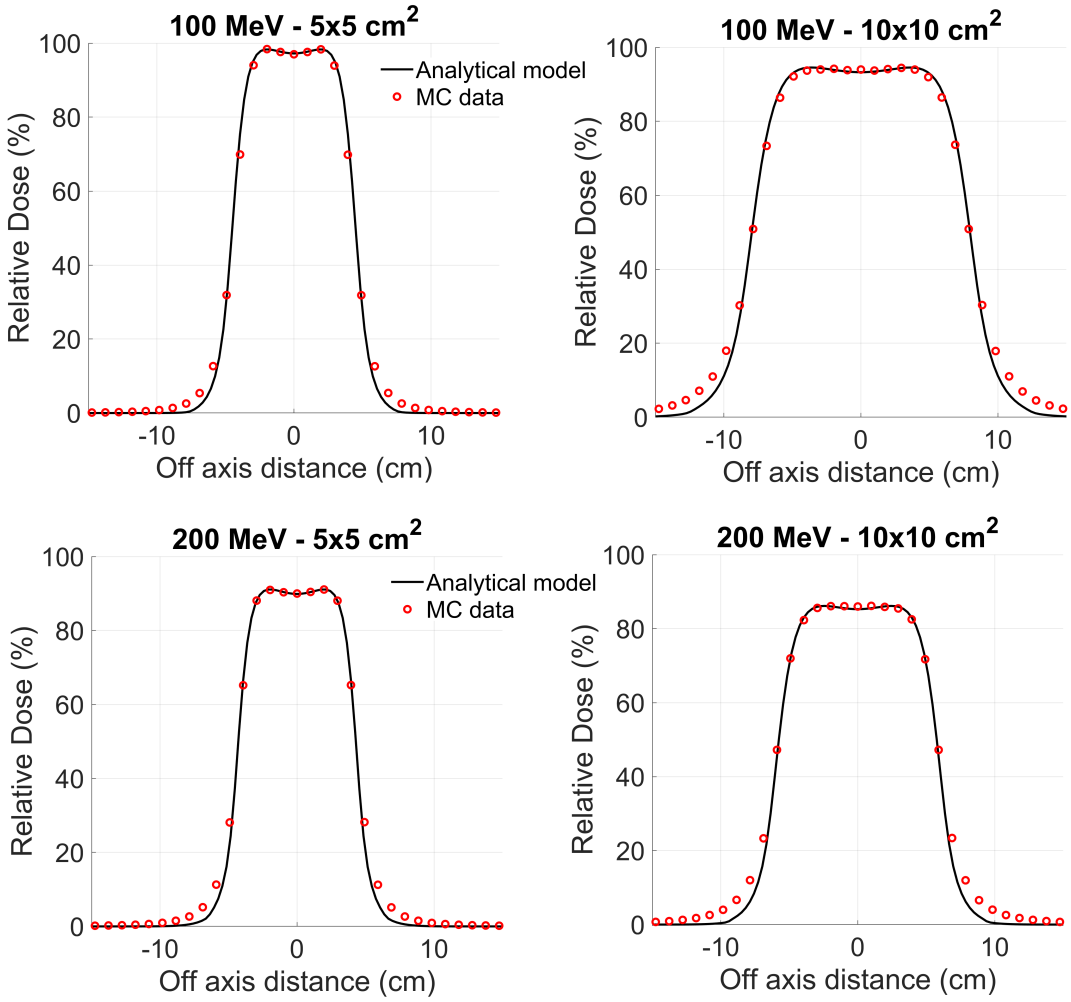

Figure 3.8: Comparison of the calculated VHEE lateral dose profile in air at isocenter with Monte Carlo simulations (SAD of 1 m). The dose distributions correspond to 5x5 cm^2 and 10x10 cm^2 treatment field size configurations for 100 and 200 MeV electron beams at the nozzle entrance.

Parameters		
Energy at the entrance [MeV]	100	200
Mean energy at isocenter [MeV]	90	160
1st scatterer material	Au	Au
2nd scatterer material	Al	Al
1st scatterer thickness [mm]	0.25	0. 50
2nd scatterer thickness [mm]	2.5	8.5
Source-isocenter distance [m]	1	1.5
Charge required [nC/Gy]	70	170
Intensity required [mA/Gy/μs]	70	170

Table 3.2: Summary of parameters providing a 10x10 cm^2 field size at isocenter with a DS delivery system.

3.7.2 Pencil beam scanning study for VHEEs

Temporal parameters considerations

For irradiation carried out with a realistic PBS system, the effect of the various parameters and their impact in terms of dose rate were characterised (i.e. charge and intensity needed to get a homogeneous dose over an area of a few tens of cm^2 with 100-200 MeV energy electron beams). An example of values for these parameters for a 100 MeV beam and for two different pencil beam sizes (5 and 10 mm) is listed in table 3.3. The magnet parameters used are the same as existing proton beam lines with similar design [163] and with SAD of $\sim$1.5 m. In particular, the beam size (i.e. the standard deviation of the Gaussian distribution defining the beam lateral dose profile) correlates with the total irradiation duration, which depends on the number of positions to be irradiated. The number of spots can be reduced by increasing the spot spacing, thus reducing the irradiation time. However, the distance between the spots cannot be increased without compromising the dose homogeneity or conformation accuracy. Therefore, in the rest of the study, the maximum spot spacing was set to 1.5 σ as a compromise between ensuring a homogeneous dose distribution and minimising the total number of spots, thus reducing the irradiation time. Furthermore, for frequencies up to 500 Hz, the dead time between pulses ($\sim$2 ms) is long enough to adjust the scanning magnets parameters and should therefore not extend the duration of treatment. Assuming the dose per spot can be delivered within a single pulse, the irradiation time will then only depend on the number of pencil beams to be irradiated, as the pulse duration is much shorter than the time between pulses.

Spot size (σ) at isocenter	5 mm		10 mm	
Spacing [mm]	1 σ	1.5 σ	1 σ	1.5 σ
tmove-X [ms]	<2	<2	<2	<2
tmove-Y [ms]	<0.1	<0.1	<0.1	<0.1
Pulse duration [μs]	1	1	1	1
Distance between spots [mm]	5	7.5	10	15
Number of spots	441	225	121	64
Charge required/spot [nC/Gy]	0.134	0.307	0.55	1.14
Intensity required [mA/Gy/μs]	0.134	0.307	0.55	1.14

Table 3.3: Summary of parameters providing a 10x10 cm^2 field size at isocenter with a PBS delivery system using a 100 MeV VHEE beam

3.7.3 Experimental characterisation of a VHEE beam

Dosimetry and detectors comparison

The comparison between the different detectors used to characterise a laser plasma accelerated VHEE beam showed an agreement within 2% for the alanine and EBT-XD film measurements, as shown in table 3.4. However, the Razor ionisation chamber and scintillator gave poorer agreement (about 10% differences) compared to the film and alanine data, probably due to a problem with the alignment of the detectors along the central beam axis, for which the homogeneous dose area is very small. A further measurement was made to estimate the recombination coefficient of the Razor chamber, using film measurements and Jaffé plots (equation 1.20) at different chamber operating voltages, as shown in figure 3.9. This estimation gave a coefficient smaller than 3%, but again with very uncertain measurements due to the large variations in beam properties during the acquisitions.

	Number of pulses	Dose [Gy]	Deviations [%]
Film	50	90.3	na
Razor		82	-9
Scintillator		79	-12
Alanine		92	+2

Table 3.4: Dose measurement results from the comparison of different detectors: Razor ionisation chamber, EBT-XD films, Medscint HyperScint RP-100 scintillator and Alanine pellets.

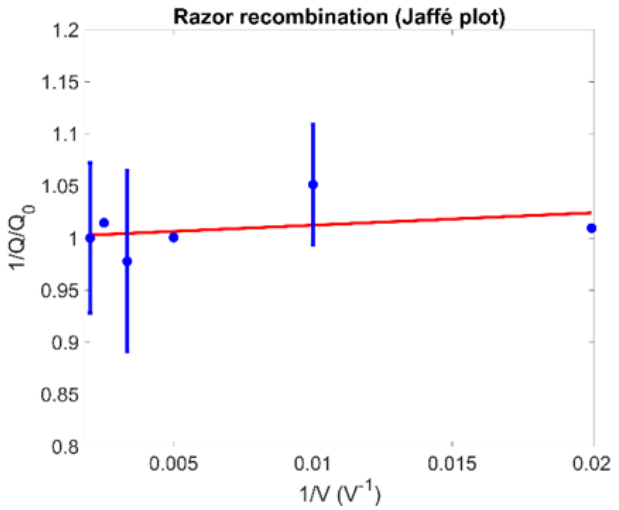

Figure 3.9: Inverse of the collected charge, 1/Q, normalized to the charge at 500 V (fluctuations corrected from film measurement) as a function of the inverse of the polarizing voltage, 1/V.

Monte Carlo modelling of the LOA VHEE beamline

Monte Carlo simulations were fitted to the measurements to obtain the modelling of the beam source parameters. Figure 3.10 shows the optimisation of the beam source process as well as a plot of the measured source dimensions in the air compared to the MC simulations. The final agreement between Monte Carlo simulations and measurements obtained was less than 2% for an initial beam size of 10 mm with a divergence of 25 mrad and a SAD of 35 cm. The agreement obtained was considered promising for this preliminary study. Indeed, the MC modelling of the beam was not further improved due to the poor reproducibility of the beam characteristics between fractions and for the given laser-plasma acceleration conditions. The beam parameters obtained using MC simulation were then used to optimise the following scatterer.

Using the previous results, the double scatterer optimisation method (presented in section 3.3.3) was used to design a compact scattering system adapted to the LOA beamline (based on measurements taken in November 2022): two aluminium scatterers (a flat one and a Gaussian-shaped profile), 5 cm apart, produced theoretically a homogeneous field of 25 mm diameter, as can be seen in figure 3.11a, where the comparison between the analytical calculation and the final MC simulation is shown. The total energy loss in the system is smaller than 20 MeV. The system was then tested in a second experiment, but it did not work, mainly because of beam instability. However, the size of the beam had also changed together with its spectrum. In fact, the energy spectrum of the beam (as shown in figure 3.6) had changed dramatically between the two measurements. The effect of

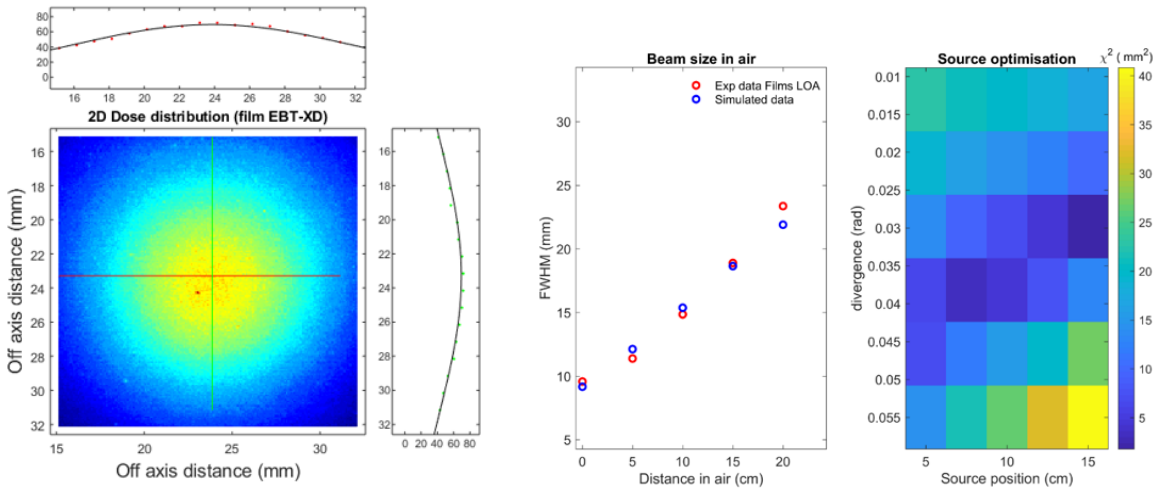

Figure 3.10: On the left: comparison between measured and simulated beam profile. On the right: comparison between measured and simulated beam size at several distances along the beam axis and mean error calculated for different pairs of parameters (SAD and divergence).

just changing the energy spectrum in the MC simulation (thus keeping the same scatterer) on the beam lateral profile is illustrated in figure 3.11b.

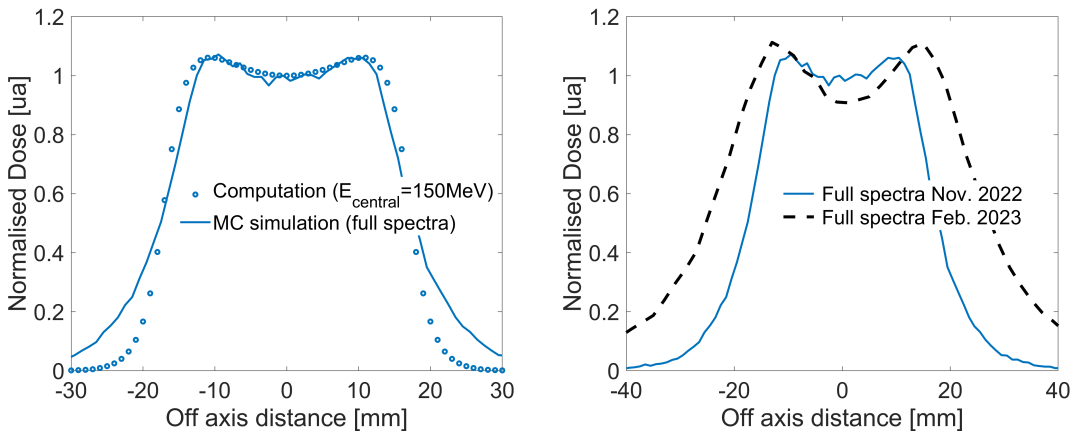

Figure 3.11: (a) Lateral dose profile obtained at the exit of the double scattering system (analytical model and MC simulations), adapted to the specific emittance of the laser plasma accelerated VHEE beam measured at LOA on November 2022 (b) MC simulation of the lateral profile obtained using the two different energy spectra of both experiments.

3.8 Discussion

In this chapter, two conformation techniques (PBS and DS) for VHEE beams were described and optimised. For both techniques, beam parameters were obtained to achieve VHEE irradiation over large treatment fields. A temporal description also allowed to obtain the intensity required to meet the dose rate requirements for FLASH irradiation. For PBS mode, the impact of several parameters (beam current, pulse duration and accelerator PRF, etc.) on the dose rate was characterised. For DS mode, the scattering system parameters (scattering foil thickness and materials, Gaussian profile of the second scatterer) were optimised using an existing formalism first developed by Green [131] and improved by Kainz et al. [135], allowing to design a scattered field greater than 10x10 cm^2 while maintaining a dose rate compatible with FLASH constraints as well as limiting the energy loss in the system. The model also included two sets of collimators to improve the lateral beam profile, comparable to that obtained with the PBS system. However, the collimation geometry could certainly be improved by considering elements such as jaws or other secondary collimators, ionisation chambers, etc., which may also influence the scattering of the primary beam and the secondary particle contamination. In fact, since the beam fluence after passing through the scatterers is characterised by a considerable penumbra, collimators or beam limiting devices are usually used to limit the penumbra, to confine the irradiation field to the target volume, and to limit the secondary particle contamination. Therefore, the design and optimisation of the collimation system depends on the type of application and may require a dedicated study. An example of a system consisting only of a primary collimator and then jaws is proposed, as the aim was instead to compare the overall ballistic performance of two VHEE systems optimised to operate under ultra-high dose rate conditions. For both the conformation systems, MC simulations were used to quantify the absolute number of particles required to apply these systems to the range of dose and dose rate requirement of FLASH irradiations. The process has allowed the determination of the VHEE required beam specifications, and in particular the beam intensity.

Tests were also carried out with an experimental laser plasma accelerated electron beam produced and optimised by the LOA, capable of delivering VHEEs between 50 and 300 MeV. However, the tests were inconclusive due to problems with the reproducibility of the beam parameters. In particular, the main difficulty with regard to the dosimetric characterisation of the beam was to obtain a beam that was stable, especially between pulses, and of sufficiently large dimensions with respect to the size of the detectors. Nevertheless, the MC model developed for this

beam as well as the model for creating a scattering system proved in principle that it is possible to apply the double scattering model to a laser-plasma accelerated beam with complex polyenergetic spectrum. Therefore, this double scattering system allows theoretically the beam to be extended by several centimetres, which could simplify radiobiological or dosimetric experiments.

3.9 Conclusion

A computational method (analytical algorithms and Monte Carlo simulations) was developed in this chapter to evaluate the dose distributions and dose rates for the two main charged particle beam delivery techniques (DS and PBS modes). The results allowed an estimation of the intensities and physical parameters required to operate with VHEE beams and in the ultra-high dose rate range of the VHEE FLASH effect. For the PBS mode, the irradiation time and the average dose rate depend mainly on the size of the target volume and the organisation of the spots, and are therefore mainly limited by the accelerator pulse frequency. For DS, a realistic beamline model with two complex scatterers has been simulated, making it possible to obtain large irradiation fields (greater than 10x10 cm^2), for beam intensities of the order of a hundred mA. The energy lost by the beam in this type of system is significant and could constitute a limit to the size of the fields that can be obtained. Optimisation of various parameters (effective diameter of the second scatterer and the source-axis distance) could also further increase the efficiency of the system. These preliminary results can be used as a basis for improving the design of future VHEE machines.
A DS model has also been developed for a laser plasma accelerated VHEE beam, produced at the LOA facility. This was done after characterising the beam using MC simulations. Further tests using improved laser plasma conditions (e.g. with different gaseous targets) are planned to improve the beam stability and could allow testing the double scattering system.

Chapter 4

Treatment planning for VHEE beams

Contents

4.1 Introduction

VHEEs may be a potential candidate for the translation of FLASH irradiation into the clinic, as its application could benefit from the combination of VHEE properties with the radiobiological advantages of the FLASH effect. Although many preclinical studies have been conducted using simple irradiation fields and low energy electron beams, the development of a specific treatment planning software for the evaluation of VHEE-FLASH-RT is now essential to allow more realistic research. In radiation therapy, dose calculations are based on several fast and

accurate dose calculation algorithms, such as pencil beam algorithms or Monte Carlo methods, particularly for PBS techniques. These dose engines are currently integrated into several commercial clinical TPS [167, 168], which can be used to calculate doses or optimise plans for clinical cases in a few dozen of seconds. Protons, photons and low energy electron beams (up to 20 MeV) are currently used in cancer treatment, therefore treatment planning systems are available for these techniques. As VHEEs and FLASH-RT are not yet clinically available, none of the commercial TPS could be tested on realistic clinical cases, and the adaptation of current calculation codes to VHEEs is not yet widespread. Few research tools (open source or commercial software) exist for testing FLASH or VHEE modalities in complex geometries, as well as for the possible introduction of the FLASH effect into mathematical models of dose optimisation functions. Moreover, a possible interest in using VHEEs is related to ultra-high dose rate irradiation, as VHEE physical dose distribution are intermediate between VMAT and proton PBS (pPBS) plans [122, 152, 169]. Therefore, a specific treatment planning system for VHEE should also take into account the constraints associated with FLASH irradiation.

The aim of the work presented in this chapter is twofold: first, to compare the various possible irradiation modes (DS and PBS VHEE plans) in terms of physical dose distribution and temporal characteristics (in particular dose rate and amplitude of the FLASH effect). The dose calculation model and beam conformation methods, presented in Chapters 2 and 3, are applied to a few representative clinical cases. Different tumour locations are considered: two brains (adult and adolescent), a pancreas and a prostate case to reflect the possible different geometries in humans. PBS and DS VHEE plans are compared, in particular, the target coverage and mean dose to organs at risk. For the VHEE plans, the dose rate distribution and total irradiation time are studied to evaluate the FLASH effect sparing in terms of biological equivalent dose. Second, the pencil beam scanning double Gaussian model is introduced and tested in the open-source TPS matRad environment [170] along with features and options dedicated to VHEE dose calculations. To evaluate the accuracy of the dose calculation for complex patient-based geometries, two clinical cases (brain and prostate) are computed with this TPS and compared with Monte Carlo simulations using TOPAS.

4.2 Treatment planning for VHEE: state of the art

Several studies have already compared possible VHEE treatment plans to currently used techniques, such as VMAT or IMRT for photons, and proton PBS for various clinical cases. When compared to IMRT (15 MV), scanned VHEE

(200 MeV) treatment plans have shown reduced integral doses and OAR doses by around 10%, as well as better conformity for a prostate case [24]. These results were confirmed by a second, more comprehensive prostate study, which showed that the scanned VHEE plans resulted in better dose sparing of both the rectum and bladder, as well as resulting in a lower integral dose to the normal tissues. The authors also found that an electron energy greater than 100 MeV was preferable for that case. A large number of beams in the range of 9–21 from the fixed gantry angle position was needed to achieve acceptable plans, which were not significantly improved using arc therapy or energy modulation [121]. A second study comparing 15 MV IMRT, 250 MeV VHEEs, and a two-beam IMPT plan with 200 MeV protons showed that, for the same prostate case, intensity-modulated protons always spared more healthy tissue (between 15% and 20% of the prescribed target dose) but had a conformation relatively comparable to VHEEs. VHEEs, on the other hand, allowed for a slightly higher mean target dose, a greater target dose homogeneity, and significantly greater dose sparing of the sensitive structures compared to photons [121]. Another study found similar results [33], which used a clinically approved seven-field prostate treatment plan with 6 MV photons and VHEEs between 150 and 250 MeV. A 15 MV VMAT plan was also compared to a 100 MeV scanned VHEE plan, showing a VHEE dose distribution for prostate case similar to the clinical VMAT plan [122]. The VHEE plan becomes significantly better than VMAT when the electron energy is increased to 200 MeV [152].

For a pediatric intracranial case, the 100 MeV scanned VHEE dose to all critical organs was up to 70% lower than the clinical 6 MV VMAT dose for the same target coverage, and the integral dose was also decreased by 33% compared to the VMAT plan. The optimisation of the VHEE plans proved sufficient when 13 beams and more than 100 MeV were used [122]. A 100 MeV VHEE lung plan was also compared to a 6 MV VMAT plan, resulting in a mean dose decrease to all OARs by up to 27% for the VHEE plan.
This study of various treatment plans was extended to several other clinical cases, such as acoustic neuroma, liver, lung, esophagus, and anal cancer cases, with target sizes ranging from 1 cm^3 to hundreds of cm^3 in [169]. The cases with bigger targets benefited most from the reduction of the dose to normal tissues. In contrast, the normal tissue sparing was similar to the VMAT plans for smaller and shallower targets. In that study, the mean doses to OARs were, on average, 22% lower for the VHEE plans compared to the VMAT plans. Dose conformity was equal or superior compared to the VMAT plans, and the integral dose to the body was, on average, 14% lower for the VHEE plans. In the end, the VHEE plans with scanned beams seem intermediate between photon VMAT and proton PBS plans for OAR sparing, except that the OAR sparing could be made comparable to protons plans for a shallower target [152]. The sparing generally increases with VHEE energy, as well as the dose conformity and homogeneity, and requires a significant number of entry points, which must be carefully optimised according to the position of the

organs at risk.

As these studies do not generally take into account temporal aspects nor realistic beam models, simulations of clinical cases using the delivery modes and beamlines modeled in Chapter 3 are described in the following sections. In particular, dose and dose rate distribution required to operate in the ultra-high dose rate range of the FLASH effect are taken into account when optimising plans.

4.3 Clinical cases: FLASH dose rate and delivery mode comparison

4.3.1 Treatment plan design

Four realistic cases were first selected from the Institut Curie clinical database (two brains, one pancreas, and one prostate case) based on their Planning Target Volume (PTV) position and size (deep seated and <10 cm diameter to benefit from VHEE treatments). Fully anonymised computed tomography images were used in this study, and all procedures were in accordance with the ethical standards, guidelines and regulations of the Institut ethics committee. The PBS spot configuration of VHEE treatment plans was performed in the ECLIPSE treatment planning system (Varian, a Siemens Healthineers Company) using the Nonlinear Universal Proton Optimised algorithm (NUPO) (v.15.6.05) with PBS algorithm and delivery. The optimisation for VHEE was subsequently modified considering seamless irradiations (single-field-uniform-dose, that is, each field is optimised individually to deliver a fraction of the prescribed dose to the entire target volume and produce a uniform dose). In particular, a σ spot size of 5 mm with an inter-spot distance of 1.5σ was used to minimise the number of spots and thus maximise the mean dose rate. In addition, for each plan, the different fields were placed in a configuration that minimised overlap to avoid re-irradiating the same healthy tissue. In order to determine the theoretical optimum electron beam energy according to the target volume depth and lateral size, a look-up table providing electron energy as a function of Therapeutic Range (TR) and field width at 90% of the maximum dose in water was computed using Monte Carlo simulations. This optimal energy is shown in figure 4.1 as a function of the TR and FS, and was also parameterised using a second-order polynomial regression as follows:

$$E = \frac{1}{p_1}(TR - p_2) \tag{4.1}$$

p_1 and p_2 are (second-order) parameters that depend on the field size:

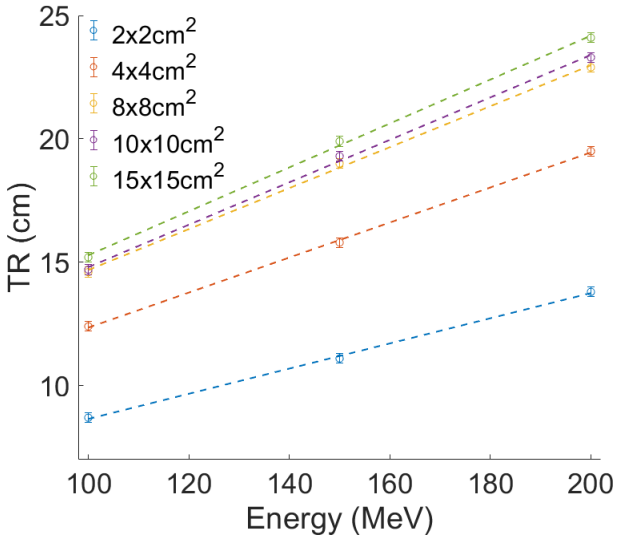

Figure 4.1: TR of divergent VHEE beams with an SSD of 150 cm (right) for field sizes between 2×2 cm^2 and 15×15 cm^2 as a function of VHEE beam energy.

$$p_1 = -0.0003FS^2 + 0.0078FS + 0.0395$$
$$p_2 = -0.0284FS^2 + 0.6711FS + 2.6210$$

For each treatment plan, the optimal energy was optimised for each field separately. These energies are shown in table 4.2.

A 65 mm-thick brass collimator, optimised to shape the beam to the PTV, was also modelled and placed at the nozzle exit for the passive scattering technique. In line with research showing that FLASH sparing starts at 3-10 Gy per fraction [171], VHEE-PBS and DS treatment plans were computed with a single (daily) fraction for each beam (the possibility of performing this technique with multiple fractions will be discussed hereafter) and multiple but well-separated beams to provide optimal plan quality while minimizing the dose to healthy tissues. DS and PBS plans were compared using the same beam arrangement to ensure minimal bias in plan comparisons. Patient data and treatment specifications for each field are summarised in table 4.1-4.2. For the PBS-DS comparison, the beam energies used were the same for all the beams: 100 MeV for both the brain cases (adult and child) and 150 MeV for the pancreas and prostate cases. Indeed, the DS lines included in the simulation (discussed in Chapter 3 and whose parameters are listed in table 3.2) were optimised in order to obtain these two energy values at the simulation isocenter.

Tumor Location	Total Dose (Gy)	Number of fields	Dose per field (Gy)			
Brain Adolescent	50.4	4	14.4	14.4	10.8	10.8
Brain Adult	59.4	3	19.8	19.8	19.8	-
Pancreas	55.8	3	21.6	21.6	12.6	-
Prostate	60.0	3	20.0	20.0	20.0	-

Table 4.1: Clinical cases evaluated in this study. For each plan, the dose was delivered using both PBS and DS delivery.

Tumor Location	Gantry/Table angles (°)				Optimized beam energy (MeV)			
Brain Adolescent	230/30	270/0	130/0	90/315	80	80	102	167
Brain Adult	330/90	120/335	270/35	-	125	96	118	-
Pancreas	135/0	0/0	225/0	-	156	80	193	-
Prostate	70/0	290/0	0/0	-	216	222	127	-

Table 4.2: Field specifications for the four cases investigated. The optimal beam energies are also shown (used for the PBS energy study in section 4.5.1).

4.3.2 Treatment plan evaluation

In order to compare the plans with each other, several quantities were evaluated. For this purpose, all plans were normalised so that 95% of the PTV received 100% of the prescribed dose. The Dose Volume Histograms (DVHs) were therefore evaluated for the target volume and the OARs. The mean dose to the OARs, the mean dose to the body ($\bar{D}_{Body}$), the conformity indices CI_{100} and CI_{50} and the Homogeneity Index (HI) were calculated. The CI_{100} and CI_{50} were defined as the ratio between the volume covered by the 100% or 50% isodoses and the PTV volume, respectively:

$$\begin{aligned} CI_{100} &= V_{100}/V_{PTV} \\ CI_{50} &= V_{50}/V_{PTV} \end{aligned} \tag{4.2}$$

HI is defined as the ratio between the maximum and minimum dose in the PTV, chosen as the 98% and 2% of the dose to the PTV, and the dose received by the 50% of the PTV, as in [172]:

$$HI = (D_2 - D_{98})/D_{50} \tag{4.3}$$

4.3.3 FLASH Modifying Factor

To complement the study with considerations of the influence of the FLASH effect on the biological dose, the FLASH modifying factor (FMF) was used in the plan comparison between scattered and scanned beams. This factor has recently been defined as the ratio between the dose at a conventional dose rate (D_{CONV}) and the dose at ultra-high dose rate (D_{UHDR}) that achieves the same effect for a given biological system and endpoint [173]:

$$FMF = \left.\frac{D_{CONV}}{D_{UHDR}}\right|_{isoeffect} \tag{4.4}$$

A dose D delivered by irradiation with UHDR is thus equivalent to an isoeffective dose delivered with conventional dose rates of:

$$D_{FMF} = FMF * D \tag{4.5}$$

The FMF is a function of the absorbed dose and depends on two parameters: the dose threshold, D_t, and FMF^{min}. Experimental FMF values have recently been reviewed in order to define these two parameters. For our work, FMF^{min} was set to 0.67, as estimated by Böhlen et al. [173] when considering all the published data from in vivo experiments comparing UHDR and conventional irradiation. Also, two different values of D_t (3 and 9.6 Gy) are considered and for the dose rate threshold, 40 and 100 Gy/s. The FMF(D) function, which depends on the dose delivered in a single fraction, is then described by:

$$FMF(D) = \begin{cases} 1, & D \leq D_T = 0 \\ (1 - FMF^{min})\frac{D_T}{D} + FMF^{min}, & D > D_T \end{cases} \tag{4.6}$$

The evolution of the FMF(D) function (equation 4.6) for FMF^{min}=0.67 and for two different values of the dose threshold, $D_T = 3$ Gy and $D_T = 9.6$ Gy, is shown in figure 4.2. When the FMF is equal to 1, both conventional and FLASH irradiation result in the same biological effect on healthy tissues, whereas a sparing effect is found when the FMF decreases, reaching its minimum around 0.67.
In this study, the FMF is applied when a specific region (outside of the Gross Tumour Volume (GTV)) is irradiated with a dose higher than D_t and a dose rate higher than the dose rate threshold, DR_T. Since in Böhlen's work [173], the FMF depends only on the dose per fraction and not on the local dose rate, the same sparing is obtained for a given dose value if the dose rate is higher than the DR_T, (regardless of its value). For the cases studied, the corresponding FMF values were obtained in each voxel of the dose matrix, taking into account the actual dose rate as in equation 3.20 for both modalities (DS and PBS).

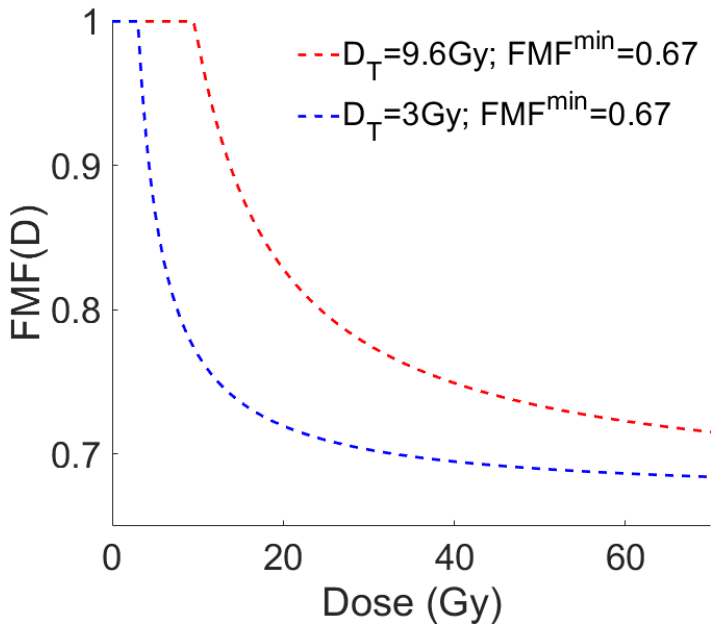

Figure 4.2: FMF(D) function (equation 4.5 as proposed by Böhlen et al. [173]) for FMF^{min}=0.67 and for two different values of D_t, 3 and 9.6 Gy.

4.3.4 MatRad TPS comparison with Monte Carlo simulations

In order to carry out the clinical studies that follow, we have implemented and validated our VHEE double Gaussian PBS model in the open-source TPS matRad environment [170], with features and options dedicated to VHEE dose calculations. MatRad is indeed an open source code facilitating any new modifications and is written with the commonly used Matlab software (Mathwork, US). Indeed, the main approach to optimise a pencil beam scanning plan is to optimise the weights of all spots in all fields simultaneously to produce the desired dose distribution. As this method is not possible with the tools we used previously, the use of a TPS would allow for the incorporation of more complex criteria during the inverse spot optimisation and make it possible to benefit from the full potential of pencil beam scanning VHEE-RT. The implementation of the VHEE modality, performed by Mateusz Sitarz during his post-doctoral fellow contract at Institut Curie, was followed by a series of verifications, comparing doses calculated in matRad against Monte Carlo simulations. Various beam models have been tested, such as a divergent pencil beam scanning system or focused beams (as recently characterised

experimentally [39]). As far as I am concerned, I was mainly involved in comparing the matRad model and Monte Carlo calculations for the various clinical cases.

To evaluate the accuracy of the VHEE dose calculation in matRad for complex patient-based geometries, two clinical cases, brain and prostate tumour locations, were selected among the four VHEE plans described previously and their PBS plan was computed using matRad and TOPAS. The PBS spot configuration and relative spot weights for the VHEE plans were optimised on the basis of seamless irradiation (single-field-uniform-dose SFUD, which is commonly used with scanned proton beams) and are listed in table 4.3. A beam energy of 100 and 150 MeV was chosen for the brain and prostate cases, respectively. Indeed, only a few discrete energy values have been modelled in the matRad libraries, and the selected energies were closest to the optimal VHEE energy for each specific field (see figure 4.1, which gives the electron energy as a function of the electron therapeutic range). Figure 4.3 shows the interface and dose calculation for a VHEE treatment plan in matRad (resulting from a collaboration between Institut Curie and Deutsches Krebsforschungszentrum Institute (DKFZ). The optimisation module is used to simulate treatments, taking into account possible physical or temporal aspects.

Tumor location	Total dose (Gy)	Beam energy (MeV)	Number of fields	Gantry/Table angles (°)
Brain adolescent	50.4	100	4	230/30, 130/0 270/0, 90/315
Prostate	60.0	150	3	70/0, 290/0, 0/0

Table 4.3: Field specifications for the two representative cases investigated for the matRad-TOPAS comparison.

4.4 Monte Carlo simulations

The VHEE treatment plans were simulated using TOPAS (v3.8 with Geant4.10.07p03). The physics modules used were the same as those described in the previous chapters. The treatment plan simulations also included PBS and DS beamlines (described in Chapter 3). In addition, the source parameters for the PBS simulations were adjusted to obtain a 5 mm spot width (σ) at the isocenter. An example of the source parameters for 100, 150 and 200 MeV is shown in the table 2.3. Dose distributions were simulated in water or in the patients' clinical cases, with a number of histories adapted to achieve a relative statistical uncertainty of less than 3% (type A, calculated as the average statistical uncertainty of voxels with a dose higher than 50% of the maximum dose).

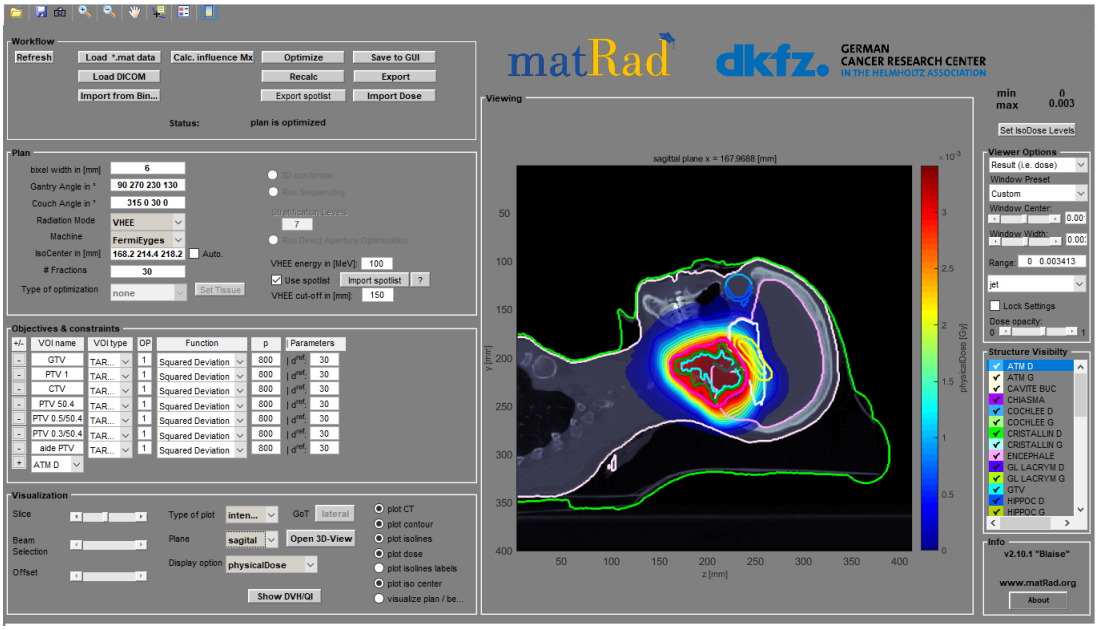

Figure 4.3: Interface and dose calculation for a VHEE treatment plan in matRad (Institut Curie-DKFZ collaboration). The optimisation module is used to simulate treatments, taking into account possible physical or temporal aspects.

4.5 Results of the clinical cases comparison

4.5.1 PBS Study

Energy Comparison

Figure 4.4 shows the comparison of PBS plans for different beam energies: 100, 125 and 150 MeV and the optimised energy plan. The beam energies for this last plan were calculated using equation 4.1 and are given in table 4.2. Figure 4.5 also shows the DVHs for the target volume and some OARs for the adult brain case. Table 4.4 shows the mean dose difference to the OARs for all the case considered. The optimised energy plan was used as the reference for this calculation. This comparison shows that the initial electron energy modifies the mean dose values delivered to the organs at risk. Therefore, using the same energy for all the beams instead of the optimised energy can increase the mean dose to the organs at risk by 2% to 8%, depending on the clinical case. The most unfavourable cases are pediatric or deep-seated tumours, for which the optimal energy theoretically varies between 80 and 200 MeV. These results may, of course, vary depending on the orientation of the beam chosen and the size and position of the target volume.

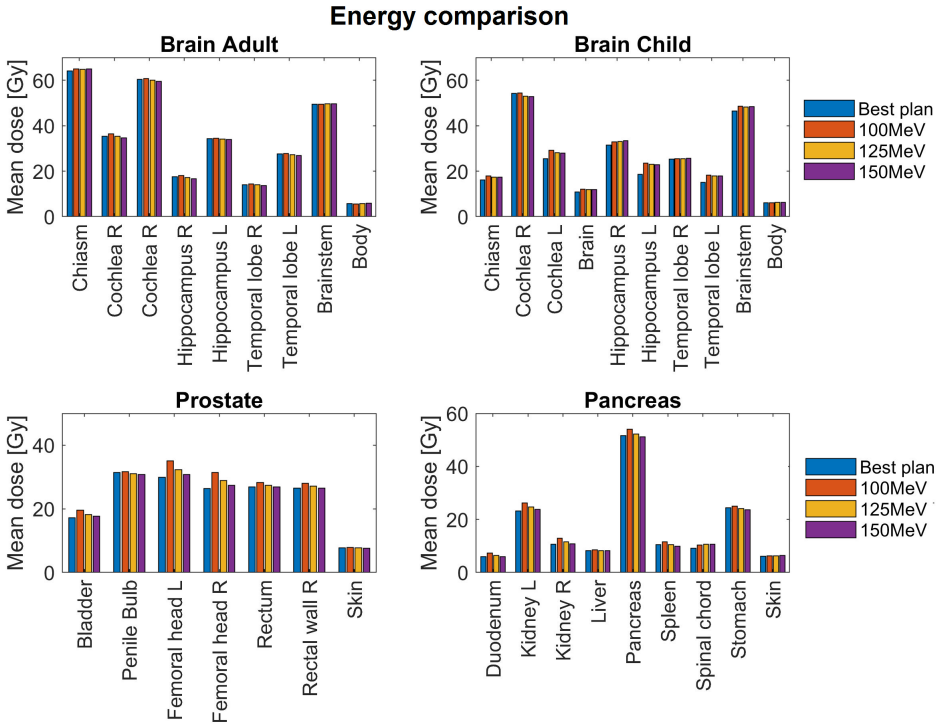

Figure 4.4: Mean dose (Gy) to the OARs for the four clinical cases comparing the different energies used for PBS plans.

Tumor Location	Mean dose difference OAR (energy comparison)	Conformity index difference PTV (energy comparison)
Brain Adolescent	8%	5%
Brain Adult	2%	3%
Pancreas	8%	7%
Prostate	4.6%	14%

Table 4.4: Comparison of the mean dose difference to the OARs for the different energies used for three PBS plans: 100, 125 and 150 MeV, using the optimised energy plan as reference.

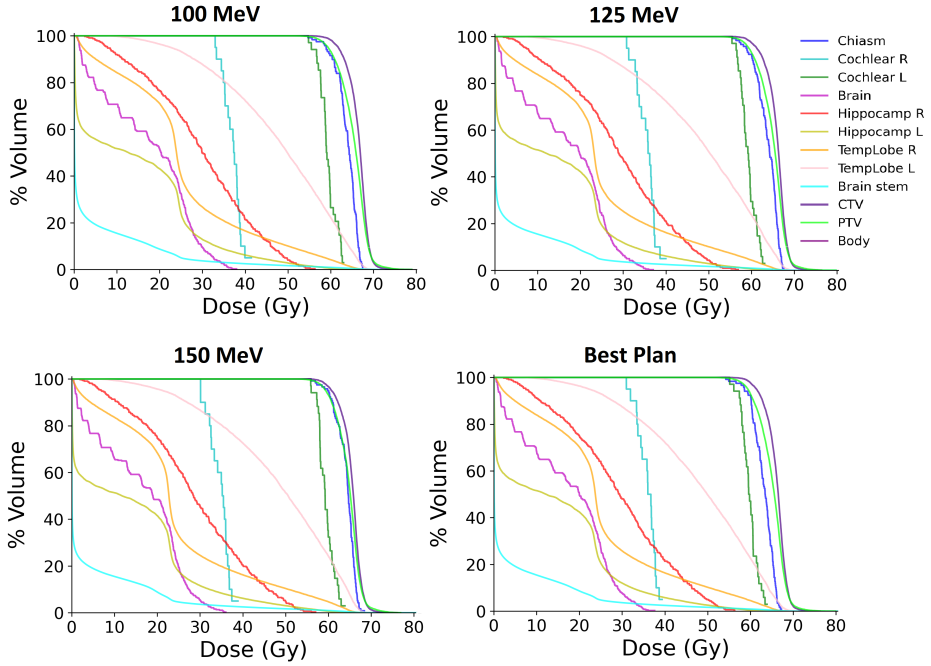

Figure 4.5: DVHs for the adult brain case for the 100, 125, 150 MeV plans and the optimised energy plan (beam energies in table 4.2).

Dose Averaged Dose Rate

Figure 4.6 shows the Dose Rate Volume Histograms (DRVHs) for the brain adult case. The Best Plan (energy values in table 4.2) is used (it is assumed that each beam is treated only once and separately) and each beam contribution is considered separately for calculations. The red and blue vertical lines correspond to the 40 and 100 Gy/s DR thresholds, respectively. These theoretical limits are represented in order to highlight the proportion of organs irradiated at higher dose rates (and therefore for which the FLASH effect occurs). Indeed, the figure shows that almost the entire OAR is irradiated at a dose rate higher than 40 Gy/s, but a smaller fraction of the OAR is irradiated at dose rates higher than 100 Gy/s. This trend highlights the different percentage of OARs likely to benefit from the FLASH sparing effect when considering various dose rate thresholds.
Figure 4.7 show the comparison of the DRVHs for the second case (brain adolescent) and for two different spot spacing. The Best Plan (energy values in table 4.2) is also considered and each beam contribution is considered separately. As the distance between the spots increases from 1 to 1.6σ, the number of spots irradiated and, therefore, the total irradiation time decreases. This reduction leads to a significant increase in the dose rate distribution over the various volumes, while the dose to the tissues remains similar (the total irradiation time indeed decreases

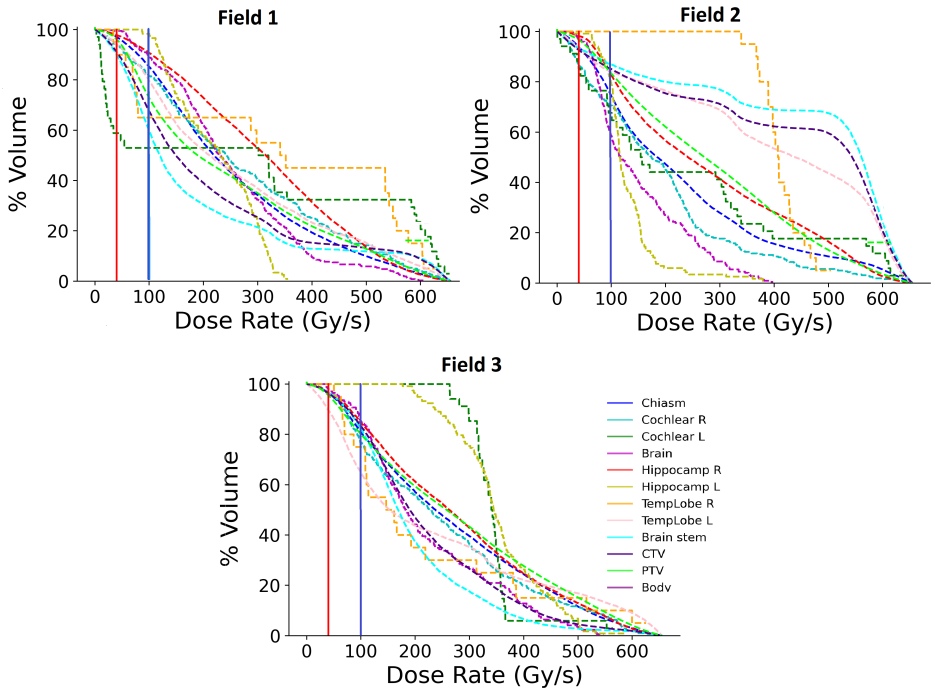

Figure 4.6: DRVH for the adult brain case (best plan) where each field is considered separately. In red and blue are shown the 40 and 100 Gy/s DR thresholds, respectively.

because fewer nearby spots contribute to the dose).
In fact, for a spot distance of 1σ, few organs have more than 50% of their volume irradiated at dose rates higher than 40 Gy/s, but none have a dose rate higher than 100 Gy/s. The dose rate is even lower when the 90% of the organ volume is considered, as shown in the table 4.5. Also, for a spot distance of 1σ, the average dose rate to the 50% of the organs over all beams is 40.8 Gy/s, while it decreases to 25.3 Gy/s when the average dose rate over the 90% of the organs is considered. However, when the spot distance increases to 1.6σ, the average dose rate over the 50% of the organ volume increases to 108.7 Gy, so that most organs have half of their volume irradiated at dose rates higher than 100 Gy/s, as shown in the table 4.5. Also, the average dose rate over the 90% of the organ volume is 69.7 Gy/s, higher than 40 Gy/s for most of the organs considered.
These results suggest that an inter-spot spacing equal to sigma (which is classically used in clinical practice) is too small to allow fast irradiation, and that it is useful to increase the inter-spot spacing up to 1.6 sigma for FLASH applications. This value is however close to the upper limit, as it would not be possible to ensure homogeneity or dose conformity at larger values.

Figure 4.8 shows the evolution of the instantaneous dose rate and the cumulative dose for a voxel at the centre of the target volume for two different spot spacings of 1 and 1.6 σ (the field 2 of the adolescent brain case is considered). The central

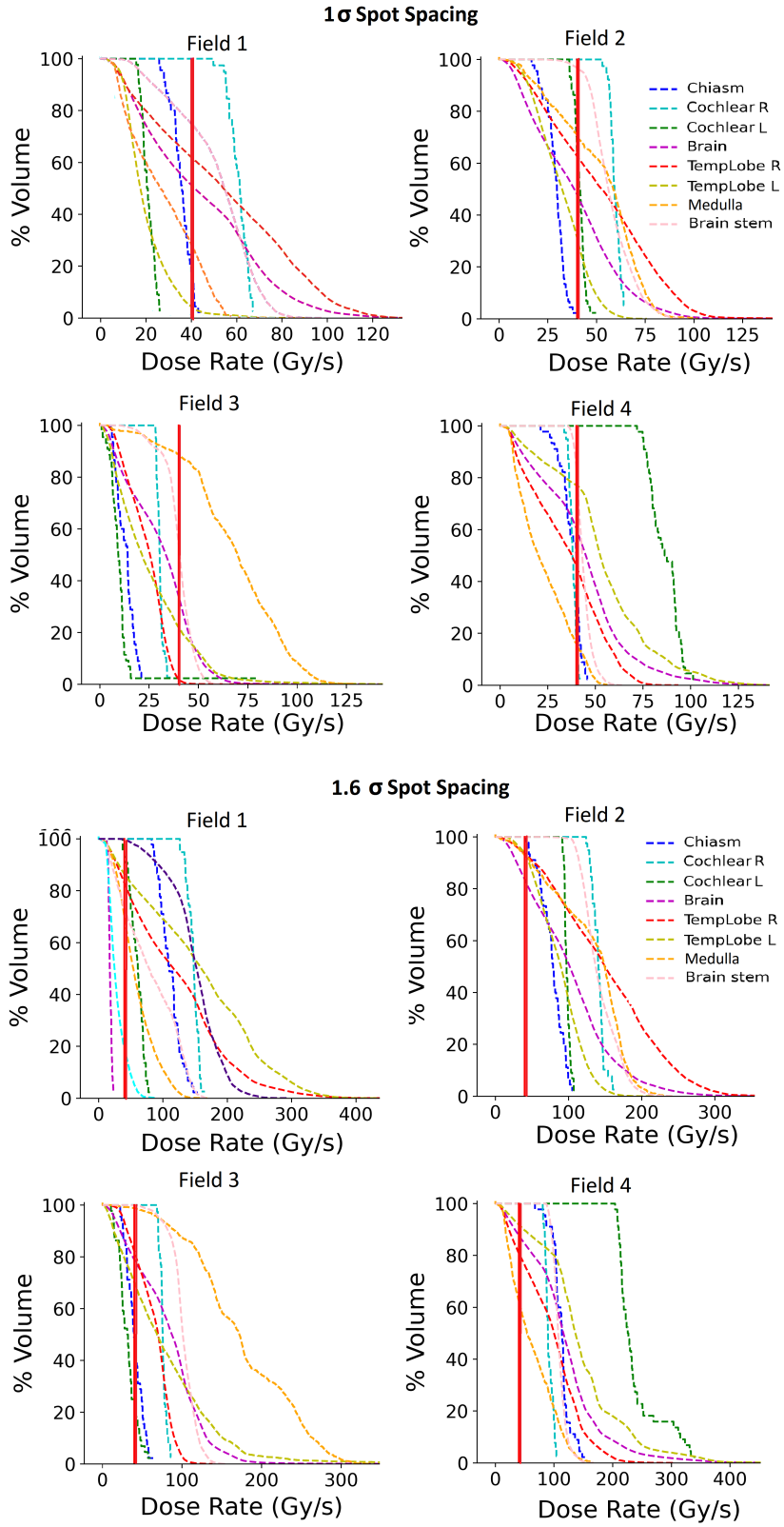

Figure 4.7: DRVHs for the brain adolescent case (optimised energy plan) for two inter-spot distances, 1 and 1.6σ, for each field. In red the 40 Gy/s DR thresholds.

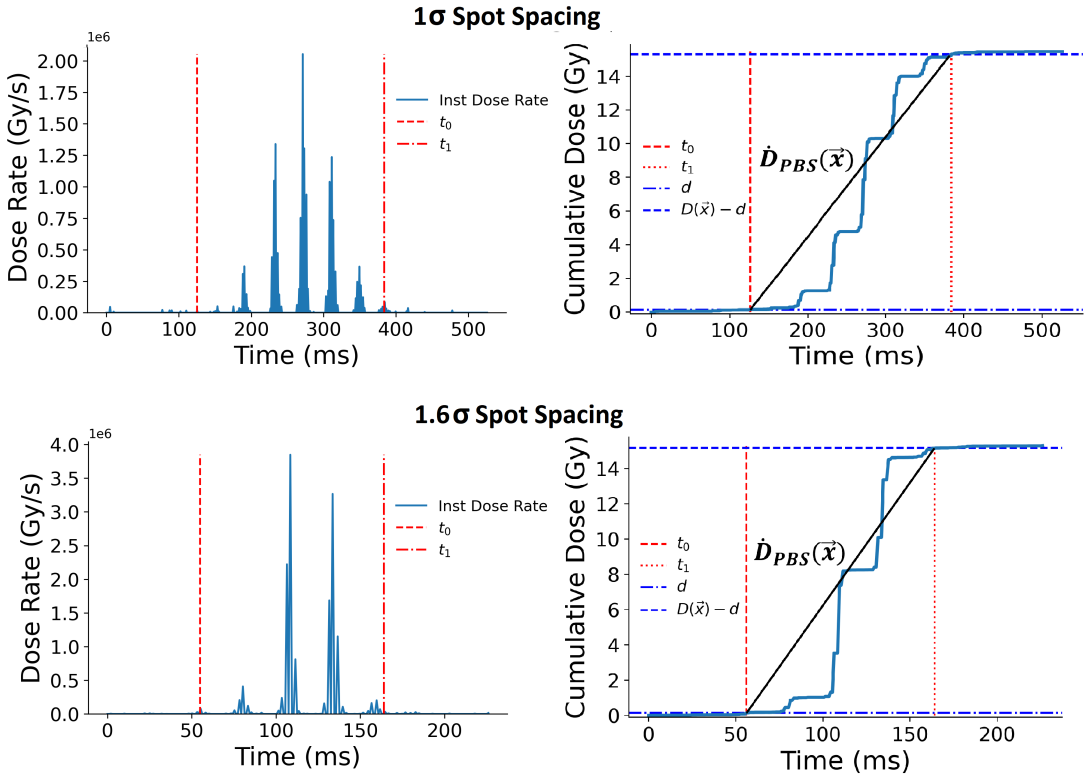

Figure 4.8: Evolution of instantaneous dose rate and cumulative dose for a voxel at the centre of the irradiated volume varying the spot spacing from 1 to 1.6σ. The vertical lines correspond to t_1 and t_2 according to equation 3.21.

voxel has the highest irradiation time as it is irradiated in the middle of the field and has the maximum number of spots in the vicinity, contributing to the local dose. On the contrary, a location at the edge of the target volume is surrounded by fewer spots, and therefore, has a shorter irradiation time. Figure 4.8 also shows that when the spot distance is set to 1σ, up to seven rows of spots can contribute to the total dose. On the contrary, the number of rows contributing to the dose is significantly reduced (to a max of three rows) for a spot spacing of 1.6σ. As shown in figure 4.8, the irradiation time for the evaluated voxel decreases dramatically while increasing the spot spacing, ranging from 259 to 109 ms for a spot spacing of 1 and 1.6 σ, respectively (considering a threshold of 1% of the prescribed dose). Therefore, in the following, a spot distance of 1.6σ will be set for all PBS simulations in order to minimise the irradiation time and maximise the local and mean dose rate.

DR (Gy/s) at 50 and 90 % organ volumes 1 σ Spot Spacing								
	Beam 1		Beam 2		Beam 3		Beam 4	
ORGAN	50 %	90 %	50 %	90 %	50 %	90 %	50 %	90 %
Chiasma	36.38	29.87	30.04	22.30	14.29	7.68	40.41	31.36
Cochlear R	61.93	55.60	59.93	56.79	30.56	28.75	38.44	36.07
Cochlear L	21.25	17.78	41.99	38.83	10.17	6.07	90.37	77.37
Brain	47.71	13.93	41.81	12.82	35.86	9.73	47.07	15.90
Temp Lobe R	59.45	15.02	57.52	20.12	26.89	11.94	40.49	10.47
Temp Lobe L	18.67	11.35	34.52	17.57	24.10	7.34	54.53	24.99
Bone marrow	29.70	9.17	60.51	23.96	72.16	46.32	22.87	7.58
Brainstem	56.51	29.27	57.42	47.96	41.17	34.31	43.60	39.89
1.6 σ Spot Spacing								
	Beam 1		Beam 2		Beam 3		Beam 4	
ORGAN	50 %	90 %	50 %	90 %	50 %	90 %	50 %	90 %
Chiasma	115.66	92.87	79.99	60.36	41.25	28.83	115.16	100.67
Cochlear R	148.83	135.14	142.37	130.42	75.83	70.06	89.80	84.57
Cochlear L	62.75	46.48	98.41	94.55	32.90	20.67	229.48	211.88
Brain	132.76	36.81	108.63	37.69	93.19	29.81	122.06	48.55
Temp Lobe R	172.71	44.40	160.61	69.64	72.24	36.94	106.20	31.93
Temp Lobe L	57.83	29.38	93.83	52.07	75.68	20.13	142.80	74.71
Bone marrow	88.12	26.81	152.88	64.26	176.52	113.20	63.06	20.63
Brainstem	156.70	109.54	140.35	118.50	102.82	88.70	108.36	97.50

Table 4.5: DR at 50 and 90% volume for the brain adult case and several organs for 1σ and 1.6σ spot distance.

4.5.2 DS-PBS comparison

Figure 4.9 shows the DVH comparison (for the target volume and some OARs) between the PBS (1.6σ spot spacing) and DS plans for the adult brain case. Also, the mean dose differences to the organs at risk between the DS and PBS techniques are compared in table 4.6 and figure 4.10. These differences vary according to the location: for cranial cases, there is little difference between the irradiation modes, and the DS is slightly better than the PBS (mean dose difference of 2.9% and 5.8% for adult and adolescent cases, respectively), a priori because the lateral penumbra is slightly sharper due to the presence of the collimator. In the other

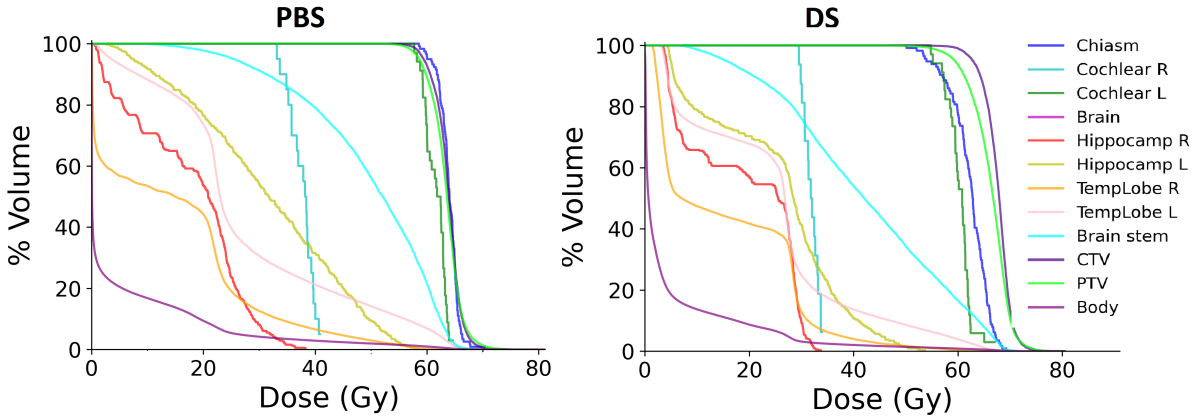

Figure 4.9: Comparison of the DVHs of the PBS and DS plans for the adult brain case.

Tumor Location	Mean dose difference OAR (PBS-DS)	Max. dose difference OAR (PBS-DS)	Conformity index difference PTV (PBS-DS)
Brain Adolescent	6%	14%	-5%
Brain Adult	3%	-57%	-5%
Pancreas	-38%	-100%	21%
Prostate	-10%	-17%	36%

Table 4.6: Comparison of the mean dose difference to the OARs for the four clinical cases, for the DS and PBS plans.

two cases, PBS is the technique that delivers the lowest mean dose to the organs at risk, with a mean difference of 10% to 38% for the prostate and pancreas cases, respectively, compared with the DS technique. This difference is mainly attributed to the limitations of the DS beamline design, which does not allow energies above 160 MeV to be delivered (due to the compromise that was made on the scatterer thickness and energy loss in the system). An example of the dose distribution in a transverse plan is shown in figure 4.11 for the four patients. The PBS calculation was performed by optimising the energies of each beam independently. A comparison of the total irradiation time is also shown in table 4.7, calculated using equation 3.19 and the beam parameters described in table 3.3. The results show a total treatment time of the order of a few ms for the DS mode, while a much longer time of the order of hundreds of ms is required to perform a PBS irradiation. The calculation also included the scanning time for the PBS mode.

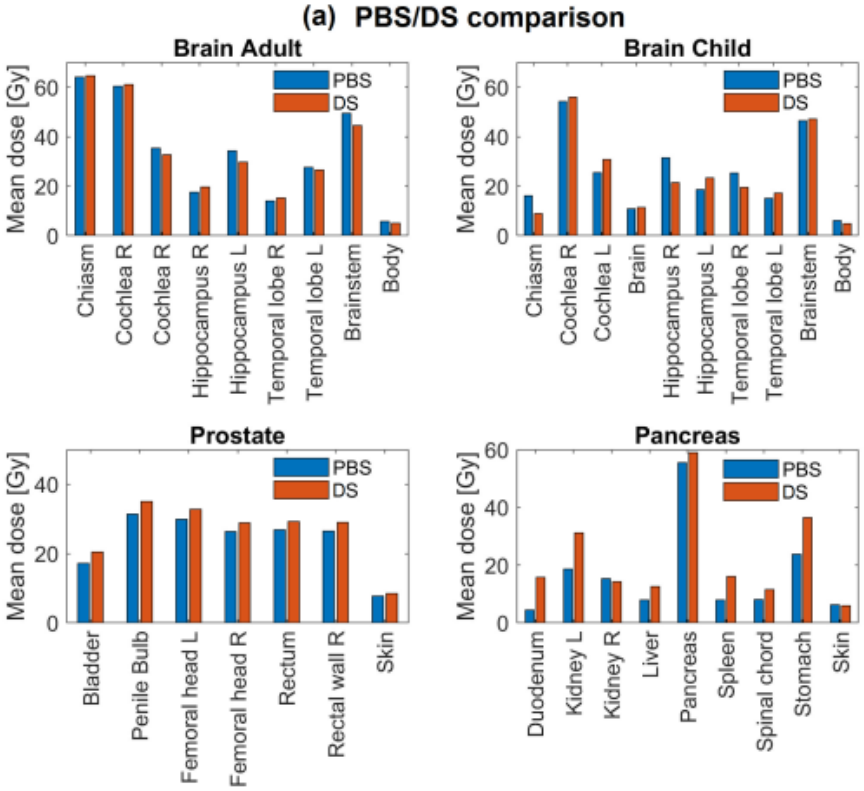

Figure 4.10: Comparison of the mean dose (Gy) to the OARs for the four clinical cases, for the DS and PBS plans.

Tumor Location	Irradiation time (ms)							
	Beams DS				Beams PBS			
Brain Adolescent	5	5	2.5	2.5	281	312	330	298
Brain Adult	12.5	12.5	12.5	-	190	204	165	-
Pancreas	17	20	10	-	326	347	337	-
Prostate	15	15	15	-	358	354	368	-

Table 4.7: Irradiation times in milliseconds for the four cases investigated and different beams for the DS and PBS techniques.

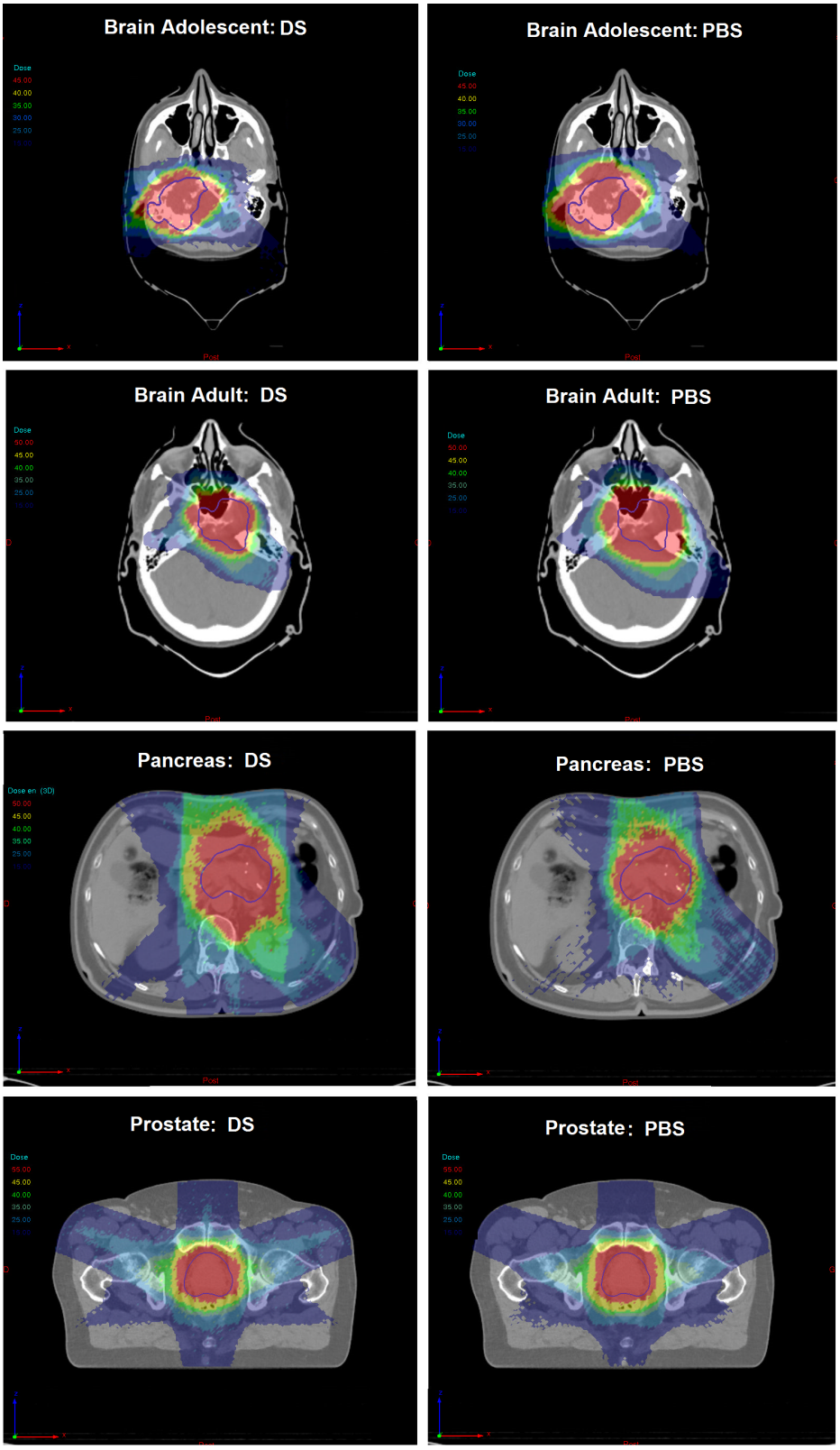

Figure 4.11: Dose distributions of the DS and PBS plans for the four clinical cases (Monte Carlo simulations). CTV in blue.

4.5.3 Evaluating the FLASH sparing using the FMF

Figure 4.12 shows the DVHs for the PBS and DS plans and the adult brain case. The spot spacing for the PBS plans was set to 1.6σ in order to maximise the dose rate, as previously mentioned. The DVHs are given with and without consideration of the biological sparing associated with the FLASH effect using the FMF (according to equation 4.6) with two D_t (3 and 9.6 Gy) and DR_t (40 and 100 Gy/s). The mean doses to organs at risk, with or without FMF, are also shown in figure 4.13 for the DS and PBS modes, together with the various parameters used to calculate the FMF, using equation 4.6. Table 4.8 compares the mean dose difference to the OARs when the FMF factor is applied for the DS and PBS plans. The physical dose was considered as the reference dose for the calculation.

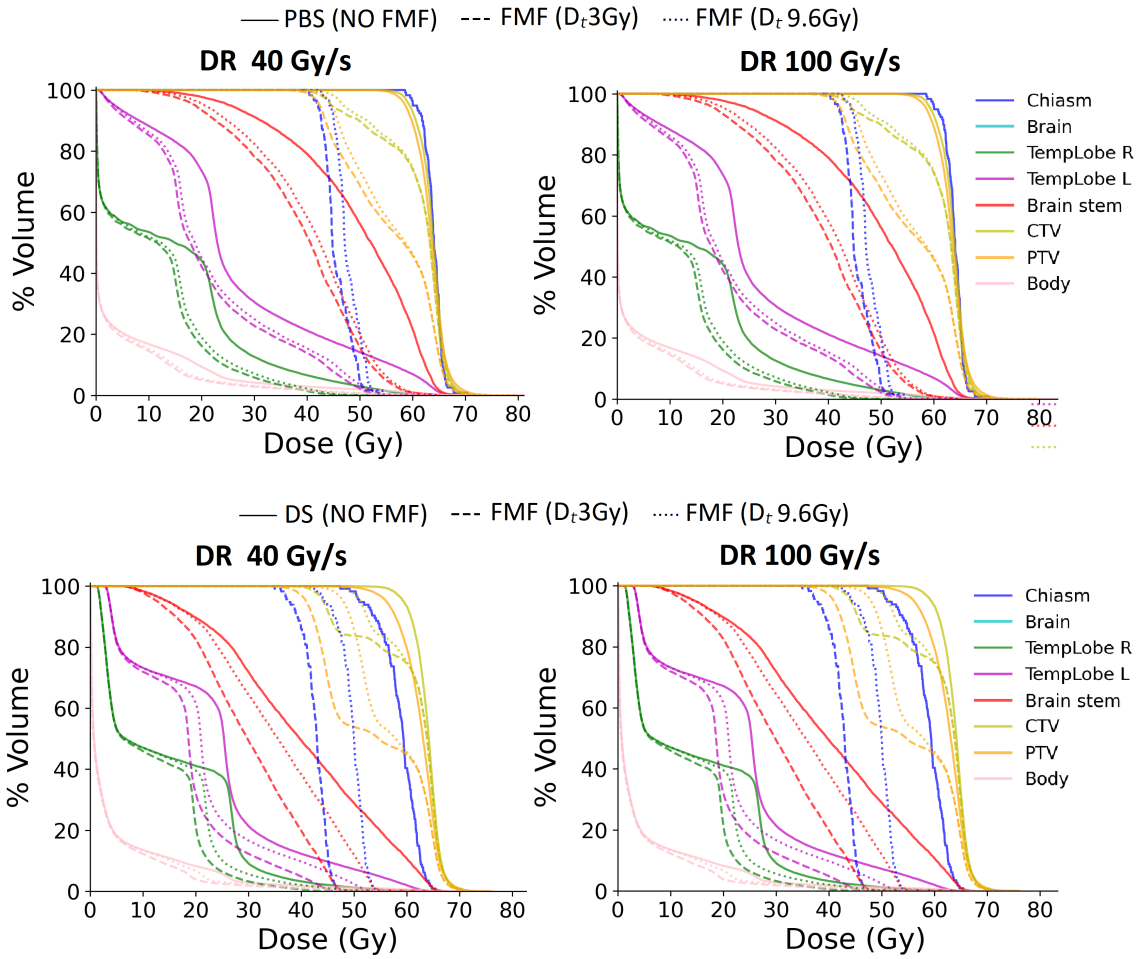

Figure 4.12: DVHs with and without FMF (according to equation 4.6) considering two D_t (3 and 9.6 Gy) and DR_t (40 and 100 Gy/s) for the PBS (top) and DS plans (bottom) for the adult brain case.

PBS - Mean dose difference OAR

	DR_t=40 Gy/s		DR_t=100 Gy/s	
Tumor Location	D_t=3 Gy	D_t=9.6 Gy	D_t=3 Gy	D_t=9.6 Gy
Brain Adolescent	-19%	-3%	-15%	-3%
Brain Adult	-27%	-23%	-24%	-18%
Pancreas	-21%	-9%	-14%	-7%
Prostate	-24%	-12%	-20%	-10%

DS - Mean dose difference OAR

	DR_t=40 Gy/s		DR_t=100 Gy/s	
Tumor Location	D_t=3 Gy	D_t=9.6 Gy	D_t=3 Gy	D_t=9.6 Gy
Brain Adolescent	-17%	-4%	-15%	-3%
Brain Adult	-24%	-13%	-24%	-13%
Pancreas	-20%	-9%	-20%	-9%
Prostate	-22%	-10%	-22%	-10%

Table 4.8: Mean dose difference to the OARs (the physical dose was considered as reference) when the FMF factor is applied to the DS and PBS plans for different values of the D_t and DR_t.

Several tendencies can be deduced from these results: first, there is little difference in the FMF values obtained between the DS and PBS irradiation modes selected (<4%), except in the adult case where a maximum dose difference (∼10%) difference is observed. The gain in terms of sparing effect varies between 11% and 27% depending on the clinical case. Second, the expected gain (between 3% and 23%) due to the FLASH effect depends on the type of treatment and organ and varies significantly according to the minimum FLASH dose threshold D_t. According to the equation 4.6, the effect is greater when the dose threshold is lower.

4.5.4 MatRad pencil beam model vs Monte Carlo simulations

Figure 4.14 shows the planar dose distributions calculated with matRad and TOPAS for both brain and prostate treatment cases. Qualitatively, it can be seen that there is a good agreement between the two calculations. The dose distributions were normalised so that the mean dose to the target was equal to the prescribed dose. Relative dose differences of less than 6% and 2% were observed for the brain and prostate cases, respectively. The maximum dose differences for the OARs were found to be 0.7 and 0.6 Gy for the brain and prostate cases, respectively, which can be attributed to the limitations of the analytical algorithm

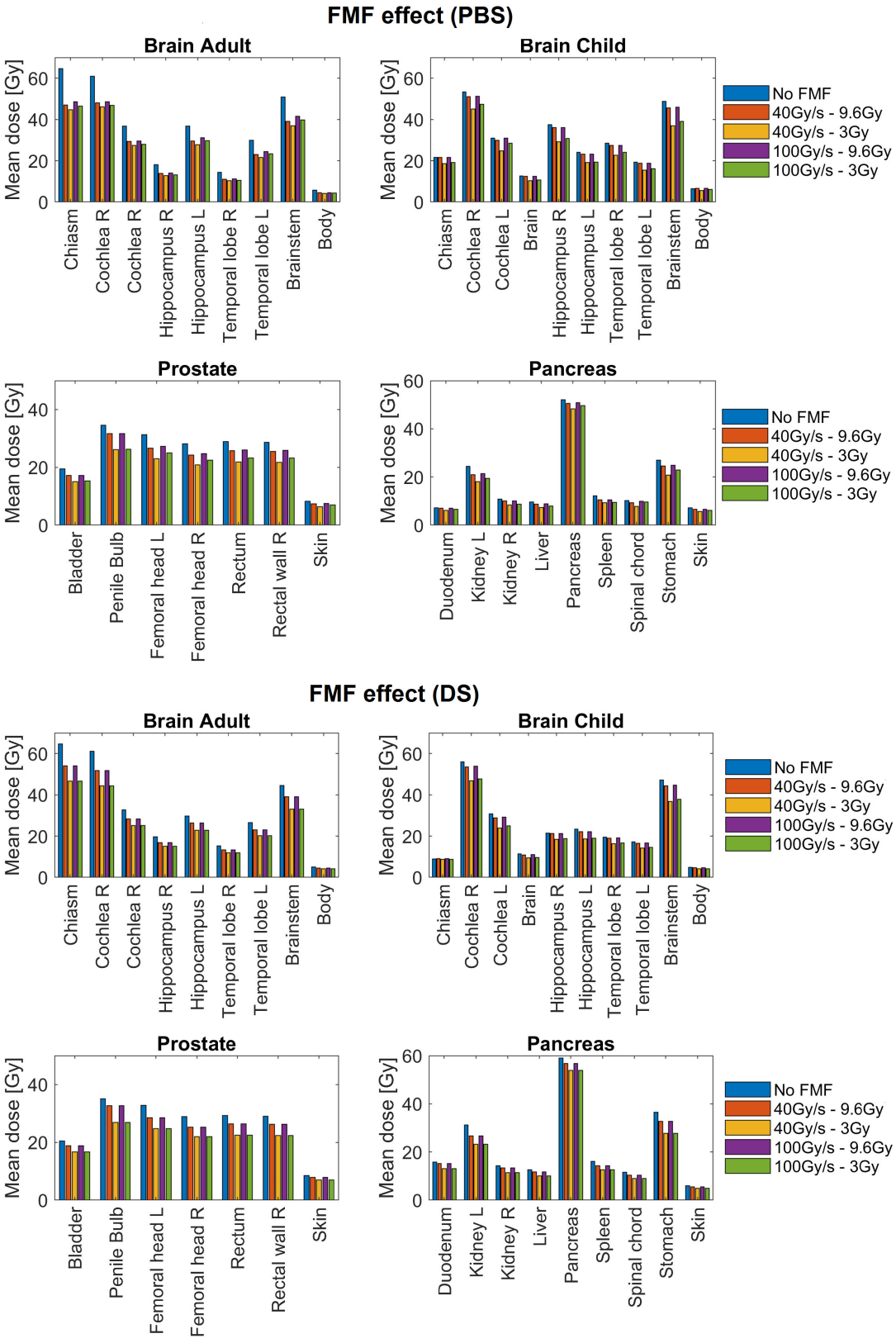

Figure 4.13: Mean dose (Gy) to the organs at risk for the four clinical cases. Top: Comparison using the FMF factor for the DS plans with different D_t and minimum average dose rate threshold. Bottom: Comparison using the FMF factor for the PBS plans with different D_t and minimum average dose rate thresholds.

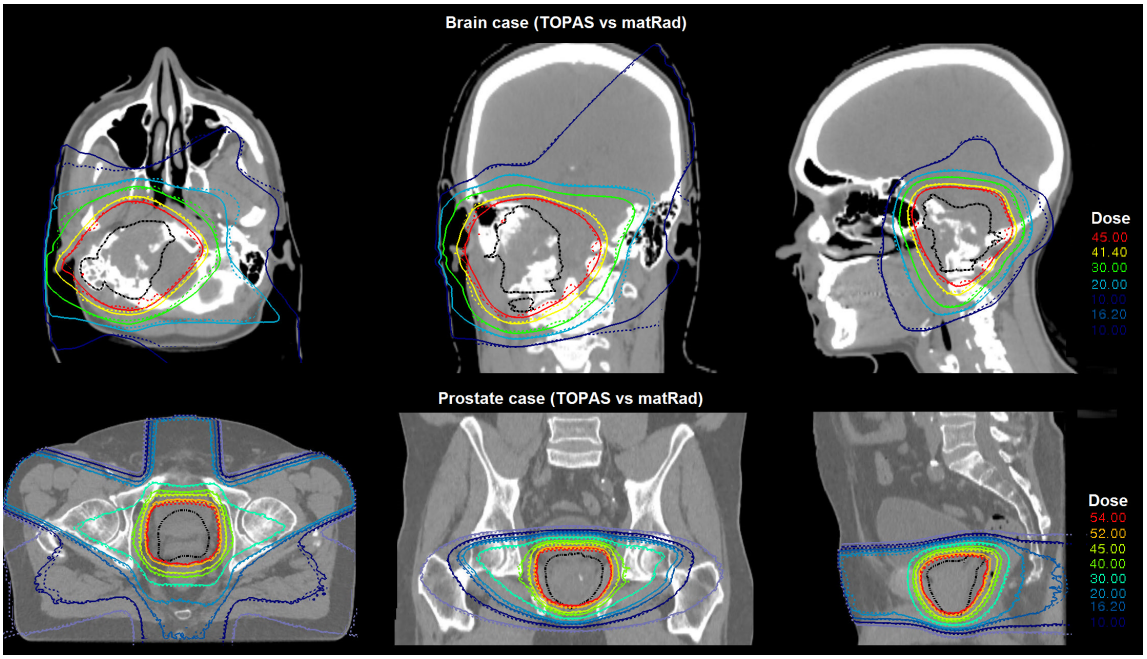

Figure 4.14: Comparison of isodose distribution between TOPAS (solid line) and matRad (dashed line) for the two clinical cases: brain (top) and prostate (bottom). The target volume is outlined in black.

in accurately modelling the electron scattering in the high and low density tissues. The mean doses delivered to the target and to the OARs with matRad pencil beam model and TOPAS are listed in table 4.9. Figure 4.15 shows the DVHs for the main relevant organs and for the different treatment plans and the two clinical cases.

4.6 Discussion

In this chapter, VHEE treatment plans were modelled and evaluated for four different clinical cases: brain (adult and adolescent), pancreas, and prostate. The two conformation techniques (PBS and DS) for VHEE beams described in Chapter 3 and optimised to meet the dose rate requirements for FLASH irradiation were used. The PBS model was then implemented in the matRad treatment planning system and benchmarked against Monte Carlo simulations performed with TOPAS.
The obtained results concerning the plan quality and the energy of the beams are consistent with those previously reported [122, 152, 174, 175], with higher energies resulting in better plan quality. In particular, for deep seated tumours, it was

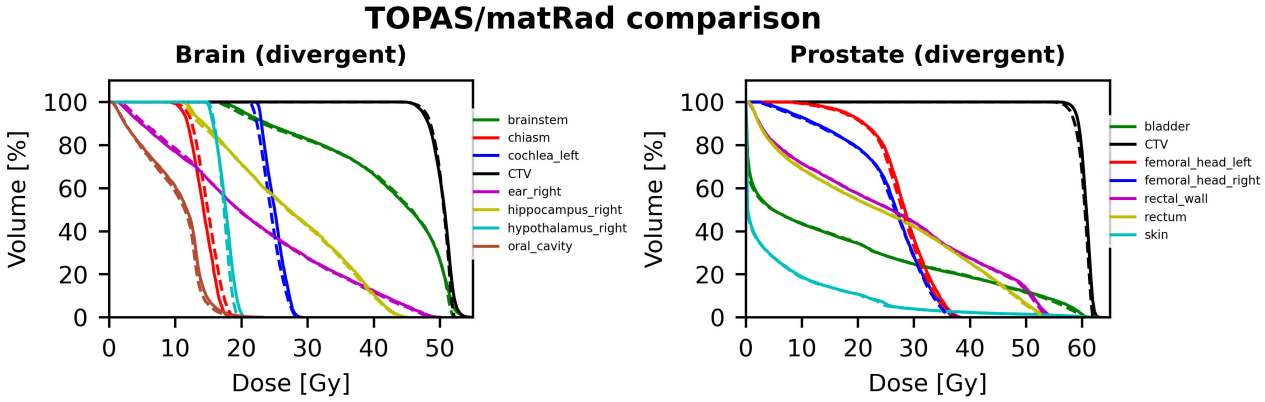

Figure 4.15: Comparison of matRad and TOPAS DVHs (TOPAS: solid line, matRad: dashed line) for brain and prostate cases.

Mean dose brain (Gy)			Mean dose prostate (Gy)		
Organ	TOPAS	matRad	Organ	TOPAS	matRad
CTV	50.4	50.4	CTV	60.7	60.3
Brain stem	41.8	41.6	Bladder	16.4	16.4
Chiasm	14.2	14.9	Femoral head right	25.1	24.9
Cochlea left	25.0	24.5	Femoral head left	28.1	27.5
Ear right	21.6	21.6	Rectal wall	25.6	25.7
Hippocampus right	27.4	27.2	Rectum	24.2	24.3
Hypothalamus right	17.6	17.3	Skin	5.7	5.5
Oral cavity	10.0	9.7			

Table 4.9: Mean dose (Gy) to the OARs and to the target volume for the two clinical cases, brain and prostate, obtained with TOPAS and matRad calculations.

found that high energies (up to 200 MeV) are needed to obtain high-quality plans, which may depend on the beam angular arrangement. However, further improvement in plan quality can be achieved by optimising the energy based on target depth, resulting in a slightly better VHEE treatment plan in terms of target coverage and organ at risk mean dose. For tumours located in the brain or pelvis, this would, for example, imply varying the energy of the beams between 80 and 220 MeV. A similar result, but for more superficial targets, had already been obtained by Zhang et al. [176] for a brain tumour case. In this study, a specific function was used to evaluate in 3D the biological dose and the tissue-sparing effect of FLASH irradiation: with the different parameters used, comparable results to an earlier study were obtained [177], in which the authors reported sparing of between 20 and 35% for a chordoma and meningioma case respectively. A temporal description of the irradiation was performed to take into account the dose rate threshold requirements. The scanning time and pulse repetition frequency (beam pauses) were also considered for the PBS mode.

One of the limitations of our work concerns the optimisation algorithm used to generate the treatment plans: a simple Single Field Uniform Dose (SFUD) optimisation was used because no clinical TPS was available for modelling and optimising VHEE plans. A multi-criterion optimisation approach with inverse planning would certainly have produced better plans, in particular using dose rate constraints as proposed for the proton beams [178]. Optimising the spot delivery pattern or reducing the number of spots, for example, using "pencil beam resampling" algorithms can also be used to enhance the local dose rate to conventional treatment plans, as shown for proton therapy FLASH applications [146]. The possible impact on plan quality, level of conformation, and degrees of freedom on intensity modulation remains, therefore, to be studied for such VHEE PBS systems. Further investigations on more patients, various angular beam arrangements, including different tumor sites, are also needed to confirm the results obtained. A configuration with a limited number of beams was also chosen, without testing the effect of increasing their number. Indeed, recent studies have shown that VHEE plans with three or four incidences can provide an improvement over IMRT clinical plans [122, 152, 175, 177]. It was also demonstrated that VHEE-RT may deliver conformal treatments to targets in the brain and the thorax using a limited (3 to 7) number of beams [174]. In addition, there are still many unknowns about the possibility of maintaining the FLASH effect while multiplying the number of beams used during a single irradiation session or a fractionated treatment. A maximum number of four fields was thus used for each plan, with a prescribed dose per field greater than 10 Gy. Comparing VHEE-FLASH treatment plans with other FLASH techniques, such as with protons, would also be needed but is beyond the scope of our study, particularly while the optimisation functions have not been fully implemented for both modalities.

The function proposed by Böhlen et al. [174] to parameterise the amplitude of the FLASH effect according to the single fraction dose was used to compare the

plans with each other. One assumption of the model is that below a certain dose threshold D_t, the FLASH sparing factor is equal to 1. A value of 9.6 Gy for this threshold was obtained by the authors, which was used in this calculation. However, FMF calculations were also performed with a $D_t = 3$ Gy to determine whether this parameter could modify the results in the clinical cases tested. The average dose rate limit below which there would be no FLASH is also an unclear parameter for the moment, often estimated in recent publications between 40 and 100 Gy/s. These two values were, therefore, tested as the threshold dose rate for applying the FMF factor. However, this study did not consider any variations in the equivalent biological dose during hypofractionated regimens compared with a normofractionated regimen, which would be necessary for an objective assessment of the benefits of the technique. Indeed, the FLASH sparing effect may be less significant with a normofractionated regimen if we assume that FLASH can only be obtained and delivered at high doses per fraction [174]. In addition, there is very little preclinical data on the effect of fractionation on FMF values, making any comparison between treatment types and various fractionations highly speculative.
The VHEE double Gaussian beam model (presented in Chapter 3) was also implemented in the matRad treatment planning system and compared with Monte Carlo simulations. The two clinical cases investigated in this work have been found to be in good agreement between the matRad pencil beam model and TOPAS calculations. Despite small differences and the aforementioned limitation in scattering predictions, a clear advantage of the TPS calculation time has been observed, around 100 times faster than Monte Carlo simulations. For other clinical cases, calculation time and precision in matRad can be further altered with dose calculation resolution and cut-off. These results encourage more clinical cases and beam models to be tested to investigate the potential of the VHEE modality further. Further adaptation of the VHEE modality in matRad could, for example, include focused beam models, different energies per field, and automatic optimisation of the parameters. Similarly, FLASH-related optimisation tools could be added, including the FLASH modifying factor, dose rate volume histograms, or optimisation of the spot positions in order to minimise the delivery time.

4.7 Conclusion

This chapter focuses on treatment planning for VHEEs. The potential of VHEEs was investigated in four clinical cases: two brain tumours (adult and adolescent), pancreas and prostate. First, an energy study was performed for the PBS modality to investigate the influence of beam energy on plan quality. The PBS and DS modalities were then evaluated and compared using MC simulations. An existing model for estimating the amplitude of the FLASH effect was also used to compare

these two beam delivery methods. Finally, the plans were also implemented using matRad TPS. Two patient cases (brain and prostate) were studied to evaluate the TPS against accurate Monte Carlo simulations, demonstrating matRad usefulness for conducting preliminary studies, for example, in the area of FLASH VHEE radiotherapy.

Chapter 5

Secondary radiation in VHEE radiotherapy

Contents

5.1 Introduction

Among the many aspects to be studied for the implementation of VHEE radiotherapy is that of the secondary dose produced. Indeed, this secondary dose, and in particular the bremsstrahlung and neutron components generated in the treatment head or in the tissues, must be taken into account when calculating the energy deposition, which has to be validated in the energy range of VHEEs.
As described in section 1.3.5, bremsstrahlung is the dominant electromagnetic process for high energy electron beams interacting with matter, whose contribution to the total dose increases with the energy of the beam and is greater than 10% for energies above 50 MeV. High energy electron bremsstrahlung theories have been documented in detail for a large range of energies, showing good agreement with experimental data, although small underestimations outside the 90–120 MeV range have been reported [51]. On the other hand, the development of VHEEs also requires an accurate estimation of neutron generation yields and induced radioactivity from the point of view of patient and staff radiation protection. Indeed, three main photoneutron production processes are possible from the high-energy bremsstrahlung photons (described in section 1.3.5), with giant resonance being the dominant process for VHEE beams. Based on MC simulations, the total body neutron dose due to VHEE irradiation with pencil beam scanning was estimated to be around 1–2 orders of magnitude smaller than that for scanned proton beams or 15–18 MV photon IMRT [55]. A neutron yield around 10^{-5} neutrons per incident electron was simulated by [179] for a 165 MeV scanned electron beam in water, which is still an order of magnitude lower than for a 20 MV nominal energy X-ray beam, and much lower than the previous estimates; the authors also found that induced activity due to radionuclide production had a negligible effect on the total dose deposited. These estimations may, however, vary considerably depending on the type of beam delivery chosen in the future machines (type of collimation, scanned, or scattered mode), as realistic conditions are lacking for shielding calculations.
In principle, both PBS or DS conformation techniques could be valid for the implementation of VHEE therapy and have advantages and disadvantages if they are to remain in the UHDR. The advantage of the PBS is that the beams do not interact with active components in the treatment head of the accelerator and the dose distribution can be accurately adapted to the shape of the tumour and position of surrounding healthy tissue using intensity modulation techniques. Consequently, the PBS mode will deliver a significantly lower bremsstrahlung contribution to the total central-axis dose of the beam [24]. Nevertheless, most systems that produce electrons at UHDR and have demonstrated the existence of the FLASH effect are based on scattered beams [67, 150, 152]. Several teams have therefore accurately

assessed the secondary particle rates for existing low-energy machines, and have also considered the consequences of UHDR use (raising the importance of the design of the vaults concerned), [180] but little work exists on very high energies.

In this context, this chapter examines the secondary dose produced by VHEEs, with particular emphasis on bremsstrahlung photons. The electron and x-ray dose distributions arising from various beam delivery systems (DS or PBS as described in Chapter 3) will be compared in water. A preliminary assessment of the secondary dose for a clinical VHEE treatment will then be performed using a whole-body phantom obtained by merging a patient CT with an anthropomorphic phantom. Finally, an evaluation of the secondary dose produced by a preliminary design of a VHEE machine in a clinical facility will be performed, taking into account the PBS or DS nozzle configurations, in order to assess the bremsstrahlung photon requirements in a clinical vault.

5.2 Background and general considerations

5.2.1 Shielding for UHDR charged particle therapy

The safety and protection of staff, patients and the public are the primary motivating factors for a radiation protection program, whose aspects must be critically re-examined and assessed if dose rates become very high compared with current clinical conditions. For example, conventional dose rate treatments in the order of Gy/s are frequently achieved (in particular in proton therapy) and radiation protection requirements are generally met by current radiotherapy facilities. However, these requirements may not be respected by UHDR irradiations with dose rates several orders of magnitude higher. This concern is currently being studied for both proton and low-energy electron beams, as well as for VHEEs, even though few studies have been published at the moment. In particular, Monte Carlo simulations can be used to estimate dose rates for key locations and to assess whether the existing shielding will allow a safe operation in FLASH mode.
For protons, in particular, there are a number of special features to bear in mind. First, the spread-out Bragg peak is used to cover the tumour profile in depth, therefore the proton dose rapidly drops to zero and there is no beam coming out of the patient. The use of pencil beam scanning, based on theoretical grounds, also provides a potential reduction in neutron production compared to a passive scattering technique. However, when proton beams are delivered in FLASH mode, the beam is sometimes used in transmission mode: shoot through proton beams (delivered at maximum machine energy) can then interact with the gantry or treatment room elements. For that reason, Xiao et al. [181] proposed the use of a solid water slab beam stopper to absorb the proton beam downstream from the patient. Besides, the energy parameter is known to strongly influence neutron production:

Monte Carlo neutron exposures for proton beam energies have shown that a ratio of 6 for neutron equivalent dose could be expected between 100 MeV and 160 MeV [182]. In addition, as the transmission dose at the Bragg peak entrance (or plateau) is much lower than at the Bragg peak position, more protons are required to deliver the same prescribed dose. For these reasons, the evaluation of the secondary neutron dose for FLASH proton beams is paramount to validate the safety of the existing shielding design, which for proton therapy is driven by secondary neutron production [181].
Different considerations also need to be made for electron facilities. Electrons are usually not considered when calculating the shielding requirements in conventional linacs because it is assumed that sufficient shielding for 6-18 MV photons is also sufficient for electrons. Although low energy electrons produce some bremsstrahlung photon contamination (particularly in the scattering foils or collimators), this contamination is only a fraction of the output of photons at clinical energies. A study by Poirier et al. [180] for example found that, after a linac had been converted to deliver 16 MeV electron beams at dose rates 200 times higher than clinical ones, the bremsstrahlung photon contamination had a dose rate 15 times higher than that of a clinical 18 MV beam (at conventional dose rate). The study also investigated whether the vault shielding designed for the 18 MV photon beam was sufficient to shield the bremsstrahlung photons produced by a 16 MeV FLASH-RT electron beam, since the bremsstrahlung spectrum produced in the scattering foil is different from that produced by the thick target used to convert the electrons to a photons beam. The shielding of the considered vault was, however, found to be sufficient, as the bremsstrahlung photons were estimated to have concrete Tenth-Value Layers (TVLs) similar to those of megavolt photon beams of similar energy, corresponding to the thickness of concrete required to reduce their absorbed dose to one tenth.
Secondary dose assessment for VHEE radiotherapy need also careful assessment as the VHEE beam is not expected to stop completely in the patient and no experimental characterisation has yet been carried out on clinical machines. Also, the bremsstrahlung photons produced for VHEE energies are, for their part, expected to be much higher than for low energy electrons, especially if the scattering mode with a high Z material foil of about half mm is needed to produce a large irradiation field (as discussed in Chapter 3). A first theoretical study [183] evaluated the neutron yield produced by a 200 MeV VHEE beam incident on a water phantom, which showed a similar neutron yield and ambient dose equivalent to conventional proton therapy. However, the secondary dose assessment of VHEE and in particular the bremsstrahlung contamination in a clinical environment has not been adequately investigated.

5.2.2 Radiation survey and regulatory implications

The regulatory limits for the instantaneous dose rate in uncontrolled areas are much less stringent in the USA (regulations of 1 mSv/yr, 20 μSv in any one hour) than those applied in Europe, as highlighted in the Poirier et al. [180] study. In France, in particular, the labour code (articles L. 4451-1 and seq. and R. 4451-1 and seq.) sets the maximum permissible exposure limits for the protection of workers against the risks associated with ionising radiation [184]. The limit for the instantaneous dose rate in uncontrolled areas, defined as areas to which access is neither restricted nor controlled, is about 80 μSv/month. Considering 160 working hours in a month, the limit results in an hourly regulation of 0.5 μSv/h. Once the type of machine has been defined, these figures will be used to finalise the layout and geometry of a possible beamline and bunker for FLASH applications.

5.3 Analytical models for the bremsstrahlung component in pencil beam scanning mode

There are several distinct sources of radiation exposure, including primary particles, stray neutrons and photons emanating from the treatment delivery system (scattering and collimation systems, or pencil beam scanning), photons and neutrons produced by therapeutic electron radiation inside the body. In what follows, the data relating to the study of these components will be analysed separately, starting with the case of scanned beams, which is the simplest. Indeed, in the 1960s and with the pioneering use of the first electron beams (in particular at the University of Chicago), several cohorts of patients were treated with scanned electron beams between 3 MeV and 50 MeV, and betatrons or racetrack microtrons were first considered as potentially capable of delivering high energy electrons [31]. These developments have led to a number of studies on the modelling of electron beams and secondary photon doses.

5.3.1 Analytical models for the depth dose curve of the phantom generated bremsstrahlung photons

The total photon background in electron beams is the sum of the photon contamination generated in the accelerator head, and the bremsstrahlung tail generated in the phantom. Therefore, both components have been studied and analytically modelled for low energy electrons. In particular, analytical expressions exist for estimating the bremsstrahlung contamination (in terms of percentage depth dose along the central axis), which has been derived for phantom generated bremsstrahlung photons in the energy range from 1 to 50 MeV [144]. The

absorbed dose due to the phantom generated bremsstrahlung $D_{X,p}$, at any depth, z, in a semi-infinite phantom with infinite SSD can then be calculated by folding the bremsstrahlung photon energy fluences, $\Psi(z)$, with the one-dimensional energy deposition kernel h(z), according to [144]:

$$D(z) \approx \frac{\bar{\mu}_X \mu_p \mu_e}{\rho \bar{\mu}_0 \, (\mu_e - \nu \mu_p)} \Bigg[(1-\nu)\Psi(z) + \nu(\mu_e - \bar{\mu_0}) \int_0^z \Psi(z') \, e^{-\mu_e (z-z')} \, dz' + (\bar{\mu}_0 - \mu_p) \int_0^z \Psi(z') \, e^{-\mu_p (z-z')} \, dz' \Bigg] \quad (5.1)$$

$\bar{\mu}_X$ is the mean linear attenuation coefficient for the bremsstrahlung photons produced in the phantom (tabulated in water for energies up to 50 MeV in [185]). The other parameters, $\bar{\mu}_0$, μ_p, and μ_e are related to the dose and fluence distribution of a primary photon beam incident on a phantom. In particular, the primary photon fluence can be expressed as a function of the depth as:

$$\Psi_p(z) = \Psi_{p,0} \, e^{-\bar{\mu}_0 z} \quad (5.2)$$

with $\bar{\mu}_0$ the primary photons mean attenuation coefficient and $\Psi_{p,0}$ the incident photon fluence. The photon depth dose distribution is given by [186]:

$$D(z) = D_c \, (e^{-\mu_p z} - \nu e^{\mu_e z}) \quad (5.3)$$

where D_c is a constant, μ_p is the mean attenuation coefficient of primary and high-energy scattered photons, μ_e is the mean attenuation coefficient of the secondary electrons and low-energy secondary photons, and (1-ν) is a factor related to the surface dose. The parameters μ_p and μ_e have been tabulated by Brahme and Svensson [186] for different photon beams at an SSD of 100 cm and for energies up to 45 MeV.

The kernel h(z) in equation 5.1 is obtained by combining equations 5.2-5.3 and considering the following relation between the dose and the fluence distribution:

$$D(z) = \frac{\bar{\mu}}{\rho} \int_0^z \Psi_p(z') \, h(z - z') \, dz' \quad (5.4)$$

The analytical solution of the equation 5.1 and an analytical description of the photon fluence, $\Psi(z)$ can be found in [144] (equation 15).
A comparison between the absorbed dose due to the phantom generated bremsstrahlung from monoenergetic electron beams obtained from equation 5.1 and the MC simulation is also given by [144] and shown in figure 5.1, for energies between 5 and 50 MeV.

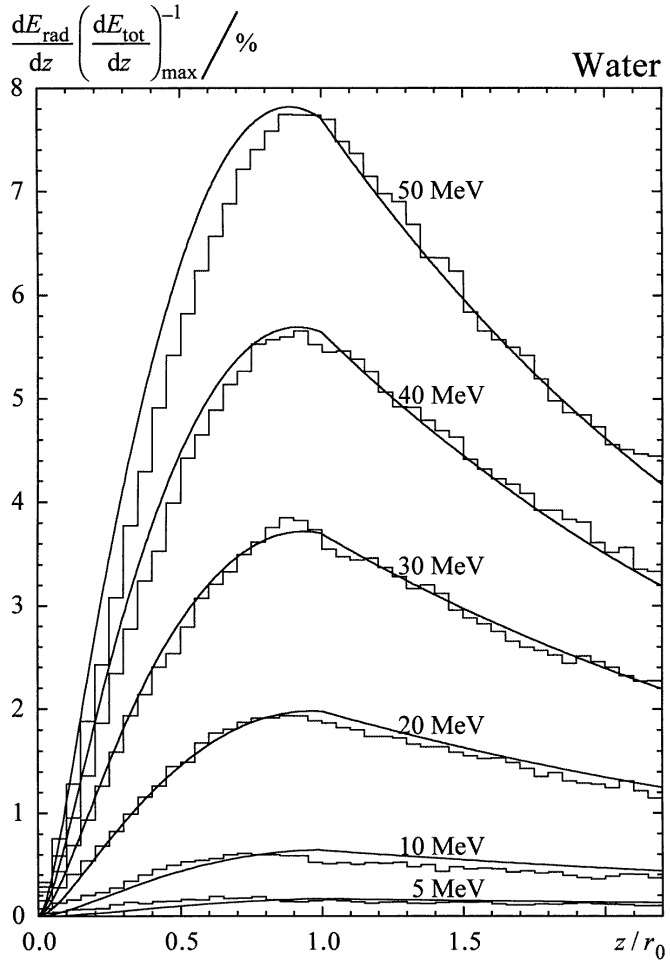

Figure 5.1: Comparison between the absorbed dose due to the phantom generated bremsstrahlung from monoenergetic electron beams obtained from equation 5.1 and from MC simulation for energies between 5 and 50 MeV. Taken from [144].

5.3.2 Analytical description of the phantom generated bremsstrahlung tail

At depths greater than the maximum range of the incident electrons, the tail of the electron depth dose distribution is mainly due to photons generated in the phantom when the system is in pencil beam scanning mode [187] (as can also be seen in figure 5.2). An exponential function with an effective linear attenuation coefficient, $\bar{\mu}_X$, can therefore be used to describe the bremsstrahlung tail generated in a water phantom at large depths [144]:

$$D_X(z) = D_X(r_0)\, e^{-\mu_X(z-r_0)} \tag{5.5}$$

where $D_X(r_0)$ is the photon dose due to bremsstrahlung in the phantom at a depth r_0, corresponding to the depth at which the initial electron energy is zero. $\bar{\mu}_X$ is the same parameter used in equation 5.3 and tabulated in [185].

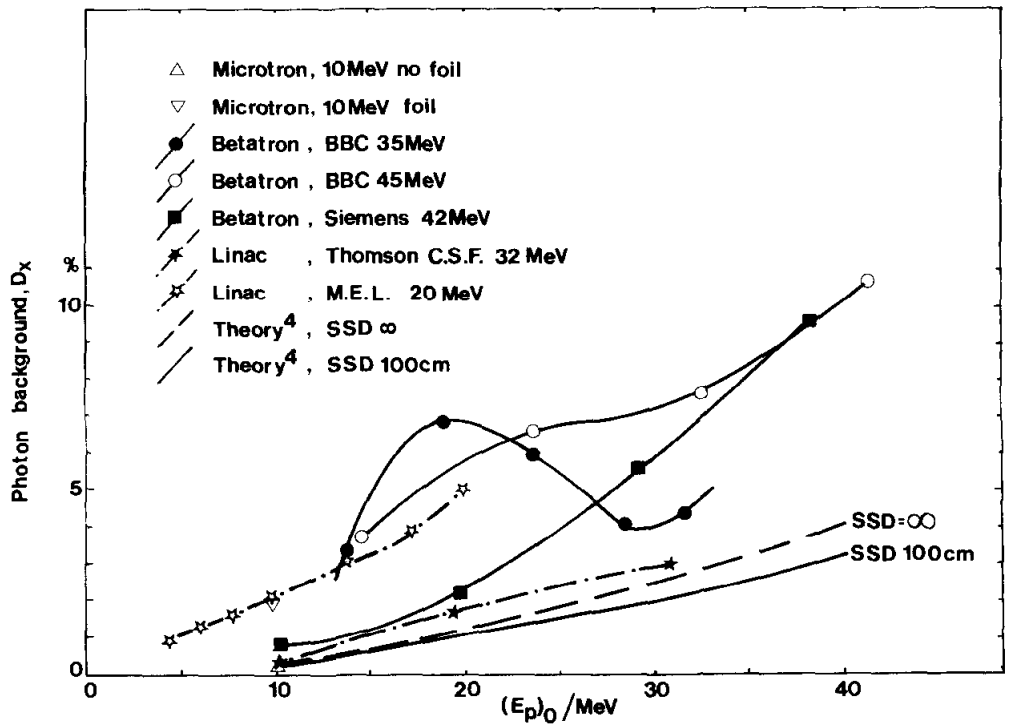

Figure 5.2: Photon background dependence $\%D_X$ as a function of the most probable energy at the phantom surface (analytical and experimental values). Taken from [188].

Figure 5.2 shows the photon background dependence as a function of the most probable energy at the phantom surface for various clinical accelerators. The theoretical curves correspond to the analytical model, in equation 5.5, which includes only the photon contribution from the WT. Therefore, the difference between the experimental and analytical curves corresponds to the fact that the experimental measurements also include the bremsstrahlung contamination from the beamline elements, such as the scattering foils. For the moment, this model has never been extrapolated or tested for VHEEs.

5.4 Analytical models for the bremsstrahlung component in scattering mode

Most clinical accelerators use scattering foils to generate broad beams and their beams have, therefore significant bremsstrahlung contamination, particularly at higher energies. In what follows, an existing model for the scattered electron beam will be tested and adapted to the VHEE beam model proposed earlier. This work was carried out in collaboration with Umberto Deut during his Master internship at the Institut Curie.

5.4.1 Relative photon dose model

In order to quantify the production of bremsstrahlung photons coming from the scattering VHEE system and to quickly estimate the impact of a specific design on the total dose, the analytical formalism proposed by Carver et al. [137] was implemented and tested for clinical (from 6 to 20 MeV) as well as VHEE (from 20 to 200 MeV) beam configurations. In this model, the number of bremsstrahlung photons emitted per unit area at an off-axis distance r and a distance z from the accelerator exit window is given by:

$$\phi_\gamma(z,r,E) = \frac{K_\gamma}{z^2}\sum_{i=1}^{3}\frac{\Delta_{rad,i}(E)}{T_i(E)t_i}\left[E_1\left(\frac{(r/z)^2}{A_{0,i}(E)+T_i(E)t_i}\right) - E_1\left(\frac{(r/z)^2}{A_{0,i}(E)}\right)\right] \quad (5.6)$$

where the summation is made over the scattering elements through which the electron beam passes: the exit window, the primary and the secondary foils. $\Delta E_{rad,i}(E)$ is the radiative energy loss of the i-th scattering element for the energy E, $T_i(E)$ and t_i correspond respectively to the linear scattering power calculated as from the Kainz formulation in equations 2.18,2.22,2.23 and the mean thickness of the i-th scattering element. E_1 is the integral function, and K_γ is a relative proportionality factor. Thus, the $A_{0,i}$ term is the zeroth-order scattering moment of the electron entering the i-th scattering element and can be defined as:

$$A_{0,i}(E) = A_{0,i-1}(E) + T_i(E)t_i \quad (5.7)$$

where $A_{0,0}$ is the moment relative to the 0.0125 cm accelerator exit window, which has been assumed as proposed by [137] since the material and the thickness were kept the same as that proposed in their paper:

$$A_{0,0} = 0.05E^{-1.6} \quad (5.8)$$

The term in parentheses of equation 5.6 can be evaluated for r=0 using a series

expansion to give:

$$\lim_{r\to 0}\left[E_1\left(\frac{(r/z)^2}{A_{0,i}(E)+T_i(E)t_i}\right)-E_1\left(\frac{(r/z)^2}{A_{0,i}(E)}\right)\right]=ln\left(1+\frac{T_i t_i}{A_{0,i}}\right) \tag{5.9}$$

In the implementation of the algorithm, the $\Delta E_{rad}(E)$ radiative energy losses and the collisional energy losses were calculated by calculating the product of the thickness of the scattering element and the stopping power taken from the NIST database for the specific mean energies of the beam (the quoted uncertainty for the reference data are estimated to be around 1%-2% for high energies [189, 190]).

5.4.2 Central axis approximation for the bremsstrahlung dose

The methodology proposed by Carver et al. [137] to estimate the relative photon dose is based on various assumptions and fits the experimental measured data or MC simulated results. In the following, the definitions of the model used are briefly recalled, along with possible differences for a very high energy application. MC simulations were used to propose new parameters of the fit function and extend the parametrization to the VHEE energy range. The bremsstrahlung dose is then expressed as a percentage of the maximum total dose on the central axis (CAX) and can be written as:

$$\%D_{\gamma,CAX}(d=R_p+2,r=0,E)=\frac{D_{\gamma,CAX}(R_p+2,E)}{D_{\gamma,CAX}(R_{100},E)+D_{e,CAX}(R_{100},E)}\ *\ 100 \tag{5.10}$$

where R_p+2 cm is defined as the practical range at which the PDD distribution reaches the lowest dose level (see next sections) and R_{100} corresponds to the depth at which the total dose reaches the maximum. Considering that the X-ray dose component is much smaller than the electron dose component ($D_\gamma(R_{100}) \ll D_e(R_{100})$), equation 5.10 can be approximate as:

$$\%D_{\gamma,CAX}(d=R_p+2,r=0,E)\approx\frac{D_{\gamma,CAX}(R_p+2,E)}{D_{e,CAX}(R_{100},E)}\ *\ 100 \tag{5.11}$$

In its work, Carver et al. [137] assume that the central axis electron dose maximum is proportional to the central-axis electron fluence at the surface of the water phantom and that the central axis photon per cent dose can be calculated by introducing the energy-dependent term X(E), where:

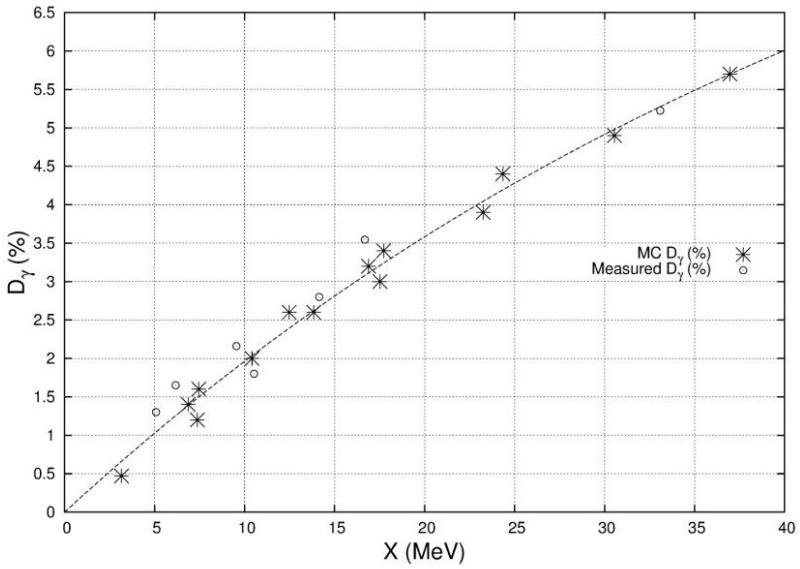

Figure 5.3: $\%D_{\gamma,CAX}$ function 5.13 showing percent doses at d = Rp + 2 cm for electron energies up to 40 MeV (MC-calculated (stars) and measured (circles)). Taken from [137].

$$X(E) = \frac{1}{(SAD + R_p + 2)^2} \left[\frac{\sum_{i=1}^{3} \frac{\Delta E_{rad,i}}{T_i t_i} \, ln(1 + \frac{T_i t_i}{A_{0,i}})}{\Phi_e^p(d = 0, r = 0, E)} \right] \tag{5.12}$$

where SAD is the distance of the source from the isocenter, and the logarithmic term has been obtained using a series expansion around the r=0 point of the term with the exponential integral. The Φ_e^p term is the electron planar fluence per incident electron at the calculation plane (equation 3.7).

The equation used to parameterise the central-axis x-ray percent depth dose calculation is shown in figure 5.3 (up to X(E)=40 MeV) and reported below:

$$\%D_{\gamma,CAX}(d = R_p + 2, E) = aX(E) + b(1 - exp(\ cX(E)\ )) \tag{5.13}$$

The coefficients reported by Carver et al. [137] for energies up to 40 MeV are: $a = -0.035 MeV^{-1}$, b=15.77 % and c=0.016 MeV^{-1}

5.4.3 Off-axis approximation for the bremsstrahlung dose

The work of Carver et al. [137] also proposes a model to approximate the off-axis bremsstrahlung dose. The off-axis percent photon dose is expressed as the

product of the central-axis x-ray percent dose and the off-axis x-ray relative dose profile, as:

$$\%D_{\gamma}(d,r,E) = \frac{D_{\gamma}(SAD+d,r,E)}{D_{\gamma}(SAD+d,0,E)}\ \%D_{\gamma,CAX}(d,E) \tag{5.14}$$

The ratio $D_{\gamma}(SAD+d,r,E)/D_{\gamma}(SAD+d,0,E)$ is calculated using equation 5.6 and equation 5.9 is used for the dose calculation at $r=0$. The central axis x-ray percent depth dose was calculated using equation 5.9 and corrected for the inverse square to depth d:

$$\%D_{\gamma,CAX}(d,E) = \%D_{\gamma,CAX}(R_p+2,E)\ \left(\frac{SAD+R_p+2}{SAD+d}\right)^2 \tag{5.15}$$

5.4.4 Modelling the bremsstrahlung component for the VHEE scattering mode

Based on the analytical model of Carver et al. [137] describing the bremsstrahlung contamination for the scattering mode at low energies, an extension of the model to VHEE was proposed by our group [191]. Monte Carlo simulations were used to propose new parameters of the fit function (equation 5.13) and to extend the parameterisation to the VHEE energy range of the central axis x-ray percent dose at a depth of R_p+2. The new parameters proposed for the 20-200 MeV energy range are [191]:

$$\begin{aligned} a\ (\%MeV^{-1}) &= 0.016 \pm 0.005 \\ b\ (\%) &= 17.28 \pm 1.71 \\ c\ (MeV^{-1}) &= 0.002 \pm 0.001 \end{aligned} \tag{5.16}$$

A parameterisation for the scatterers generated bremsstrahlung tail has also been proposed in the same study [191]. Indeed, as suggested by several authors, [179, 185, 192] and described a previous section 5.4.2 a pencil beam photons depth dose can be described analytically by a (bi)exponential expression (equation 5.3) whose parameters reflect the effective attenuation coefficient for photons and rate of build-up by secondary electrons. In addition, the analytical modelling of the bremsstrahlung component in the pencil beam mode allows for a description of the phantom generated bremsstrahlung tail (equation 5.5). The same modelling has been adapted to describe the bremsstrahlung component coming from the scattering system. Analytical models and optimisation of the parameters were therefore developed in-house using the Matlab computing environment with a standard weighted Chi-square minimization algorithm (Mathworks, US,R2021b). Assuming a decrease of the photon fluence along the central axis with the inverse square of

the depth (as from equation 5.15) and considering the exponential attenuation as for the phantom generated bremsstrahlung component (described in equation 5.5), the dose can be estimated for every depth greater than the practical range, $d \geq R_p + 2$ cm, as:

$$\%D_{\gamma,CAX}(d,E) = \%D_{\gamma,CAX}(R_p{+}2cm,E)\left(\frac{SAD+Rp+2}{SAD+d}\right)^2 e^{-\mu(d-(R_p+2))} \quad (5.17)$$

where R_p is the practical range and the additional 2 cm have been assumed to obtain a photon dose at a sufficient depth to be outside the PDD's fall-off region and at the beginning of the bremsstrahlung tail, thus at the maximum range of the electrons. The μ parameter corresponds to the absorption coefficient of the water assumed to be 0.01813 cm^{-1} (note that this has a negligible variation with energy).

5.5 Secondary dose assessment to the whole patient body

The secondary particle dose delivered to a patient receiving VHEE therapy would be highly dependent on age and size, as well as tumour morphology and location in addition to the beamline configuration and field parameters such as the energy and angular incidence. Methods to accurately estimate the dose delivered to normal tissues of pediatric or adult patients and computational tools to perform a comprehensive comparison of normal tissue dose and risk across different VHEE beams are therefore needed.
For this purpose, an evaluation of the secondary dose to a whole body patient is proposed in the following section, following the same method used to study secondary dose in proton treatments [193]. By applying this method to one of the clinical cases discussed in Chapter 4 (i.e. brain adult), a comparison with proton therapy and VHEE treatments is also proposed with the aim of separating the neutron and photon components, which are in different proportions between these two techniques. For both protons and VHEE, the secondary dose is mainly due to neutral particles, which, in the case of neutrons, can travel several centimetres before interacting. Besides, the neutron dose is highly dependent on the patient's position and distance relative to the nozzle, as well as beam parameters. Therefore, a whole body patient is needed for a proper evaluation of the secondary dose, as normal tissues of interest may be located outside the target volume coverage. To extend the partial patient anatomy to the whole body, the CT scan of the patient is merged with a computational phantom in DICOM format with corresponding age, size and gender, developed by the University of Florida (UF) and the US

National Cancer Institute (NCI) [194]. These phantoms belong to the UFH family of hybrid phantoms of different ages, sizes and both genders and represent the ICRP reference phantoms, including the reference organ masses from ICRP Publication 89 [195], the reference tissue densities and elemental compositions from both ICRP Publication 89 and ICRU Report 46 [196]. The merging procedure was performed using LIFEx freeware [197] and resulted in a whole body image, in which the upper part was composed of the patient's CT and the lower part of the phantom's CT. The phantom with the closest weight and height (Height=165 cm and Weight=50 kg) is then selected from the library and merged with the real patient image. This results in a realistic whole-body patient, as shown in figure 5.4, which shows a sagittal and a coronal view. The image also shows, for example, two structures: the PTV in red and the liver in green. The secondary dose for the VHEE PBS and DS treatment plans (described in tables 4.1-4.2) can then be evaluated and compared with the secondary dose from proton PBS and DS plans. For secondary dose assessment to the OARs, the patient's structures are used to evaluate the average dose to an organ placed in the upper part (corresponding to the CT image) of the full phantom body, and the phantom structures are used for the lower part of the body.

The secondary dose was evaluated using MC simulations. For each field, the resulting dose matrices for both secondary contributions (photons and neutrons) were normalised to the prescribed VHEE dose to the PTV according to the following formula:

$$\frac{D_{sec}}{D_{VHEE}} = \frac{D_{simu,sec}}{N_{simu,sec}} \frac{N_{pr,VHEE}}{D_{pr,VHEE}} \tag{5.18}$$

where $D_{simu,sec}$ is the secondary dose obtained from $N_{simu,sec}$ simulated VHEE histories, and $N_{pr,VHEE}$ is the number of VHEE histories required to obtain the prescribed dose, $D_{pr,VHEE}$. The contribution of each beam was then summed and the total absorbed neutron dose per prescribed dose to the target volume was obtained as a dose $\mathrm{Gy.Gy^{-1}}$ to the various organs.

5.6 Monte Carlo simulations

Geometry

The MC simulation code TOPAS was used to simulate the secondary dose distributions. The geometry of the simulations was already described in Chapter 3 and the source parameters for the PBS simulations are given in table 2.3. To complement our study with a realistic design and to approximately assess the impact of the collimators on the amount of secondary radiation produced, a collimated DS system was also modelled, as shown in figure 3.1b. In most conventional machines,

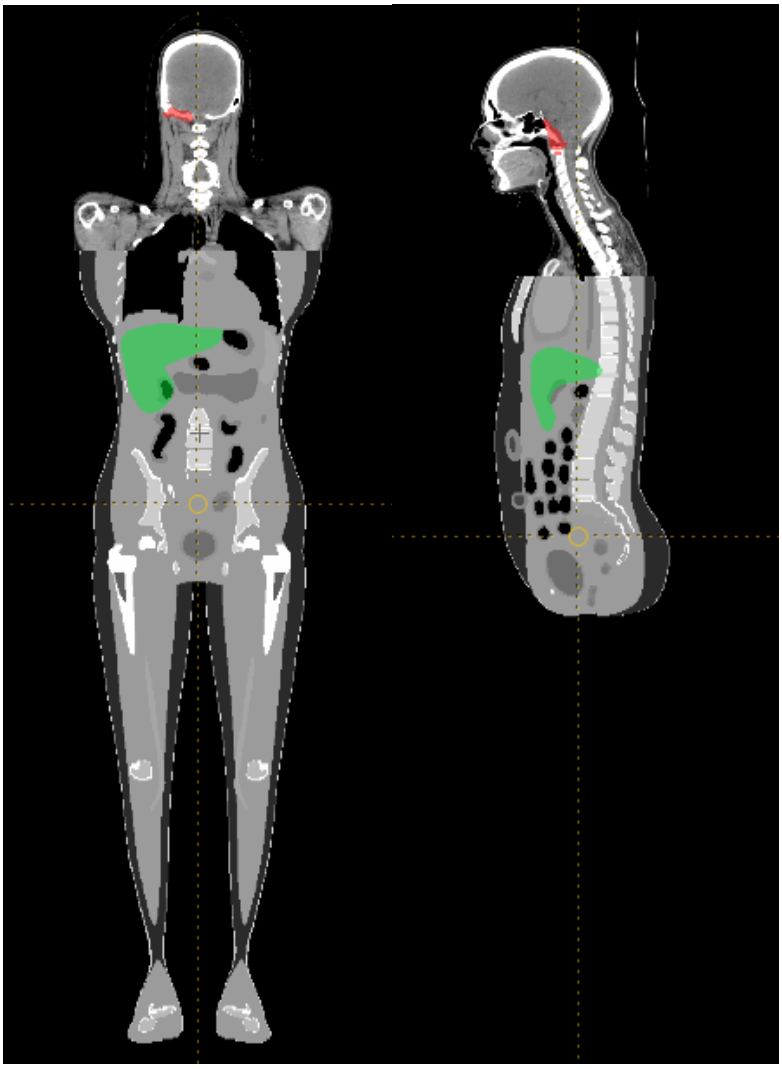

(a) (b)

Figure 5.4: Full-body patient obtained by merging the patient CT and the NCI phantom: (a) coronal and (b) sagittal plans.

two pre-collimation systems are employed, consisting of a primary collimator and moveable jaws in order to reduce radiation leakage outside the field. For this system, a first circular collimator was placed at the exit of the second scatterer, as well as a second circular collimator further in the treatment head at a distance $z_c = 80$ cm from the electron source, both being modelled by 8-cm thick solid tungsten rings. In a second phase, the treatment plans (discussed in Chapter 4) for the whole-body adult brain patient were also simulated. A python script developed previously at CPO converted the treatment plans into TOPAS parameter files

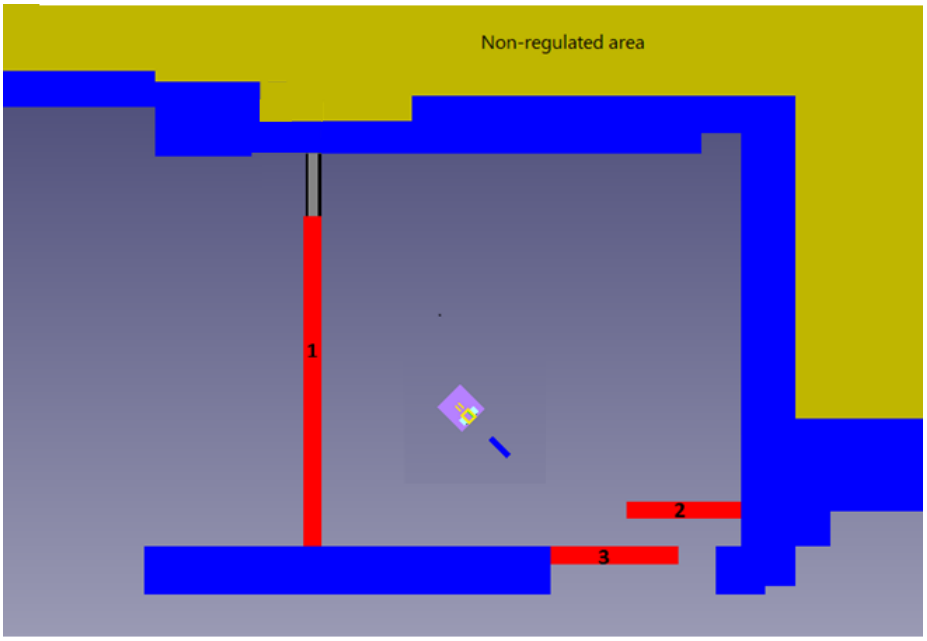

Figure 5.5: TOPAS model of a CPO treatment room: the unregulated zone is in yellow, the walls are in blue and red and an example of a nozzle beamline is shown roughly in the centre of the room.

that were then used to realistically simulate the treatment. Finally and in order to provide an initial assessment of the expected secondary dose produced by VHEE radiotherapy within a treatment room and in adjacent unregulated areas, a realistic model of a CPO treatment room (designed for proton therapy) was performed in TOPAS. No changes were made to the room geometry to test its suitability for a possible VHEE machine. The treatment room modelling is shown in figure 5.5, where non regulated areas (public) are highlighted in yellow. In this figure, the blue elements have a height of 7.91 m, while the red elements have different heights (2.6 m for the element marked with the number 1 and 2.84 m for the elements 2-3). The material used for the walls was 'G4 CONCRETE', as defined in the NIST database [11] with a density of 2.3 g/cm^3. The treatment head (including the nozzle but not the beam transport line or the accelerator), previously described in Chapter 3, was placed in the centre of the room at a height of 1.3 m. A door with a thickness of 43.2 cm and a height of 2.6 m was also introduced, shown in grey in the figure, made of a combination of 35% lead and 65% polyethylene. The VHEE beam with a field size of 10x10 cm^2 and an energy of 200 MeV was delivered to a WT. The energy and field size were chosen to maximise possible bremsstrahlung production. The dose produced in the treatment room and adjacent public areas of the hospital was evaluated and compared with regulatory requirements.

Physics parameters

The gamma and neutron doses were first scored in a WT with a 6×6×6 to 10×10×10 mm^3 grid resolution (the latter was increased according to the source distance, beam size and profile orientation). The TOPAS 'DoseToMedium' scorer was combined with a filter to tally the different particle doses. In particular, 'OnlyIncludeParticleOrAncestorNamed' was used to ensure that the dose evaluation included not only the particles defined in the filter (e.g. neutron or photon) but also the secondary particles they generated. This is because neutral radiation deposits its dose through the secondary charged particles it produces when it interacts (see section 1.2). The previous filter was also combined with another filter to evaluate the analytical model for bremsstrahlung production in the scattering elements (as described in section 5.4). The 'OnlyIncludeParticlesNotFromVolume' filter was combined with the 'OnlyIncludeParticleOrAncestorNamed' filter (in TOPAS a combination of different filters operates as a logical AND) to exclude the photon contribution generated in the water phantom and thus to evaluate the photon dose generated only by the components of the accelerator (for example the two foil scatterers, the exit window and the air, the collimators). The dose distribution recorded in a 60×60×100 cm^3 water phantom was simulated for each geometry using $10^8 - 10^9$ particles to achieve a relative statistical uncertainty of less than 3% (type A, calculated as the average statistical uncertainty of voxels with a dose higher than 50% of the maximum dose). Type B uncertainties (for example to estimate the neutron dose) have been discussed by [183] and estimated to be around 20%. With regard to the clinical case simulations, the 'DoseToMedium' scorer was combined with the 'OnlyIncludeParticlesOfGeneration' filter to estimate the secondary dose. This filter was further combined with the 'OnlyIncludeParticleOrAncestorNamed' filter to separate the photon contribution from the neutron contribution. The resulting dose distributions were normalised to the dose to the PTV due to the VHEE plan (total dose simulation). Finally, the TOPAS 'DoseToMedium' scorer was used for dose assessment in the treatment room. A 2D scoring volume of 30x20 m^2 with a thickness of 50 cm and a grid resolution of 50x50x50 cm^3 was placed at the height of the beamline.

5.7 Results

5.7.1 Depth dose distribution comparisons

Photon dose variation with energy

The simulated depth dose distributions (PDDs) in water obtained for two configurations of the double scattering system without collimators are shown in figure 5.6. For clinical electron beams up to 20 MeV, the difference between the total photon

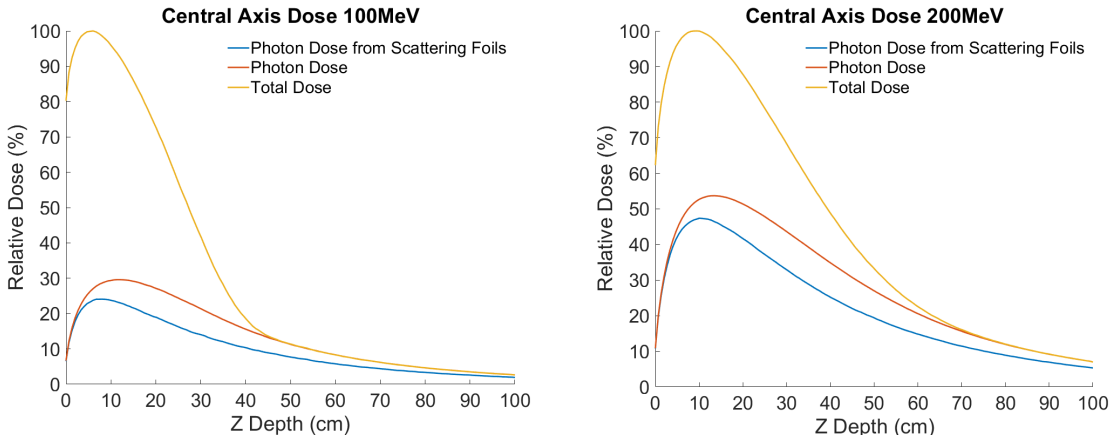

(a) (b)

Figure 5.6: Central-axis percent depth dose distribution in WT from DS MC simulations for 100 and 200 MeV electron beams and for a field of 10 × 10 cm^2. The photon dose contributions are separated into the total photon dose and the photon dose generated only from the scattering system.

dose and the photon dose excluding the photons generated in the water phantom, is typically in the order of a few percent points [185, 188]. For higher energies, the proportion of photons coming from the scatterer is increasingly higher and can reach a maximum of 25% and 45% of the total dose between 100 and 200 MeV, respectively.

Comparison between DS and PBS modes

A comparison of the simulated depth dose curve distribution along the central axis for DS and PBS systems (150 MeV beam energy without collimator) and two field sizes of 5x5 and 10x10 cm^2 is shown in figure 5.7. The photon dose distribution in water obtained with the PBS simulation is significantly smaller than that obtained with the DS technique, since in the PBS mode the photons are only generated in the water phantom. A maximum photon dose of 20% is observed for the PBS technique, with small differences between the two treatment field sizes. In contrast, for the DS technique, the total photon dose at maximum can contribute up to 50% of the total dose, with a significant difference between the various field sizes. In fact, the larger the field size, the thicker the scatterer thicknesses and therefore the higher the proportion of photons produced. Moreover, a significantly more pronounced build-up in the first few centimetres is observed for the DS setup, which could be attributed to the difference in the relative photon contribution between the two techniques as well as to the broader energy spectrum of the electron beam after the interaction with the scatterers.

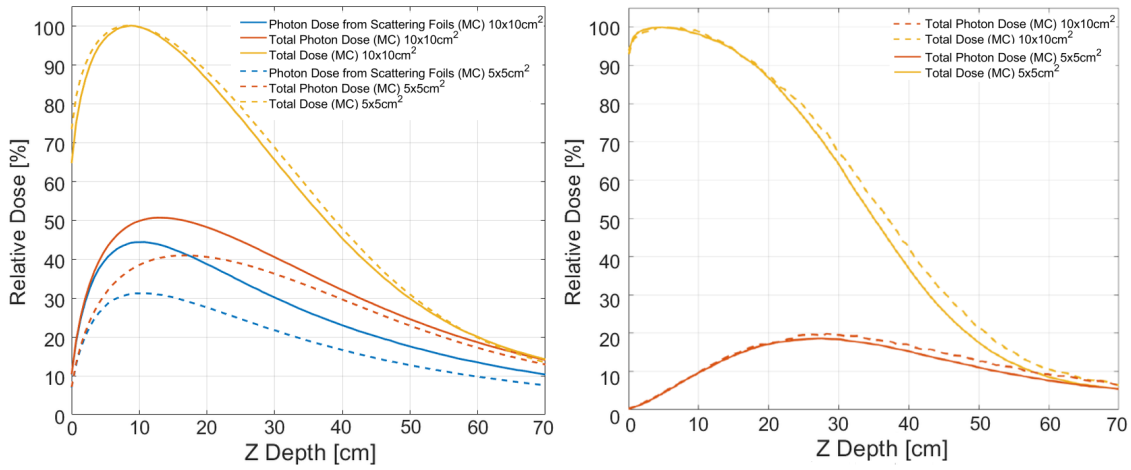

Figure 5.7: Comparison between central-axis PDDs in WT from MC simulations for a 150 MeV electron beam. The two delivery techniques are compared for two field sizes (5×5 cm^2 and 10×10 cm^2). (a) Double scattering technique the relative contribution to the total photon dose or photon dose coming from the scattering system are shown. (b) Pencil beam scanning technique.

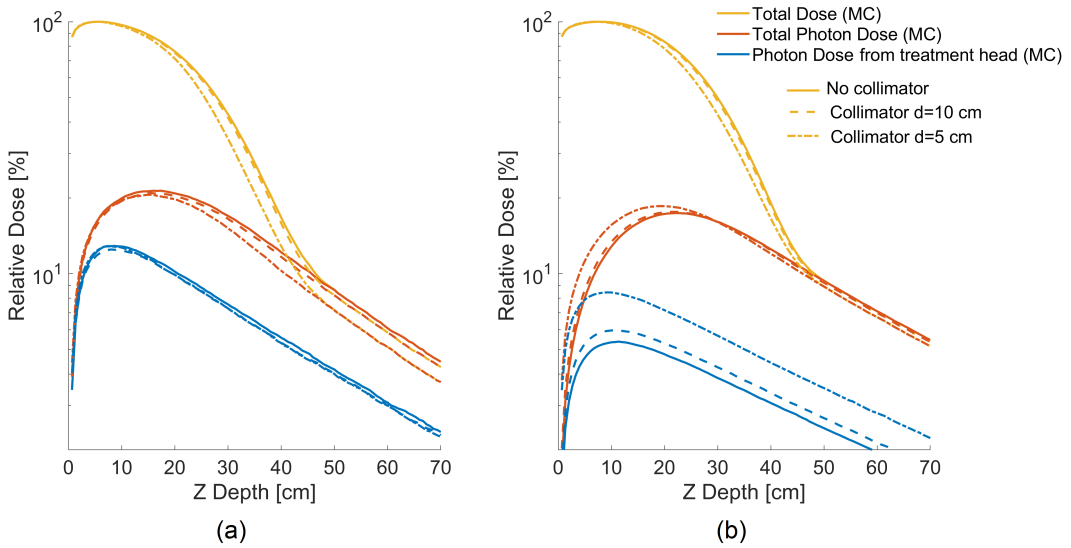

Figure 5.8: Field size dependence of the PDDs in water for a 100 MeV VHEE beam and relative contribution of the photon dose coming from the treatment head to the total photon dose (MC simulations for DS mode) for: (a) central-axis PDDs and (b) integrated PDDs.

Contribution from the treatment head

The simulated percent depth dose (normalised to the value of the dose maximum) and photon dose contribution for the DS technique with and without collimator are shown in figure 5.8. For clarity, only the 100 MeV–10×10 cm^2 configuration is shown. The influence of the second collimator opening on the total bremsstrahlung photon dose is presented for both the central axis and integrated PDDs as the bremsstrahlung is produced predominantly in the forward direction but is also influenced by collimator setting, scatterer geometry, and phantom generated contribution. In particular, the total photon dose component increases by 1.8% at the Rp+2 cm depth (figure 5.8a) while the proportion of photon dose from the treatment head decreases by 1% at the Rp+2 cm depth with increasing field size (figure 5.8b), probably because there is less tungsten (and less scattered photons) in the field and the bremsstrahlung is produced further away from the central axis.

5.7.2 Secondary dose contributions for a clinical case

Figure 5.9 shows the mean secondary dose normalised to the prescribed dose (according to equation 5.18) for selected organs. A comparison is shown for the bremsstrahlung photon (figure 5.9(a)) and neutron contributions (figure 5.9(b)) for the PBS and DS plans of the adult brain case. The plot shows that for the PBS plan the bremsstrahlung contamination for the organs closest to the tumour location is of the order of 10% of the prescribed dose, while for the DS plan it's about 20-40% of the prescribed dose. However, the secondary photon contribution drops rapidly down to $\sim 10^{-5}$ and to $\sim 10^{-4}$ (Gy.Gy^{-1} prescribed to the PTV) for PBS and DS plans, respectively, with distance from the treated zone. A general tendency with increasing distance of the organs with respect to the irradiated target area is also found for the neutron dose contribution, which falls by about one order of magnitude (from 10^{-5} to 10^{-6} Gy.Gy^{-1}) for distant organs as shown in figure 5.10. The figure also shows a comparison between the secondary dose from proton and VHEE plans for both PBS (figure 5.10 on the right) and DS (figure 5.10 on the left) modes. The details for the organs are provided in table 5.1, which gives the secondary dose values due to bremsstrahlung photons and secondary neutrons. A statistical relative uncertainty (type A) of less than 3% was obtained for all the considered organs. The bremsstrahlung mean dose to the PTV ranges from 0.22 Gy.Gy^{-1} and 0.53 Gy.Gy^{-1} for the PBS and DS plans, respectively. The mean doses received by the patient undergoing double scattering irradiation were found to be up to 3.6-fold and 6.8-fold higher for in-field organs for photons and neutrons, respectively. The mean doses to out-of-field organs were up to 5.3-fold and 2.9-fold higher, respectively, compared to the PBS plan. Figure 5.10 shows a comparison of the mean normalised neutron dose for the VHEE-PBS and proton pPBS plans (data for the proton plan are taken from a previous study [193]). Also, an example of the dose distributions in a transverse plan for the proton and VHEE (both PBS and DS) plans is shown in figure 5.11 for the brain adult case.

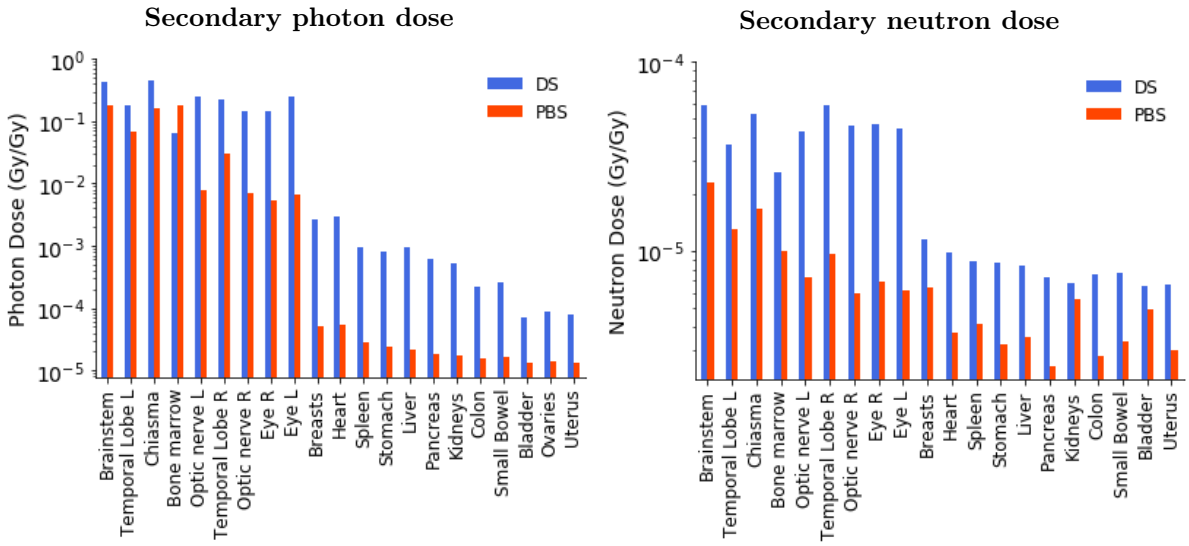

Figure 5.9: Comparison of the secondary dose per prescribed dose between PBS and DS VHEE plans for bremsstrahlung photon (on the left) and neutron contributions (on the right). Abbreviations: R-right, L-left.

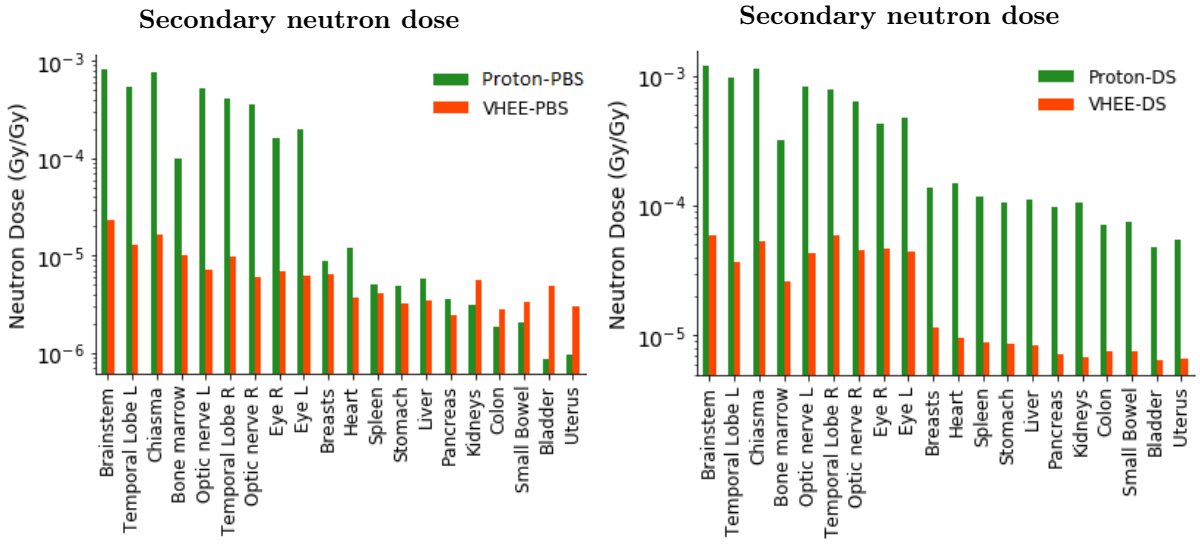

Figure 5.10: Comparison of the secondary neutron dose per prescribed dose between proton and VHEE plans for selected organs brain adult case. On the right: pPBS and VHEE-PBS comparison. On the left: Proton and VHEE DS plans. Abbreviations: R-right, L-left.

Secondary dose per prescribed dose (Gy/Gy)				
	Photon		Neutron	
Organs	PBS	DS	PBS	DS
PTV	2.18E-01	5.29E-01	2.54E-05	6.06E-05
Brainstem	1.84E-01	4.38E-01	2.28E-05	5.88E-05
Temporal Lobe L	6.87E-02	1.78E-01	1.30E-05	3.67E-05
Chiasma	1.64E-01	4.62E-01	1.66E-05	5.29E-05
Bone marrow	1.84E-01	6.54E-02	9.94E-06	2.62E-05
Optic nerve L	7.98E-03	2.53E-01	7.20E-06	4.28E-05
Temporal Lobe R	3.02E-02	2.24E-01	9.67E-06	5.94E-05
Optic nerve R	7.12E-03	1.46E-01	5.95E-06	4.57E-05
Eye R	5.32E-03	1.42E-01	6.91E-06	4.72E-05
Eye L	6.78E-03	2.47E-01	6.17E-06	4.43E-05
Breasts	5.18E-05	2.60E-03	6.37E-06	1.16E-05
Heart	5.44E-05	2.90E-03	3.67E-06	9.73E-06
Spleen	2.88E-05	9.50E-04	4.12E-06	8.77E-06
Stomach	2.41E-05	8.09E-04	3.22E-06	8.73E-06
Liver	2.13E-05	9.29E-04	3.51E-06	8.42E-06
Pancreas	1.81E-05	6.09E-04	2.47E-06	7.22E-06
Kidneys	1.76E-05	5.18E-04	5.56E-06	6.74E-06
Colon	1.52E-05	2.18E-04	2.80E-06	7.56E-06
Small Bowel	1.60E-05	2.55E-04	3.32E-06	7.59E-06
Bladder	1.36E-05	7.10E-05	4.91E-06	6.50E-06
Uterus	1.36E-05	8.09E-05	2.97E-06	6.70E-06

Table 5.1: Comparison of the total absorbed secondary dose per prescribed dose (Gy/Gy) from secondary photon and neutron contributions according to equation 5.18 for the PBS and DS VHEE plans for the adult brain patient. Abbreviations: R-right, L-left.

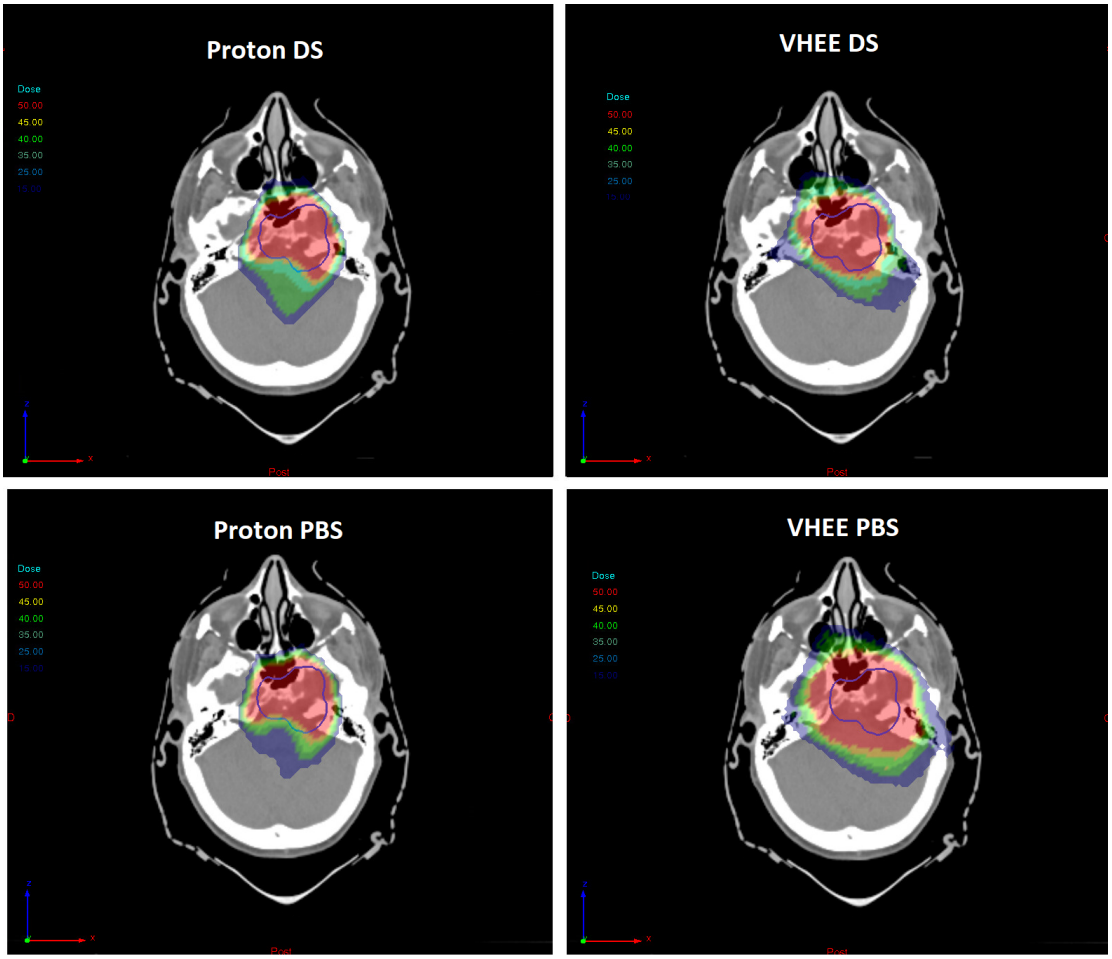

Figure 5.11: Dose distributions of the proton and VHEE (both DS and PBS) plans for the adult brain clinical case (Monte Carlo simulations). PTV in blue.

5.7.3 Evaluation of a conventionally shielded proton treatment room for VHEE radiotherapy

Figure 5.12 shows the DS and PBS dose distributions for the treatment room model used (see figure 5.5). The 200 MeV beamline was simulated and a 10x10 cm^2 field was sent to the WT to maximise the secondary dose production condition in the treatment head and WT. The dose distributions correspond to an absorbed dose of 1 Gy to the WT. Figure 5.12 also shows two different colour bars for the two delivery modes: the blue zones correspond to the zones exceeding the dose of 0.1 μSv for a dose of 1 Gy to the WT, while the red zones correspond to the

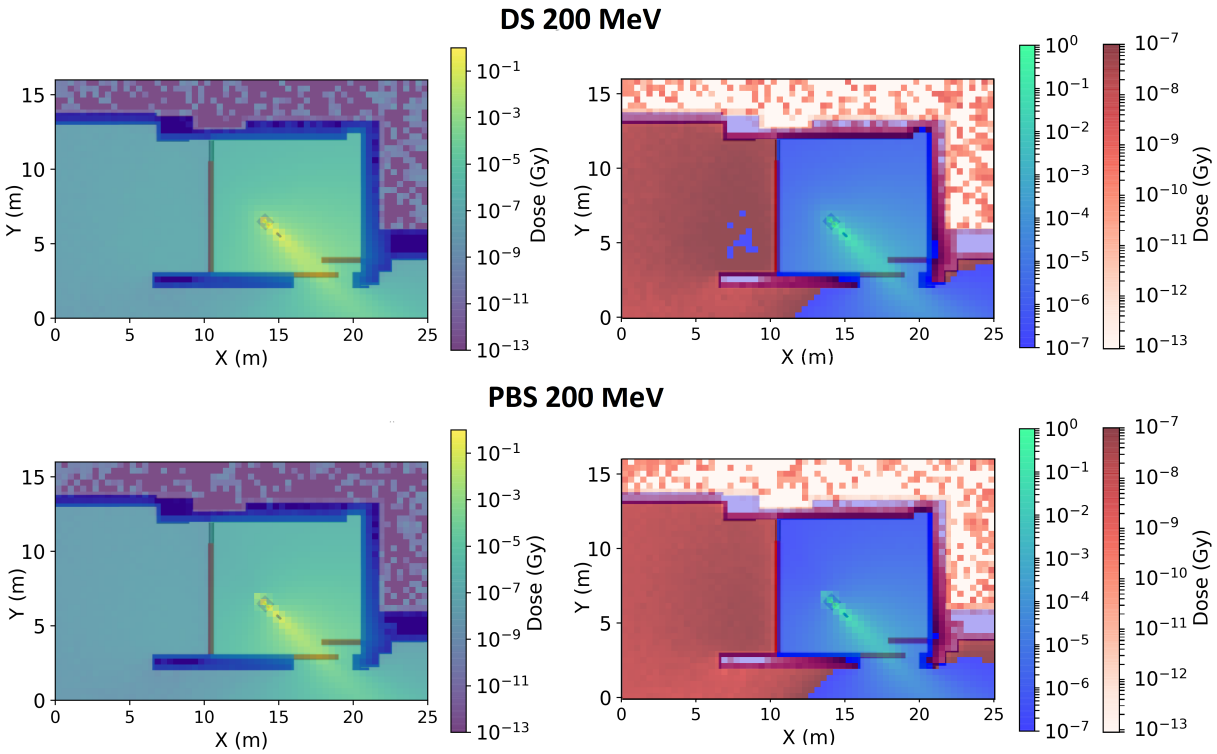

Figure 5.12: Dose distributions in the modelled treatment room for 1 Gy delivered dose to the WT with 200 MeV VHEE (PBS and DS) irradiations with a field size of 10x10 cm^2. For the plot on the right, a second red colour bar is added to separate the zones receiving a dose lower than 0.1 μSv.

zones remaining below this dose threshold. Assuming that 4 patients are typically treated in 1 hour, the regulatory limit of 0.5 $\mu Sv/h$ gives a restriction of 0.125 μSv per patient. The red area in figure 5.12 therefore corresponds to the zone that meets such regulatory limit for uncontrolled (public) areas for 1 Gy delivered dose. For a dose of 1 Gy delivered, the maximum dose to the unregulated area (yellow zone in the figure 5.5) was found to be 2.05x10^{-9} and 1.20x10^{-9} Sv for DS and PBS delivery, respectively. Thus, it is possible to estimate the maximum dose that can be delivered in an hour per patient to the isocenter to comply with the French public area limit of 0.5 $\mu Sv/h$ and for the considered treatment room, namely 61 Gy for the DS mode and 105 Gy for the PBS mode.

5.8 Discussion

For this study, the two VHEE beam production methods were first compared with each other in terms of secondary particle production. However, there are many limitations to this preliminary investigation. The simple nature of the geometry considered in this work for the two techniques suggests that future studies would be required with a more realistic accelerator head to account for a realistic beam shaping with jaws, collimators or applicators in order to guarantee an optimal lateral profile of the electron beam. The model used for pencil beam scanning is also quite simple, though realistic, since few elements are supposed to interact with the beam on this type of beamline (ionisation chambers for dose monitoring are for example missing). The emittance used for the calculations is also based on data for scanned proton beams, which might be a good estimate for preliminary calculations. Numerous studies have already been carried out to quantify and compare the proportions of photons generated in accelerators equipped with electron-beam scattering foils. For example, it has been shown that bremsstrahlung generated in the treatment head generally dominates, but the phantom-generated bremsstrahlung can be as much as 20% of total bremsstrahlung dose for clinical electron energies up to 22 MeV [192]. Besides, it seems that a major contribution to the photon contamination is generated in the scattering foils rather than in the collimators, which is in agreement with our results [198].
With regard to the clinical plan we tested, our simulated results for the secondary particle dose in intracranial treatments demonstrate the advantage of VHEE over proton beams to reduce the out-of-field secondary neutron dose in particular for organs close to the target volume. The orders of magnitude found in the patient are also in agreement with those obtained during the theoretical study in water [191], with neutron doses around 0.01 % of the maximum prescribed dose. The results for the double scattering irradiation are also concordant with those reported in the literature. As with protons, there are differences due to the type of beam shaping, particularly between DS and PBS.
The calculations for the radiation protection study are also very preliminary and there would be various ways of making these estimates. Current regulations on maximum permissible exposure with the concepts of workload, use and occupancy factor were discussed. However, different beamline orientations could also be tested. In particular, shielding problems such as door thickness, shielding material, vault or maze design and geometrical approximations, are all data that will need to be studied to adapt an existing room to this type of machine.

5.9 Conclusion

In this chapter, a preliminary evaluation of the secondary dose production in VHEE radiotherapy has been performed. Also, the bremsstrahlung proportion from the treatment head (scattering foils, collimators of a DS beamline) has been compared with that produced in the irradiated water phantom. The scattering system was found to be the main contributor in terms of secondary photon dose, which is peaked in the forward direction, and dose can be as much as 50% of the total photon dose for the 200 MeV VHEE beam, and depends significantly on the field size defined by the scattering system. For the particular geometry studied, the beam collimators are also a source of photon dose, which increases as the collimator closes down but is significantly smaller than that from the scattering foils. The magnitude of the bremsstrahlung dose for the PBS technique, mostly generated in the water phantom, is twice as small as the total photon dose obtained for the DS technique and varies little with field size.

Chapter 6

Final discussion and conclusion

The work described in this thesis addresses the need for new RT techniques to overcome one of the major limitations of RT in cancer treatment, namely radiation side effects. Among the possible strategies currently being investigated to limit radiation to normal tissues without compromising tumour control are new paradigms in treatment temporal fractionation. In particular, recent studies initiated at Institut Curie have demonstrated the radiobiological advantages of ultra-fast delivery of radiation treatment at dose rates several orders of magnitude higher than those currently used in clinical practice, resulting in efficient tumour inhibition with dramatically less damage to healthy tissue [67]. In addition, VHEEs could be a potential candidate for translating UHDR radiation into the clinic due to their ballistic properties, as well as being little affected by tissue heterogeneities [25]. The feasibility of **combining ultra-high dose rate irradiation with very high energy electrons**, FLASH-VHEE radiotherapy, has therefore been studied during this three-year CIFRE thesis as part of a collaboration between Institut Curie and Thales AVS-MIS.

The first part of the study focuses on a **fast analytical description of the VHEE beam dose distribution in various media**, such as water and different tissues, extending the Fermi-Eyges theory of multiple scattering to the VHEE energy range. The proposed analytical model, compared against Monte Carlo simulations, has however several limitations. In particular, it does not explicitly take into account the bremsstrahlung photon dose. **A second analytical approach was therefore developed in order to model the secondary photon dose for double scattering system** (in Chapter c), while the phantom-generated photon dose is still not tested for the VHEE energy range. A general modelling of the bremsstrahlung dose contribution, including both the contribution coming from the scattering system and that generated in the phantom, will probably be a further step for the translation of VHEE radiotherapy into the clinic, as the secondary photon contributions can account for up to about 50% of the total deposited dose. Comparison with experimental data is also necessary.

The first analytical model was then used to **design an optimised VHEE treatment nozzle for active scanning (PBS) and passive scattering (DS)**. These nozzle geometries were optimised to provide treatment fields of up to 10x10 cm^2 for VHEE irradiation. In addition, a first assessment of the charge requirements for the two techniques to perform VHEE irradiation was proposed. The **beam current requirements for FLASH-VHEE irradiations** to meet the UHDR constraints has also been estimated.

An essential part of the work also focused on the design and evaluation of VHEE treatment plans for possible clinical applications. Four clinical cases were investigated, and **PBS and DS plans were evaluated and compared using MC simulations**. For the PBS mode, the effect of different beam energies on plan quality was investigated. To compare the two techniques, a reference PBS plan (by adapting the beam energies for each field direction) was also compared with the DS plan. For both techniques, the plans were designed taking into account the nozzle characteristics. As the DS scattering system was only optimised for a couple of energies for practical reasons (100 and 150 MeV), only these two energies were considered for the design of the DS clinical plans. A realistic assessment of the dose rate was obtained using the ADR formulation, considering a pulsed beam and realistic scan times (for the PBS case). This allowed us to calculate **the possible FLASH sparing effect using the previously published FMF model**, which resulted in a in a reduction in the mean dose to organs at risk ranging from 5 to 20% depending on the location and parameters used for the model.

Various tests involving the optimisation of beam energies, or the beam model as for example investigating the possibility of focusing the beam, as suggested in a recent study [50], were then performed. This was made possible **using the matRad TPS tool [170], where the analytical model describing the PBS-VHEE beam was introduced and tested** using two PBS treatment plans. The matRad tool could also be used to optimise PBS treatment plans by automatically changing the weights of the spots. Such algorithms therefore improve the quality of the VHEE plans in terms of target homogeneity and dose to the OARs, compared to the first plans tested in this study. In addition, a simultaneous optimisation of dose and dose rate distributions could be used to design FLASH-VHEE plans, which will be the subject of a later development. For example, the placement of the pencil beams could be investigated to find an optimal path which could reduce the treatment duration and thus increase the dose rate. Furthermore, an increased dose rate can also be obtained by reducing the number of spots, for example using "pencil beam resampling" algorithms, as already proposed for proton irradiation [146]. Finally, a FLASH sparing quantification (through dose rate analysis) could be directly introduced into the optimisation model.

Secondary dose assessment is another important part of the study. An **initial assessment of the secondary dose from VHEE irradiation was performed**. The dose to the public area surrounding a possible treatment room located at the Institut Curie proton therapy centre was assessed and the maximum dose that could be delivered to meet regulatory limits was determined. The **secondary dose from bremsstrahlung photons and neutrons to a patient's organs at risk was also assessed for a clinical case**. However, further studies are needed to assess the secondary dose from VHEE treatments to the patient's healthy tissues and, more generally, in a clinical environment. A multi-patient study is needed to estimate the secondary dose to various organs at risk, from bremsstrahlung photons or neutrons. Although in this study a decreasing trend of the secondary dose with distance from the treatment volume was observed for the clinical case considered, a general trend could be verified, as for the case of proton therapy [199]. An age-dependent effect was also observed for the secondary neutron dose in proton therapy and could be investigated for VHEE considering patients of different ages. Finally, the TVLs for the bremsstrahlung photons produced by VHEEs would be required to assess whether conventional vault shielding is sufficient for VHEE beams.

Another consideration involves the combination of temporal and spatial fractionation, which could be investigated. Indeed, Spatially Fractionated Radiotherapy (SFRT), which is based on spatial fractionation of the dose, also appears to induce a distinct tissue response, resulting in a remarkable gain in normal tissue sparing, together with a relatively high efficacy in tumour control [200]. The combination of FLASH and SFRT could be a winning alliance, as proposed in [201] and [175], as it could benefit from the use of VHEE to reach deep-seated tumours, although FLASH and SFRT are probably based on different mechanisms.

In conclusion, the aim of this thesis was to contribute to the development of FLASH-VHEE systems as a new RT technique. Specifically, the requirements for future machine parameters and design (in terms of beam charge and current) and the potential of FLASH-VHEE radiotherapy for a few representative clinical cases or conditions were proposed.

List of contributions by the author

This chapter presents the publications and scientific communications derived from the work performed in this PhD thesis.

Publications in peer-reviewed journals

MG Ronga, U Deut, F Gesualdi, A Bonfrate, M Sitarz, A Patriarca, E Jouglar, R Ferrand, G Créhange, I Buvat, P Girault, L De Marzi, Conformation techniques for ultra-high dose rate very high energy electrons (VHEE) radiation therapy, submitted to Medical Physics

M Sitarz, **MG Ronga**, F Gesualdi, A Bonfrate, N Wahl, L De Marzi, Implementation and validation of Very High Energy Electron model in matRad treatment planning system, submitted to Medical Physics

MG Ronga, U Deut, A Bonfrate, L De Marzi, Very high-energy electron dose calculation using multiple scattering theory and a simplified pencil beam model. Medical Physics, 2023;1-14: https://doi.org/10.1002/mp.16697, (2023)

U Deut, **MG Ronga**, A Bonfrate, L De Marzi, Secondary radiation dose modeling in passive scattering and pencil beam scanning very high energy electron (VHEE) radiation therapy. Medical Physics, 50(7), 4491–4504, https://doi.org/10.1002/mp.16443, (2023)

AMM Leite, M Cavallone, **MG Ronga**, F Trompier, A Patriarca and L De Marzi, Ion recombination correction factors and benchmark of detectors in a very-high dose rate proton scanning beam. Physica Medica, 106:102518, doi: 10.1016/j.ejmp.2022.102518. (2023)

AMM Leite, **MG Ronga**, M Giorgi, Y Ristic, Y Perrot, F Trompier, Y Prezado, G Créhange, L De Marzi, Secondary neutron dose contribution from pencil beam scanning, scattered and spatially fractionated proton therapy. Physics in medicine and biology, 24;66(22), doi: 10.1088/1361-6560/ac3209.(2021)

MG Ronga, M Cavallone, A Patriarca, AMM Leite, P Loap, V Favaudon, G

Créhange, L De Marzi. Back to the Future: Very High-Energy Electrons (VHEEs) and Their Potential Application in Radiation Therapy. Cancers, 13(19):4942, doi: 10.3390/cancers13194942 (2021)

Presentations at international conferences

MG Ronga, A Bonfrate, U Deut, P Girault, L De Marzi Conformation techniques for FLASH-VHEE radiation therapy , Flash Radiotherapy and Particle Therapy (FRPT) conference, Barcelona, oral poster, (02/12/2022).

MG Ronga, L Martelli, A Panchal, A Bonfrate, F Trompier, E Bayart, A Flacco & L De Marzi Experimental characterisation of an ultra-high dose rate laser plasma accelerated VHEE beam , Flash Radiotherapy and Particle Therapy (FRPT) conference, Barcelona, Oral communication, (02/12/2022).

Résumé du travail de thèse en français

Contexte et enjeu

Le développement de méthodes innovantes susceptibles de réduire la sensibilité des tissus sains aux radiations, tout en maintenant l'efficacité du traitement sur la tumeur, est un aspect central de l'amélioration de l'efficacité de la radiothérapie pour le traitement du cancer. La radiothérapie repose sur un équilibre délicat entre atteindre le contrôle de la tumeur et limiter les complications graves pour les tissus sains. Parmi les avancées et innovations méthodologiques possibles pour réduire la sensibilité des tissus sains à l'irradiation tout en maintenant l'efficacité du traitement, la combinaison d'une irradiation à ultra-haut débit de dose (FLASH) et des électrons de très haute énergie (VHEE) est une perspective très intéressante. L'association de ces deux techniques permettrait, en utilisant les caractéristiques balistiques des VHEE, d'exploiter les avantages radiobiologiques de l'effet FLASH sur le traitement des tumeurs profondes. La radiothérapie par VHEE, proposée pour la première fois dans les années 2000, est peu affectée par les hétérogénéités tissulaires (contrairement aux électrons ou photons de basse énergie), et pourrait s'appliquer à un grand nombre de localisations anatomiques. De plus, les VHEEs sont particulièrement intéressants d'un point de vue balistique et biologique dans le cadre des irradiations FLASH, au cours desquelles une dose élevée est administrée aux tissus en un temps extrêmement court. Cette méthode permet de réduire simultanément l'apparition et la gravité des complications précoces et tardives affectant les tissus sains, tout en maintenant l'efficacité du traitement. Bien que prometteuse, plusieurs aspects de la radiothérapie FLASH par VHEE (FLASH-VHEE) doivent être étudiées avant qu'elle puisse être employée dans un contexte clinique.

Dans ce contexte, les travaux présentés dans cette thèse de doctorat ont été réalisés au cours d'une thèse CIFRE de trois ans dans le cadre d'une collaboration entre l'Institut Curie et Thales AVS-MIS. L'objectif principal de cette thèse est d'évaluer l'utilisation possible des VHEEs en radiothérapie et en particulier leur utilisation à ultra-haut débit de dose pour contribuer au développement de la radiothérapie FLASH-VHEE.

Plus précisément, un modèle analytique de calcul de la dose basé sur la théorie de la diffusion multiple de Fermi-Eyges a été étendue à la gamme d'énergie des VHEE. Ce modèle, en combinaison avec des simulations MC, a été ensuite exploité pour évaluer la possible adaptation des méthodes de conformation conventionnelles du faisceau de particules pour la thérapie avec VHEE. Il a également été utilisé pour obtenir une première estimation des spécifications nécessaires pour une future machine qui répondrait aux contraintes des irradiations FLASH avec VHEE.

Le potentiel de la radiothérapie FLASH-VHEE pour quelques cas cliniques représentatifs a été aussi évalué. Quatre plans cliniques, correspondant à des différentes localisations anatomiques, ont été étudiés. L'impact de l'énergie du faisceau sur la qualité du plan a été évalué. Les différentes techniques de conformation ont été comparées entre elles et l'épargne possible des tissues saines dues à l'effet FLASH a aussi été évaluée.

Enfin, l'estimation des doses liées aux particules secondaires et les questions de radioprotection ont été abordées. La dose secondaire due aux photons de Bremsstrahlung et aux neutrons provenant des deux systèmes de conformation de la dose a été évaluée. La dose due aux particules secondaires reçues par divers organes a également été évaluée dans le cadre de traitements intracrâniens et afin de démontrer l'avantage des faisceaux VHEE par rapport aux faisceaux de protons en terme de dose neutrons hors champ.

Principaux résultats

Modèle analytique pour le calcul de la dose de VHEE

La première partie des travaux décrits dans cette thèse se concentre sur une description analytique de la distribution de dose du faisceau VHEE dans divers milieux, tels que l'eau et différents tissus. À cette fin, la théorie de Fermi-Eyges de la diffusion multiple, utilisée pour décrire la diffusion des électrons à basse énergie (jusqu'à 50 MeV), a été étendue à la gamme d'énergie des VHEE. Le modèle de Fermi-Eyges décrit la fluence d'un faisceau étroit d'électrons passant à travers une feuille de diffusion. La fluence est approximée à l'aide d'une fonction gaussienne pour la distribution radiale et angulaire du faisceau. Le modèle, qui prend aussi en compte la perte d'énergie du faisceau dans le milieu et la dispersion des électrons, a été adapté aux énergies des VHEE et testé par rapport à des simulations Monte-Carlo (MC).

Une concordance satisfaisante a été obtenue entre les distributions de dose obtenues avec le modèle analytique et celles produites par les simulations Monte-Carlo dans l'eau pour la gamme d'énergie 100-200 MeV. Cependant, le modèle ne prend en compte que la dose déposée par le faisceau d'électrons primaires. La contribution secondaire à la dose peut en effet être négligée dans le cas d'électrons

de faible énergie. En revanche, dans le cas des VHEE, la contribution due aux photons secondaires ne peut plus être négligée, étant donné qu'elle peut représenter jusqu'à environ 50 % de la dose totale déposée. Pour améliorer encore la méthode, il est donc nécessaire d'intégrer un modèle capable de déterminer la contribution des photons de bremsstrahlung à la dose totale déposée.

Une deuxième approche analytique a été développée afin de modéliser la dose de photons secondaires pour un système à double diffusion. Cependant, la dose des photons générés par le fantôme n'a toujours pas été évaluée pour la gamme d'énergie des VHEEs. Une modélisation générale de la dose déposée par bremsstrahlung, comprenant la contribution provenant du système de diffusion et celle générée dans le fantôme, constitue probablement une étape supplémentaire avant l'application clinique de la radiothérapie par VHEE. Une comparaison avec les données expérimentales est également nécessaire.

Techniques de conformation pour la radiothérapie FLASH avec VHEE

Une fois le modèle analytique optimisé pour les énergies des VHEE, il a été utilisé pour étudier l'adaptabilité des techniques de conformation de la dose dans le cas d'irradiations FLASH avec VHEE. En radiothérapie la plupart des faisceaux cliniques peuvent être décrits comme des petits faisceaux sortant d'un accélérateur, qui sont ensuite convertis en un faisceau large soit grâce à un système de balayage (Pencil Beam Scanning ou PBS) soit grâce à un système de double diffusion (Double Scattering ou DS). Le système DS utilise généralement une ou deux feuilles pour obtenir une distribution homogène de la dose adaptée à la dimension latérale de la tumeur. Le balayage magnétique de petits faisceaux permet de lui traiter des tumeurs dont la conformation 3D est améliorée. Plusieurs méthodes pour optimiser la conception de ces lignes de faisceaux ont déjà été suggérées pour la thérapie FLASH, mais ces modalités n'ont pas été étudiées de manière approfondie pour les VHEE à très haut débit de dose.

L'un des objectifs de cette étude était donc d'évaluer la possibilité d'adapter les méthodes de conformation conventionnelles aux VHEEs et de quantifier le nombre absolu d'électrons ainsi que le débit de dose requis pour utiliser le faisceau d'électrons élargi dans le domaine d'application de la thérapie FLASH. Le modèle analytique optimisé pour les VHEE a été utilisé pour concevoir un système DS pour les faisceaux d'électrons, et des simulations MC ont été réalisées pour valider les calculs analytiques. Les simulations ont aussi permis une première évaluation des charges nécessaires pour les deux techniques afin d'obtenir des champs de traitement VHEE allant jusqu'à 10x10 cm^2. Les courants de faisceau nécessaires pour répondre aux contraintes de l'UHDR dans les cas d'irradiations FLASH-VHEE ont aussi été évalués. Les résultats préliminaires obtenus lors de cette étude pourront servir de base à l'amélioration de la conception des futures machines VHEE.

Planification du traitement avec les faisceaux VHEE

Une partie essentielle du travail de thèse a également porté sur la conception et l'évaluation des plans de traitement avec des faisceaux VHEE. Quatre cas cliniques ont été étudiés. Leurs plans de traitement en PBS et DS ont été évalués et comparés à l'aide de simulations MC. Pour le mode PBS, l'effet de l'énergie du faisceau sur la qualité du plan a été étudié. Pour comparer les deux techniques, un plan PBS de référence a également été comparé au plan DS. Le système de diffusion DS a été optimisé pour deux énergies (100 et 150 MeV), donc seules ces deux énergies ont été prises en compte pour la conception des plans DS.

Une évaluation réaliste du débit de dose a été obtenue en utilisant la formulation du débit de dose moyen (Average Dose Rate ou ADR). Pour la modalité DS, le calcul de l'ADR a été réalisé en utilisant un faisceau pulsé avec des temps de balayages réalistes. L'épargne des tissus sains liée à l'effet FLASH a donc été évalué en utilisant le facteur de modification FLASH (FLASH Modifying Factor ou FMF). La réduction de la dose moyenne aux organes à risque a été évaluée allant de 5 à 20 %, en fonction de l'emplacement et des paramètres utilisés pour le modèle.

Le modèle analytique décrivant le faisceau PBS VHEE a été introduit et testé dans le logiciel de planification de plans de traitement matRad. Cet outil a permis d'effectuer plusieurs tests, comme par exemple l'étude de faisabilité pour la focalisation du faisceau. MatRad a également été utilisé pour optimiser les plans de traitement PBS en ajustant automatiquement les poids des spots. Cela a permis d'améliorer la qualité des plans VHEE en réduisant la dose reçue par les organes à risque comparativement aux premiers plans testés dans cette étude. En outre, une optimisation simultanée des distributions de dose et de débit de dose pourrait être utilisée pour la conception des plans FLASH-VHEE. Par exemple, en mode PBS, les emplacements des spots du faisceau pourrait être optimisés afin de réduire la durée du traitement et d'augmenter le débit de dose. Enfin, une quantification de l'épargne des tissus sains grâce à l'effet FLASH (par l'analyse du débit de dose) pourrait être directement introduite dans le modèle d'optimisation.

Rayonnement secondaire dans la radiothérapie avec VHEE

Un autre aspect crucial à considérer lors de la mise en pratique de la radiothérapie avec VHEE est le rayonnement secondaire produit. En effet, la dose secondaire, et en particulier les composantes bremsstrahlung et neutron générées dans la tête d'irradiation ou dans les tissus, doit être prise en compte dans le calcul du dépôt d'énergie.

Une première évaluation de la dose secondaire due aux VHEEs a donc été

proposée. La dose reçue par la zone publique entourant une éventuelle salle de traitement de l'Institut Curie a également été évaluée et la dose maximale qui peut être délivrée pour respecter les limites réglementaires a été déterminée. En outre, la proportion de bremsstrahlung provenant de la tête de traitement (feuilles de diffusion, collimateurs d'une ligne de faisceaux DS) a été comparée à celle produite dans un fantôme d'eau irradié. Il a été remarqué que le système de diffusion est le principal contributeur en termes de dose de photons secondaires. Sa contribution peut représenter jusqu'à 50 % de la dose totale de photons pour le faisceau VHEE de 200 MeV et elle dépend de manière significative de la taille du champ. La dose de bremsstrahlung pour la technique PBS, principalement générée dans le fantôme d'eau, s'est avérée deux fois plus faible que la dose totale de photons obtenue pour la technique DS et varie peu en fonction de la taille du champ.

La dose secondaire de photons et de neutrons de Bremsstrahlung aux organes à risque d'un patient a également été évaluée pour un cas clinique. Une diminution de la dose secondaire en fonction de la distance par rapport au volume de traitement a été constatée. Cependant, seule une étude plus approfondie avec plus de cas cliniques permettrait de vérifier si c'est une tendance générale, comme dans le cas de la protonthérapie. D'autres études sont aussi nécessaires pour évaluer la dose secondaire des traitements par VHEE aux tissus sains du patient et, plus généralement, dans un environnement clinique.

Conclusions

Les travaux réalisés au cours de cette thèse ont permis de contribuer au développement des systèmes FLASH-VHEE en tant que nouvelle technique de radiothérapie. Plus précisément, les exigences en matière de charge et de courant de faisceau pour une future machine qui pourrait délivrer des VHEEs en mode FLASH ont été étudiées. En outre, le potentiel de la radiothérapie FLASH-VHEE pour quelques cas cliniques représentatifs a été évalué. Enfin, une première évaluation de la dose secondaire liée à la radiothérapie avec VHEEs a été réalisée.
En conclusion, la radiothérapie FLASH-VHEE s'avère être une technique prometteuse pour le traitement des tumeurs profondes qui permettra de réduire les effets secondaires liés à la radiothérapie sur les tissus sains.

List of Figures

List of Tables

Bibliography

[1] M. Abdel-Wahab, S. S. Gondhowiardjo, A. A. Rosa, Y. Lievens, N. El-Haj, J. A. Polo Rubio, G. B. Prajogi, H. Helgadottir, E. Zubizarreta, A. Meghzifene, V. Ashraf, S. Hahn, T. Williams, and M. Gospodarowicz, "Global Radiotherapy: Current Status and Future Directions—White Paper," *JCO Global Oncology*, pp. 827–842, Dec. 2021. Publisher: Wolters Kluwer.

[2] Office for National Statistics, "Cancer survival in England: adult, stage at diagnosis and childhood - patients followed up to 2018," 2019.

[3] E. B. Podgorsak and I. Atomenergie-Organisation, eds., *Radiation oncology physics: a handbook for teachers and students*. No. 1196 in STI/PUB, Vienna: International Atomic Energy Agency, 2005.

[4] International Commission on Radiation Units and Measurements, "Report 85: Fundamental quantities and units for ionizing radiation," *Journal of the ICRU*, vol. 11, pp. 1–31, Apr. 2011.

[5] "Quantities used in radiological protection," *Annals of the ICRP*, vol. 21, pp. 4–11, Jan. 1991.

[6] T. Pawlicki, D. J. Scanderbeg, and G. Starkschall, eds., *Hendee's Radiation Therapy Physics*. Wiley, 1 ed., Apr. 2016.

[7] J. Deasy, "ICRU Report 49, Stopping Powers and Ranges for Protons and Alph Particles," *Medical Physics*, vol. 21, pp. 709–710, May 1994.

[8] E. B. Podgorsak, *Radiation Physics for Medical Physicists*. Springer, Nov. 2016. Google-Books-ID: lwpwDQAAQBAJ.

[9] I. C. on Radiation Units and Measurements, eds., *Stopping powers for electrons and positrons*. No. 37 in ICRU report, Bethesda, Md., U.S.A: International Commission on Radiation Units and Measurements, 1984.

[10] G. F. Knoll, *Radiation detection and measurement*. Hoboken, N.J: John Wiley, 4th ed ed., 2010. OCLC: ocn612350364.

[11] S. Seltzer, "Stopping-Powers and Range Tables for Electrons, Protons, and Helium Ions, NIST Standard Reference Database 124," 1993.

[12] K. Olive, "Review of Particle Physics," *Chinese Physics C*, vol. 40, p. 100001, Oct. 2016.

[13] K. Koka, A. Verma, B. S. Dwarakanath, and R. V. L. Papineni, "Technological Advancements in External Beam Radiation Therapy (EBRT): An Indispensable Tool for Cancer Treatment," *Cancer Management and Research*, vol. 14, pp. 1421–1429, Apr. 2022.

[14] O. Kandemir Gursel, "Recent Technological Advances in Radiotherapy," *European Archives of Medical Research*, vol. 34, pp. 55–60, Dec. 2018.

[15] J. Osborn, "Is VMAT beneficial for patients undergoing radiotherapy to the head and neck?," *Radiography (London, England: 1995)*, vol. 23, pp. 73–76, Feb. 2017.

[16] A. Kaiser, J. G. Eley, N. E. Onyeuku, S. R. Rice, C. C. Wright, N. E. McGovern, M. Sank, M. Zhu, Z. Vujaskovic, C. B. Simone 2Nd, and A. Hussain, "Proton Therapy Delivery and Its Clinical Application in Select Solid Tumor Malignancies," *Journal of Visualized Experiments*, p. 58372, Feb. 2019.

[17] K. R. Hogstrom and P. R. Almond, "Review of electron beam therapy physics," *Physics in Medicine & Biology*, vol. 51, p. R455, June 2006.

[18] A. Pilar, M. Gupta, S. Ghosh Laskar, and S. Laskar, "Intraoperative radiotherapy: review of techniques and results," *Ecancermedicalscience*, vol. 11, p. 750, 2017.

[19] R. Mohan and D. Grosshans, "Proton Therapy – Present and Future," *Advanced drug delivery reviews*, vol. 109, pp. 26–44, Jan. 2017.

[20] U. Amaldi and G. Kraft, "Radiotherapy with beams of carbon ions," *Reports on Progress in Physics*, vol. 68, pp. 1861–1882, Aug. 2005.

[21] "PTCOG - Facilities in Operation."

[22] H. Paganetti, *Proton Beam Therapy*. IOP Publishing, Jan. 2017.

[23] C. DesRosiers, V. Moskvin, A. F. Bielajew, and L. Papiez, "150-250 meV electron beams in radiation therapy," vol. 45, no. 7, pp. 1781–1805.

[24] L. Papiez, C. DesRosiers, and V. Moskvin, "Very high energy electrons (50-250 MeV) and radiation therapy," vol. 1, no. 2, pp. 105–110.

[25] A. Lagzda, D. Angal-Kalinin, J. Jones, A. Aitkenhead, K. J. Kirkby, R. MacKay, M. Van Herk, W. Farabolini, S. Zeeshan, and R. M. Jones, "Influence of heterogeneous media on very high energy electron (VHEE) dose penetration and a monte carlo-based comparison with existing radiotherapy modalities," vol. 482, pp. 70–81.

[26] S. Mueller, M. K. Fix, D. Henzen, D. Frei, D. Frauchiger, K. Loessl, M. F. M. Stampanoni, and P. Manser, "Electron beam collimation with a photon MLC for standard electron treatments," *Physics in Medicine & Biology*, vol. 63, p. 025017, Jan. 2018. Publisher: IOP Publishing.

[27] M. C. Lee, S. B. Jiang, and C.-M. Ma, "Monte Carlo and experimental investigations of multileaf collimated electron beams for modulated electron radiation therapy," *Medical Physics*, vol. 27, no. 12, pp. 2708–2718, 2000. _eprint: https://onlinelibrary.wiley.com/doi/pdf/10.1118/1.1328082.

[28] A. Rodrigues, F.-F. Yin, and Q. Wu, "Dynamic electron arc radiotherapy (DEAR): a feasibility study," *Physics in Medicine & Biology*, vol. 59, p. 327, Dec. 2013. Publisher: IOP Publishing.

[29] E. W. Korevaar, H. Huizenga, J. Löf, J. C. Stroom, J. W. H. Leer, and A. Brahme, "Investigation of the added value of high-energy electrons in intensity-modulated radiotherapy: four clinical cases," *International Journal of Radiation Oncology, Biology, Physics*, vol. 52, pp. 236–253, Jan. 2002. Publisher: Elsevier.

[30] I. J. Chetty, B. Curran, J. E. Cygler, J. J. DeMarco, G. Ezzell, B. A. Faddegon, I. Kawrakow, P. J. Keall, H. Liu, C.-M. C. Ma, D. W. O. Rogers, J. Seuntjens, D. Sheikh-Bagheri, and J. V. Siebers, "Report of the AAPM Task Group No. 105: Issues associated with clinical implementation of Monte Carlo-based photon and electron external beam treatment planning," *Medical Physics*, vol. 34, no. 12, pp. 4818–4853, 2007. _eprint: https://onlinelibrary.wiley.com/doi/pdf/10.1118/1.2795842.

[31] C. M. DesRosiers, "An evaluation of very high energy electron beams (up to 250 MeV) in radiation therapy," *Theses and Dissertations Available from ProQuest*, pp. 1–143, Jan. 2004.

[32] Y. Glinec, J. Faure, V. Malka, T. Fuchs, H. Szymanowski, and U. Oelfke, "Radiotherapy with laser-plasma accelerators: Monte carlo simulation of dose deposited by an experimental quasimonoenergetic electron beam," vol. 33, no. 1, pp. 155–162. _eprint: https://onlinelibrary.wiley.com/doi/pdf/10.1118/1.2140115.

[33] T. Fuchs, H. Szymanowski, U. Oelfke, Y. Glinec, C. Rechatin, J. Faure, and V. Malka, "Treatment planning for laser-accelerated very-high energy electrons," vol. 54, no. 11, pp. 3315–3328.

[34] H. Zha and A. Grudiev, "Design and optimization of Compact Linear Collider main linac accelerating structure," *Physical Review Accelerators and Beams*, vol. 19, p. 111003, Nov. 2016. Publisher: American Physical Society.

[35] G. Geschonke and A. Ghigo, "CTF3 Design Report," tech. rep., CERN, Geneva, 2002.

[36] C. Adolphsen and others, "Status and Upgrades of the NLCTA for Studies of Advanced Beam Acceleration, Dynamics, and Manipulation," *Conf. Proc. C*, vol. 110328, pp. 130–132, 2011.

[37] D. Alesini, S. Bertolucci, M. E. Biagini, C. Biscari, R. Boni, M. Boscolo, M. Castellano, A. Clozza, G. Di Pirro, A. Drago, A. Esposito, M. Ferrario, V. Fusco, A. Gallo, A. Ghigo, S. Guiducci, M. Incurvati, P. Laurelli, C. Ligi, F. Marcellini, M. Migliorati, C. Milardi, L. Palumbo, L. Pellegrino, M. Preger, P. Raimondi, R. Ricci, C. Sanelli, F. Sgamma, B. Spataro, M. Serio, A. Stecchi, A. Stella, F. Tazzioli, C. Vaccarezza, M. Vescovi, C. Vicario, M. Zobov, E. Acerbi, F. Alessandria, D. Barni, G. Bellomo, I. Boscolo, F. Broggi, S. Cialdi, C. DeMartinis, D. Giove, C. Maroli, V. Petrillo, M. Rome', L. Serafini, E. Chiadroni, G. Felici, D. Levi, M. Mastrucci, M. Mattioli, G. Medici, G. S. Petrarca, L. Catani, A. Cianchi, A. D'Angelo, R. Di Salvo, A. Fantini, D. Moricciani, C. Schaerf, R. Bartolini, F. Ciocci, G. Dattoli, A. Doria, F. Flora, G. P. Gallerano, L. Giannessi, E. Giovenale, G. Messina, L. Mezi, P. L. Ottaviani, L. Picardi, M. Quattromini, A. Renieri, C. Ronsivalle, L. Avaldi, C. Carbone, A. Cricenti, A. Pifferi, P. Perfetti, T. Prosperi, V. R. Albertini, C. Quaresima, and N. Zema, "The SPARC project: a high-brightness electron beam source at LNF to drive a SASE-FEL experiment," *Nuclear Instruments and Methods in Physics Research Section A: Accelerators, Spectrometers, Detectors and Associated Equipment*, vol. 507, pp. 345–349, July 2003.

[38] A. Lagzda, *VHEE Radiotherapy Studies at CLARA and CLEAR facilities*. PhD thesis, Manchester University, 2019.

[39] K. Kokurewicz, E. Brunetti, A. Curcio, D. Gamba, L. Garolfi, A. Gilardi, E. Senes, K. N. Sjobak, W. Farabolini, R. Corsini, and D. A. Jaroszynski, "An experimental study of focused very high energy electron beams for radiotherapy," vol. 4, no. 1, pp. 1–7. Number: 1 Publisher: Nature Publishing Group.

[40] K. L. Small, N. T. Henthorn, D. Angal-Kalinin, A. L. Chadwick, E. Santina, A. Aitkenhead, K. J. Kirkby, R. J. Smith, M. Surman, J. Jones, W. Farabolini, R. Corsini, D. Gamba, A. Gilardi, M. J. Merchant, and R. M. Jones, "Evaluating very high energy electron RBE from nanodosimetric pBR322 plasmid DNA damage," *Scientific Reports*, vol. 11, p. 3341, Feb. 2021.

[41] D. Poppinga, R. Kranzer, W. Farabolini, A. Gilardi, R. Corsini, V. Wyrwoll, H. K. Looe, B. Delfs, L. Gabrisch, and B. Poppe, "VHEE beam dosimetry at CERN Linear Electron Accelerator for Research under ultra-high dose rate

conditions," *Biomedical Physics & Engineering Express*, vol. 7, p. 015012, Dec. 2020. Publisher: IOP Publishing.

[42] M. McManus, F. Romano, N. D. Lee, W. Farabolini, A. Gilardi, G. Royle, H. Palmans, and A. Subiel, "The challenge of ionisation chamber dosimetry in ultra-short pulsed high dose-rate Very High Energy Electron beams," *Scientific Reports*, vol. 10, p. 9089, June 2020. Number: 1 Publisher: Nature Publishing Group.

[43] P. G. Maxim, S. G. Tantawi, and B. W. Loo, "PHASER: A platform for clinical translation of FLASH cancer radiotherapy," *Radiotherapy and Oncology*, vol. 139, pp. 28–33, Oct. 2019. Publisher: Elsevier.

[44] C. McGuffey, A. G. R. Thomas, W. Schumaker, T. Matsuoka, V. Chvykov, F. J. Dollar, G. Kalintchenko, V. Yanovsky, A. Maksimchuk, K. Krushelnick, V. Y. Bychenkov, I. V. Glazyrin, and A. V. Karpeev, "Ionization Induced Trapping in a Laser Wakefield Accelerator," *Physical Review Letters*, vol. 104, p. 025004, Jan. 2010. Publisher: American Physical Society.

[45] J. Faure, C. Rechatin, A. F. Lifschitz, X. Davoine, E. Lefebvre, and V. Malka, "Experiments and Simulations of the Colliding Pulse Injection of Electrons in Plasma Wakefields," *IEEE Transactions on Plasma Science*, vol. 36, pp. 1751–1759, Aug. 2008. Conference Name: IEEE Transactions on Plasma Science.

[46] A. Pak, K. A. Marsh, S. F. Martins, W. Lu, W. B. Mori, and C. Joshi, "Injection and trapping of tunnel-ionized electrons into laser-produced wakes," *Physical Review Letters*, vol. 104, p. 025003, Jan. 2010.

[47] L. Gizzi, L. Labate, F. Baffigi, F. Brandi, G. Bussolino, L. Fulgentini, P. Koester, D. Palla, and F. Rossi, "Laser–plasma acceleration of electrons for radiobiology and radiation sources," *Nuclear Instruments and Methods in Physics Research Section B: Beam Interactions with Materials and Atoms*, vol. 355, pp. 241–245, July 2015.

[48] V. Malka, S. Fritzler, E. Lefebvre, E. d'Humières, R. Ferrand, G. Grillon, C. Albaret, S. Meyroneinc, J.-P. Chambaret, A. Antonetti, and D. Hulin, "Practicability of protontherapy using compact laser systems," *Medical Physics*, vol. 31, pp. 1587–1592, June 2004.

[49] K. Kokurewicz, E. Brunetti, G. H. Welsh, S. M. Wiggins, M. Boyd, A. Sorensen, A. J. Chalmers, G. Schettino, A. Subiel, C. DesRosiers, and D. A. Jaroszynski, "Focused very high-energy electron beams as a novel radiotherapy modality for producing high-dose volumetric elements," vol. 9, no. 1, p. 10837.

[50] L. Whitmore, R. I. Mackay, M. van Herk, J. K. Jones, and R. M. Jones, "Focused VHEE (very high energy electron) beams and dose delivery for radiotherapy applications," vol. 11, no. 1, p. 14013.

[51] M. Yuly, J. Mittelstaedt, E. Kinney, C. Maher, J. Matthews, W. Sapp, T. Soos, and R. Owens, "A test of high-energy electron bremsstrahlung calculations," *Nuclear Instruments and Methods in Physics Research Section A: Accelerators, Spectrometers, Detectors and Associated Equipment*, vol. 488, pp. 262–270, Aug. 2002.

[52] V. Vylet and J. C. Liu, "Radiation protection at high energy electron accelerators," *Radiation Protection Dosimetry*, vol. 96, no. 4, pp. 333–343, 2001.

[53] W. Duane and F. Hunt, "On X-Ray Wave-Lengths," *Physical Review*, vol. 6, pp. 166–172, Aug. 1915.

[54] M. Alpsten, "Radiological safety aspects of the operation of electron linear accelerators," *Nuclear Instruments and Methods*, vol. 166, p. 591, Dec. 1979.

[55] B. W. Loo, P. G. Maxim, and V. A. Dolgashev, "Pluridirectional very high electron energy radiation therapy systems and processes," Dec. 31 2013. US Patent 8,618,521.

[56] S. M. Bentzen and S. L. Tucker, "Quantifying the position and steepness of radiation dose-response curves," *International Journal of Radiation Biology*, vol. 71, pp. 531–542, May 1997.

[57] U. S. Srinivas, B. W. Q. Tan, B. A. Vellayappan, and A. D. Jeyasekharan, "ROS and the DNA damage response in cancer," *Redox Biology*, vol. 25, p. 101084, July 2019.

[58] M. Goldstein and M. B. Kastan, "The DNA Damage Response: Implications for Tumor Responses to Radiation and Chemotherapy," *Annual Review of Medicine*, vol. 66, no. 1, pp. 129–143, 2015. _eprint: https://doi.org/10.1146/annurev-med-081313-121208.

[59] K. Ledingham, P. Bolton, N. Shikazono, and C.-M. C. Ma, "Towards Laser Driven Hadron Cancer Radiotherapy: A Review of Progress," *Applied Sciences*, vol. 4, Apr. 2014.

[60] J. V. Belloni, M. Mostafavi, and T. Douki, *Radiation Chemistry: From basics to applications in material and life sciences.* EDP Sciences, Nov. 2020.

[61] E. J. Hall and A. J. Giaccia, *Radiobiology for the radiologist.* Philadelphia, Pa. Londo: Wolters Kluwer Lippincott Williams & Wilkins, 7th ed ed., 2012.

[62] A. Trenner and A. A. Sartori, "Harnessing DNA Double-Strand Break Repair for Cancer Treatment," *Frontiers in Oncology*, vol. 9, 2019.

[63] C. M. Yashar, "23 - Basic Principles in Gynecologic Radiotherapy," in *Clinical Gynecologic Oncology (Ninth Edition)* (P. J. DiSaia, W. T. Creasman, R. S. Mannel, D. S. McMeekin, and D. G. Mutch, eds.), pp. 586–605.e3, Elsevier, Jan. 2018.

[64] National Bureau of Standards, "Radiation quantities and units: International Commission on Radiological Units and Measurements (ICRU) report 10a 1962," Tech. Rep. NBS HB 84, National Bureau of Standards, Gaithersburg, MD, 1962.

[65] R. K.Sachs, D. J.Brenner, P. J.Hahnfeldt, and L. R. Hlatkys, "A formalism for analysing large-scale clustering of radiation-induced breaks along chromosomes," *International Journal of Radiation Biology*, vol. 74, pp. 185–206, Jan. 1998.

[66] B. S. Sørensen, J. Overgaard, and N. Bassler, "In vitro RBE-LET dependence for multiple particle types," *Acta Oncologica*, vol. 50, pp. 757–762, Aug. 2011. Publisher: Taylor & Francis _eprint: https://doi.org/10.3109/0284186X.2011.582518.

[67] V. Favaudon, L. Caplier, V. Monceau, F. Pouzoulet, M. Sayarath, C. Fouillade, M.-F. Poupon, I. Brito, P. Hupé, J. Bourhis, J. Hall, J.-J. Fontaine, and M.-C. Vozenin, "Ultrahigh dose-rate FLASH irradiation increases the differential response between normal and tumor tissue in mice," vol. 6, no. 245, p. 245ra93.

[68] K. Levy, S. Natarajan, J. Wang, S. Chow, J. T. Eggold, P. E. Loo, R. Manjappa, S. Melemenidis, F. M. Lartey, E. Schüler, L. Skinner, M. Rafat, R. Ko, A. Kim, D. H Al-Rawi, R. von Eyben, O. Dorigo, K. M. Casey, E. E. Graves, K. Bush, A. S. Yu, A. C. Koong, P. G. Maxim, B. W. Loo, and E. B. Rankin, "Abdominal FLASH irradiation reduces radiation-induced gastrointestinal toxicity for the treatment of ovarian cancer in mice," vol. 10, no. 1, p. 21600.

[69] V. Favaudon, R. Labarbe, and C. L. Limoli, "Model studies of the role of oxygen in the FLASH effect," vol. 49, no. 3, pp. 2068–2081.

[70] T. Inada, H. Nishio, S. Amino, K. Abe, and K. Saito, "High dose-rate dependence of early skin reaction in mouse," vol. 38, no. 2, pp. 139–145. Publisher: Taylor & Francis _eprint: https://doi.org/10.1080/09553008014551031.

[71] L. A. Soto, K. M. Casey, J. Wang, A. Blaney, R. Manjappa, D. Breitkreutz, L. Skinner, S. Dutt, R. B. Ko, K. Bush, A. S. Yu, S. Melemenidis, S. Strober, E. Englemann, P. G. Maxim, E. E. Graves, and B. W. L. Jr, "FLASH irradiation results in reduced severe skin toxicity compared to conventional-dose-rate irradiation," vol. 194, no. 6, pp. 618–624. Publisher: Radiation Research Society.

[72] J. H. Hendry, J. V. Moore, B. W. Hodgson, and J. P. Keene, "The constant low oxygen concentration in all the target cells for mouse tail radionecrosis," vol. 92, no. 1, pp. 172–181. Publisher: Radiation Research Society.

[73] M.-C. Vozenin, P. d. Fornel, K. Petersson, V. Favaudon, M. Jaccard, J.-F. Germond, B. J.-M. Petit, M. Burki, G. Ferrand, D. Patin, H. Bouchaab, M. Ozsahin, F. Bochud, C. Bailat, P. Devauchelle, and J. Bourhis, "The advantage of flash radiotherapy confirmed in mini-pig and cat-cancer patients," vol. 25, no. 1, p. 35.

[74] J. Atkinson, E. Bezak, H. Le, and I. Kempson, "The current status of FLASH particle therapy: a systematic review," vol. 46, no. 2, pp. 529–560.

[75] J. Bourhis, W. J. Sozzi, P. G. Jorge, O. Gaide, C. Bailat, F. Duclos, D. Patin, M. Ozsahin, F. Bochud, J.-F. Germond, R. Moeckli, and M.-C. Vozenin, "Treatment of a first patient with FLASH-radiotherapy," vol. 139, pp. 18–22.

[76] O. Gaide, F. Herrera, W. Jeanneret Sozzi, P. Gonçalves Jorge, R. Kinj, C. Bailat, F. Duclos, F. Bochud, J.-F. Germond, M. Gondré, T. Boelhen, L. Schiappacasse, M. Ozsahin, R. Moeckli, and J. Bourhis, "Comparison of ultra-high versus conventional dose rate radiotherapy in a patient with cutaneous lymphoma," *Radiotherapy and Oncology*, vol. 174, pp. 87–91, Sept. 2022.

[77] A. E. Mascia, E. C. Daugherty, Y. Zhang, E. Lee, Z. Xiao, M. Sertorio, J. Woo, L. R. Backus, J. M. McDonald, C. McCann, K. Russell, L. Levine, R. A. Sharma, D. Khuntia, J. D. Bradley, C. B. Simone, J. P. Perentesis, and J. C. Breneman, "Proton FLASH radiotherapy for the treatment of symptomatic bone metastases: The FAST-01 nonrandomized trial," vol. 9, no. 1, pp. 62–69.

[78] C. Rohrer Bley, F. Wolf, P. Gonçalves Jorge, V. Grilj, I. Petridis, B. Petit, T. T. Böhlen, R. Moeckli, C. Limoli, J. Bourhis, V. Meier, and M.-C. Vozenin, "Dose- and Volume-Limiting Late Toxicity of FLASH Radiotherapy in Cats with Squamous Cell Carcinoma of the Nasal Planum and in Mini Pigs," *Clinical Cancer Research: An Official Journal of the American Association for Cancer Research*, vol. 28, pp. 3814–3823, Sept. 2022.

[79] B. Borresen, M. L. Arendt, E. Konradsson, K. Bastholm Jensen, S. A. Bäck, P. Munck Af Rosenschöld, C. Ceberg, and K. Petersson, "Evaluation of single-fraction high dose FLASH radiotherapy in a cohort of canine oral cancer patients," *Frontiers in Oncology*, vol. 13, p. 1256760, 2023.

[80] A. Alanazi, J. Meesungnoen, and J.-P. Jay-Gerin, "A Computer Modeling Study of Water Radiolysis at High Dose Rates. Relevance to FLASH Radiotherapy," *Radiation Research*, vol. 195, Dec. 2020.

[81] J. Ramos-Méndez, N. Domínguez-Kondo, J. Schuemann, A. McNamara, E. Moreno-Barbosa, and B. Faddegon, "LET-Dependent Intertrack Yields in Proton Irradiation at Ultra-High Dose Rates Relevant for FLASH Therapy," *Radiation Research*, vol. 194, pp. 351–362, Aug. 2020.

[82] F. Romano, C. Bailat, P. G. Jorge, M. L. F. Lerch, and A. Darafsheh, "Ultra-high dose rate dosimetry: Challenges and opportunities for FLASH radiation therapy," *Medical Physics*, vol. 49, no. 7, pp. 4912–4932, 2022. _eprint: https://onlinelibrary.wiley.com/doi/pdf/10.1002/mp.15649.

[83] I. A. E. Agency, "Absorbed Dose Determination in External Beam Radiotherapy," text, International Atomic Energy Agency, 2000. ISBN: 9789201022004 Publication Title: Absorbed Dose Determination in External Beam Radiotherapy.

[84] M. T. Niatel, "An experimental study of ion recombination in parallel-plate free-air ionization chambers," *Physics in Medicine and Biology*, vol. 12, pp. 555–563, Oct. 1967.

[85] J. W. Boag and J. Currant, "Current collection and ionic recombination in small cylindrical ionization chambers exposed to pulsed radiation," *The British Journal of Radiology*, vol. 53, pp. 471–478, May 1980. Publisher: The British Institute of Radiology.

[86] A. Subiel and F. Romano, "Recent developments in absolute dosimetry for FLASH radiotherapy," *The British Journal of Radiology*, vol. 96, p. 20220560, Aug. 2023. Publisher: The British Institute of Radiology.

[87] K. Petersson, M. Jaccard, J.-F. Germond, T. Buchillier, F. Bochud, J. Bourhis, M.-C. Vozenin, and C. Bailat, "High dose-per-pulse electron beam dosimetry - A model to correct for the ion recombination in the Advanced Markus ionization chamber," *Medical Physics*, vol. 44, pp. 1157–1167, Mar. 2017.

[88] F. Di Martino, D. Del Sarto, S. Barone, M. Giuseppina Bisogni, S. Capaccioli, F. Galante, A. Gasparini, G. Mariani, L. Masturzo, M. Montefiori, M. Pacitti, F. Paiar, J. Harold Pensavalle, F. Romano, S. Ursino, V. Vanreusel, D. Verellen, and G. Felici, "A new calculation method for the free electron fraction of an ionization chamber in the ultra-high-dose-per-pulse regimen," *Physica Medica*, vol. 103, pp. 175–180, Nov. 2022.

[89] S. Siddique, H. E. Ruda, and J. C. L. Chow, "FLASH Radiotherapy and the Use of Radiation Dosimeters," *Cancers*, vol. 15, p. 3883, Jan. 2023. Number: 15 Publisher: Multidisciplinary Digital Publishing Institute.

[90] R. Kranzer, D. Poppinga, J. Weidner, A. Schüller, T. Hackel, H. K. Looe, and B. Poppe, "Ion collection efficiency of ionization chambers in ultra-high

dose-per-pulse electron beams," *Medical Physics*, vol. 48, no. 2, pp. 819–830, 2021. _eprint: https://onlinelibrary.wiley.com/doi/pdf/10.1002/mp.14620.

[91] F. Gómez, D. M. Gonzalez-Castaño, N. G. Fernández, J. Pardo-Montero, A. Schüller, A. Gasparini, V. Vanreusel, D. Verellen, G. Felici, R. Kranzer, and J. Paz-Martín, "Development of an ultra-thin parallel plate ionization chamber for dosimetry in FLASH radiotherapy," *Medical Physics*, vol. 49, pp. 4705–4714, July 2022.

[92] M. Jaccard, K. Petersson, T. Buchillier, J.-F. Germond, M. T. Durán, M.-C. Vozenin, J. Bourhis, F. O. Bochud, and C. Bailat, "High dose-per-pulse electron beam dosimetry: Usability and dose-rate independence of EBT3 Gafchromic films," *Medical Physics*, vol. 44, no. 2, pp. 725–735, 2017. _eprint: https://onlinelibrary.wiley.com/doi/pdf/10.1002/mp.12066.

[93] A. Patriarca, C. Fouillade, M. Auger, F. Martin, F. Pouzoulet, C. Nauraye, S. Heinrich, V. Favaudon, S. Meyroneinc, R. Dendale, A. Mazal, P. Poortmans, P. Verrelle, and L. De Marzi, "Experimental Set-up for FLASH Proton Irradiation of Small Animals Using a Clinical System," *International Journal of Radiation Oncology*Biology*Physics*, vol. 102, pp. 619–626, Nov. 2018.

[94] P. G. Jorge, M. Jaccard, K. Petersson, M. Gondré, M. T. Durán, L. Desorgher, J.-F. Germond, P. Liger, M.-C. Vozenin, J. Bourhis, F. Bochud, R. Moeckli, and C. Bailat, "Dosimetric and preparation procedures for irradiating biological models with pulsed electron beam at ultra-high dose-rate," *Radiotherapy and Oncology*, vol. 139, pp. 34–39, Oct. 2019.

[95] D. Villoing, C. Koumeir, A. Bongrand, A. Guertin, F. Haddad, V. Métivier, F. Poirier, V. Potiron, N. Servagent, S. Supiot, G. Delpon, and S. Chiavassa, "Technical note: Proton beam dosimetry at ultra-high dose rates (FLASH): Evaluation of GAFchromic™ (EBT3, EBT-XD) and OrthoChromic (OC-1) film performances," *Medical Physics*, vol. 49, no. 4, pp. 2732–2745, 2022. _eprint: https://onlinelibrary.wiley.com/doi/pdf/10.1002/mp.15526.

[96] I. S. Organization and A. International, "Standard practice for use of an alanine-epr dosimetry system," 2018.

[97] L. Archambault, A. S. Beddar, L. Gingras, R. Roy, and L. Beaulieu, "Measurement accuracy and Cerenkov removal for high performance, high spatial resolution scintillation dosimetry," *Medical Physics*, vol. 33, no. 1, pp. 128–135, 2006. _eprint: https://onlinelibrary.wiley.com/doi/pdf/10.1118/1.2138010.

[98] A. Darafsheh, *Radiation Therapy Dosimetry: A Practical Handbook*. Names: Darafsheh, Arash, editor. Title: Radiation therapy dosimetry : a practical handbook / edited by Arash Darafsheh. Description: First edition. | Boca Raton : CRC Press, 2021.: CRC Press, 1 ed., Mar. 2021.

[99] S. Vigdor, A. Klyachko, K. Solberg, and M. Pankuch, "A gas scintillator detector for 2D dose profile monitoring in pencil beam scanning and pulsed beam proton radiotherapy treatments," *Physics in medicine and biology*, vol. 62, pp. 4946–4969, June 2017.

[100] E. Jean, F. Therriault-Proulx, and L. Beaulieu, "Comparative optic and dosimetric characterization of the HYPERSCINT scintillation dosimetry research platform for multipoint applications," *Physics in Medicine & Biology*, vol. 66, p. 085009, Apr. 2021. Publisher: IOP Publishing.

[101] Y. Poirier, J. Xu, S. Mossahebi, F. Therriault-Proulx, and A. Sawant, "Technical note: Characterization and practical applications of a novel plastic scintillator for online dosimetry for an ultrahigh dose rate (FLASH)," *Medical Physics*, vol. 49, no. 7, pp. 4682–4692, 2022. _eprint: https://onlinelibrary.wiley.com/doi/pdf/10.1002/mp.15671.

[102] V. Favaudon, J.-M. Lentz, S. Heinrich, A. Patriarca, L. de Marzi, C. Fouillade, and M. Dutreix, "Time-resolved dosimetry of pulsed electron beams in very high dose-rate, FLASH irradiation for radiotherapy preclinical studies," *Nuclear Instruments and Methods in Physics Research Section A: Accelerators, Spectrometers, Detectors and Associated Equipment*, vol. 944, p. 162537, Nov. 2019.

[103] M. Rahman, M. R. Ashraf, R. Zhang, D. J. Gladstone, X. Cao, B. B. Williams, P. Jack Hoopes, B. W. Pogue, and P. Bruza, "Spatial and temporal dosimetry of individual electron FLASH beam pulses using radioluminescence imaging," *Physics in Medicine and Biology*, vol. 66, June 2021.

[104] R. Kranzer, A. Schüller, A. Bourgouin, T. Hackel, D. Poppinga, M. Lapp, H. K. Looe, and B. Poppe, "Response of diamond detectors in ultrahigh dose-per-pulse electron beams for dosimetry at FLASH radiotherapy," *Physics in Medicine & Biology*, vol. 67, p. 075002, Mar. 2022. Publisher: IOP Publishing.

[105] M. Marinelli, G. Felici, F. Galante, A. Gasparini, L. Giuliano, S. Heinrich, M. Pacitti, G. Prestopino, V. Vanreusel, D. Verellen, C. Verona, and G. Verona Rinati, "Design, realization, and characterization of a novel diamond detector prototype for FLASH radiotherapy dosimetry," *Medical Physics*, vol. 49, no. 3, pp. 1902–1910, 2022. _eprint: https://onlinelibrary.wiley.com/doi/pdf/10.1002/mp.15473.

[106] G. Verona Rinati, G. Felici, F. Galante, A. Gasparini, R. Kranzer, G. Mariani, M. Pacitti, G. Prestopino, A. Schüller, V. Vanreusel, D. Verellen, C. Verona, and M. Marinelli, "Application of a novel diamond detector for commissioning of FLASH radiotherapy electron beams," *Medical Physics*, vol. 49, no. 8, pp. 5513–5522, 2022. _eprint: https://onlinelibrary.wiley.com/doi/pdf/10.1002/mp.15782.

[107] M. H. Kalos and P. A. Whitlock, *Monte Carlo Methods*. Wiley, 1 ed., Sept. 2008.

[108] J. Perl, J. Shin, J. Schumann, B. Faddegon, and H. Paganetti, "TOPAS: an innovative proton Monte Carlo platform for research and clinical applications," *Medical Physics*, vol. 39, pp. 6818–6837, Nov. 2012.

[109] R. A. Forster and T. N. K. Godfrey, "MCNP - a general Monte Carlo code for neutron and photon transport," in *Monte-Carlo Methods and Applications in Neutronics, Photonics and Statistical Physics* (R. Alcouffe, R. Dautray, A. Forster, G. Ledanois, and B. Mercier, eds.), Lecture Notes in Physics, (Berlin, Heidelberg), pp. 33–55, Springer, 1985.

[110] S. Agostinelli, J. Allison, K. Amako, J. Apostolakis, H. Araujo, P. Arce, M. Asai, D. Axen, S. Banerjee, G. Barrand, F. Behner, L. Bellagamba, J. Boudreau, L. Broglia, A. Brunengo, H. Burkhardt, S. Chauvie, J. Chuma, R. Chytracek, G. Cooperman, G. Cosmo, P. Degtyarenko, A. Dell'Acqua, G. Depaola, D. Dietrich, R. Enami, A. Feliciello, C. Ferguson, H. Fesefeldt, G. Folger, F. Foppiano, A. Forti, S. Garelli, S. Giani, R. Giannitrapani, D. Gibin, J. J. Gómez Cadenas, I. González, G. Gracia Abril, G. Greeniaus, W. Greiner, V. Grichine, A. Grossheim, S. Guatelli, P. Gumplinger, R. Hamatsu, K. Hashimoto, H. Hasui, A. Heikkinen, A. Howard, V. Ivanchenko, A. Johnson, F. W. Jones, J. Kallenbach, N. Kanaya, M. Kawabata, Y. Kawabata, M. Kawaguti, S. Kelner, P. Kent, A. Kimura, T. Kodama, R. Kokoulin, M. Kossov, H. Kurashige, E. Lamanna, T. Lampén, V. Lara, V. Lefebure, F. Lei, M. Liendl, W. Lockman, F. Longo, S. Magni, M. Maire, E. Medernach, K. Minamimoto, P. Mora de Freitas, Y. Morita, K. Murakami, M. Nagamatu, R. Nartallo, P. Nieminen, T. Nishimura, K. Ohtsubo, M. Okamura, S. O'Neale, Y. Oohata, K. Paech, J. Perl, A. Pfeiffer, M. G. Pia, F. Ranjard, A. Rybin, S. Sadilov, E. Di Salvo, G. Santin, T. Sasaki, N. Savvas, Y. Sawada, S. Scherer, S. Sei, V. Sirotenko, D. Smith, N. Starkov, H. Stoecker, J. Sulkimo, M. Takahata, S. Tanaka, E. Tcherniaev, E. Safai Tehrani, M. Tropeano, P. Truscott, H. Uno, L. Urban, P. Urban, M. Verderi, A. Walkden, W. Wander, H. Weber, J. P. Wellisch, T. Wenaus, D. C. Williams, D. Wright, T. Yamada, H. Yoshida, and D. Zschiesche, "Geant4—a simulation toolkit," *Nuclear Instruments and Methods in Physics Research Section A: Accelerators, Spectrometers, Detectors and Associated Equipment*, vol. 506, pp. 250–303, July 2003.

[111] A. Ferrari, P. Sala, A. Fasso, and J. Ranft, "FLUKA: A Multi-Particle Transport Code," Tech. Rep. SLAC-R-773, 877507, Dec. 2005.

[112] S. Jan, G. Santin, D. Strul, S. Staelens, K. Assié, D. Autret, S. Avner, R. Barbier, M. Bardiès, P. M. Bloomfield, D. Brasse, V. Breton, P. Bruyndonckx, I. Buvat, A. F. Chatziioannou, Y. Choi, Y. H. Chung, C. Comtat, D. Donnarieix, L. Ferrer, S. J. Glick, C. J. Groiselle, D. Guez, P.-F.

Honore, S. Kerhoas-Cavata, A. S. Kirov, V. Kohli, M. Koole, M. Krieguer, D. J. V. D. Laan, F. Lamare, G. Largeron, C. Lartizien, D. Lazaro, M. C. Maas, L. Maigne, F. Mayet, F. Melot, C. Merheb, E. Pennacchio, J. Perez, U. Pietrzyk, F. R. Rannou, M. Rey, D. R. Schaart, C. R. Schmidtlein, L. Simon, T. Y. Song, J.-M. Vieira, D. Visvikis, R. V. D. Walle, E. Wieërs, and C. Morel, "GATE: a simulation toolkit for PET and SPECT," *Physics in Medicine and Biology*, vol. 49, pp. 4543–4561, Oct. 2004.

[113] J. Allison, K. Amako, J. Apostolakis, P. Arce, M. Asai, T. Aso, E. Bagli, A. Bagulya, S. Banerjee, G. Barrand, B. Beck, A. Bogdanov, D. Brandt, J. Brown, H. Burkhardt, P. Canal, D. Cano-Ott, S. Chauvie, K. Cho, G. Cirrone, G. Cooperman, M. Cortés-Giraldo, G. Cosmo, G. Cuttone, G. Depaola, L. Desorgher, X. Dong, A. Dotti, V. Elvira, G. Folger, Z. Francis, A. Galoyan, L. Garnier, M. Gayer, K. Genser, V. Grichine, S. Guatelli, P. Guèye, P. Gumplinger, A. Howard, I. Hřivnáčová, S. Hwang, S. Incerti, A. Ivanchenko, V. Ivanchenko, F. Jones, S. Jun, P. Kaitaniemi, N. Karakatsanis, M. Karamitros, M. Kelsey, A. Kimura, T. Koi, H. Kurashige, A. Lechner, S. Lee, F. Longo, M. Maire, D. Mancusi, A. Mantero, E. Mendoza, B. Morgan, K. Murakami, T. Nikitina, L. Pandola, P. Paprocki, J. Perl, I. Petrović, M. Pia, W. Pokorski, J. Quesada, M. Raine, M. Reis, A. Ribon, A. Ristić Fira, F. Romano, G. Russo, G. Santin, T. Sasaki, D. Sawkey, J. Shin, I. Strakovsky, A. Taborda, S. Tanaka, B. Tomé, T. Toshito, H. Tran, P. Truscott, L. Urban, V. Uzhinsky, J. Verbeke, M. Verderi, B. Wendt, H. Wenzel, D. Wright, D. Wright, T. Yamashita, J. Yarba, and H. Yoshida, "Recent developments in Geant4," *Nuclear Instruments and Methods in Physics Research Section A: Accelerators, Spectrometers, Detectors and Associated Equipment*, vol. 835, pp. 186–225, Nov. 2016.

[114] A. L. Fielding, "Monte-Carlo techniques for radiotherapy applications I: introduction and overview of the different Monte-Carlo codes," *Journal of Radiotherapy in Practice*, vol. 22, p. e80, Jan. 2023. Publisher: Cambridge University Press.

[115] P. Arce, P. Rato, M. Canadas, and J. I. Lagares, "GAMOS: A Geant4-based easy and flexible framework for nuclear medicine applications," in *2008 IEEE Nuclear Science Symposium Conference Record*, pp. 3162–3168, Oct. 2008. ISSN: 1082-3654.

[116] T. Aso, A. Kimura, S. Kameoka, K. Murakami, T. Sasaki, and T. Yamashita, "GEANT4 based simulation framework for particle therapy system," in *2007 IEEE Nuclear Science Symposium Conference Record*, vol. 4, pp. 2564–2567, Oct. 2007. ISSN: 1082-3654.

[117] B. Faddegon, J. Ramos-Méndez, J. Schuemann, A. McNamara, J. Shin, J. Perl, and H. Paganetti, "The TOPAS tool for particle simulation, a Monte

Carlo simulation tool for physics, biology and clinical research," *Physica Medica*, vol. 72, pp. 114–121, Apr. 2020.

[118] L. Eyges, "Multiple Scattering with Energy Loss," *Physical Review*, vol. 74, pp. 1534–1535, Nov. 1948.

[119] K. R. Hogstrom, M. D. Mills, and P. R. Almond, "Electron beam dose calculations," *Physics in Medicine and Biology*, vol. 26, pp. 445–459, May 1981.

[120] A. S. Shiu and K. R. Hogstrom, "Pencil-beam redefinition algorithm for electron dose distributions," *Medical Physics*, vol. 18, pp. 7–18, Feb. 1991.

[121] C. Yeboah and G. A. Sandison, "Optimized treatment planning for prostate cancer comparing IMPT, VHEET and 15 MV IMXT," *Physics in Medicine & Biology*, vol. 47, p. 2247, June 2002.

[122] M. Bazalova-Carter, B. Qu, B. Palma, B. Hårdemark, E. Hynning, C. Jensen, P. G. Maxim, and B. W. Loo Jr., "Treatment planning for radiotherapy with very high-energy electron beams and comparison of VHEE and VMAT plans," *Medical Physics*, vol. 42, no. 5, pp. 2615–2625, 2015. _eprint: https://onlinelibrary.wiley.com/doi/pdf/10.1118/1.4918923.

[123] T. T. Böhlen, J.-F. Germond, E. Traneus, J. Bourhis, M.-C. Vozenin, C. Bailat, F. Bochud, and R. Moeckli, "Characteristics of very high-energy electron beams for the irradiation of deep-seated targets," *Medical Physics*, vol. 48, no. 7, pp. 3958–3967, 2021. _eprint: https://onlinelibrary.wiley.com/doi/pdf/10.1002/mp.14891.

[124] A. Sarti, P. De Maria, G. Battistoni, M. De Simoni, C. Di Felice, Y. Dong, M. Fischetti, G. Franciosini, M. Marafini, F. Marampon, I. Mattei, R. Mirabelli, S. Muraro, M. Pacilio, L. Palumbo, L. Rocca, D. Rubeca, A. Schiavi, A. Sciubba, V. Tombolini, M. Toppi, G. Traini, A. Trigilio, and V. Patera, "Deep Seated Tumour Treatments With Electrons of High Energy Delivered at FLASH Rates: The Example of Prostate Cancer," *Frontiers in Oncology*, vol. 11, p. 777852, 2021.

[125] E. Fermi, "The Ionization Loss of Energy in Gases and in Condensed Materials," *Physical Review*, vol. 57, pp. 485–493, Mar. 1940.

[126] H. A. Bethe, "Molière's Theory of Multiple Scattering," *Physical Review*, vol. 89, pp. 1256–1266, Mar. 1953.

[127] I. A. D. Bruinvis, W. A. F. Mathol, and P. Andreo, "Inclusion of electron range straggling in the Fermi-Eyges multiple-scattering theory," *Physics in Medicine and Biology*, vol. 34, pp. 491–507, Apr. 1989. Publisher: IOP Publishing.

[128] "ICRU Reports," *Reports of the International Commission on Radiation Units and Measurements*, vol. os-11, pp. 60–62, May 1972.

[129] B. Rossi and W. B. Fretter, "High-Energy Particles," *American Journal of Physics*, vol. 21, pp. 236–236, Mar. 1953.

[130] "ICRU Reports," *Reports of the International Commission on Radiation Units and Measurements*, vol. os-12, no. 2, pp. 26–29, 1984. Publisher: SAGE Publications.

[131] G. A. D, "Modeling of dual foil scattering systems for clinical electron beams," Master's thesis, The University of Texas Health Science Center at Houston, Houston, TX, 1991.

[132] P. Andreo and A. Brahme, "Restricted Energy-Loss Straggling and Multiple Scattering of Electrons in Mixed Monte Carlo Procedures," *Radiation Research*, vol. 100, p. 16, Oct. 1984.

[133] G. Moliere, "Theorie der Streuung schneller geladener Teilchen I. Einzelstreuung am abgeschirmten Coulomb-Feld," *Zeitschrift für Naturforschung A*, vol. 2, pp. 133–145, Mar. 1947. Publisher: De Gruyter.

[134] H. Huizenga and P. R. M. Storchi, "Numerical calculation of energy deposition by broad high-energy electron beams," *Physics in Medicine and Biology*, vol. 34, pp. 1371–1396, Oct. 1989. Publisher: IOP Publishing.

[135] K. K. Kainz, J. A. Antolak, P. R. Almond, C. D. Bloch, and K. R. Hogstrom, "Dual scattering foil design for poly-energetic electron beams," *Physics in Medicine and Biology*, vol. 50, pp. 755–767, Feb. 2005. Publisher: IOP Publishing.

[136] W. T. Scott, "The Theory of Small-Angle Multiple Scattering of Fast Charged Particles," *Reviews of Modern Physics*, vol. 35, pp. 231–313, Apr. 1963.

[137] R. L. Carver, K. R. Hogstrom, M. J. Price, J. D. LeBlanc, and G. M. Pitcher, "Real-time simulator for designing electron dual scattering foil systems," *Journal of Applied Clinical Medical Physics*, vol. 15, pp. 323–342, Nov. 2014.

[138] P. Andreo and A. Brahme, "Mean energy in electron beams," *Medical Physics*, vol. 8, pp. 682–687, Oct. 1981.

[139] A. Brahme, "Simple relations for the penetration of high energy electron beams in matter," tech. rep., Sweden, 1975. SSI–1975-011 INIS Reference Number: 7254382.

[140] H. Huizenga and P. R. Storchi, "The in-air scattering of clinical electron beams as produced by accelerators with scanning beams and diaphragm collimators," *Physics in Medicine and Biology*, vol. 32, pp. 1011–1029, Aug. 1987.

[141] I. Lax and A. Brahme, "Electron beam dose planning using Gaussian beams. Energy and spatial scaling with inhomogeneities," *Acta Radiologica. Oncology*, vol. 24, pp. 75–85, Feb. 1985.

[142] J. Dyk, R. Barnett, J. Cygler, and P. Shragge, "Commissioning and quality assurance of treatment planning computers," *International Journal of Radiation Oncology*Biology*Physics*, vol. 26, pp. 261–273, May 1993.

[143] L. De Marzi, A. Da Fonseca, C. Moignier, A. Patriarca, F. Goudjil, A. Mazal, I. Buvat, and J. Hérault, "Experimental characterisation of a proton kernel model for pencil beam scanning techniques," *Physica Medica*, vol. 64, pp. 195–203, Aug. 2019.

[144] B. B. Sorcini, S. Hyödynmaa, and A. Brahme, "The role of phantom and treatment head generated bremsstrahlung in high-energy electron beam dosimetry," *Physics in Medicine and Biology*, vol. 41, pp. 2657–2677, Dec. 1996.

[145] P. van Marlen, M. Dahele, M. Folkerts, E. Abel, B. J. Slotman, and W. F. Verbakel, "Bringing FLASH to the Clinic: Treatment Planning Considerations for Ultrahigh Dose-Rate Proton Beams," *International Journal of Radiation Oncology*Biology*Physics*, vol. 106, pp. 621–629, Mar. 2020.

[146] S. van de Water, S. Safai, J. M. Schippers, D. C. Weber, and A. J. Lomax, "Towards FLASH proton therapy: the impact of treatment planning and machine characteristics on achievable dose rates," *Acta Oncologica*, vol. 58, pp. 1463–1469, Oct. 2019.

[147] G. Zhang, J. Wang, Y. Wang, and H. Peng, "Proton FLASH: passive scattering or pencil beam scanning?," *Physics in Medicine & Biology*, vol. 66, p. 03NT01, Feb. 2021.

[148] M. M. Folkerts, E. Abel, S. Busold, J. R. Perez, V. Krishnamurthi, and C. C. Ling, "A framework for defining FLASH dose rate for pencil beam scanning," *Medical Physics*, vol. 47, pp. 6396–6404, Dec. 2020.

[149] H. Gao, B. Lin, Y. Lin, S. Fu, K. Langen, T. Liu, and J. Bradley, "Simultaneous dose and dose rate optimization (SDDRO) for FLASH proton therapy," *Medical Physics*, vol. 47, pp. 6388–6395, Dec. 2020.

[150] M. Jaccard, M. T. Durán, K. Petersson, J.-F. Germond, P. Liger, M.-C. Vozenin, J. Bourhis, F. Bochud, and C. Bailat, "High dose-per-pulse electron beam dosimetry: Commissioning of the Oriatron eRT6 prototype linear

accelerator for preclinical use," *Medical Physics*, vol. 45, pp. 863–874, Feb. 2018.

[151] P. Lansonneur, V. Favaudon, S. Heinrich, C. Fouillade, P. Verrelle, and L. De Marzi, "Simulation and experimental validation of a prototype electron beam linear accelerator for preclinical studies," *Physica medica: PM: an international journal devoted to the applications of physics to medicine and biology: official journal of the Italian Association of Biomedical Physics (AIFB)*, vol. 60, pp. 50–57, Apr. 2019.

[152] E. Schüler, S. Trovati, G. King, F. Lartey, M. Rafat, M. Villegas, A. J. Praxel, B. W. Loo, and P. G. Maxim, "Experimental Platform for Ultra-high Dose Rate FLASH Irradiation of Small Animals Using a Clinical Linear Accelerator," *International Journal of Radiation Oncology*Biology*Physics*, vol. 97, pp. 195–203, Jan. 2017.

[153] E. S. Diffenderfer, I. I. Verginadis, M. M. Kim, K. Shoniyozov, A. Velalopoulou, D. Goia, M. Putt, S. Hagan, S. Avery, K. Teo, W. Zou, A. Lin, S. Swisher-McClure, C. Koch, A. R. Kennedy, A. Minn, A. Maity, T. M. Busch, L. Dong, C. Koumenis, J. Metz, and K. A. Cengel, "Design, Implementation, and in Vivo Validation of a Novel Proton FLASH Radiation Therapy System," *International journal of radiation oncology, biology, physics*, vol. 106, pp. 440–448, Feb. 2020.

[154] S. Jolly, H. Owen, M. Schippers, and C. Welsch, "Technical challenges for FLASH proton therapy," *Physica Medica*, vol. 78, pp. 71–82, Oct. 2020.

[155] S. Cunningham, S. McCauley, K. Vairamani, J. Speth, S. Girdhani, E. Abel, R. A. Sharma, J. P. Perentesis, S. I. Wells, A. Mascia, and M. Sertorio, "FLASH Proton Pencil Beam Scanning Irradiation Minimizes Radiation-Induced Leg Contracture and Skin Toxicity in Mice," *Cancers*, vol. 13, p. 1012, Mar. 2021.

[156] B. S. Sørensen, M. K. Sitarz, C. Ankjærgaard, J. G. Johansen, C. E. Andersen, E. Kanouta, C. Grau, and P. Poulsen, "Pencil beam scanning proton FLASH maintains tumor control while normal tissue damage is reduced in a mouse model," *Radiotherapy and Oncology*, vol. 175, pp. 178–184, Oct. 2022.

[157] L. Iturri, A. Bertho, C. Lamirault, M. Juchaux, C. Gilbert, J. Espenon, C. Sebrie, L. Jourdain, F. Pouzoulet, P. Verrelle, L. De Marzi, and Y. Prezado, "Proton FLASH Radiation Therapy and Immune Infiltration: Evaluation in an Orthotopic Glioma Rat Model," *International Journal of Radiation Oncology, Biology, Physics*, vol. 116, pp. 655–665, July 2023.

[158] D. H. Jeong, M. Lee, H. Lim, S. K. Kang, S. J. Lee, H. C. Kim, K. Lee, S. H. Kim, D. E. Lee, and K. W. Jang, "Electron beam scattering device for

FLASH preclinical studies with 6-MeV LINAC," *Nuclear Engineering and Technology*, vol. 53, pp. 1289–1296, Apr. 2021.

[159] E. Grusell, A. Montelius, A. Brahme, G. Rikner, and K. Russell, "A general solution to charged particle beam flattening using an optimized dual-scattering-foil technique, with application to proton therapy beams," *Physics in Medicine and Biology*, vol. 39, pp. 2201–2216, Dec. 1994.

[160] A. Przemyslaw, "New and efficient method for designing dual foil electron beam forming systems," 2016.

[161] J. W. Carpender, L. S. Skaggs, L. H. Lanzl, and M. L. Griem, "Radiation therapy with high-energy electrons using pencil beam scanning," *Am. J. Roentgenol., Radium Therapy Nucl. Med.*

[162] S. Dowdell, "Pencil beam scanning proton therapy: the significance of secondary particles," *University of Wollongong Thesis Collection 1954-2016*, Jan. 2011.

[163] A. Patriarca, *Characterization and implementation of Pencil Beam Scanning proton therapy techniques: from spot scanning to continuous scanning*. PhD thesis, La Sapienza, 2017.

[164] M. Schwarz, E. Traneus, S. Safai, A. Kolano, and S. van de Water, "Treatment planning for Flash radiotherapy: General aspects and applications to proton beams," *Medical Physics*, vol. 49, no. 4, pp. 2861–2874, 2022. _eprint: https://onlinelibrary.wiley.com/doi/pdf/10.1002/mp.15579.

[165] M. Kang, S. Wei, J. I. Choi, C. B. Simone, and H. Lin, "Quantitative Assessment of 3D Dose Rate for Proton Pencil Beam Scanning FLASH Radiotherapy and Its Application for Lung Hypofractionation Treatment Planning," *Cancers*, vol. 13, p. 3549, July 2021.

[166] M. Krieger, S. van de Water, M. M. Folkerts, A. Mazal, S. Fabiano, N. Bizzocchi, D. C. Weber, S. Safai, and A. J. Lomax, "A quantitative FLASH effectiveness model to reveal potentials and pitfalls of high dose rate proton therapy," *Medical Physics*, vol. 49, no. 3, pp. 2026–2038, 2022. _eprint: https://onlinelibrary.wiley.com/doi/pdf/10.1002/mp.15459.

[167] J. Y. Huang, D. Dunkerley, and J. B. Smilowitz, "Evaluation of a commercial Monte Carlo dose calculation algorithm for electron treatment planning," *Journal of Applied Clinical Medical Physics*, vol. 20, pp. 184–193, June 2019.

[168] G. X. Ding, D. M. Duggan, C. W. Coffey, P. Shokrani, and J. E. Cygler, "First macro Monte Carlo based commercial dose calculation module for electron beam treatment planning—new issues for clinical consideration," *Physics in Medicine & Biology*, vol. 51, p. 2781, May 2006.

[169] B. Palma, M. Bazalova-Carter, B. Hårdemark, E. Hynning, B. Qu, B. W. Loo, and P. G. Maxim, "Assessment of the quality of very high-energy electron radiotherapy planning," *Radiotherapy and Oncology*, vol. 119, pp. 154–158, Apr. 2016.

[170] H.-P. Wieser, E. Cisternas, N. Wahl, S. Ulrich, A. Stadler, H. Mescher, L.-R. Müller, T. Klinge, H. Gabrys, L. Burigo, A. Mairani, S. Ecker, B. Ackermann, M. Ellerbrock, K. Parodi, O. Jäkel, and M. Bangert, "Development of the open-source dose calculation and optimization toolkit matRad," *Medical Physics*, vol. 44, pp. 2556–2568, June 2017.

[171] Y. Alaghband, B. D. Allen, E. A. Kramár, R. Zhang, O. G. G. Drayson, N. Ru, B. Petit, A. Almeida, N.-L. Doan, M. A. Wood, J. E. Baulch, P. Ballesteros-Zebadua, M.-C. Vozenin, and C. L. Limoli, "Uncovering the Protective Neurologic Mechanisms of Hypofractionated FLASH Radiotherapy," *Cancer Research Communications*, vol. 3, pp. 725–737, Apr. 2023.

[172] T. Kataria, K. Sharma, V. Subramani, K. P. Karrthick, and S. S. Bisht, "Homogeneity Index: An objective tool for assessment of conformal radiation treatments," *Journal of Medical Physics / Association of Medical Physicists of India*, vol. 37, no. 4, pp. 207–213, 2012.

[173] T. T. Böhlen, J.-F. Germond, J. Bourhis, M.-C. Vozenin, E. M. Ozsahin, F. Bochud, C. Bailat, and R. Moeckli, "Normal Tissue Sparing by FLASH as a Function of Single-Fraction Dose: A Quantitative Analysis," *International Journal of Radiation Oncology*Biology*Physics*, vol. 114, pp. 1032–1044, Dec. 2022.

[174] T. T. Böhlen, J. Germond, E. Traneus, V. Vallet, L. Desorgher, E. M. Ozsahin, F. Bochud, J. Bourhis, and R. Moeckli, "3D-conformal very-high energy electron therapy as candidate modality for FLASH-RT: A treatment planning study for glioblastoma and lung cancer," *Medical Physics*, p. mp.16586, July 2023.

[175] N. Clements, N. Esplen, and M. Bazalova-Carter, "A feasibility study of ultra-high dose rate mini-GRID therapy using very-high-energy electron beams for a simulated pediatric brain case," *Physica Medica*, vol. 112, p. 102637, Aug. 2023.

[176] G. Zhang, Z. Zhang, W. Gao, and H. Quan, "Treatment planning consideration for very high-energy electron FLASH radiotherapy," *Physica Medica*, vol. 107, p. 102539, Mar. 2023.

[177] A. Muscato, L. Arsini, G. Battistoni, L. Campana, D. Carlotti, F. De Felice, A. De Gregorio, M. De Simoni, C. Di Felice, Y. Dong, G. Franciosini, M. Marafini, I. Mattei, R. Mirabelli, S. Muraro, M. Pacilio, L. Palumbo,

V. Patera, A. Schiavi, A. Sciubba, M. Schwarz, S. Sorbino, V. Tombolini, M. Toppi, G. Traini, A. Trigilio, and A. Sarti, "Treatment planning of intracranial lesions with VHEE: comparing conventional and FLASH irradiation potential with state-of-the-art photon and proton radiotherapy," *Frontiers in Physics*, vol. 11, 2023.

[178] S. Wei, H. Lin, J. I. Choi, C. B. Simone, and M. Kang, "A Novel Proton Pencil Beam Scanning FLASH RT Delivery Method Enables Optimal OAR Sparing and Ultra-High Dose Rate Delivery: A Comprehensive Dosimetry Study for Lung Tumors," *Cancers*, vol. 13, p. 5790, Nov. 2021.

[179] A. Subiel, V. Moskvin, G. H. Welsh, S. Cipiccia, D. Reboredo Gil, P. Evans, M. Partridge, C. Desrosiers, M. P. Anania, A. Cianchi, A. Mostacci, E. Chiadroni, D. Di Giovenale, F. Villa, R. Pompili, M. Ferrario, M. Bellaveglia, G. Di Pirro, G. Gatti, C. Vaccarezza, B. Seitz, R. Issac, E. Brunetti, M. Wiggins, B. Ersfeld, M. Islam, M. S. Mendonca, A. Sorensen, M. Boyd, and D. Jaroszynski, "Dosimetry of very high energy electrons (VHEE) for radiotherapy applications : using radiochromic film measurements and Monte Carlo simulations," *Physics in Medicine and Biology*, vol. 59, pp. 5811–5829, Oct. 2014. Num Pages: 19 Number: 19.

[180] Y. Poirier, S. Mossahebi, S. J. Becker, B. Koger, J. Xu, N. Lamichhane, P. G. Maxim, and A. Sawant, "Radiation shielding and safety implications following linac conversion to an electron FLASH-RT unit," *Medical Physics*, vol. 48, pp. 5396–5405, Sept. 2021.

[181] Z. Xiao, Y. Zhang, J. Speth, E. Lee, A. Mascia, and M. Lamba, "Evaluation of a conventionally shielded proton treatment room for FLASH radiotherapy," *Medical Physics*, vol. 49, pp. 6765–6773, Nov. 2022.

[182] C. Schneider, W. Newhauser, and J. Farah, "An Analytical Model of Leakage Neutron Equivalent Dose for Passively-Scattered Proton Radiotherapy and Validation with Measurements," *Cancers*, vol. 7, pp. 795–810, May 2015.

[183] T. A. M. Masilela, R. Delorme, and Y. Prezado, "Dosimetry and radioprotection evaluations of very high energy electron beams," *Scientific Reports*, vol. 11, p. 20184, Oct. 2021.

[184] "Décret n° 2018-437 du 4 juin 2018 relatif à la protection des travailleurs contre les risques dus aux rayonnements ionisants," June 2018.

[185] B. B. Sorcini, S. Hyödynmaa, and A. Brahme, "Quantification of mean energy and photon contamination for accurate dosimetry of high-energy electron beams," *Physics in Medicine & Biology*, vol. 42, p. 1849, Oct. 1997.

[186] A. Brahme and H. Svensson, "Radiation Beam Characteristics of a 22 MeV Microtron," *Acta Radiologica: Oncology, Radiation, Physics, Biology*, vol. 18, pp. 244–272, Jan. 1979. Publisher: Taylor & Francis _eprint: https://doi.org/10.3109/02841867909128212.

[187] M. E. Masterson, C. S. Chui, R. Febo, J. D. Hung, Z. Fuks, R. Mohan, C. C. Ling, G. J. Kutcher, S. Bjork, and J. Enstrom, "Beam characteristics of a new generation 50 MeV racetrack microtron," *Medical Physics*, vol. 22, pp. 781–792, June 1995.

[188] A. Brahme and H. Svensson, "Specification of electron beam quality from the central-axis depth absorbed-dose distribution," *Medical Physics*, vol. 3, no. 2, pp. 95–102, 1976.

[189] P. Adrich, "A new method for designing dual foil electron beam forming systems. I. Introduction, concept of the method," *Nuclear Instruments and Methods in Physics Research Section A: Accelerators, Spectrometers, Detectors and Associated Equipment*, vol. 817, pp. 93–99, May 2016.

[190] P. Adrich, "Technical Note: Monte Carlo study on the reduction in x-ray contamination of therapeutic electron beams for Intraoperative Radiation Therapy by means of improvements in the design of scattering foils," *Medical Physics*, vol. 46, pp. 3378–3384, Aug. 2019.

[191] U. Deut, M. G. Ronga, A. Bonfrate, and L. De Marzi, "Secondary radiation dose modeling in passive scattering and pencil beam scanning very high energy electron (VHEE) radiation therapy," *Medical Physics*, vol. n/a, no. n/a. _eprint: https://onlinelibrary.wiley.com/doi/pdf/10.1002/mp.16443.

[192] T. C. Zhu, I. J. Das, and B. E. Bjärngard, "Characteristics of bremsstrahlung in electron beams," *Medical Physics*, vol. 28, pp. 1352–1358, July 2001.

[193] A. M. M. Leite, M. G. Ronga, M. Giorgi, Y. Ristic, Y. Perrot, F. Trompier, Y. Prezado, G. Créhange, and L. De Marzi, "Secondary neutron dose contribution from pencil beam scanning, scattered and spatially fractionated proton therapy," *Physics in Medicine and Biology*, vol. 66, Nov. 2021.

[194] C. Lee, D. Lodwick, J. Hurtado, D. Pafundi, J. L. Williams, and W. E. Bolch, "The UF family of reference hybrid phantoms for computational radiation dosimetry," *Physics in Medicine and Biology*, vol. 55, pp. 339–363, Jan. 2010.

[195] J. Valentin, "Basic anatomical and physiological data for use in radiological protection: reference values: ICRP Publication 89," *Annals of the ICRP*, vol. 32, pp. 1–277, Sept. 2002.

[196] J. A. Scott, "Photon, Electron, Proton and Neutron Interaction Data for Body Tissues: ICRU Report 46. International Commission on Radiation

Units and Measurements, Bethesda, 1992, $40.00," *Journal of Nuclear Medicine*, vol. 34, pp. 171–171, Jan. 1993. Publisher: Society of Nuclear Medicine Section: Departments.

[197] C. Nioche, F. Orlhac, S. Boughdad, S. Reuzé, J. Goya-Outi, C. Robert, C. Pellot-Barakat, M. Soussan, F. Frouin, and I. Buvat, "LIFEx: A Freeware for Radiomic Feature Calculation in Multimodality Imaging to Accelerate Advances in the Characterization of Tumor Heterogeneity," *Cancer Research*, vol. 78, pp. 4786–4789, Aug. 2018.

[198] D. Gur, A. G. Bukovitz, and C. Serago, "Photon contamination in 8–20-MeV electron beams from a linear accelerator," *Medical Physics*, vol. 6, no. 2, pp. 145–146, 1979. _eprint: https://onlinelibrary.wiley.com/doi/pdf/10.1118/1.594525.

[199] R. Sayah, J. Farah, L. Donadille, J. Hérault, S. Delacroix, L. D. Marzi, A. D. Oliveira, I. Vabre, F. Stichelbaut, C. Lee, W. E. Bolch, and I. Clairand, "Secondary neutron doses received by paediatric patients during intracranial proton therapy treatments," *Journal of Radiological Protection*, vol. 34, p. 279, Apr. 2014. Publisher: IOP Publishing.

[200] Y. Prezado, "Divide and conquer: spatially fractionated radiation therapy," *Expert Reviews in Molecular Medicine*, vol. 24, p. e3, Jan. 2022. Publisher: Cambridge University Press.

[201] J. Reindl and S. Girst, "pMB FLASH - Status and Perspectives of Combining Proton Minibeam with FLASH Radiotherapy," *Journal of Cancer Immunology*, vol. Volume 1, pp. 0–0, Oct. 2019. Number: Issue 1 Publisher: Scientific Archives.